Quantum Many-Body Effects in the Optoelectronic Response of Plasmonic Nanostructures and their Coupling to Quantum Emitters

Antton Babaze Aizpurua

PhD Thesis, September 2022

eman ta zabal zazu

Universidad del País Vasco

Euskal Herriko Unibertsitatea

EUSKAL HERRIKO UNIBERTSITATEA
THE UNIVERSITY OF THE BASQUE COUNTRY

Department of Electricity and Electronics

CAMPUS OF INTERNATIONAL EXCELLENCE

Quantum Many-Body Effects in the Optoelectronic Response of Plasmonic Nanostructures and their Coupling to Quantum Emitters

Thesis by

Antton Babaze Aizpurua

Supervised by

Prof. Javier Aizpurua Iriazabal

and

Dr. Rubén Esteban Llorente

Donostia-San Sebastián, September 2022

Ama eta Aitari,
tesi honen oinarri sendoak ezartzeagatik.

ACKNOWLEDGMENTS

Han pasado casi cinco años desde el 2 de octubre de 2017, primer día que acudí a la oficina de Rubén, por aquel entonces en el DIPC. Javi estaba en algún viaje de los suyos. Aquel día empezaba mi primer trabajo "serio", donde me pagaban por "estudiar". Me pagaban poco para mi gusto, pero eso es otro tema. Ese primer día Rubén me imprimió unos 10 artículos, no sé cuántas hojas en total (muchas), "para que vayas leyendo y haciéndote una idea", me decía. Antes de imprimirlos, claro, me explicó lo mejor que pudo de qué iban esos artículos y cómo se relacionaban con lo que iba a ser mi tesis. Tesis que culmino ahora, cinco años más tarde, con estas palabras de agradecimiento. También me mostró uno por uno los posters que había colgados en la pared del pasillo en el CFM. Creo que fingí bastante bien que más o menos estaba siguiendo lo que me decía, pero he de confesar que, en realidad, no estaba entendiendo nada. No sé si Rubén era consciente de ello, puede que sí. Tardé unos cuantos meses en saber, por ejemplo, qué era un plasmón. Creo que ahora puedo afirmar que entiendo los artículos que me imprimió hace cinco años como referencia. En gran parte, gracias al constante aprendizaje que he recibido por parte de Rubén. No sabes cuánto tiempo tardé en averiguar cómo se relacionaban las pelotitas de metal iluminadas con láser con el par de muelles acoplados que oscilan siguiendo las ecuaciones que aprendimos en segundo de carrera. Además, aparte de haber sido capaz de entender aquellos artículos, me siento bastante orgulloso de haber contribuido, aunque sea mínimamente, en el campo de la plasmónica. Contribuciones que no serían posibles sin tu conocimiento, trabajo incansable, y esfuerzo por enseñarme. Gracias, Rubén.

A los pocas días de empezar mi doctorado entró Javi en escena. Fue en un café en el DIPC. De primeras supe que iba a ser muy sencillo tratar con él como supervisor. Y así ha sido. Por supuesto, no sabía ni que era el director del CFM ni que era un tío tan conocido en el campo de la Nanofotónica, con un índice h de no sé cuánto. Me hacía mucha gracia cuando, en las conferencias, todo el mundo me decía: "Of course I know Javier Aizpurua". Al principio no sabía muy bien por qué. Tampoco sabía la importancia que iba a tener Javi en mi tesis, que desde luego ha sido mucha. Urte hauetan zehar, sarritan izan dut gogoan Pernando Amezketarraren marrazki bizidunetan behinola entzundako esaldia: "Galdera zailik ez dago, erantzunak dira zailak". Denon artean, hain errazak ez ziren erantzun batzuk sikiera topatu ditugu. Ez dago gaizki. Horretan, pisu handia izan duzu zuk, Javi. Eskerrik asko urte hauetan irakatsitako guztiarengatik: zientzian eta

zientziatik kanpo irakatsitakoagatik. Punta-puntako talde batean ikertzeko aukera emateagatik. Nire ikerketa-lana maisuki gidatzeagatik. Arazo txikien aurrean beti irtenbiderik hoberena bilatzeagatik. Nire lana aurrera ateratzeko egindako esfortzuarengatik. Nire alde egindako apustuarengatik. Eskerrik asko, Javi.

In May 2018, just seven months after I started with my PhD thesis, I had the opportunity to meet Andrei Borisov in ISMO, Orsay. Andrei has been my third supervisor, along with Rubén and Javi. He has been the key person in this thesis. The one who has taught me everything I know about TDDFT and quantum many-body approach to plasmonics. All the research in this thesis has been carried out together with Andrei. Thank you for sharing with me your WPP codes. Thank you for your patience, guidance, and willingness to teach me. Willingness to discuss with me. So many calls. So many e-mails (321 during the last four years). Only one remark: I think we shouldn't refer to sodium as "a simple metal". This thesis is also yours. Thank you, Andrei.

Si he tenido suerte con los supervisores de mi tesis, he tenido aún mucha más suerte con los compañeros de trabajo que he tenido en el CFM. Compañeros de trabajo que son ahora amigos. No recuerdo en qué tesis leí que los agradecimientos son la parte más difícil de escribir. Para nada. Me resulta verdaderamente fácil escribir estas líneas de forma honesta. Habéis sido la hostia. Creo que nunca tendré un trabajo donde vaya todos los días con tantas ganas a trabajar. Ha sido súper divertido haber compartido tantos momentos con vosotros. Dentro del trabajo, y por supuesto, fuera. Con el riesgo de olvidarme de gente importante, procedo a nombrar a varios de vosotros.

Empiezo por Álvaro, Alvariño, mi masajista particular. Compañero de doctorado desde el principio hasta el final. Compañero en las clases magistrales de Rubén. Cómo me aliviaba saber que tú tampoco te enterabas de mucho al principio. No sé en qué punto empezamos a investigar cosas tan distintas, cuando al principio parecía que estudiábamos exactamente lo mismo: el dipolo junto a la pelotita. Ha sido un placer haber hecho todo el doctorado contigo, haber charlado sobre ciencia, y, sobre todo, haber charlado sobre tantas otras cosas fuera de la ciencia. Muchos buenos momentos fuera de la oficina. Viajes. También dentro de la oficina. Muchas risas. Muchas estupideces. Mucho tiempo "perdido", pero con mucho gusto. Suerte con tu tesis, tío. En nada lo tienes.

Continúo con los demás muchachos de la oficina. Carlos, Charly, Carlitos. Teoremán. Qué capacidad, wey. Siempre que he tenido alguna duda sobre física o matemática, ahí estabas tú con tus teoremas. Sé que muchos eran inventados, aunque nunca lo reconozcas. A ver cuándo me pones de autor en uno de tus papers. Un máquina con inkscape y blender. Cuando nadie te ve, claro. Nunca olvidaré todos esos días de charleta en la oficina cuando todo el mundo ya se había marchado a casa. O los skypes durante la pandemia. O aquellos días previos a Navidad, cuando nos quedábamos los dos solos trabajando y tú ponías villancicos a todo volumen fingiendo ser feliz. Yo me lo pasaba bien. Jon, Joneto, qué tío. Siempre dispuesto a ayudar en lo que sea, pero también a sacarle punta a todo lo que digo. Berdin du nik zer esan, beti egongo zarela kontran. Un titán. Dibertigarria izan da jokoa, benetan. Jarraitu horrela, motel. Bruno, el más listo del CFM. Seguramente

también el más rápido con el coche. Haciendo TDDFT como yo, pero bien. Zorte on doktoretzarekin. Adrián, el más gracioso, otro que se quedaba haciendo guardia hasta bien tarde en la oficina del CFM. Jonathan, con ese humor tan particular, siempre "hueveando".

Cambiemos de oficina. Mikel, Mikelats, Hondarribiko bizilaguna. Tipo bikaina. Denetan ona. Plazera izan da tesia zurekin batera egitea. Zorte on zuri ere, aurki bukatuko duzula. Jorge, otro grande. A ver cuándo te sacas el título de euskera. Ha sido un auténtico placer intercambiar tantos y tantos vaciles por parte de los dos. Ejemplo a seguir en muchas cosas. Roberto, Rober, ídolo. Me he reído mucho contigo, eta asko eskertzen dut euskararekin egiten duzun ahalegina. Ez nuen espero Asturiar batekin euskaraz hitz egiten bukatuko nuenik. Martín, Martini, qué buena filosofía la tuya. Puntualidad ante todo, claro que sí. Muy buen chorizo, sí señor. Miriam, qué simpatía, qué felicidad. Iker, mi Bilbaino favorito. Lástima la última Copa. Gracias por haberme dejado vacilarte tanto. Gracias a otros muchos también: Mattin, Fernando, Sofía, Josu, Joseba, Cris, Mario, Raulillo, Edurne, Txemikel... Todos vosotros habéis conseguido que haya sido una gozada trabajar en esta tesis.

Lanean egindako lagunez gain, lanetik kanpo ditudan lagunak ere aipatu nahi nituzke. Lerro gutxietan bada ere. Irungo betiko lagunak. Artalekuko Hintxak. Muerte a los Geólogos. Simon-eneako Cortijeroak. Hulk. Kemenkideak. Dultzaineroak. "Noiz entregatzen duzu proiektua?"; "Zer moduz daramazu master-a?"; "Joe, doktoretza fisikan! Ze zaila, ez?"; "Nola doaz zure super-ordenagailuan egindako kalkulu luze horiek?"; "Baina, tira, zurea ez da "lana-lana", ez?"; "Zertan datza zure tesiak? Baina tontoentzako moduan, eh!". Eskerrik asko denoi.

Bukatzeko, lerro batzuk eskaini nahi dizkiet tesi honen benetako euskarri izan zaretenei: etxekoei. Tesi hau zuena da. Zuek gabe ez nuke sekula tesi hau aurrera aterako. Ama, horrenbeste gauza irakasteagatik. Nik hartutako erabaki guztiak babesteagatik. Nire helburuak betetzeko beti zure esku dagoen guztia egiteagatik. Ez dut inoiz ahaztuko momentu zailetan egindako esfortzua. Ondo dakizu zertaz ari naizen. Aita, bizitzan bide onetik noala behin eta berriro azpimarratzeagatik. Niregan beti jarrera kritikoa bultzatzeagatik. Gauzak esfortzuarekin ateratzen direla irakasteagatik. Niregan duzun konfiantzagatik. Iñaki, zuregandik jasotako animo eta laudorioengatik. Nire tesiaz, eta bizitzaz, horrenbeste arduratzeagatik. Gure bizitzetan azaltzeagatik. Peio, beti animoak emateko prest egoteagatik. Nire lorpen txikiekin ni bezain beste pozteagatik. Azken urteetan lanetik kanpoko bizitza askoz atseginagoa egiteagatik. Jokin, inoiz aitortu ez arren, txikitatik gauza askotan nire eredu izateagatik. Horrenbeste gauza irakasteagatik. Mundu akademikoan sartzera animatzeagatik. Aizpea, zer esan. Ezagutzen dudan pertsonarik onena izateagatik. Bizitzan ausardia izan behar dela irakasteagatik. Beti nire ondoan egoteagatik. Bihotz-bihotzez, eskerrik asko denoi.

Irun-Donostia, 2022ko iraila.

Antton Babaze Aizpurua

LABURPENA

Argiaren eta materiaren arteko elkarrekintza aspalditik izan da aztergai zientzialarientzat. Esaterako, 1850eko hamarkadan, Michael Faraday-k aurkitu zuen tamaina nanometrikoko urrezko partikulek eta bolumen handiko urrezko egiturek propietate optiko oso desberdinak dituztela [1]. Propietate optiko berezi horiek dira, adibidez, urre-errubi beiraren kolore gorri distiratsua sortzen dutenak [2, 3]. Aurkikuntza haren azalpen fisikoa Gustav Mie-k eman zuen zenbait urte geroago [4], 1908an, James Clerk Maxwell-en teoria elektromagnetikoa [5] erabiliz urrezko nanopartikula txikien sakabanatze-propietateak aztertu zituenean [6–8]. Nanopartikula metaliko txiki hauek argia maiztasun jakin batzuetan (normalean espektro ikusgaian) modu eraginkorrean barreiatzen dutela aurkitu zuen Mie-k; maiztasun hauek materialaren, partikularen tamainaren eta ingurune dielektrikoaren propietateen araberakoak izanik [9]. Maiztasun jakin horiek gainazaleko plasmoi lokalizatuei dagozkie [10–12], argiaren bidez kitzika daitezkeen nanopartikula metalikoen gainazaleko karga-oszilazioen erresonantziei, alegia [13–16].

Azken urteetan, nanopartikula metalikoen plasmoi erresonantziek interes handia piztu dute Nanofotonika alorrean [17–19], uhin elektromagnetiko erasotzailearen anplitudea areagotzeko eta argia uhin-luzera baino eskualde txikiagoetan lokalizatzeko duten ahalmena dela-eta [20–22]. Adibidez, bi nanopartikula metalikoren arteko eskualde nanometrikoan (nanobarrunbe plasmoniko deiturikoa, *nanogap* edota *nanocavity* ingelesez), eremu elektromagnetikoaren anplitudea 100-1000 aldiz handitu daiteke [23]. Ondorioz, gaur egun plasmoi erresonantziak asko erabiltzen dira hainbat espektroskopia eta mikroskopia tekniketan, hala nola gainazalak areagotutako Raman espektroskopian (*surface-enhanced Raman spectroscopy*) [24], gainazalak areagotutako fluoreszentzian (*surface-enhanced fluorescence*) [25–27], edota molekula bakarren detekzioan (*single-molecule imaging*) [28, 29]. Gainera, plasmoi erresonantziek aplikazio itxaropentsuak dituzte, besteak beste, biomedikuntzan [30–32], energiaren biltegiratzean [33–35], edota optika ez-linealean [36, 37].

Efektu plasmonikoak elektromagnetismo klasikoaren teoriaren testuinguruan aztertu izan dira batik bat [38–45], non argiaren eta materiaren arteko elkarrekintza Maxwell-en ekuazioek deskribatzen duten eta sistemaren erantzun optikoa, oro har, linealtzat jotzen den [6]. Hala ere, egungo konfigurazio esperimentaletan (nanopartikula benetan txikiak, partikulen arteko distantziak azpi-nanometrikoak

izanik), fenomeno kuantikoek sistemaren propietate optikoetan eragina dutela behatu da [46–52]. Egoera horietan, deskribapen klasikoek ez dituzte erantzun optikoaren aspektu guztiak ongi deskribatzen [53–55], eta beraz, hurbilketa teoriko berrien beharra dago. Hurbilketa horiek sistemaren erantzun optikoaren ez-lokaltasuna [56–60], elektroien gainazaleko isurpena (*electron spill out*) [61–63], gainazalak ahalbidetutako Landau indargetzea (*surface-enabled Landau damping*) [64–66], edota elektroien tunel efektua (*electron tunneling*) [67, 68] hartu behar dituzte kontuan egitura plasmoniko txikien propietate optikoak behar bezala deskribatzeko.

Tesi honetan, denboraren menpeko dentsitatearen funtzionalaren teoria (*time-dependent density functional theory*, TDDFT, ingelesez) [69–72] izango da sistema nanometrikoen erantzun optikoa aztertzeko aukeratuko dugun metodoa, teoria honek elektroien dinamikaren izaera kuantikoa kontuan hartzen baitu nanopartikula metalikoaren elektroi-dentsitatearen eboluzioa denboran aztertuz [73]. Gainera, TDDFT kalkuluak ez dira soilik erantzun optiko lineala aztertzera mugatzen; izan ere, sistema plasmonikoen erantzun ez-lineala zuzenean lortzeko aukera ematen du TDDFT-k [74–78]. Beraz, TDDFT oso tresna erabilgarria da erantzun optiko eta elektronikoan (hots, optoelektronikoan) azaltzen diren fenomeno kuantikoak aztertzeko, eta tesi honen ardatz nagusia izango da. Bestalde, konplexutasun konputazionala dela-eta, TDDFT bidez atomo gutxi batzuez (apurka milaka atomoz) osatutako sistema txikiak baino ezin dira aztertu [79, 80], eta horregatik, hainbat eredu semiklasiko ere garatu izan dira zenbait efektu kuantiko deskribatzeko [81, 82]. Besteak beste, nanobarrunbe azpi-nanometrikoetan ematen den elektroien tunel efektua kontuan hartzen duen *Quantum-corrected model* eredua [83–87], nanoegitura metalikoen erantzun optikoaren ez-lokaltasuna barne hartzen duten deskribapen hidrodinamikoak [88–94], eta *surface-response formalism* (SRF) [95–97] aipa ditzakegu hemen. SRF eredu semiklasikoak metalaren eta ingurune dielektrikoaren arteko gainazalean deskribapen kuantikoetan oinarritutako zuzenketak ezartzen ditu [98] (Feibelman-en $d_\perp(\omega)$ eta $d_\parallel(\omega)$ parametroak), horrela gainazalean induzitutako elektroi-dentsitatearen isurpena eta Landau indargetzea kontuan hartuz. TDDFT-rekin batera, tesi honetan SRFean oinarritutako simulazioak ere burutuko ditugu.

TDDFT eta aipatutako eredu semiklasikoak sarritan erabiltzen dira nanoegitura plasmoniko isolatuen erantzun optikoa aztertzeko, baina nanoegitura plasmonikoen eta igorle kuantikoen (*quantum emitter* ingelesez, hala nola atomoak, puntu kuantikoak, edota molekula organikoak) arteko elkarrekintza optoelektronikoa aztertzeko ere erabil daitezke. Nanoegitura plasmoniko eta igorle kuantiko batez osatutako sistema akoplatua oso sistema garrantzitsua da Nanofotonikan, eremu plasmonikoaren areagotze eta konfinamenduari esker igorle kuantikoak argiarekin askoz modu eraginkorragoan akoplatzen baitira, fenomeno interesgarri ugari sortuz [99, 100]. Efektu horietako batzuk kalkulu klasikoen bidez deskriba daitezke, hala nola, igorle kuantikoaren igorpen-tasa espontaneoaren handitzea (*Purcell effect* [101, 102]), edota erresonantzia-maiztasunaren aldaketa (*Lamb shift*, [103, 104]). Bestalde, egitura plasmoniko baten eta igorle kuantiko baten arteko elkarrekintzak egoera elektronikoen akoplamendu kuantikoa sor dezake, zeinak

igorlearen propietate kimikoak alda ditzakeen [105], nanopartikulen eta igorlearen arteko elektroi-transferentzia eragin dezakeen [106–109], edota sistema akoplatuaren erantzun optiko ez-lineala alda dezakeen [110, 111].

Tesi honek nanoegitura plasmonikoen erantzun optoelektronikoan eta igorle kuantikoekin duten interakzioan azaltzen diren fenomeno kuantiko berriak teorikoki aztertzea du helburu. Hala, tamaina nanometriko edo txikiagokoak diren egitura plasmonikoetan gertatzen diren efektu kuantikoei buruzko oinarrizko ezagutza sakonagoa bilatuko dugu, non ez-lokaltasunak, ez-linealtasunak edo elektroi-transferentzia efektuek zeresan handia izan dezaketen. Horretarako, TDDFT simulazioak erabiliko ditugu batez ere, baina erantzun optiko lokalean oinarritutako kalkulu klasikoak eta SRFean oinarritutako eredu semiklasikoak ere erabiliko ditugu emaitzen analisia errazteko eta informazio osagarria erdiesteko.

1. kapituluan, argiaren eta materiaren arteko elkarrekintza klasikoaren oinarriak berrikusiko ditugu, eta tesi honetan garrantzitsuak izango diren oinarrizko kontzeptuak ikuspegi klasikotik deskribatuko ditugu. Nanopartikula metaliko esferikoek eta haien dimeroek sostengatutako gainazaleko plasmoien deskribapen klasikoan jarriko dugu arreta, eta baita nanoegitura plasmonikoen eta igorle kuantikoen arteko elkarrekintza elektromagnetikoan ere. Beraz, 1. kapituluan azaldutako kontzeptuek argiaren eta materiaren arteko elkarrekintza klasikoaren oinarriak eskainiko dituzte, eta erreferentzia gisa balioko dute gerora deskribapen klasikoetatik at dauden fenomeno kuantikoak aztertzeko.

2. kapituluan, tesi honetan erabilitako TDDFT metodologia eta *surface-response formalism* (SRF) delako eredu semiklasikoa aurkeztuko ditugu, argiaren eta materiaren arteko elkarrekintzan azaltzen diren efektu kuantikoak aztertzeko erabilgarri izango direnak. Gainera, tesi honetan berebiziko garrantzia izango duten efektu kuantikoak deskribatuko ditugu, hala nola, elektroien tunel efektua, gainazalak ahalbidetutako Landau indargetzea, eta gainazalean induzitutako elektroi-dentsitatearen isurpena. Horretarako, nanoegitura plasmoniko kanonikoen erantzun optikoa aztertuko dugu. Beraz, 2. kapituluan azaldutako metodologiek eta kontzeptuek argiaren eta materiaren arteko elkarrekintzaren ikuspegi kuantikoaren oinarriak ezarriko dituzte, eta erreferentzia gisa balioko dute hurrengo kapituluetan nanoegitura plasmonikoen eta igorle kuantikoen arteko akoplamendu optiko eta elektronikoen ondorioz sortutako fenomeno kuantiko berriak aztertzeko.

3. kapituluan, nanopartikula esferikoen eta igorle kuantikoen arteko akoplamendu elektromagnetikoa aztertuko dugu, igorlearen eta nanopartikularen arteko akoplamendu elektronikoaren eragina baztertu daitekeen egoeretan. Igorle kuantikoa, kasu honetan, dipolo puntual bat bezala deskribatuko dugu. TDDFT erabiliko dugu (elektroi-askeko metalen *jellium* eredua baliatuz) nanopartikulen eta igorleen arteko elkarrekintza elektromagnetikoan presente dauden gainazaleko efektu kuantikoen eragina aztertzeko. Gainazaleko efektu kuantikoak direla-eta elkarrekintza elektromagnetikoa deskribatzen duen auto-elkarrekintzako Green-en funtzioan (*self-interaction Green's function*) plasmoi erresonantziak asko aldatzen direla erakutsiko dugu. Izan ere, gainazaleko Landau indargetzeak eta induzitutako karga-dentsitatearen isurpenak kalkulu klasikoek deskriba ezin ditzaketen plasmoi erresonantzien zabalketa eta gorriranzko lerrakuntza eragiten dituztela ikusiko dugu.

Gainera, egoera gehienetan Feibelman-en $d_\perp(\omega)$ parametroan oinarritutako SRF eredu semiklasiko estandarra (gainazal metalikoarekiko paralelo den norabidean erantzun optikoaren ez-lokaltasuna arbuiatzen duena) gainazaleko efektu kuantikoak deskribatzeko metodologia zehatza dela erakutsiko dugu. Hala ere, igorlearen eta nanopartikulen arteko distantzia oso txikietarako SRF eredu semiklasiko estandarra guztiz zehatza ez dela erakutsiko dugu.

4. kapituluan, SRF eredu semiklasiko estandarraren gabeziak gainditzen dituen SRF eredu dispertsiboa (*dispersive SRF*) proposatuko dugu, zeinak gainazal metalikoan zehar norabide paraleloan erantzun optikoaren ez-lokaltasuna esplizituki kontuan hartzen duen. Horretarako, Feibelman-en parametroak $k_\parallel$ uhin-zenbaki paraleloarengan daukan menpekotasuna hartuko dugu kontuan. Lehenik eta behin, TDDFT simulazioak erabiliko ditugu nanohari metaliko (*metallic nanowire*) baten erantzun optikoa lortzeko *jellium* eredua baliatuz. Emaitza horiek Feibelman-en $d_\perp(\omega, k_\parallel)$ parametroa kalkulatzeko erabiliko ditugu, ω kanpo-kitzikapenaren maiztasunaren eta gainazal metalikoarekiko paraleloa den $k_\parallel$ uhin-zenbakiaren menpekoa dena. Gainera, nanohari zilindriko baten zein nanopartikula esferikoen erantzun optikoa aztertuko dugu $d_\perp(\omega, k_\parallel)$ erabiliz, eta erakutsiko dugu kapitulu honetan proposatutako SRF eredu dispertsiboa gai dela eskualde oso txikietan lokalizatutako eremu plasmonikoak induzitzen diren egoeretan sistemaren ez-lokaltasuna deskribatzeko, betiere karga-transferentzia prozesuek eta efektu ez-linealek parte hartzen ez badute.

5. kapituluan, bi maila elektronikoko igorle kuantiko baten eta bi nanopartikula metaliko esferikoz osatutako dimero baten arteko akoplamendu elektronikoaren eragina aztertuko dugu, elkarrekintza elektromagnetiko estandarraz gain. Igorlearen eta nanopartikulen arteko akoplamendu elektronikoa deskribapen klasikoetan arbuiatu ohi da, eta baita beste eredu semiklasikoetan ere, hala nola, 3. eta 4. kapituluetan erabilitako SRFean (non igorlea dipolo puntual gisa deskribatzen den). Sistema hibrido osorako TDDFT kalkuluak erabiliz, igorlearen eta nanoegituraren egoera elektronikoen arteko hibridazioak sistema akoplatuaren erresonantzia optikoen maiztasuna eta zabalera erabat aldatzen dituela erakutsiko dugu. Izan ere, igorle kuantikoaren exzitoiaren kitzikapena ikaragarri ahultzen dela erakutsiko dugu igorlearen eta nanoegitura metalikoen arteko gainazaletik-gainazalerako distantzia 0.5 nm baino txikiagoa denean. Hortaz, nanobarrunbe azpi-nanometrikoen erantzun optoelektronikoa modu zehatzean aztertzeko igorlearen eta nanoegituraren arteko elektroi-transferentzia prozesuak egoki deskribatzen dituen tratamendu kuantikoen aplikazioa beharrezkoa dela ondorioztatuko dugu.

6. kapituluan, igorle kuantiko batez eta nanopartikula metaliko esferiko batez osatutako sistemaren erantzun optiko ez-lineala aztertuko dugu, bigarren harmonikoaren sorkuntzan (*second-harmonic generation*, SHG) arreta jarriz. Igorlearen trantsizio elektronikoaren maiztasuna argi erasotzailearen maiztasunaren bigarren harmonikoarekin erresonantzian dagoenean, igorleak SHG nabarmena ahalbidetzen duela erakutsiko dugu. Nanopartikula esferikoaren inbertsio-simetria dela-eta, igorlearen presentziarik gabe ezin daiteke SHG-ik lortu. TDDFT kalkuluen bidez, efektu ez-lineal hori bultzatzen duen mekanismo nagusia identifikatuko dugu, non igorleak gertu dagoen nanopartikula metalikoak sortutako eremu elektriko

ez-linealak sentitzen dituen, horrela erresonadore optiko baten papera jokatuz. Gainera, TDDFT eta kalkulu klasikoak konbinatuz, prozesu ez-lineal honen eragina eta ekarpen nagusiak jasotzen dituen eredu semi-analitiko bat garatuko dugu, konputazionalki TDDFT baino askoz sinpleago dena. Eredu semi-analitiko hau erabiliz, igorlearen eta nanopartikularen posizioa eta propietate intrintsekoak aldatuz sistema honetan SHG kontrolatu daitekeela erakutsiko dugu.

Beraz, tesi honetan nanoegitura plasmonikoen eta igorle kuantikoen erantzun optikoaren inguruko azterketa mekaniko-kuantikoa aurkeztuko dugu, non elektroi-transferenzia prozesuek, gainazaleko efektu kuantikoek, eta prozesu ez-linealek garrantzia handia dutela erakutsiko dugun. Efektu horiek guztiek berebiziko garrantzia dute gaur egungo Nanofotonikan. Espero dugu tesi honetan egindako ikerketak igorleen eta egitura plasmonikoen arteko elkarrekintzaren oinarrizko ezagutza sakonagoa lortzen laguntzea. Gainera, ziurrenik tesi honetan aurkeztutako emaitzek galdera berriak ere sortuko dituzte, hemen erabili eta proposatuko ditugun metodologiekin aztertu litezkeenak. Besteak beste, uste dugu uhin-paketeen hedapenean (*wave-packet propagation*) oinarritutako TDDFT metodologia aplika daitekeela, adibidez, dimentsio azpi-nanometrikoko plasmoi–exzitoi sistemetan eman daitezkeen prozesu optoelektroniko ez-linealak aztertzeko, bai eta pultsu ultra-bizkorrek (*ultrafast pulse*) kitzikaturiko nanobarrunbe plasmonikoetan karga-transferentzia efektuak aztertzeko ere. Gainera, gure iragarpenen zehaztasun kuantitatiboa hobetu liteke nanoegitura plasmonikoen eta igorle kuantikoen eskala atomikoko bereizitasunak kontuan hartuko balira, tesi honetan erabilitako egitura elektronikoaren *jellium* deskribapenetik haratago joaz.

Bestalde, tesi honetan proposatutako SRF eredu dispertsiboa Nanofotonikan erabiltzen diren zenbakizko metodoetan modu nahiko errazean inplementa daitekeela espero dugu, eta, beraz, tresna baliotsua bihur daitekeela efektu optiko ez-lokalak nanoeskalako konfigurazio plasmoniko esperimentaletan aurreikusteko. Esperimentuetan normalean erabiltzen diren sistemak kontuan hartzeko, Feibelmanen $d_\perp(\omega, k_\parallel)$ parametro dispertsiboa $k_\parallel$-ren funtzioan kalkulatu beharko litzateke. Plasmonikan garrantzitsuak diren materialetan, hala nola zilarra edo urrea, d elektroi-bandako trantsizioek eragin handia dute erantzun optikoan, non induzituriko elektroi-dentsitatea gainazaletik kanpo isuri beharrean barrurantz isurtzen den. Tesi honetan erabilitako *jellium* ereduak d-elektroien eragina arbuiatzen du; beraz, eredu sofistikatuagoak edo egungo *jellium* ereduaren hobekuntzak beharko lirateke Feibelman-en parametroak kalkulatzeko eta, horrela, tesi honetan proposatutako SRF eredu dispertsiboa egungo egoera esperimentaletan erabil ahal izateko. Oro har, espero dugu tesi honetan aurkeztutako TDDFT metodologia kuantikoa eta SRF metodologia semiklasikoa etorkizunean erabil ahal izango direla Nanofotonikan fenomeno kuantiko berriak ikertzeko eta, horrela, aurrerapen teknologikoetan laguntzeko.

LIST OF ABBREVIATIONS

ALDA	Adiabatic local-density approximation
au	Atomic units
BDP	Bonding dipolar plasmon
BQP	Bonding quadrupolar plasmon
CTP	Charge-transfer plasmon
DFG	Difference-frequency generation
DFT	Density functional theory
DP	Dipolar plasmon
FGH	Fourier grid Hamiltonian
FWHM	Full width at half maximum
HOMO	Highest occupied molecular orbital
KS	Kohn–Sham
LDA	Local-density approximation
LR	Lower resonance
LRA	Local-response approximation
LSPP	Localized surface plasmon polariton
LUMO	Lowest unoccupied molecular orbital
MNP	Metallic nanoparticle
OP	Octupolar plasmon
PDOS	Projected density of electronic states
QE	Quantum emitter
QP	Quadrupolar plasmon
RHS	Right-hand side
SFG	Sum-frequency generation
SHG	Second-harmonic generation
SI	International system of units
SPP	Surface plasmon polariton
SRF	Surface-response formalism
TDDFT	Time-dependent density functional theory
THG	Third-harmonic generation
UR	Upper resonance
WPP	Wave-packet propagation

Contents

Acknowledgments **v**

Laburpena **ix**

List of abbreviations **xv**

Introduction **1**

1 Classical description of light–matter interaction **5**
1.1 Maxwell's equations 5
1.1.1 The local-response approximation 7
1.1.2 Boundary conditions 9
1.1.3 The nonretarded approximation 11
1.2 Plasmonics 16
1.2.1 Bulk plasmons 16
1.2.2 Surface plasmons and surface plasmon polaritons 17
1.2.3 Localized surface plasmon polaritons (LSPPs) 18
1.3 Nonlinear optical response of small nanostructures 24
1.4 Plexcitonics: Quantum emitter excitons coupled to plasmons . . . 27
1.4.1 The point-dipole approximation 28
1.4.2 The self-interaction dyadic Green's function 28
1.4.3 Coupled harmonic-oscillator model 31
1.5 Summary 34

2 Quantum many-body description of light–matter interaction **35**
2.1 Fundamentals of density functional theory (DFT) 36
2.1.1 The local-density approximation (LDA) 38
2.1.2 The jellium model of free-electron metals 39
2.2 Fundamentals of time-dependent density functional theory (TDDFT) 41
2.2.1 The wave-packet propagation (WPP) method 42
2.3 Linear optical response of canonical plasmonic nanostructures addressed within TDDFT 48
2.3.1 Individual spherical metallic nanoparticles 49
2.3.2 Dimers of spherical metallic nanoparticles 55
2.3.3 Cylindrical metallic nanowires 61

2.4 Nonlinear effects in the optical response of spherical plasmonic nanoparticles addressed within TDDFT 65
2.5 Semiclassical surface-response formalism (SRF) 69
2.5.1 Optical response of spherical nanostructures using the SRF 72
2.6 Summary 75

3 Quantum surface effects in the electromagnetic coupling between quantum emitters and metallic nanoparticles 77
3.1 System and methods 78
3.1.1 Time-dependent density functional theory (TDDFT) 80
3.1.2 Classical local-response approximation (LRA) 82
3.1.3 Semiclassical surface-response formalism (SRF) 82
3.2 Results and discussion 83
3.2.1 Quantum TDDFT vs. classical LRA 84
3.2.2 Quantum TDDFT vs. semiclassical nondispersive SRF . . . 87
3.2.3 Interpretation of the quantum effects within the nondispersive SRF and its limitations 88
3.2.4 Quantum TDDFT vs. nondispersive SRF in a nanoparticle dimer 91
3.3 Summary 94

4 Dispersive surface-response formalism to address optical nonlocality in situations of extreme plasmonic field confinement 97
4.1 System and methods 98
4.2 Results and discussion 101
4.2.1 TDDFT study of the energy dispersion of multipolar plasmon resonances in a metallic nanowire 101
4.2.2 Calculation of the dispersive Feibelman parameter $d_\perp(\omega, k_\parallel)$ 103
4.2.3 Validation of the dispersive SRF 107
4.3 Summary 112

5 Electronic exciton–plasmon coupling in a nanocavity beyond the electromagnetic interaction picture 115
5.1 System and methods 116
5.1.1 Characterization of the model quantum emitter (QE) . . . 118
5.2 Results and discussion 120
5.2.1 Influence of the QE exciton quenching at optical frequencies 120
5.2.2 Quantum finite-size effects vs. electronic QE–MNPs coupling 127
5.2.3 Charge-transfer resonances at low frequencies 128
5.3 Summary 130

6 Second-harmonic generation from a quantum emitter coupled to a metallic nanoparticle 131
6.1 System and methods 132
6.2 Results and discussion 134

6.2.1 TDDFT results 134
6.2.2 TDDFT vs. semi-analytical model 138
6.2.3 Influence of the intrinsic losses and the position of the QE on the efficiency of SHG 141
6.2.4 Polarization conversion of the second-harmonic field 146
6.3 Summary 147

Conclusions and Outlook **149**

Appendices

A Atomic units **155**

B Electric near field induced by a spherical nanoparticle within the classical local-response approximation (LRA) **157**

C Dynamics of quantum emitters in the time domain **159**

D Dispersive Feibelman parameter obtained for cylindrical nanowires of different size **163**

E Plasmon resonances sustained by a cylindrical nanowire within the surface-response formalism **165**

F Relationship between the results obtained under finite Gaussian pulses and plane-wave excitation **169**

List of publications **173**

Bibliography **175**

INTRODUCTION

The interaction between light and matter has been at the focus of the scientific community over the last centuries. For example, in the 1850s, Michael Faraday discovered that nanoscopic gold colloids exhibit optical properties different to those in bulk metals [1], giving rise, e.g., to the bright red color of gold-ruby glass [2, 3]. Some years later, in 1908, Gustav Mie provided the physical explanation to this effect [4] when he applied the electromagnetic theory developed by James Clerk Maxwell [5] to study the scattering properties of small gold nanoparticles [6–8]. Mie found that such small metallic nanoparticles efficiently scatter light at specific frequencies (typically in the visible range) which depend upon the material and size of the nanoparticle as well as upon the properties of the dielectric environment [9]. It would be later known that these specific frequencies correspond to the so-called localized surface plasmons [10–12], the resonances of the surface charge oscillation sustained by the collective oscillation of the free electrons in metallic nanoparticles that can be excited by light [13–16].

In the last years, the excitation of plasmon resonances in metallic nanoparticles has attracted great interest in Nanophotonics [17–19] due to their capability to enhance and squeeze incident electromagnetic fields into subwavelength regions [20–22]. For example, it is possible to obtain electromagnetic fields up to 100-1000 times larger than the incident field in the nanometric region between two metallic nanoparticles (referred to as a plasmonic *gap* or plasmonic nanocavity) [23]. As a result, plasmon resonances are widely used in a variety of spectroscopy and microscopy techniques such as surface-enhanced Raman spectroscopy [24], surface-enhanced fluorescence [25–27], or single-molecule imaging [28, 29], and enable promising applications in biomedicine [30–32], energy storage [33–35], and nonlinear optics [36, 37], among others.

Theoretically, plasmonic effects have been usually studied within the context of classical electromagnetism [38–45], where the interaction between light and matter is described by Maxwell's equations and the optical response of the system is generally considered to be linear [6]. However, current experimental configurations involving nanometer-sized metallic nanoparticles and interparticle distances push light–matter interaction to the limit where quantum many-body phenomena influence optical properties [46–52]. In these extreme situations, classical descriptions are no longer valid [53–55], and alternative theoretical approaches allowing for incorporating nonlocality [56–60], electronic spill in/out [61–63], surface-enabled Landau damping

[64–66], and electron tunneling [67, 68] are required to describe the optical properties of miniaturized plasmonic structures correctly.

In this context, time-dependent density functional theory (TDDFT) [69–72] is the method of choice to address the optical response of nanoscale systems in this thesis, since this theory accounts for the quantum nature of the electron dynamics from first principles by addressing the time evolution of the electron density in metallic nanoparticles subjected to external illumination [73]. In addition, the use of TDDFT calculations is not restricted to obtaining only the linear optical response, but it also enables to directly obtain the nonlinear response of plasmonic systems [74–78]. TDDFT is thus a very powerful tool to capture quantum many-body phenomena involved in the optical and electronic (i.e., *optoelectronic*) response, and it sets up the cornerstone of this thesis. On the other hand, since TDDFT is limited to addressing small systems that contain a few thousands of atoms due to its computational complexity [79, 80], less-demanding semiclassical models have also been developed to capture various quantum effects [81, 82]. Here we can mention, for instance, the quantum-corrected model accounting for electron tunneling in subnanometric metallic junctions [83–87], several hydrodynamic descriptions incorporating nonlocality of the optical response of metallic nanostructures [88–94], and the surface-response formalism (SRF) [95–97] based on the inclusion of quantum surface-response corrections (the so-called Feibelman parameters) at the metal–dielectric boundaries [98]. Together with TDDFT, in this thesis we also perform simulations based on the SRF, which captures important quantum effects such as the spill in/out of the induced charge density and surface-enabled Landau damping, but cannot account e.g. for electron tunneling between two nanoparticles in close proximity.

TDDFT and the aforementioned semiclassical models are often used to study the optical response of isolated plasmonic nanostructures, but they can also be used to analyze quantum effects in the optoelectronic interaction between plasmonic nanostructures and quantum emitters such as atoms, quantum dots or organic molecules. Indeed, the optical response of a coupled emitter–plasmonic nanostructure system has been widely studied in Nanophotonics. The plasmonic field enhancement and confinement allow quantum emitters to interact much more efficiently with light, leading to a plethora of interesting phenomena [99, 100]. Some of these effects can be described by classical calculations, such as the enhancement of the spontaneous emission rate (Purcell effect [101, 102]) and the modification of the resonant frequency (Lamb shift [103, 104]) of a quantum emitter located near a plasmonic nanostructure. On the other hand, the coupling between a plasmonic cavity and a quantum emitter can also involve quantum-mechanical effects that can affect the chemical properties of the emitter [105], induce electron transfer between the nanoparticles and the emitter [106–109], and eventually modify drastically the nonlinear optical response of the coupled system [110, 111].

This thesis aims at theoretically studying novel quantum many-body phenomena in the optoelectronic response of plasmonic nanostructures and their interaction with quantum emitters. In particular, we seek a deeper fundamental knowledge into quantum-mechanical effects that occur in plasmonic cavities of nanometric size

or smaller, where nonlocality, nonlinearity, or electron-transfer effects can all play an important role. To this end, quantum TDDFT simulations are used primarily, but classical calculations based on the local-response approximation within the dielectric framework as well as semiclassical models based on the SRF are also employed to complete the analysis and provide additional insights.

In Chapter 1, we review the fundamentals of classical light–matter interaction and explain the key concepts of this thesis from a classical perspective, focusing on the classical description of localized surface plasmon polaritons sustained by spherical metallic nanoparticles and their dimers as well as on the electromagnetic interaction between plasmonic nanostructures and quantum emitters. In Chapter 2, we describe the quantum TDDFT methodology and the semiclassical SRF adopted in this thesis to account for quantum many-body effects present in the light–matter interaction, and introduce quantum-mechanical concepts such as electron tunneling, surface-enabled Landau damping, and electron spill out with the examples of the optical response of canonical plasmonic nanostructures. In Chapter 3, we use TDDFT to study the influence of quantum surface effects in the electromagnetic interaction between quantum emitters and metallic nanoparticles. We identify the dominant effects when electron tunneling and the electronic coupling between the quantum emitter and the metallic nanoparticle are negligible. We further analyze the origin of the observed effects with semiclassical calculations based on a SRF that neglects the optical nonlocality in the direction parallel to the metallic surface, as usually implemented in the literature, and establish the validity range of this standard implementation of the semiclassical SRF. In Chapter 4, we show that the standard implementation of the SRF can be extended by explicitly accounting for the nonlocality of the optical response in the parallel direction along the metallic surface in the calculation of the Feibelman parameters. The inclusion of this nonlocality has not been so far considered in the literature to the best of our knowledge, and produces a broader range of validity of the SRF including extreme subnanometric configurations. In Chapter 5, we analyze the effect of electronic coupling between the electronic states of a quantum emitter and those of a metallic nanoparticle dimer when the distance between the nanoparticles and the emitter is subnanometric. This effect has been neglected in Chapters 3 and 4, which focused on the electromagnetic interaction. We demonstrate that, in such situations, the electronic interaction between the emitter and the nanoparticles drastically modifies the optical resonances of the coupled system. Finally, in Chapter 6, we study the nonlinear optical response of a system consisting of a quantum emitter and a spherical metallic nanoparticle, and show that the electromagnetic emitter–nanoparticle coupling can enable strong nonlinear second-harmonic generation, otherwise forbidden due to symmetry constrains if an isolated spherical nanoparticle were considered.

The content of this thesis thus presents a quantum mechanical many-body approach to the optical response of plasmonic cavities, which provides new insights into coupling with emitters, electron transfer processes and nonlinear effects. All these effects are of paramount importance in nowadays state-of-the-art Nanophotonics.

CHAPTER 1

CLASSICAL DESCRIPTION OF LIGHT–MATTER INTERACTION

1.1 Maxwell's equations

The interaction between light and matter is well addressed from a classical and macroscopic point of view by the time-dependent Maxwell's equations [6, 22],

$$\nabla \times \mathbf{E}(\mathbf{r},t) = -\frac{\partial}{\partial t}\mathbf{B}(\mathbf{r},t), \tag{1.1a}$$

$$\nabla \times \mathbf{H}(\mathbf{r},t) = \frac{\partial}{\partial t}\mathbf{D}(\mathbf{r},t) + \mathbf{J}_{\text{ext}}(\mathbf{r},t), \tag{1.1b}$$

$$\nabla \cdot \mathbf{D}(\mathbf{r},t) = 4\pi\rho_{\text{ext}}(\mathbf{r},t), \tag{1.1c}$$

$$\nabla \cdot \mathbf{B}(\mathbf{r},t) = 0, \tag{1.1d}$$

which represent a set of coupled partial differential equations where light is described as an electromagnetic wave with electric $\mathbf{E}(\mathbf{r},t)$ and magnetic $\mathbf{H}(\mathbf{r},t)$ field components.[1] The time-dependent Maxwell's equations in Eq. (1.1) determine the dynamics of the electromagnetic wave (light) at a position $\mathbf{r}$ and instant of time t through a given dielectric material in response to an external charge density $\rho_{\text{ext}}(\mathbf{r},t)$ and current density $\mathbf{J}_{\text{ext}}(\mathbf{r},t)$ that act as sources of electromagnetic radiation. For the nonmagnetic materials that we consider in this thesis, the magnetic induction $\mathbf{B}(\mathbf{r},t)$ is straightforwardly linked to $\mathbf{H}(\mathbf{r},t)$ by $\mathbf{B}(\mathbf{r},t) = \frac{1}{c^2}\mathbf{H}(\mathbf{r},t)$, with c the speed of light in a vacuum. Finally, the displacement vector, $\mathbf{D}(\mathbf{r},t)$, is related to the electric field $\mathbf{E}(\mathbf{r},t)$ within the linear-response regime by the following constitutive

[1] Atomic units (au) are used throughout this manuscript unless otherwise stated (see Appendix A).

relationship

$$\mathbf{D}(\mathbf{r},t) = \int_{-\infty}^{\infty}\int_{-\infty}^{\infty} d\mathbf{r}'\ dt'\ \varepsilon(\mathbf{r}-\mathbf{r}',t-t')\mathbf{E}(\mathbf{r}',t'), \tag{1.2}$$

where $\varepsilon(\mathbf{r}-\mathbf{r}',t-t')$ is the dielectric function describing optical excitations in the material. We assume in Eq. (1.2) that the medium is isotropic and homogeneous by considering that the dielectric function ε is a scalar quantity that spatially depends on $\mathbf{r}-\mathbf{r}'$. Moreover, the causality of the dielectric response is introduced by imposing $\varepsilon(\mathbf{r}-\mathbf{r}',t-t')=0$ for any $t'>t$.

According to Eq. (1.2), the displacement vector $\mathbf{D}$ at a particular position $\mathbf{r}$ and instant of time t depends on the value of the electric field $\mathbf{E}$ at all positions $\mathbf{r}'$ and times $t'<t$. Thus, the dielectric response of a material is, in general, nonlocal both in space and time. To deal with the temporal nonlocality, it is convenient to use the time-to-frequency Fourier transform[2] and express Eq. (1.2) in the domain of the angular frequency ω of the electromagnetic field,

$$\mathbf{D}(\mathbf{r},\omega) = \int_{-\infty}^{+\infty} d\mathbf{r}'\ \varepsilon(\mathbf{r}-\mathbf{r}',\omega)\mathbf{E}(\mathbf{r}',\omega). \tag{1.4}$$

Consequently, by applying the same Fourier transform to Eq. (1.1), Maxwell's equations can be expressed in the frequency domain as:

$$\nabla\times\mathbf{E}(\mathbf{r},\omega) = i\omega\mathbf{B}(\mathbf{r},\omega), \tag{1.5a}$$
$$\nabla\times\mathbf{H}(\mathbf{r},\omega) = -i\omega\mathbf{D}(\mathbf{r},\omega)+\mathbf{J}_{\text{ext}}(\mathbf{r},\omega), \tag{1.5b}$$
$$\nabla\cdot\mathbf{D}(\mathbf{r},\omega) = 4\pi\rho_{\text{ext}}(\mathbf{r},\omega), \tag{1.5c}$$
$$\nabla\cdot\mathbf{B}(\mathbf{r},\omega) = 0. \tag{1.5d}$$

Equations (1.1) and (1.5) are, of course, equivalent, and can be solved by adopting different techniques. Among numerical methods to solve Maxwell's equations, we can cite the Boundary Element Method [112], the Finite-Difference Time-Domain method [113], the Discrete-Dipole Approximation [114] or the Finite-Element Method [115].

On the other hand, the influence of the spatial nonlocality of the dielectric function present in Eq. (1.4) on the optical response of different materials is currently an active research topic by itself [81], and many efforts have been devoted

[2] In this thesis, we use the following definitions for the time-to-frequency ($\mathcal{F}$) and for the frequency-to-time ($\mathcal{F}^{-1}$) Fourier transforms of a function f:

$$\begin{aligned} f(\omega) &= \mathcal{F}[f(t)] = \int_{-\infty}^{+\infty} f(t)e^{i\omega t}\ dt, \\ f(t) &= \mathcal{F}^{-1}[f(\omega)] = \frac{1}{2\pi}\int_{-\infty}^{+\infty} f(\omega)e^{-i\omega t}\ d\omega, \end{aligned} \tag{1.3}$$

to the development of numerical methods that correctly account for such nonlocality [59, 60, 88, 89, 91, 92, 94, 116–123]. Using these methods, it has been shown that spatial nonlocality can play a significant role in defining the properties of the optical response of metallic nanostructures with characteristic dimensions below ~ 10 nm [56, 86, 124], as it is the case of the systems studied in this thesis. Indeed, we discuss in Chapters 2, 3, 4 and 5 the role that spatial nonlocality (and other quantum phenomena) plays in different scenarios involving small metallic nanoparticles when they interact with light and with quantum emitters. We account for such effects by using quantum time-dependent density functional theory (TDDFT) simulations (see Chapter 2), and, at a different level of approximation, by a semiclassical surface-response formalism (SRF) incorporating the Feibelman parameters obtained *ab initio* (Section 2.5). In contrast, the classical calculations performed within this thesis are based on a local description of the optical response of metals, so that nonlocal effects can only be partially introduced with the use of phenomenological parameters [58, 125, 126], as we detail in the following Subsection 1.1.1.

1.1.1 The local-response approximation

The local-response approximation (LRA) neglects the spatial nonlocality of the dielectric function $\varepsilon(\mathbf{r}-\mathbf{r}',\omega)$ by assuming that the dielectric response of a material at a position $\mathbf{r}$ is independent of the response at any other position $\mathbf{r}' \neq \mathbf{r}$. This assumption can be expressed as

$$\varepsilon(\mathbf{r}-\mathbf{r}',\omega) = \varepsilon(\mathbf{r},\omega)\delta(\mathbf{r}-\mathbf{r}'), \tag{1.6}$$

with $\delta(\mathbf{r}-\mathbf{r}')$ the Dirac delta function. The displacement vector $\mathbf{D}(\mathbf{r},\omega)$ thus transforms from Eq. (1.4) to a much simpler constitutive relationship,

$$\begin{aligned}\mathbf{D}(\mathbf{r},\omega) &= \int_{-\infty}^{+\infty} d\mathbf{r}'\ \varepsilon(\mathbf{r},\omega)\delta(\mathbf{r}-\mathbf{r}')\mathbf{E}(\mathbf{r}',\omega) \\ &= \varepsilon(\mathbf{r},\omega)\mathbf{E}(\mathbf{r},\omega).\end{aligned} \tag{1.7}$$

Despite its simplicity, the LRA has successfully described many physical phenomena of interest in the context of light–matter interaction at the nanoscale, particularly in situations where the characteristic length scale of the studied nanostructures is substantially larger than the Fermi wavelength of electrons in metals.

The Drude response model of free-electron metals

The simplest way to estimate the (frequency-dependent) local dielectric function $\varepsilon(\mathbf{r},\omega)$ of a metal is to adopt the Drude model [127, 128]. This model considers that conduction electrons freely move within a homogeneous gas in response to an external electric field $\mathbf{E}(t)$ while the heavy metal ions remain immobile. The equation of motion of a conduction electron is then

$$\ddot{\mathbf{x}}(t) + \gamma_p \dot{\mathbf{x}}(t) = -\mathbf{E}(t), \tag{1.8}$$

where $\mathbf{x}$ is the displacement of the electron from its equilibrium position, γ_p is a phenomenological damping parameter that accounts for elastic and inelastic events of electrons moving in the crystal lattice, and the dot $\cdot$ denotes the time derivative. In the frequency domain, the displacement $\mathbf{x}(\omega)$ can be expressed as

$$\mathbf{x}(\omega) = \frac{\mathbf{E}(\omega)}{\omega^2 + i\gamma_p\omega}. \tag{1.9}$$

The macroscopic polarization density, $\tilde{\mathbf{P}}(\omega)$, of a homogeneous gas with an average electron density $\overline{n}$ is $\tilde{\mathbf{P}}(\omega) = -\overline{n}\mathbf{x}(\omega) = -\overline{n}\frac{\mathbf{E}(\omega)}{\omega^2+i\gamma_p\omega}$. Then, using the relationship $\mathbf{D}(\omega) = \varepsilon(\omega)\mathbf{E}(\omega) = \mathbf{E}(\omega) + 4\pi\tilde{\mathbf{P}}(\omega)$, the dielectric function $\varepsilon(\omega)$ within the Drude model can be expressed as:

$$\begin{aligned}\varepsilon(\omega) &= 1 - \frac{4\pi\overline{n}}{\omega^2 + i\gamma_p\omega}, \\ &= 1 - \frac{\omega_p^2}{\omega^2 + i\gamma_p\omega},\end{aligned} \tag{1.10}$$

where $\omega_p = \sqrt{4\pi\overline{n}}$ is the plasma frequency of the considered metal. Moreover, the electron density $\overline{n}$ is typically expressed in terms of the Wigner–Seitz radius

$$r_s = \left(\frac{3}{4\pi\overline{n}}\right)^{1/3}, \tag{1.11}$$

which is defined as the radius of a sphere whose volume is equal to the average volume per conduction electron. Thus, the plasma frequency ω_p equals to

$$\omega_p = \sqrt{\frac{3}{r_s^3}}, \tag{1.12}$$

and determines the maximum frequency at which a Drude metal displays a metallic behavior (negative dielectric function). The plasma frequency ω_p of typical metals falls in the visible-ultraviolet range, $\omega_p \sim 4 - 15$ eV. In Figure 1.1a, we show by solid lines the real part (blue) and imaginary part (red) of the dielectric function $\varepsilon(\omega)$ obtained from Eq. (1.10) for $\omega_p = 5.89$ eV ($r_s = 4$ a$_0$) and $\gamma_p = 0.1$ eV, typical values used to characterize sodium within the LRA [124]. Here, a$_0 = 0.053$ nm stands for the Bohr radius.

However, as pointed out above, nonlocal effects (and other finite-size phenomena) can significantly influence the optical response of small metallic nanostructures. As a result, using a Drude dielectric function [Eq. (1.10)] parametrized according to the plasma frequency ω_p given by Eq. (1.12) shows limitations to describe these extreme situations. Moreover, the losses in the metal expected from the damping parameter γ_p can be increased because of nonlocal phenomena. In a first correction, such effects can be partially captured within the classical LRA approach

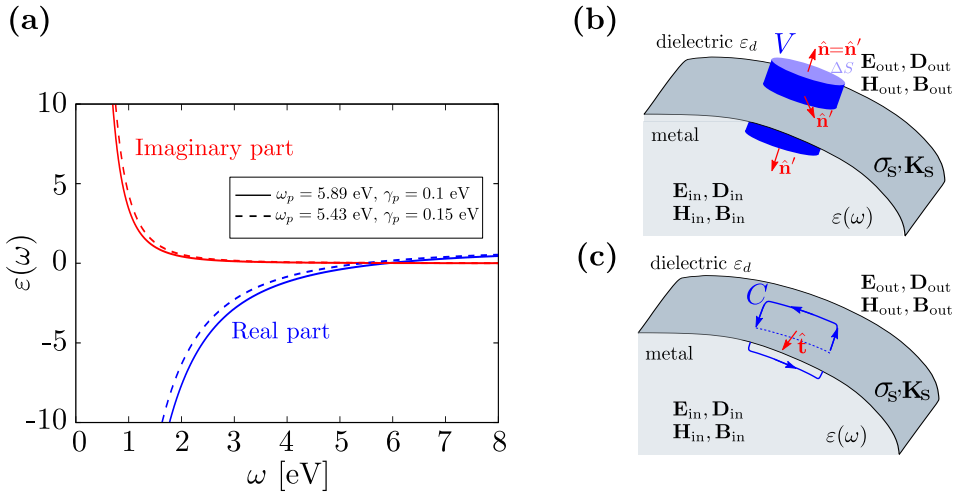

Figure 1.1: **(a)** Imaginary part (red) and real part (blue) of the dielectric function $\varepsilon(\omega)$ obtained from the Drude model [Eq. (1.10)]. Solid lines: $\omega_p = 5.89$ eV ($r_s = 4$ a$_0$) and $\gamma_p = 0.1$ eV. Dashed lines: $\omega_p = 5.43$ eV ($r_s = 4.22$ a$_0$) and $\gamma_p = 0.15$ eV. These values are typically used to characterize sodium, which is the material predominantly considered in this thesis. **(b)** Schematic representation of a metal–dielectric interface with external surface charge and current densities σ_s and $\mathbf{K}_s$. A shallow blue pillbox of volume V crosses the interface along the normal direction to the metal surface. The area of the top and bottom surface sections is ΔS. The normal unit vector $\hat{\mathbf{n}}'$ is pointing outward from the surface of the pillbox, and $\hat{\mathbf{n}}$ is the normal vector pointing from the interior side of the interface ("in") to the outer side ("out"). **(c)** Same as in **(b)**, but for a rectangular closed contour C with its plane oriented normal to the metal surface. The unit vector $\hat{\mathbf{t}}$ is normal to the surface enclosed by C, and thus parallel to the metal surface.

by effectively modifying the value of ω_p (or, equivalently, r_s) and γ_p [125]. We adopt this strategy in Chapters 5 and 6. As an example, we show in Figure 1.1a the real part (blue dashed line) and imaginary part (red dashed lines) of the Drude dielectric function $\varepsilon(\omega)$ obtained for $\omega_p = 5.43$ eV ($r_s = 4.22$ a$_0$) and $\gamma_p = 0.15$ eV, which are the values used within the classical calculations in Chapter 5 attempting to account for nonlocal effects.

1.1.2 Boundary conditions

When the system under study involves more than one medium, the electromagnetic problem can be solved by obtaining the solution of Maxwell's equation [Eq. (1.5)] separately at each medium and applying appropriate boundary conditions at the corresponding interfaces. The classical electromagnetic theory employed in this thesis thus adopts the *piecewise-constant approximation* [81, 129], which assumes that the dielectric function $\varepsilon(\mathbf{r}, \omega)$ experiences an abrupt change at the interface between different media. Therefore, in contrast with the TDDFT and the semiclassical SRF employed in this thesis (see Chapter 2), the classical calculations neglect any surface effect related to the smooth variation of the induced electron

density.

In the case of the metal–dielectric interfaces studied here, the abrupt change of $\varepsilon(\mathbf{r},\omega)$ at the metal boundary can be expressed with the following spatially-dependent dielectric function,

$$\varepsilon(\mathbf{r},\omega) = \begin{cases} \varepsilon(\omega) & \text{inside the metal} \\ \varepsilon_d & \text{outside the metal} \end{cases}, \tag{1.13}$$

where $\varepsilon(\omega)$ is the Drude dielectric function given by Eq. (1.10), and ε_d is the dielectric constant characterizing the environment. In this thesis, we consider that the metallic nanoparticles are surrounded by vacuum, so that $\varepsilon_d = 1$.

The boundary conditions that the electromagnetic fields must satisfy at the metal–dielectric interface are obtained by applying the divergence theorem and Stokes's theorem [6]. On the one hand, by applying the divergence theorem to Eqs. (1.5c) and (1.5d) one obtains

$$\oint_S dS\ \mathbf{D}(\mathbf{r},\omega)\cdot\hat{\mathbf{n}}' = 4\pi\int_V dV\,\rho_{\text{ext}}(\mathbf{r},\omega), \tag{1.14a}$$

$$\oint_S dS\ \mathbf{B}(\mathbf{r},\omega)\cdot\hat{\mathbf{n}}' = 0, \tag{1.14b}$$

where V is an arbitrary finite volume in space, S is the enclosing surface, dS is the infinitesimal element of area on S, and $\hat{\mathbf{n}}'$ is the unit vector normal to the surface pointing outward from the enclosed volume. In order to obtain the first two boundary conditions, we evaluate the integrals of Eq. (1.14) within a shallow pillbox crossing the metal–dielectric interface along the normal direction, as sketched in Figure 1.1b. We focus on the dielectric response of the interface, and thus the height of the pillbox tends to zero. Therefore, the side surface does not contribute to the left-hand integral of Eqs. (1.14a) and (1.14b), and only the top and bottom surfaces of area ΔS contribute,

$$\oint_S dS\ \mathbf{D}(\mathbf{r},\omega)\cdot\hat{\mathbf{n}}' = \Delta S\ \hat{\mathbf{n}}\cdot(\mathbf{D}_{\text{out}} - \mathbf{D}_{\text{in}})\,, \tag{1.15a}$$

$$\oint_S dS\ \mathbf{B}(\mathbf{r},\omega)\cdot\hat{\mathbf{n}}' = \Delta S\ \hat{\mathbf{n}}\cdot(\mathbf{B}_{\text{out}} - \mathbf{B}_{\text{in}})\,. \tag{1.15b}$$

In Eq. (1.15), the subscript "in" defines the fields within the region inside the metal while the subscript "out" those in the surrounding dielectric medium, and $\hat{\mathbf{n}}$ is the normal unit vector pointing outwards from the metal boundary, as shown in Figure 1.1b. Moreover, the right-hand integral of Eq. (1.14a) is simply $\sigma_s\Delta S$, where σ_s is the surface charge density associated with external charges. Then, the first two boundary conditions are given by

$$\hat{\mathbf{n}}\cdot(\mathbf{D}_{\text{out}} - \mathbf{D}_{\text{in}}) = 4\pi\sigma_s, \tag{1.16a}$$

$$\hat{\mathbf{n}}\cdot(\mathbf{B}_{\text{out}} - \mathbf{B}_{\text{in}}) = 0. \tag{1.16b}$$

On the other hand, by applying Stokes's theorem to Eqs. (1.5a) and (1.5b) one obtains

$$\oint_C \mathbf{E}(\mathbf{r},\omega)\cdot d\mathbf{l} = i\omega \int_{S'} dS' \mathbf{B}(\mathbf{r},\omega)\cdot \hat{\mathbf{t}}, \tag{1.17a}$$

$$\oint_C \mathbf{H}(\mathbf{r},\omega)\cdot d\mathbf{l} = \int_{S'} dS' \left[-i\omega \mathbf{D}(\mathbf{r},\omega) + \mathbf{J}_{\text{ext}}(\mathbf{r},\omega)\right]\cdot \hat{\mathbf{t}}, \tag{1.17b}$$

where C is an arbitrary closed contour in space with its plane oriented normal to the metal surface, S' is the surface enclosed within this contour, dS' is the infinitesimal element of area on S', $d\mathbf{l}$ is the infinitesimal line element on C, and $\hat{\mathbf{t}}$ is the unit vector normal to the surface S'. Using similar arguments as those used in the derivation of Eq. (1.16), one can obtain the last two boundary conditions by evaluating the integrals of Eq. (1.17) within a closed contour C as the one depicted in Figure 1.1c [6]. These conditions are given by:

$$\hat{\mathbf{n}}\times(\mathbf{E}_{\text{out}}-\mathbf{E}_{\text{in}}) = 0, \tag{1.18a}$$

$$\hat{\mathbf{n}}\times(\mathbf{H}_{\text{out}}-\mathbf{H}_{\text{in}}) = \mathbf{K}_s, \tag{1.18b}$$

where $\mathbf{E}_{\text{out}}$ ($\mathbf{H}_{\text{out}}$) and $\mathbf{E}_{\text{in}}$ ($\mathbf{H}_{\text{in}}$) are the electric (magnetic) fields at the outer and inner sides of the metal–dielectric interface, respectively, and $\mathbf{K}_s$ is the external surface current density. In all the situations addressed in this thesis, there is no charge and current densities associated with external charges, $\sigma_s = \mathbf{K}_s = 0$. Therefore, the boundary conditions given by Eqs. (1.16) and (1.18) indicate that the normal component of $\mathbf{D}(\mathbf{r},\omega)$ and $\mathbf{B}(\mathbf{r},\omega)$ along the metal–dielectric interface as well as the tangential components of $\mathbf{E}(\mathbf{r},\omega)$ and $\mathbf{H}(\mathbf{r},\omega)$ are continuous. Importantly, since the dielectric function $\varepsilon(\mathbf{r},\omega)$ experiences an abrupt change in the metal boundary within the piecewise-constant approximation [Eq. (1.13)], the normal component of $\mathbf{E}(\mathbf{r},\omega)$ is discontinuous at the metal–dielectric interface.

1.1.3 The nonretarded approximation

In the limit of very small structures, as compared to the wavelength of the incident light, the electromagnetic interaction between different spatial points of the structure is almost instantaneous, and therefore the speed of light can be considered as infinite. In this situation, Eq. (1.5a) becomes (with $\mathbf{B}(\mathbf{r},\omega) = \frac{1}{c^2}\mathbf{H}(\mathbf{r},\omega)$)

$$\nabla\times\mathbf{E}(\mathbf{r},\omega) = \nabla\times\Big(\mathbf{E}^{\text{ext}}(\mathbf{r},\omega)+\mathbf{E}^{\text{ind}}(\mathbf{r},\omega)\Big) = 0, \tag{1.19}$$

where $\mathbf{E}(\mathbf{r},\omega)$ has been decomposed into a sum of the electric field of the external excitation, $\mathbf{E}^{\text{ext}}(\mathbf{r},\omega)$, and the field induced by the nanostructure, $\mathbf{E}^{\text{ind}}(\mathbf{r},\omega)$. From Eq. (1.19), the total electric field $\mathbf{E}(\mathbf{r},\omega)$ within the nonretarded approximation can be expressed as the gradient of a scalar function, $\phi(\mathbf{r},\omega) = \phi^{\text{ext}}(\mathbf{r},\omega)+\phi^{\text{ind}}(\mathbf{r},\omega)$,

known as the electrostatic potential:

$$\mathbf{E}(\mathbf{r},\omega) = -\nabla\phi(\mathbf{r},\omega) = -\nabla\left(\phi^{\text{ext}}(\mathbf{r},\omega) + \phi^{\text{ind}}(\mathbf{r},\omega)\right), \tag{1.20}$$

with $\phi^{\text{ext}}(\mathbf{r},\omega)$ and $\phi^{\text{ind}}(\mathbf{r},\omega)$ the external and induced potentials, respectively. The minus (-) sign in Eq. (1.20) is introduced by convention. Finally, from Eq. (1.5c), $\phi^{\text{ext}}(\mathbf{r},\omega)$ satisfies Poisson's equation,

$$\nabla^2\phi^{\text{ext}}(\mathbf{r},\omega) = -4\pi\rho_{\text{ext}}, \tag{1.21}$$

while $\phi^{\text{ind}}(\mathbf{r},\omega)$ satisfies Laplace's equation,

$$\nabla^2\phi^{\text{ind}}(\mathbf{r},\omega) = 0, \tag{1.22}$$

Moreover, the boundary conditions at the metal–dielectric interface given by Eqs. (1.16a) and (1.18a) can be expressed within the nonretarded approximation in terms of $\phi(\mathbf{r},\omega)$ as:

$$\phi_{\text{out}} = \phi_{\text{in}}, \tag{1.23a}$$

$$\varepsilon_d\ \hat{\mathbf{n}}\cdot\nabla\phi_{\text{out}} = \varepsilon(\omega)\ \hat{\mathbf{n}}\cdot\nabla\phi_{\text{in}}, \tag{1.23b}$$

where ϕ_{out} and ϕ_{in} expresses the electrostatic potential $\phi(\mathbf{r},\omega)$ at the outer and inner sides of the metal–dielectric interface, respectively. Therefore, under the nonretarded limit, the application of the complex (vector) Maxwell's equations [Eq. (1.5)] and the associated boundary conditions [Eqs. (1.16) and (1.18)] to obtain the optical response of a nanostructure reduces to finding the solution of Laplace's (scalar) equation [Eq. (1.22)] with the boundary conditions at the interfaces given by Eq. (1.23).

Depending on the geometry of the nanostructure and the illumination field, Eq. (1.22) can be solved either analytically or by using numerical methods. In this thesis, we place special attention to individual spherical nanoparticles and to dimers composed by two spherical nanoparticles (see Chapters 3, 5, and 6), and thus we explain below how to obtain the classical optical response of such nanostructures within the nonretarded limit. We note that, due to the small size of the studied systems, all the calculations in this thesis are performed under the nonretarded approximation.

Optical response of a spherical nanoparticle

We derive next the optical response of an individual spherical nanoparticle of radius a characterized by a dielectric function $\varepsilon(\omega)$ and surrounded by a material of dielectric function ε_d. The position vector $\mathbf{r}$ is written in spherical coordinates (r,θ,ϕ) with the origin at the center of the nanoparticle, $\mathbf{r} \equiv (r\sin\theta\cos\varphi, r\sin\theta\sin\varphi, r\cos\theta)$, as we show in Figure 1.2a. An arbitrary external potential $\phi^{\text{ext}}(\mathbf{r},\omega)$ excites the system.

The Laplace operator in spherical coordinate system (r, θ, φ) is given by

$$\nabla^2 \equiv \frac{1}{r^2}\frac{\partial}{\partial r}\left(r^2\frac{\partial}{\partial r}\right) + \frac{1}{r^2\sin^2\theta}\frac{\partial^2}{\partial\varphi^2} + \frac{1}{r^2\sin\theta}\frac{\partial}{\partial\theta}\left(\sin\theta\frac{\partial}{\partial\theta}\right), \tag{1.24}$$

and the solution of Laplace's equation [Eq. (1.22)] can be written in a spherical harmonic basis set $Y_\ell^m(\theta,\varphi)$ as [6]

$$\phi^{\text{ind}}(\mathbf{r},\omega) = \sum_{\ell=0}^{\infty}\sum_{m=-\ell}^{\ell}\left(A_\ell r^\ell + B_\ell r^{-(\ell+1)}\right)Y_\ell^m(\theta,\varphi). \tag{1.25}$$

By imposing $\phi^{\text{ind}}(\mathbf{r},\omega)$ to be finite at $r=0$ and $r\to\infty$, and by applying the boundary conditions given by Eq. (1.23) (here $\hat{\mathbf{n}} = \hat{\mathbf{r}}$), the potential $\phi^{\text{ind}}(\mathbf{r},\omega)$ induced inside $(r<a)$ and outside $(r>a)$ the spherical nanoparticle is fully determined:

$$\phi^{\text{ind}}(\mathbf{r},\omega) = \sum_{\ell=0}^{\infty}\sum_{m=-\ell}^{\ell} b_{\ell m}(\omega)Y_\ell^m(\theta,\varphi)\begin{cases} r^\ell/a^\ell & r\le a \\ a^{\ell+1}/r^{\ell+1} & r\ge a \end{cases}, \tag{1.26}$$

where

$$b_{\ell m}(\omega) = \frac{-a(\varepsilon(\omega)-\varepsilon_d)}{\varepsilon_d(\ell+1)+\ell\varepsilon(\omega)}\int d\tilde{\Omega}\,[Y_\ell^m(\theta,\varphi)]^*\frac{\partial}{\partial r}\phi^{\text{ext}}(\mathbf{r},\omega)\Big|_{r=a}. \tag{1.27}$$

The integral in Eq. (1.27) extends over the solid angle $\tilde{\Omega} = \{\theta,\varphi\}$, and, in practice, the summation in Eq. (1.26) has to be truncated at an integer number, ℓ_{max}, large enough to achieve convergence of the solution. For certain external potentials, $\phi^{\text{ext}}(\mathbf{r},\omega)$, such as the potential corresponding to a point dipole or to plane-wave illumination, the integral in Eq. (1.27) (and therefore $\phi^{\text{ind}}(\mathbf{r},\omega)$) possesses an analytical solution, as we show in Subsections 1.2.3 and 1.4.2. For arbitrary external potential $\phi^{\text{ext}}(\mathbf{r},\omega)$, the integration has to be calculated numerically. In this thesis, we use the Gauss–Legendre quadrature method [130].

Once the coefficients $b_{\ell m}(\omega)$ are obtained from Eq. (1.27) and thus the induced potential $\phi^{\text{ind}}(\mathbf{r},\omega)$ is determined [Eq. (1.26)], we can calculate other physical quantities of interest. For example, the electric field induced by the spherical nanoparticle at position $\mathbf{r}$ is directly related to the induced potential as

$$\mathbf{E}^{\text{ind}}(\mathbf{r},\omega) = -\nabla\phi^{\text{ind}}(\mathbf{r},\omega). \tag{1.28}$$

The analytical expression of the electric field $\mathbf{E}^{\text{ind}}(\mathbf{r},\omega)$ induced by a spherical nanoparticle in response to arbitrary external illumination is shown in Appendix B.

On the other hand, the dipole moment $\mathbf{p}(\omega)$ $(\ell=1)$ induced at a spherical nanoparticle can also be calculated using the coefficients $b_{\ell m}(\omega)$ given by Eq. (1.27).

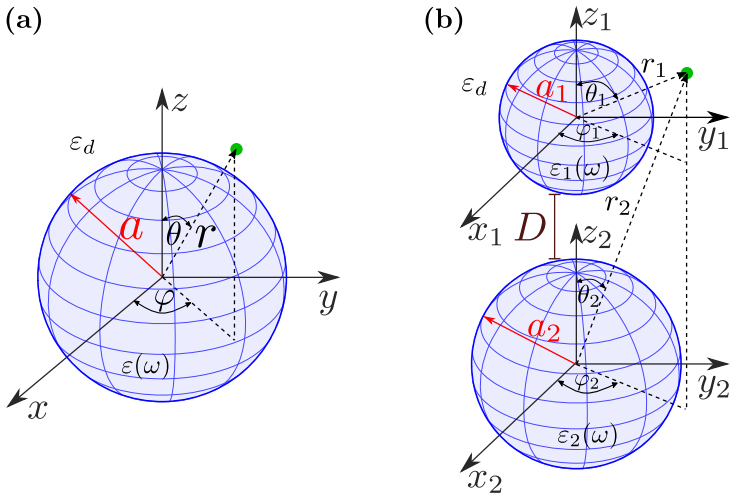

Figure 1.2: **(a)** Spherical coordinate system (r, θ, φ) with the origin at the center of a spherical nanoparticle of radius a characterized by a dielectric function $\varepsilon(\omega)$. **(b)** Coordinate system employed to address the optical response of a dimer formed by two spherical nanoparticles of radius a_1 and a_2 separated by a gap of size D. The nanoparticles are characterized by a dielectric function $\varepsilon_1(\omega)$ and $\varepsilon_1(\omega)$. The coordinates are expressed in spherical coordinates $(r_1, \theta_1, \varphi_1)$ and $(r_2, \theta_2, \varphi_2)$ with the origin at the center of each nanoparticle. In both individual nanoparticle and dimer structures, the system is surrounded by a dielectric material characterized by ϵ_d.

Since a point dipole of amplitude $\mathbf{p}(\omega)$ located at the center of the coordinate system creates an electrostatic potential at a position $\mathbf{r}$ given by $\phi^{\text{ind}}(\mathbf{r}, \omega) = \frac{\mathbf{r}\cdot\mathbf{p}(\omega)}{|\mathbf{r}|^3}$, $\mathbf{p}(\omega)$ can be obtained as

$$\mathbf{p}(\omega) = \sum_{m=-1}^{m=1} b_{1m}(\omega)\, a^2 \left(Y_1^m(\frac{\pi}{2}, 0)\, \hat{\mathbf{x}} + Y_1^m(\frac{\pi}{2}, \frac{\pi}{2})\, \hat{\mathbf{y}} + Y_1^m(0, 0)\, \hat{\mathbf{z}} \right), \qquad (1.29)$$

where $\{\hat{\mathbf{x}}, \hat{\mathbf{y}}, \hat{\mathbf{z}}\}$ are the unit vectors along the $\{x, y, z\}$-axes.

Optical response of a spherical-nanoparticle dimer

We now consider the case of a dimer consisting of two spherical nanoparticles of radius a_1 and a_2 separated by a gap of size D (see Figure 1.2b). Each nanoparticle is characterized by a dielectric function $\varepsilon_1(\omega)$ and $\varepsilon_2(\omega)$, and the entire system is surrounded by a dielectric material characterized by ε_d. The numerical implementation described in this section to obtain the optical response of this system is based on a coupled-multipole method [131, 132], which uses the solution of the individual spherical nanoparticle explained above.

The potential $\phi^{\text{ind}}_{\text{dimer}}(\mathbf{r}, \omega)$ induced by the dimer in response to an external potential $\phi^{\text{ext}}(\mathbf{r}, \omega)$ is given by the sum of the potential induced by each nanoparticle

(1 and 2),

$$\phi^{\rm ind}_{\rm dimer}(\mathbf{r},\omega) = \phi^{\rm ind}_1(\mathbf{r}_1,\omega) + \phi^{\rm ind}_2(\mathbf{r}_2,\omega), \tag{1.30}$$

where the vectors $\mathbf{r}_1 \equiv (r_1\sin\theta_1\cos\varphi_1, r_1\sin\theta_1\sin\varphi_1, r_1\cos\theta_1)$ and $\mathbf{r}_2 \equiv (r_2\sin\theta_2\cos\varphi_2, r_2\sin\theta_2\sin\varphi_2, r_2\cos\theta_2)$ are written in spherical coordinates with the origins at the center of the corresponding nanoparticle, as shown in Figure 1.2b. We define the coordinates such that the centers of the nanoparticles are located at the z-axis separated by a distance $\delta = a_1 + a_2 + D$. Thus, $\mathbf{r}_1$ and $\mathbf{r}_2$ are related by

$$\begin{aligned} r_2 &= \sqrt{r_1^2 + \delta^2 - 2\delta r_1\cos\theta_1}, \\ \cos\theta_2 &= (r_1\cos\theta_1 - \delta)/r_2, \\ \varphi_2 &= \varphi_1. \end{aligned} \tag{1.31}$$

The electrostatic potential $\phi^{\rm ind}_i(\mathbf{r}_i,\omega)$ induced by the nanoparticle i (with $i = 1, 2$) follows identical expression as that of the individual nanoparticle explained above [Eq. (1.26)],

$$\begin{aligned} \phi^{\rm ind}_1(\mathbf{r}_1,\omega) &= \sum_{\ell=0}^{\ell_{\rm max}} \sum_{m=-\ell}^{\ell} b_1^{\ell m}(\omega)\; Y_\ell^m(\theta_1,\varphi_1) \begin{cases} r_1^\ell/a_1^\ell & r_1 < a_1 \\ a_1^{\ell+1}/r_1^{\ell+1} & r_1 > a_1, \end{cases} \\ \phi^{\rm ind}_2(\mathbf{r}_2,\omega) &= \sum_{\ell=0}^{\ell_{\rm max}} \sum_{m=-\ell}^{\ell} b_2^{\ell m}(\omega)\; Y_\ell^m(\theta_2,\varphi_2) \begin{cases} r_2^\ell/a_2^\ell & r_2 < a_2 \\ a_2^{\ell+1}/r_2^{\ell+1} & r_2 > a_2, \end{cases} \end{aligned} \tag{1.32}$$

with, in this case,

$$\begin{aligned} b_1^{\ell m}(\omega) &= \xi_1(\omega,\ell) \int d\tilde{\Omega}_1\; [Y_\ell^m(\theta_1,\varphi_1)]^* \frac{\partial}{\partial r_1}\Big(\phi^{\rm ext}(\mathbf{r}_1,\omega) + \phi^{\rm ind}_2(\mathbf{r}_2,\omega)\Big)\Big|_{r_1=a_1}, \\ b_2^{\ell m}(\omega) &= \xi_2(\omega,\ell) \int d\tilde{\Omega}_2\; [Y_\ell^m(\theta_2,\varphi_2)]^* \frac{\partial}{\partial r_2}\Big(\phi^{\rm ext}(\mathbf{r}_2,\omega) + \phi^{\rm ind}_1(\mathbf{r}_1,\omega)\Big)\Big|_{r_2=a_2}, \end{aligned} \tag{1.33}$$

where

$$\begin{aligned} \xi_1(\omega,\ell) &= \frac{-a_1(\varepsilon_1 - \varepsilon_d)}{\varepsilon_d(\ell+1) + \varepsilon_1\ell}, \\ \xi_2(\omega,\ell) &= \frac{-a_2(\varepsilon_2 - \varepsilon_d)}{\varepsilon_d(\ell+1) + \varepsilon_2\ell}. \end{aligned} \tag{1.34}$$

The integrals in Eq. (1.33) take into account that the potential induced by one nanoparticle acts as external potential for the other one. From Eq. (1.32), the coefficients $b_1^{\ell m}(\omega)$ and $b_2^{\ell m}(\omega)$ in Eq. (1.33) can be found from the following expression given in matrix form:

$$\begin{aligned} \overline{b_1^{\ell m}}(\omega) &= \Big(\mathbb{I} - \mathbb{T}^{2\to1}\mathbb{T}^{1\to2}\Big)^{-1}\Big(\overline{b_1^{\ell m,{\rm ext}}}(\omega) + \mathbb{T}^{2\to1}\overline{b_2^{\ell m,{\rm ext}}}(\omega)\Big), \\ \overline{b_2^{\ell m}}(\omega) &= \Big(\mathbb{I} - \mathbb{T}^{1\to2}\mathbb{T}^{2\to1}\Big)^{-1}\Big(\overline{b_2^{\ell m,{\rm ext}}}(\omega) + \mathbb{T}^{1\to2}\overline{b_1^{\ell m,{\rm ext}}}(\omega)\Big). \end{aligned} \tag{1.35}$$

Here, $\overline{b_1^{\ell m}}(\omega)$ and $\overline{b_2^{\ell m}}(\omega)$ represent column vectors containing the coefficients $b_1^{\ell m}(\omega)$ and $b_2^{\ell m}(\omega)$, $\mathbb{I}$ is the identity matrix, and $\overline{b_1^{\ell m,\mathrm{ext}}}$ and $\overline{b_2^{\ell m,\mathrm{ext}}}$ are column vectors with the following elements:

$$\begin{aligned} b_1^{\ell m,\mathrm{ext}}(\omega) &= \xi_1(\omega,\ell)\int d\tilde{\Omega}_1\ [Y_\ell^m(\theta_1,\varphi_1)]^*\frac{\partial}{\partial r_1}\phi^{\mathrm{ext}}(\mathbf{r}_1,\omega)\Big|_{r_1=a_1}, \\ b_2^{\ell m,\mathrm{ext}}(\omega) &= \xi_2(\omega,\ell)\int d\tilde{\Omega}_2\ [Y_\ell^m(\theta_2,\varphi_2)]^*\frac{\partial}{\partial r_2}\phi^{\mathrm{ext}}(\mathbf{r}_2,\omega)\Big|_{r_2=a_2}. \end{aligned} \tag{1.36}$$

Finally, the elements $(\ell m,\ell' m')$ of matrices $\mathbb{T}^{2\to1}$ and $\mathbb{T}^{1\to2}$ are given by

$$\begin{aligned} \mathbb{T}^{2\to1}_{\ell m,\ell' m'} &= \xi_1(\omega,\ell)\int d\tilde{\Omega}_1[Y_\ell^m(\theta_1,\varphi_1)]^*\frac{\partial}{\partial r_1}\left(Y_{\ell'}^{m'}(\theta_2,\varphi_2)\frac{a_2^{\ell'+1}}{r_2^{\ell'+1}}\right)\Big|_{r_1=a_1}, \\ \mathbb{T}^{1\to2}_{\ell m,\ell' m'} &= \xi_2(\omega,\ell)\int d\tilde{\Omega}_2[Y_\ell^m(\theta_2,\varphi_2)]^*\frac{\partial}{\partial r_2}\left(Y_{\ell'}^{m'}(\theta_1,\varphi_1)\frac{a_1^{\ell'+1}}{r_1^{\ell'+1}}\right)\Big|_{r_2=a_2}. \end{aligned} \tag{1.37}$$

Once the coefficients $b_1^{\ell m}(\omega)$ and $b_2^{\ell m}(\omega)$ are obtained by solving Eq. (1.35), the physical quantities of interest such as the induced electric field $\mathbf{E}^{\mathrm{ind}}(\mathbf{r},\omega)$ or the dipole moment $\mathbf{p}(\omega)$ of the dimer structure can be determined as the sum of the corresponding contributions of each nanoparticle [Eqs. (1.28) and (1.29)].

1.2 Plasmonics

Plasmons are collective oscillations of the free-electron gas inside a metal [22, 133]. From a classical electromagnetic point of view, plasmons manifest themselves as absorption and scattering resonances obtained from the solutions of Maxwell's equations and the associated boundary conditions discussed in Section 1.1. On the other hand, within quantum electrodynamics, the word *plasmon* refers to the *quantum* of the metallic electron plasma oscillation [134, 135].

Depending on the geometry of the system, plasmons can be excited in the bulk or at the metal–dielectric boundary, and, in the latter situation, they can be either propagating or localized electron-density oscillations. In the following, we describe some canonical examples of plasmonic excitations within the classical electromagnetic theory. In addition to providing the fundamental concepts of plasmonics, this classical description establishes a reference point to compare with the results obtained within a quantum many-body approach, thus allowing us to identify the origin of the effects of interest in this thesis.

1.2.1 Bulk plasmons

Bulk or volume plasmons are longitudinal excitations consisting in the coherent oscillation of the electron gas propagating in an infinitely extended metal, where the excited electrons move collectively oscillating at the same frequency. These

longitudinal electromagnetic waves ($\nabla \cdot \mathbf{E}(\mathbf{r},\omega) \neq 0$) can be described within the local-response approximation (see Subsection 1.1.1), and can only exist if $\varepsilon(\omega) = 0$ [54, 57]. Thus, assuming a lossless Drude dielectric function [Eq. (1.10), with $\gamma_p = 0$], the bulk plasmon frequency is equal to the plasma frequency, $\omega_{\text{bulk}} = \omega_p$ [Eq. (1.12)].

1.2.2 Surface plasmons and surface plasmon polaritons

When we consider a semi-infinite planar metal slab ($\varepsilon(\mathbf{r},\omega) = \varepsilon(\omega), z < 0$) in contact with vacuum ($\varepsilon(\mathbf{r},\omega) = \varepsilon_d = 1, z > 0$), the translational invariance of the bulk material along the z-direction is broken. As a consequence, a new type of plasmon emerges associated with an oscillating charge density propagating along the metal–dielectric interface. These density oscillations are referred to as surface plasmons. The resonance condition of a surface plasmon can be derived within the nonretarded approximation from the self-sustained induced potential $\phi^{\text{ind}}(\mathbf{r},\omega)$ [Eq. (1.22), with $\phi^{\text{ext}}(\mathbf{r},\omega) = 0$]. $\phi^{\text{ind}}(\mathbf{r},\omega)$ is given in this case by [10]

$$\phi^{\text{ind}}(\mathbf{r},\omega) = \begin{cases} \phi_<(\omega)\, e^{i\mathbf{k}_\parallel \cdot \mathbf{r}_\parallel} e^{|\mathbf{k}_\parallel| z} & z < 0 \\ \\ \phi_>(\omega)\, e^{i\mathbf{k}_\parallel \cdot \mathbf{r}_\parallel} e^{-|\mathbf{k}_\parallel| z} & z > 0 \end{cases}, \tag{1.38}$$

where $\mathbf{r}_\parallel$ and $\mathbf{k}_\parallel$ are the two-dimensional position and momentum vectors in the plane of the metal surface, respectively, and $\phi_<(\omega)$ and $\phi_>(\omega)$ are frequency-dependent coefficients to be determined from the boundary conditions given by Eq. (1.23). From the continuity of the potential at $z = 0$ [Eq. (1.23a)] it is obtained that $\phi_<(\omega) = \phi_>(\omega)$. Further, from the continuity of the normal component of $\mathbf{D}(\mathbf{r},\omega) = -\varepsilon(\mathbf{r},\omega)\nabla\phi(\mathbf{r},\omega)$ at $z = 0$ [Eq. (1.23b)], the resonance condition of the nonretarded surface plasmon is given by $\varepsilon(\omega) = -1$. Thus, assuming a lossless Drude dielectric function [Eq. (1.10), with $\gamma_p = 0$], the long-wavelength limit of the surface plasmon frequency is equal to

$$\omega_{\text{sp}} = \omega_p/\sqrt{2}. \tag{1.39}$$

On the other hand, a surface plasmon *polariton* (SPP) is a hybrid mode that propagates at the metal–dielectric boundary and that results from the coupling of a surface plasmon and an electromagnetic wave [136]. These SPPs are characterized by electromagnetic fields that are evanescent in the direction normal to the surface, thus exponentially decaying with increasing distance from the interface (see sketch in Figure 1.3a). Considering an electromagnetic wave that satisfies Maxwell's equations in this system [Eq. (1.5)], and applying the boundary conditions given by Eqs. (1.16) and (1.18) as well as the conservation of momentum vector $\mathbf{k}_\parallel$ along the propagation direction [22], the following dispersion relationship of SPPs is obtained (for a lossless Drude dielectric function),

$$\omega^2_{\text{spp}}(\mathrm{k}_\parallel) = \omega_p^2/2 + c^2\mathrm{k}_\parallel^2 - \sqrt{\omega_p^4/4 + c^4\mathrm{k}_\parallel^4}, \tag{1.40}$$

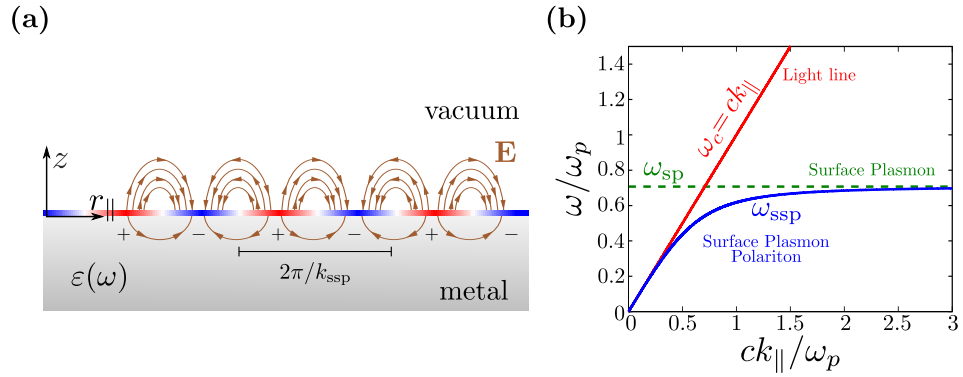

Figure 1.3: **(a)** Schematic representation of a SPP with a wavenumber k_{spp} propagating along the metal–vacuum interface located at $z = 0$. The electromagnetic field $\mathbf{E}$ associated with the SPP is represented by brown lines. **(b)** Frequency of a SPP obtained in this system from Eq. (1.40) (ω_{spp}, blue line), of light in free space (ω_c, red line), and of a long-wavelength nonretarded surface plasmon (ω_{sp}, green line) as a function of the wavenumber $k_{\parallel}$ parallel to the metal–vacuum interface. The frequency ω in the vertical axis is measured in units of ω_p, and $k_{\parallel}$ in the horizontal axis in units of ω_p/c, with c the speed of light in vacuum.

with c the speed of light in a vacuum. The amplitude of the momentum vector $\mathbf{k}_{\parallel}$ in Eq. (1.40) corresponds to the wavenumber k_{spp} of a SPP, $k_{\mathrm{spp}} = k_{\parallel}$, as schematically depicted in Figure 1.3a.

As shown in Figure 1.3b, for small $k_{\parallel}$, the SPP frequency ω_{spp} (blue line) approaches the dispersion line of light in free space, $\omega_c = ck_{\parallel}$ (red line). In contrast, for large $k_{\parallel}$, ω_{spp} yields the nondispersive ($k_{\parallel}$-independent) frequency of the nonretarded surface-plasmon frequency in the long-wavelength limit [Eq. (1.39)], $\omega_{\mathrm{sp}} = \omega_p/\sqrt{2}$ (green line) [10]. Importantly, for a given frequency ω, the momentum $k_{\parallel}$ of light in free space is always smaller than the momentum k_{spp} of SPPs, and therefore, a laser beam incident on an ideal surface cannot excite SPPs because momentum and energy cannot be simultaneously preserved. For this reason, several mechanisms have been adopted to provide the extra momentum needed to excite SPPs with light, such as the use of surface roughness or gratings [137], evanescent fields [138, 139], or sharp metallic tips placed on top of the metal–dielectric surfaces [140].

1.2.3 Localized surface plasmon polaritons (LSPPs)

When metallic nanoparticles (MNPs) of finite size are considered, a new type of plasmon resonances emerges, so-called *localized* surface plasmon polaritons (LSPPs) [11, 141]. The word *localized* is used because, unlike the SPP previously discussed, in this case the surface-charge oscillations are not propagating in space. Indeed, the translational invariance of the system is broken, and plasmons are confined in the three dimensions of space. Thus, LSPPs can often be understood as confined SPPs with a quantized wavenumber k_{spp}. Importantly, contrary to SPPs in semi-infinite

metal slabs, LSPPs in small MNPs can be excited by an incident laser beam, because the finite geometry of the MNP provides the extra momentum needed to overcome the mismatch between the momentum of light and plasmons. For simplicity, in this thesis we refer to LSPPs as "localized surface plasmons (LSPs)", or simply "plasmon resonances" or "plasmons".

In this thesis, we focus on quantum effects associated with the excitation of LSPPs in small MNPs, where special attention is paid to spherical nanoparticles and nanoparticle dimers. In the following, we describe the basic properties of LSPPs sustained in such geometries using a classical electromagnetic theory.

LSPPs in spherical nanoparticles

We first derive the resonance conditions fulfilled by LSPPs in a spherical MNP of radius a surrounded by vacuum (dielectric function $\varepsilon_d = 1$). These conditions are again determined from the self-sustained induced potential $\phi^{\text{ind}}(\mathbf{r},\omega)$ that satisfies Laplace's equation [Eq. (1.22)], which for the spherical MNP is given by Eq. (1.26). Under no external excitation, $\phi^{\text{ext}}(\mathbf{r},\omega) = 0$, the coefficients $b_{\ell m}(\omega)$ are non-null only at the poles of Eq. (1.27), so that the resonance conditions of the nonretarded LSPPs sustained in a spherical MNP are given by

$$\ell\varepsilon(\omega) + (\ell+1) = 0, \tag{1.41}$$

where ℓ is the multipole order of the LSPP resonance. Therefore, assuming a lossless Drude dielectric function [Eq. (1.10), with $\gamma_p = 0$], the frequencies ω_ℓ of LSPPs in a spherical MNP are given by:

$$\omega_\ell = \omega_p \sqrt{\frac{\ell}{2\ell+1}}, \tag{1.42}$$

which are independent of the size of the nanoparticle. However, this expression is rigorous only within the validity range of the nonretarded and local-response approximations. Indeed, it is known that the scale invariance of Eq. (1.42) is lifted when retardation effects are considered in large MNPs ($a \gtrsim 15$ nm) [7, 142], as well as when quantum-size effects are considered in very small nanostructures ($a \lesssim 5$ nm) [61, 95, 96]. We return in Chapters 2, 3, and 4 to the impact of quantum-size effects on the resonant frequencies of LSPPs, ω_ℓ.

Figure 1.4a shows the values of the LSPP frequencies ω_ℓ as a function of the multipole order ℓ [Eq. (1.42)]. For small values of ℓ, the resonance frequencies ω_ℓ of different order ℓ can be well differentiated. For example, the dipolar plasmon (DP) frequency ($\ell = 1$) is given by $\omega_{\text{DP}} = \omega_{\ell=1} = \omega_p/\sqrt{3}$, the quadrupolar plasmon (QP) frequency ($\ell = 2$) by $\omega_{\text{QP}} = \omega_{\ell=2} = \omega_p\sqrt{\frac{2}{5}}$, and the octupolar plasmon (OP) frequency ($\ell = 3$) by $\omega_{\text{OP}} = \omega_{\ell=3} = \omega_p\sqrt{\frac{3}{7}}$. In contrast, different LSPPs with large ℓ have very similar resonant frequencies, and thus, due to the broadening of each resonance given by the losses (γ_p in a Drude metal), they pile up in a single broad resonance, the so-called *pseudomode* [143, 144] (see Chapter 3). The

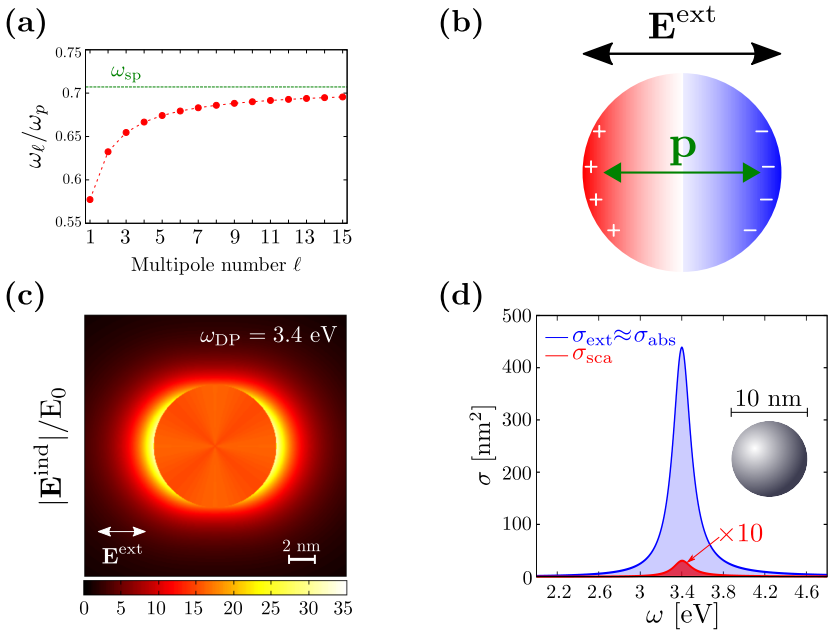

Figure 1.4: **(a)** Frequencies ω_ℓ of the nonretarded LSPP resonances sustained in a spherical MNP as a function of the multipole order ℓ, considering a lossless Drude dielectric function [Eq. (1.10)]. The frequencies ω_ℓ in the vertical axis are given in units of ω_p. The green dashed line represents the frequency of the surface plasmon, $\omega_{sp}/\omega_p = 1/\sqrt{2}$. **(b)** Sketch of the surface charge density induced in a spherical MNP by an external electromagnetic field $\mathbf{E}^{ext}$ corresponding to plane-wave illumination. The green arrow represents the oscillating dipole moment $\mathbf{p}$ induced at the MNP. **(c)** Absolute value of the electric field $\mathbf{E}^{ind}$ induced by a spherical MNP in response to an external plane wave $\mathbf{E}^{ext}$, calculated within the nonretarded approximation. The MNP has a radius $a = 5$ nm, and it is characterized by a Drude dielectric function with $\omega_p = 5.89$ eV and $\gamma_p = 0.21$ eV. The color map is shown at the DP resonance, $\omega_{DP} = 3.4$ eV. **(d)** Extinction (blue) and scattering (red, multiplied by 10) cross-section spectra of the same MNP as in panel (c). Due to the small size of the MNP, the extinction and absorption cross sections are almost equivalent, $\sigma_{ext}(\omega) \approx \sigma_{abs}(\omega)$.

frequency of this pseudomode approaches the frequency of the surface plasmon, $\omega_{\ell\to\infty} \sim \omega_p/\sqrt{2} = \omega_{sp}$ [Eq. (1.39)], since for large ℓ the local curvature of the spherical MNP is very large (approximately flat interface) as compared to the wavelength of the excited LSPPs, $\lambda_{LSPP} \sim 2\pi a/\ell$.

We next show that a plane wave illuminating a spherical MNP can excite LSPPs. We consider a plane wave linearly polarized along the z-direction, which is expressed within the nonretarded approximation as $\mathbf{E}^{ext}(\mathbf{r},\omega) = E_0\,\hat{\mathbf{z}}$. Intuitively, $\mathbf{E}^{ext}(\mathbf{r},\omega)$ polarizes the MNP along the z-direction, producing a displacement of the free-electron gas with respect to the positively charged background (see sketch in Figure 1.4b). Then, seeking to restore the equilibrium, the Coulomb interaction between the positive and negative charge densities produces a collective oscillation of the free-electron gas. The LSPP corresponds to the resonant excitation of this

collective oscillation.

A quantitative study of the excitation of LSPPs under plane-wave illumination can be done by calculating the optical response of the MNP following the procedure explained in Subsection 1.1.3. The external potential $\phi^{\text{ext}}(\mathbf{r},\omega)$ in this case is given in spherical coordinates by:

$$\phi^{\text{ext}}(\mathbf{r},\omega) = -\text{E}_0\ r\cos\theta, \tag{1.43}$$

and the integral in Eq. (1.27) providing the coefficients $b_{\ell m}(\omega)$ has an analytical solution [145], which is non-null only for $\ell = 1$. This means that, in contrast with SPPs, the DP resonance can be excited by plane-wave illumination. The electric field $\mathbf{E}^{\text{ind}}(\mathbf{r},\omega)$ induced in the proximity of the MNP is given by:

$$\mathbf{E}^{\text{ind}}(\mathbf{r},\omega) = -\nabla\phi^{\text{ind}}(\mathbf{r},\omega) = \begin{cases} -\text{E}_0 \frac{\varepsilon(\omega)-1}{\varepsilon(\omega)+2} \underbrace{(\cos\theta\ \hat{\mathbf{r}} - \sin\theta\ \hat{\boldsymbol{\theta}})}_{\hat{\mathbf{z}}} & r < a \\ \text{E}_0 \frac{\varepsilon(\omega)-1}{\varepsilon(\omega)+2} a^3/r^3 (2\cos\theta\ \hat{\mathbf{r}} + \sin\theta\ \hat{\boldsymbol{\theta}}) & r > a \end{cases}, \tag{1.44}$$

with $\hat{\boldsymbol{r}}$ and $\hat{\boldsymbol{\theta}}$ the unit vectors along the radial and tangential directions, respectively. Note that, as expected, $\mathbf{E}^{\text{ind}}(\mathbf{r},\omega)$ possesses a resonance at the DP frequency, $\omega_{\text{DP}} = \omega_p/\sqrt{3}$.

We show in Figure 1.4c the absolute value of the electric field $\mathbf{E}^{\text{ind}}(\mathbf{r},\omega)$ induced at the DP frequency, $\omega_{\text{DP}} = 3.4$ eV, in the proximity of a MNP of radius $a = 5$ nm. The MNP is characterized by a Drude dielectric function [Eq. (1.10)] using the parameters $\omega_p = 5.89$ eV and $\gamma_p = 0.21$ eV to describe sodium. Results are normalized to the amplitude of the incoming field, E_0. Crucially, the induced field is much stronger than the incident field, and it is localized in a space region much smaller ($\sim 1-5$ nm) than the wavelength of the incident field (~ 400 nm). Thus, this electromagnetic-field localization surpasses the diffraction limit.

Moreover, we note that the electric field $\mathbf{E}^{\text{ind}}(\mathbf{r},\omega)$ induced outside the MNP boundary ($r > a$) corresponds to the electrostatic field created by a point dipole placed at the center of the MNP [6, 22]. Indeed, the external field $\mathbf{E}^{\text{ext}}$ induces a dipole moment $\mathbf{p}(\omega) = \alpha(\omega)\mathbf{E}^{\text{ext}}$ at the spherical MNP that depends on the quasi-static polarizability [22]

$$\alpha(\omega) = a^3 \frac{\varepsilon(\omega)-1}{\varepsilon(\omega)+2}. \tag{1.45}$$

This induced dipole $\mathbf{p}(\omega)$ emits light into the far field. The MNP thus acts as an optical nanoantenna that can extremely localize incident electromagnetic radiation in the near field and radiate it into the far field [146]. The power $\mathcal{P}_{\text{sca}}$ scattered into the far field is related to $\mathbf{p}(\omega)$ by [6]

$$\mathcal{P}_{\text{sca}} = \frac{\omega^4}{3c^3}|\mathbf{p}(\omega)|^2. \tag{1.46}$$

Typically, the scattered power $\mathcal{P}_{\text{sca}} = \sigma_{\text{sca}} I_0$ is normalized to the intensity $I_0 = c|\mathbf{E}^{\text{ext}}|^2/(8\pi)$ of the incident plane wave, leading to the scattering cross section [7],

$$\sigma_{\text{sca}}(\omega) = \frac{8\pi}{3}\left(\frac{\omega}{c}\right)^4 |\alpha(\omega)|^2. \tag{1.47}$$

Moreover, the total power provided by the incoming light to a MNP, $\mathcal{P}_{\text{ext}}$, is given by the extinction cross section σ_{ext} through the relationship $\mathcal{P}_{\text{ext}} = \sigma_{\text{ext}} I_0$. $\sigma_{\text{ext}}(\omega)$ is defined as [7]

$$\sigma_{\text{ext}}(\omega) = \frac{4\pi\omega}{c}\text{Im}\{\alpha(\omega)\} = \sigma_{\text{abs}}(\omega) + \sigma_{\text{sca}}(\omega), \tag{1.48}$$

and corresponds to the sum of both scattering σ_{sca} and absorption σ_{abs} cross sections, the latter determining the power of light absorbed by the MNP, $\mathcal{P}_{\text{abs}} = \sigma_{\text{abs}} I_0$.

Figure 1.4d displays the extinction $\sigma_{\text{ext}}(\omega)$ (blue line) and scattering $\sigma_{\text{sca}}(\omega)$ (red line) cross-section spectra of the same spherical sodium MNP considered in Figure 1.4c ($a = 5$ nm). For such small MNP, $\sigma_{\text{sca}}(\omega) \propto a^6 \left(\frac{\omega}{c}\right)^4$ (with $\frac{\omega a}{c} << 1$) is about two-orders of magnitude smaller than $\sigma_{\text{ext}}(\omega) \propto a^3 \left(\frac{\omega}{c}\right)$. As a consequence, the extinction of the MNP is completely governed in this case by its absorption. Thus, for the small size of the MNPs considered in this thesis, $\sigma_{\text{abs}}(\omega)$ and $\sigma_{\text{ext}}(\omega)$ are almost equivalent. We therefore use the following expression to compute the absorption cross section in all the thesis [see Eq. (1.48)]:

$$\sigma_{\text{abs}}(\omega) = \frac{4\pi\omega}{c}\text{Im}\{\alpha(\omega)\}. \tag{1.49}$$

LSPPs in nanoparticle dimers

When two spherical MNPs are placed in close proximity, they form a *dimer* sustaining coupled LSPPs that can be excited by plane-wave illumination [23]. The study of LSPPs in nanoparticle dimers is particularly interesting because they induce much stronger field enhancements than individual MNPs [147, 148]. Moreover, the analysis of the optical properties of a dimer of spherical nanoparticles can help to understand the physics behind the optical response of more complex plasmonic nanostructures.

The resonant LSPP frequencies in a metallic dimer differ from those of the individual MNPs because the electromagnetic coupling between the two MNPs modifies the resulting plasmonic resonances [149]. The LSPP frequencies in this dimer configuration depend on the material and size of the MNPs forming the dimer, as well as on the surface-to-surface gap separation D. As an example, we show in Figure 1.5a the waterfall spectra of the absorption cross section, $\sigma_{\text{abs}}(\omega)$ [Eq. (1.49)], of a MNP dimer with gap separation ranging from $D = 1.05$ nm (bottom) to $D = 3.6$ nm (top). We consider the same sodium MNPs as in Figures 1.4c-d, and the external illumination is polarized along the dimer axis. Results are

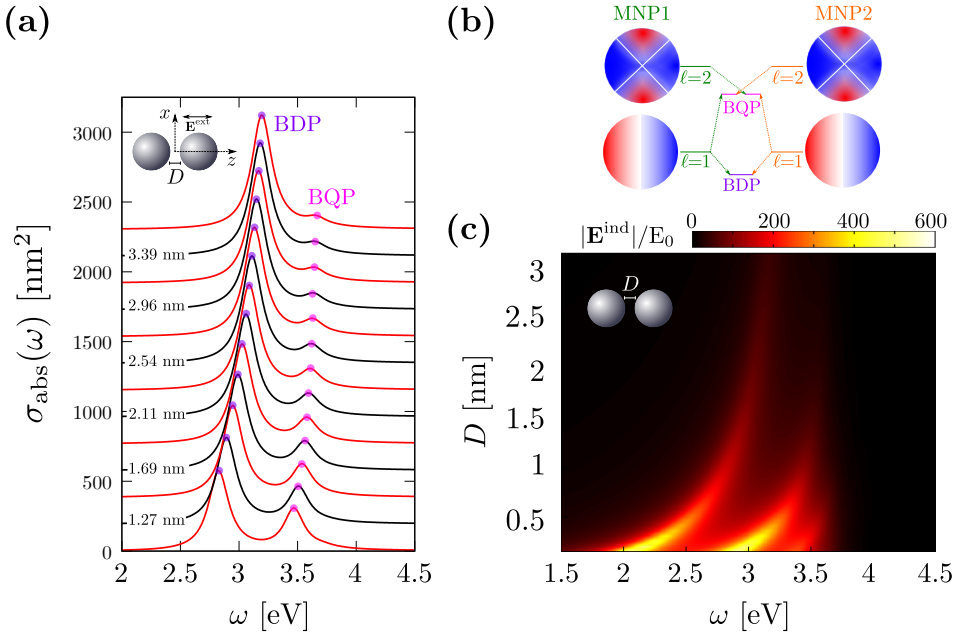

Figure 1.5: **(a)** Waterfall spectra of the absorption cross section $\sigma_{abs}(\omega)$ of a dimer composed by two spherical sodium MNPs of radius $a = 5$ nm characterized by a Drude dielectric function with $\omega_p = 5.89$ eV and $\gamma_p = 0.21$ eV (same as in Figures 1.4c-d). The gap separation is varied from $D = 1.05$ nm (bottom) to $D = 3.6$ nm (top) in steps of ~ 0.21 nm. **(b)** Sketch of the optical hybridization between LSPPs of individual MNPs leading to the bonding dipolar plasmon (BDP) and the bonding quadrupolar plasmon (BQP). **(c)** Color map of the induced electric-field enhancement $|\mathbf{E}|^{ind}/E_0$ in the middle of the gap formed by two MNPs with radius $a = 5$ nm as a function of the frequency of the external plane-wave illumination, ω, and the surface-to-surface gap distance, D. Results are obtained under the nonretarded approximation considering an external electromagnetic field, $\mathbf{E}^{ext} = E_0\hat{\mathbf{z}}$, polarized along the dimer axis (z-axis).

obtained within the nonretarded approximation following the procedure explained in Subsection 1.1.3.

Two distinct resonances can be observed in the absorption spectra of Figure 1.5a for the whole range of gap separation D considered: an intense bonding dipolar plasmon (BDP) shifting from $\omega_{BDP} \sim 3.2$ eV to ~ 2.8 eV as D is reduced, and a weaker bonding quadrupolar plasmon (BQP) at $\omega_{BQP} \sim 3.5$ eV, more pronounced for narrow gaps. The BQP also redshifts with decreasing D. The origin of these plasmon resonances can be understood using a hybridization picture that considers the coupling between the multipole modes of order ℓ of the two individual MNPs [Eq. (1.42)] similarly to the hybridization between atomic orbitals in diatomic molecules [150]. According to this hybridization picture (see sketch in Figure 1.5b), the BDP is mainly created due to the electromagnetic coupling between the DP resonances ($\ell = 1$) of the individual MNPs, while the BQP is mainly a consequence of the mixture between the DP mode of one MNP and the quadrupolar mode

($\ell = 2$) of the other one [151] (note that, strictly speaking, all the modes with $\ell \geq 1$ contribute to both the BDP and BQP).

Figure 1.5c shows the induced electric-field enhancement $|\mathbf{E}|^{\text{ind}}/\text{E}_0$ in the middle of the gap as a function of the frequency ω and the gap separation distance, D. The BDP and BQP resonances exhibit a strong redshift of the two modes with decreasing D down to the smallest value considered, $D = 0.16$ nm. In addition, a dramatic enhancement (up to $|\mathbf{E}|^{\text{ind}}/\text{E}_0 \sim 600$) of the electric field at the plasmon resonances is predicted by the classical LRA presented in this Chapter when the two MNPs are nearly in contact [23]. This enormous field enhancement is due to the fact that the classical LRA predicts a continuous increase of Coulomb interaction that induces extremely high charge densities of opposite sign at the MNP surfaces across the junction. The induced electric field $\mathbf{E}^{\text{ind}}(\mathbf{r}, \omega)$ inside the cavity shown in Figure 1.5c (e.g. $|\mathbf{E}^{\text{ind}}|/\text{E}_0 \sim 160$ for $D = 1$ nm) is generally much larger than the one obtained for the individual MNP in Figure 1.4c (maximum $|\mathbf{E}^{\text{ind}}|/\text{E}_0 \sim 35$). However, note that the behavior of $|\mathbf{E}|^{\text{ind}}/\text{E}_0$ predicted by classical theories for $D \lesssim 1$ nm is found to be nonphysical, as we discuss in Subsection 2.3.2.

1.3 Nonlinear optical response of small nanostructures

In the previous sections, we assumed that the optical response of the studied systems is linear, i.e., there is a linear dependence between $\mathbf{D}(\mathbf{r}, \omega)$ and $\mathbf{E}(\mathbf{r}, \omega)$ in the constitutive relationship given by Eq. (1.7). This assumption also imply a linear dependence between the external electric field $\mathbf{E}^{\text{ext}}$ and the induced dipole moment, $\mathbf{p}(\omega) = \alpha(\omega)\mathbf{E}^{\text{ext}}$, related through the linear polarizability $\alpha(\omega)$. However, it is known that nonlinear optical phenomena can emerge when the intensity of the illuminating field is large [36, 37, 152, 153]. In this thesis, the nonlinear optical response of plasmonic systems is directly obtained from quantum TDDFT calculations (see Section 2.4 and Chapter 6), but it is useful to briefly recall the main principles of nonlinear optics using classical electromagnetic theories.

The nonlinear scattering from a nanostructure much smaller than the wavelength of the external electric field $\mathbf{E}^{\text{ext}}$ can be studied by means of the induced dipole moment $\mathbf{p}$, since the scattered power $\mathcal{P}_{\text{sca}}$ is proportional to $\propto |\mathbf{p}|^2$ [Eq. (1.46)]. Here, we consider the nonlinear dipole moment in the time domain, $\text{p}(t)$, induced in response to a (time-dependent) electric field $\text{E}^{\text{ext}}(t)$ that drives the system. The simplest model to describe classically the nonlinear optical response expresses $\text{p}(t)$ as a power series of $\text{E}^{\text{ext}}(t)$ [152, 154],

$$\text{p}(t) = \alpha \text{E}^{\text{ext}}(t) + \alpha^{(2)} \left(\text{E}^{\text{ext}}(t)\right)^2 + \alpha^{(3)} \left(\text{E}^{\text{ext}}(t)\right)^3 + \dots, \tag{1.50}$$

where $\alpha^{(n)}$ are the n-order nonlinear hyperpolarizabilities of the structure under study (with $n = 2, 3, 4, \dots$). For simplicity, in Eq. (1.50), we use scalar notation[3]

[3] In general, $\text{p}(t)$ and $\text{E}^{\text{ext}}(t)$ are vectors, and $\alpha^{(n)}$ is a $(n+1)$-rank tensor [153].

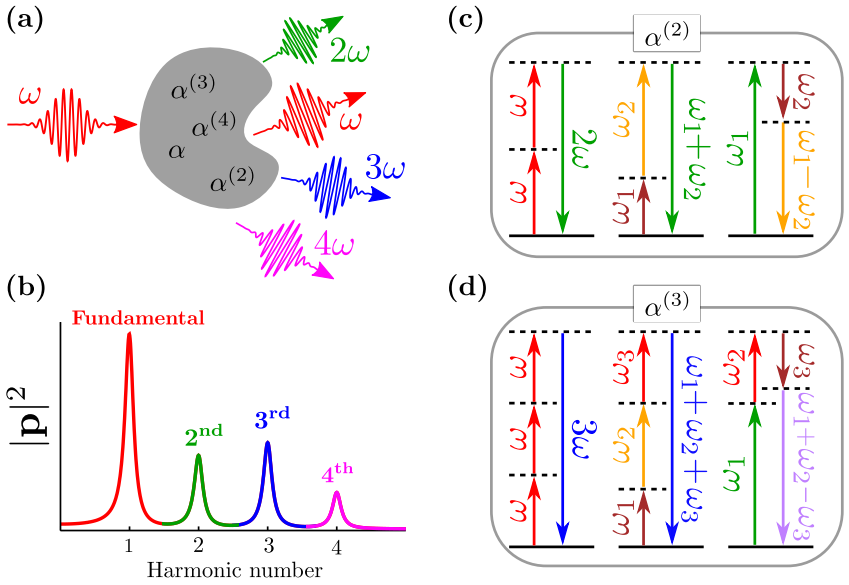

Figure 1.6: **(a)** Sketch of the nonlinear optical response of a system illuminated by an external pulse of fundamental frequency ω. Due to the nonlinear hyperpolarizabilities $\alpha^{(\mathrm{n})}$ (with $\mathrm{n} = 2, 3, 4$), the system scatters light not only at the fundamental frequency ω but also at harmonic frequencies $\Omega = \mathrm{n}\omega$. **(b)** Intensity spectrum of the nonlinear dipole moment $\mathbf{p}$ of a system as a function of the harmonic numbers $\mathrm{n} = 1, 2, 3, 4$. **(c)** Schematic representations of the nonlinear optical processes associated with the second-order nonlinear hyperpolarizability $\alpha^{(2)}$ involving two different frequencies of the external illumination ω_1 and ω_2. **(d)** Same as in **c**, but for the main nonlinear optical processes associated with the third-order $\alpha^{(3)}$ that involve three different incident frequencies ω_1, ω_2, and ω_3.

and assume that the system responds instantaneously to the external electric field $\mathrm{E}^{\mathrm{ext}}(t)$.

The nonlinear optical response of a nanostructure, classically described by Eq. (1.50), strongly depends upon the external illumination $\mathrm{E}^{\mathrm{ext}}(t)$. On the one hand, a monochromatic external electric field $\mathrm{E}^{\mathrm{ext}}(t) = \mathrm{Re}\left\{\mathrm{E}^{\mathrm{ext}}_{\omega} e^{-i\omega t}\right\}$ oscillating at a frequency ω can induce components of the dipole moment $\mathrm{p}_{\Omega}(t) \sim \mathrm{Re}\left\{\mathrm{p}_{\Omega} e^{-i\Omega t}\right\}$ oscillating at frequencies $\Omega = n\omega$ due to the nonlinear hyperpolarizabilities $\alpha^{(n)}$. This nonlinear optical process is called n-th harmonic generation, and it is schematically represented in Figure 1.6a. To understand this effect, we consider as an example a nanostructure with only a linear polarizability α and a second-order nonlinear hyperpolarizability $\alpha^{(2)}$. According to Eq. (1.50),

in this situation $\mathrm{p}(t)$ is given by (assuming $\mathrm{E}^{\mathrm{ext}}_{\omega}$ to be real)

$$\begin{aligned}\mathrm{p}(t) &= \alpha \mathrm{E}^{\mathrm{ext}}(t) + \alpha^{(2)} \left(\mathrm{E}^{\mathrm{ext}}(t)\right)^2 \\ &= \alpha \mathrm{Re}\left\{\mathrm{E}^{\mathrm{ext}}_{\omega} e^{-i\omega t}\right\} + \alpha^{(2)} \left(\mathrm{Re}\left\{\mathrm{E}^{\mathrm{ext}}_{\omega} e^{-i\omega t}\right\}\right)^2 \\ &= \alpha \mathrm{E}^{\mathrm{ext}}_{\omega} \cos(\omega t) + \alpha^{(2)} \left(\mathrm{E}^{\mathrm{ext}}_{\omega}\right)^2 \cos^2(\omega t) \\ &= \alpha \mathrm{E}^{\mathrm{ext}}_{\omega} \cos(\omega t) + \alpha^{(2)} \left(\mathrm{E}^{\mathrm{ext}}_{\omega}\right)^2 \frac{1}{2}\left(1 + \cos(2\omega t)\right).\end{aligned} \tag{1.51}$$

From the last line of Eq. (1.51), we conclude that the resulting $\mathrm{p}(t)$ has three different components (or *harmonics*): a harmonic $\mathrm{p}_{\omega}(t)$ oscillating at the fundamental frequency $\Omega = \omega$ that is linear with $\mathrm{E}^{\mathrm{ext}}_{\omega}$, and two nonlinear harmonics (proportional to $(\mathrm{E}^{\mathrm{ext}}_{\omega})^2$), one oscillating at the double frequency $\Omega = 2\omega$, $\mathrm{p}_{2\omega}(t)$ (second-harmonic generation), and another one, $\mathrm{p}_{0\omega}$, which is static ($\Omega = 0$, optical rectification) [152]. The example explained here can be extended to derive any n-th harmonic generation when considering a generic nanostructure with other hyperpolarizabilities $\alpha^{(n)}$ ($n > 2$). It can be seen that the amplitude of a particular n-harmonic, $\mathrm{p}_{n\omega}(t)$, primarily increases with the n-th power of the incident field, $\mathrm{p}_{n\omega} \propto |\mathrm{E}^{\mathrm{ext}}_{\omega}|^n$, so that the stronger the illumination intensity, the more efficient n-th harmonic generation. We show in Figure 1.6b a sketch of an intensity spectrum of the nonlinear dipole moment $\mathbf{p}(\Omega)$ in the frequency domain as a function of the harmonic numbers $n = 1, 2, 3, 4$.

Importantly, even-harmonic generation from centrosymmetric systems is forbidden because their inversion symmetry imposes $\alpha^{(2n)} = 0$ (with $n = 1, 2, 3 \ldots$). To demonstrate this effect, we can again consider the case of a nanostructure with only a linear polarizability α and a second-order hyperpolarizability $\alpha^{(2)}$, as we did in the derivation of Eq. (1.51). However, we now consider an external electric field of opposite sign, $\mathrm{E}^{\mathrm{ext}}(t) = -\mathrm{Re}\left\{\mathrm{E}^{\mathrm{ext}}_{\omega} e^{-i\omega t}\right\}$. Thus, according to Eq. (1.50), the nonlinear dipole moment $\mathrm{p}(t)$ is given in this situation by

$$p(t) = -\alpha \mathrm{E}^{\mathrm{ext}}_{\omega} \cos(\omega t) + \alpha^{(2)} \left(-\mathrm{E}^{\mathrm{ext}}_{\omega}\right)^2 \frac{1}{2}\left(1 + \cos(2\omega t)\right), \tag{1.52}$$

where it is assumed again that $\mathrm{E}^{\mathrm{ext}}_{\omega}$ is real.

Due to the inversion symmetry of the system, the amplitude of $p(t)$ given by Eqs. (1.51) and (1.52) must be the same but with opposite sign, which can be obtained only if $\alpha^{(2)} = 0$, thus preventing second-harmonic generation. This derivation can be straightforwardly generalized to demonstrate that any even-harmonic generation is forbidden from centrosymmetric nanostructures. In Chapter 6, we show that a quantum emitter coupled to a centrosymmetric MNP activates the otherwise-forbidden second-harmonic generation because it breaks the inversion symmetry of the system.

On the other hand, when the external illumination has components of different frequencies $\omega_j = \omega_1,\ \omega_2,\ \omega_3,\ \ldots$, the nonlinear optical response of the system becomes richer as compared to the one obtained under monochromatic excitation.

According to Eq. (1.50), an external electric field, $\mathbf{E}^{\text{ext}}(t) \sim \text{Re}\left\{\sum_j \mathbf{E}^{\text{ext}}_{j\omega} e^{-i\omega_j t}\right\}$, with components oscillating at frequencies ω_j (with $j = 1, 2, 3, \dots$), induces several harmonics $\mathbf{p}_\Omega(t) \sim \text{Re}\left\{\mathbf{p}_\Omega e^{-i\Omega t}\right\}$ oscillating at different frequencies Ω given by a linear combination of the incident frequencies ω_j. For example, the nonlinear optical processes activated due to $\alpha^{(2)}$ for two incident frequencies ω_1 and ω_2 lead to second-harmonic generation (SHG, where $\Omega = 2\omega_1$ or $\Omega = 2\omega_2$), sum-frequency generation (SFG, where $\Omega = \omega_1 + \omega_2$), or difference-frequency generation (DFG, where $\Omega = \omega_1 - \omega_2$) [152, 153]. In a similar way, when three different incident frequencies are combined (ω_1, ω_2, and ω_3), third-order nonlinear processes characterized by $\alpha^{(3)}$ can produce third-harmonic generation (THG, where $\Omega = 3\omega_1$, $\Omega = 3\omega_2$ or $\Omega = 3\omega_3$), and also other harmonics due to more complex combinations given by the sum and differences between three different incident frequencies ω_1, ω_2 and ω_3. Some of the nonlinear optical processes involving $\alpha^{(2)}$ and $\alpha^{(3)}$ are depicted in Figures 1.6c-d.

1.4 Plexcitonics: Quantum emitter excitons coupled to plasmons

Due to the strong electromagnetic fields and high field localization associated with the excitation of LSPPs, MNPs can strongly interact with nearby quantum emitters (QEs), such as atoms, molecules, or quantum dots. Indeed, the electronic transitions induced by optical excitations in QEs, so-called excitons[4], are much more efficiently excited in the presence of a MNP than in free space [102, 160, 161]. Moreover, the electromagnetic interaction between MNP plasmons and QE excitons can lead to hybrid resonances at optical frequencies in coupled QE–MNPs systems that are referred to as plasmon–exciton polaritons or *plexcitons* [39, 162–167].

In this thesis, we devote considerable attention to analyze quantum phenomena arising from such QE–MNPs interaction. In Chapter 5, we adopt a quantum many-body model to describe the QE, whereas in Chapter 3, Chapter 4 and Chapter 6 we treat the QE classically using the point-dipole approximation. Thus, in the following subsections we explain some important concepts in the context of electromagnetic QE–MNPs interaction, such as the point-dipole approximation, the formalism of the self-interaction dyadic Green's function to classically describe the exciton–plasmon electromagnetic coupling, and a simplified coupled harmonic-oscillator model useful to study certain aspects of such interaction.

[4] The concept of *exciton* is widely used in the context of bulk crystals [155], such as wide-gap insulators [156] and semiconductors [157], to describe the electrically-neutral quantum of electronic excitation associated with bound electron–hole pairs [158]. In this thesis, we consider excitons formed when exciting electronic transitions in quantum emitters [159], such as HOMO–LUMO transitions in organic molecules.

1.4.1 The point-dipole approximation

In spite of the strong inhomogeneity of plasmonic fields, the spatial extent of QEs is usually much smaller than the typical length scale of the plasmonic field variation, and thus QEs are often treated as polarizable point-like objects [168]. The electrostatic potential $\phi_{\mathrm{QE}}(\mathbf{r})$ created by a dipolar transition of a QE within the nonretarded limit is then given by

$$\phi_{\mathrm{QE}}(\mathbf{r}) = \mathbf{p}_{\mathrm{QE}} \cdot \frac{\mathbf{r} - \mathbf{r}_{\mathrm{QE}}}{|\mathbf{r} - \mathbf{r}_{\mathrm{QE}}|^3}, \tag{1.53}$$

with $\mathbf{p}_{\mathrm{QE}}$ the dipole moment of the QE and $\mathbf{r}_{\mathrm{QE}}$ its position. Thus, if $\mathbf{p}_{\mathrm{QE}}$ is known, one can use the methodology explained in Subsection 1.1.3 to obtain the optical response of plasmonic nanostructures interacting with QEs. The simplest way to estimate the value of $\mathbf{p}_{\mathrm{QE}}$ under weak illumination [22] is to consider that the QE possesses only two electronic states, namely a ground state at energy ϵ_{g} and an excited state at energy ϵ_{ex}. Defining the transition frequency $\omega_{\mathrm{QE}} = \epsilon_{\mathrm{ex}} - \epsilon_{\mathrm{eg}}$ of the exciton as the energy difference between the excited and the ground states of the QE, the time evolution of $\mathbf{p}_{\mathrm{QE}}$ can be described according to [22]

$$\ddot{\mathbf{p}}_{\mathrm{QE}}(t) + \gamma_{\mathrm{QE}}\dot{\mathbf{p}}_{\mathrm{QE}}(t) + \omega_{\mathrm{QE}}^2\mathbf{p}_{\mathrm{QE}}(t) = \alpha_{\mathrm{QE}}^0\mathbf{E}^{\mathrm{ext}}(t), \tag{1.54}$$

where γ_{QE} and α_{QE}^0 are the intrinsic loss rate and oscillator strength of the QE, respectively, and $\mathbf{E}^{\mathrm{ext}}(t)$ is evaluated at the position of the QE. The oscillator strength α_{QE}^0 is related to the transition dipole moment μ_{QE} through $\alpha_{\mathrm{QE}}^0 = 2\omega_{\mathrm{QE}}|\mu_{\mathrm{QE}}|^2$ [22]. For simplicity, α_{QE}^0 is always taken in this thesis as a scalar, corresponding to an isotropic QE. When considering the electromagnetic interaction between the QE and MNPs, $\mathbf{E}^{\mathrm{ext}}(t)$ in Eq. (1.54) must contain the contributions of both the external illumination and the electric field created by the MNPs. Moreover, the MNPs electric field is affected by $\mathbf{p}_{\mathrm{QE}}(t)$, and therefore, the problem has to be solved self-consistently, as we do e.g. in Chapter 6. We show in Appendix C the method used in this thesis to solve Eq. (1.54) numerically in the time domain.

To simulate the QE–MNPs interaction in the linear-response regime, it is usually convenient to use Eq. (1.54) in the frequency domain. In this way, the frequency-dependent polarizability $\alpha_{\mathrm{QE}}(\omega)$ relating the dipole moment $\mathbf{p}_{\mathrm{QE}}(\omega)$ of an isotropic QE and $\mathbf{E}^{\mathrm{ext}}(\omega)$ is:

$$\alpha_{\mathrm{QE}}(\omega) = \frac{\alpha_{\mathrm{QE}}^0}{(\omega_{\mathrm{QE}}^2 - \omega^2 - i\omega\gamma_{\mathrm{QE}})}. \tag{1.55}$$

1.4.2 The self-interaction dyadic Green's function

In this subsection, we explain the dyadic Green's function formalism adopted to address the electromagnetic coupling between a QE and a MNP in the frequency domain [22, 40]. We apply this formalism to individual spherical

MNPs and dimers interacting with a single QE, but it can be applied to any nanostructure or nanoparticle ensemble of arbitrary shape. The optical response of a coupled QE–MNP system is determined in this thesis by the total dipole moment $\mathbf{p}(\omega) = \mathbf{p}_{\mathrm{MNP}}(\omega) + \mathbf{p}_{\mathrm{QE}}(\omega)$ induced in the system, which is given as a sum of the MNP dipole, $\mathbf{p}_{\mathrm{MNP}}(\omega)$, and that of the QE, $\mathbf{p}_{\mathrm{QE}}(\omega)$.

The electromagnetic QE–MNP interaction can be understood as follows: the external illumination $\mathbf{E}^{\mathrm{ext}}$ induces an electric near field $\mathbf{E}^{\mathrm{ind}}(\mathbf{r},\omega)$ and dipole moment $\mathbf{p}_{\mathrm{MNP}}(\omega)$ at the MNP. Then, $\mathbf{E}^{\mathrm{ind}}(\mathbf{r},\omega)$ and $\mathbf{E}^{\mathrm{ext}}$ induce a dipole moment at the QE, $\mathbf{p}_{\mathrm{QE}}(\omega)$, which acts back on itself due to the presence of the MNP. Finally, due to the electromagnetic QE–MNP interaction, the dipole moment $\mathbf{p}_{\mathrm{QE}}(\omega)$ created at the QE also contributes to the induced dipole moment $\mathbf{p}_{\mathrm{MNP}}(\omega)$ at the MNP.

The first step to mathematically describe the physical picture depicted above is to introduce the *self-interaction* dyadic Green's function $\hat{\mathbb{G}}(\mathbf{r}_{\mathrm{QE}},\mathbf{r}_{\mathrm{QE}},\omega)$. It provides the electric field $\mathbf{E}^{\mathrm{self}}(\mathbf{r}_{\mathrm{QE}},\omega)$ created by the MNP at the QE position, $\mathbf{r}_{\mathrm{QE}}$, in response to the electromagnetic radiation of the QE [104, 169–172],[5]

$$\mathbf{E}^{\mathrm{self}}(\mathbf{r}_{\mathrm{QE}},\omega) = \hat{\mathbb{G}}(\mathbf{r}_{\mathrm{QE}},\mathbf{r}_{\mathrm{QE}},\omega)\cdot\mathbf{p}_{\mathrm{QE}}(\omega). \tag{1.56}$$

The optical response of the coupled QE–MNP system can be described with the following coupled equations for $\mathbf{p}_{\mathrm{QE}}(\omega)$ and $\mathbf{p}_{\mathrm{MNP}}(\omega)$,

$$\begin{aligned}
\mathbf{p}_{\mathrm{QE}}(\omega) &= \alpha_{\mathrm{QE}}(\omega)\left(\mathbb{I}-\alpha_{\mathrm{QE}}(\omega)\hat{\mathbb{G}}(\mathbf{r}_{\mathrm{QE}},\mathbf{r}_{\mathrm{QE}},\omega)\right)^{-1}\left(\mathbf{E}^{\mathrm{ext}}+\mathbf{E}^{\mathrm{ind}}(\mathbf{r}=\mathbf{r}_{\mathrm{QE}},\omega)\right),\\
\mathbf{p}_{\mathrm{MNP}}(\omega) &= \hat{\alpha}_{\mathrm{MNP}}(\omega)\cdot\mathbf{E}^{\mathrm{ext}}+\hat{\alpha}^{\mathrm{QE}}_{\mathrm{MNP}}(\omega)\cdot\mathbf{p}_{\mathrm{QE}}(\omega),
\end{aligned} \tag{1.57}$$

where $\mathbb{I}$ is the identity matrix, $\mathbf{E}^{\mathrm{ind}}(\mathbf{r}=\mathbf{r}_{\mathrm{QE}},\omega)$ is the electric field induced by the isolated MNP at $\mathbf{r}_{\mathrm{QE}}$ in response to the external illumination $\mathbf{E}^{\mathrm{ext}}$, $\hat{\alpha}_{\mathrm{MNP}}(\omega)$ is the polarizability tensor of the MNP, and $\hat{\alpha}^{\mathrm{QE}}_{\mathrm{MNP}}(\omega)$ is a tensor that provides the dipole moment induced at the MNP in response to the electromagnetic field created by a point dipole $\mathbf{p}_{\mathrm{QE}}(\omega)$ located at $\mathbf{r}_{\mathrm{QE}}$.

For individual spherical MNPs and dimers, one can use the procedure explained in Subsection 1.1.3 to obtain the quantities appearing in Eq. (1.57). In particular, for a QE coupled to an individual spherical MNP of radius a and dielectric function $\varepsilon(\omega)$, Eq. (1.57) can be solved analytically. In this situation, $\hat{\mathbb{G}}(\mathbf{r}_{\mathrm{QE}},\mathbf{r}_{\mathrm{QE}},\omega)$ can be obtained by solving Laplace's equation [Eq. (1.22)] for the external potential corresponding to an unitary point dipole with two different orientations: perpendicular ($\perp$) and parallel ($\parallel$) to the MNP surface. From the electric field induced by the MNP at the position of the dipole, $\hat{\mathbb{G}}(\mathbf{r}_{\mathrm{QE}},\mathbf{r}_{\mathrm{QE}},\omega)$ is fully defined

[5] In many references in the literature [22], one can find slightly different definitions of $\hat{\mathbb{G}}(\mathbf{r}_{\mathrm{QE}},\mathbf{r}_{\mathrm{QE}},\omega)$. In this thesis, we adopt the definition of $\hat{\mathbb{G}}(\mathbf{r}_{\mathrm{QE}},\mathbf{r}_{\mathrm{QE}},\omega)$ given by Eq. (1.56) since it simplifies the notation.

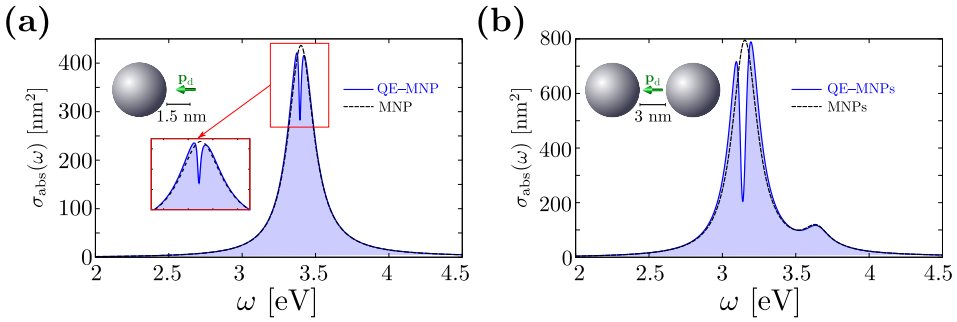

Figure 1.7: **(a)** Absorption cross-section spectra $\sigma_{\rm abs}(\omega)$ of an individual spherical MNP (dashed black line) and that of a QE–MNP coupled system (blue line). The MNP has a radius $a = 5$ nm, and it is characterized by a Drude dielectric function with $\omega_p = 5.89$ eV and $\gamma_p = 0.21$ eV. The QE, located at 1.5 nm from the surface of the MNP, is characterized by an oscillator strength $\alpha^0_{\rm QE} = 2$ au, an intrinsic loss rate $\gamma_{\rm QE} = 10$ meV, and a transition frequency $\omega_{\rm QE} = \omega_{\rm DP} = 3.4$ eV in resonance with the DP of the MNP. **(b)** Same as in panel (a) but for a MNP dimer characterized by a gap separation $D = 3$ nm. The QE emitter is at resonance with the BDP mode of the dimer, $\omega_{\rm QE} = \omega_{\rm BDP} = 3.15$ eV. The results are obtained within the nonretarded approximation.

by the corresponding components [145],

$$\mathbb{G}_{\perp}(\mathbf{r}_{\rm QE}, \mathbf{r}_{\rm QE}, \omega) = \sum_{\ell=1}^{\infty} \frac{\varepsilon(\omega) - 1}{\varepsilon(\omega) + \frac{\ell+1}{\ell}} \frac{a^{2\ell+1}}{R^{2\ell+4}} (\ell+1)^2, \tag{1.58a}$$

$$\mathbb{G}_{\parallel}(\mathbf{r}_{\rm QE}, \mathbf{r}_{\rm QE}, \omega) = \sum_{\ell=1}^{\infty} \frac{\varepsilon(\omega) - 1}{\varepsilon(\omega) + \frac{\ell+1}{\ell}} \frac{a^{2\ell+1}}{R^{2\ell+4}} \frac{1}{2} \ell(\ell+1), \tag{1.58b}$$

with R the distance between the QE position $\mathbf{r}_{\rm QE}$ and the center of the spherical MNP. Moreover, $\mathbf{E}^{\rm ind}(\mathbf{r} = \mathbf{r}_{\rm QE}, \omega)$ can be obtained from Eq. (1.44), and $\hat{\alpha}_{\rm MNP}(\omega) \equiv \alpha(\omega)$ is given by Eq. (1.45).

On the other hand, to obtain the optical response of a QE coupled to a dimer of spherical nanoparticles, we numerically solve the quantities of Eq. (1.57) by following the methodology explained in Subsection 1.1.3. Thus, the optical response of the QE–MNPs system is obtained in this case in three steps: first, we calculate $\mathbf{E}^{\rm ind}(\mathbf{r} = \mathbf{r}_{\rm QE}, \omega)$ and $\hat{\alpha}_{\rm MNP}(\omega)$ by solving Eq. (1.35) for the external potential $\phi^{\rm ext}(\mathbf{r}, \omega)$ given by Eq. (1.43) corresponding to plane-wave illumination. Second, $\hat{\mathbb{G}}(\mathbf{r}_{\rm QE}, \mathbf{r}_{\rm QE}, \omega)$ and $\hat{\alpha}^{\rm QE}_{\rm MNP}(\omega)$ are obtained by solving the same equations but considering the external potential $\phi^{\rm ext}(\mathbf{r}, \omega) \equiv \phi_{\rm QE}(\mathbf{r})$ of a unitary point dipole given by Eq. (1.53). Finally, we use Eq. (1.57) to calculate the total dipole moment induced at the coupled system, $\mathbf{p}(\omega) = \mathbf{p}_{\rm MNP}(\omega) + \mathbf{p}_{\rm QE}(\omega)$.

As an example, we show in Figure 1.7 the absorption cross-section spectra $\sigma_{\rm abs}(\omega)$ of an individual MNP (panel a) and a MNP dimer (panel b) interacting with a QE. The MNPs have a radius $a = 5$ nm and are characterized using the same Drude parameters as above (sodium). The QE is characterized [Eq. (1.45)]

by an oscillator strength $\alpha^0_{\mathrm{QE}} = 2$ au, an intrinsic loss rate $\gamma_{\mathrm{QE}} = 10$ meV, and a transition frequency ω_{QE} resonant with the main plasmon resonance of the nanostructures. In both situations, the presence of the QE strongly affects the optical absorption of the coupled system (blue lines) as compared to that of the isolated MNPs (dashed black lines). In particular, for the individual MNP Figure 1.7a shows a spectrally narrow Fano-like resonance at $\omega \sim \omega_{\mathrm{DP}} = 3.4$ eV due to the destructive interference between the excitation of the plasmon and that of the exciton [173, 174]. The effect of the QE on the optical response is stronger in the dimer configuration shown in Figure 1.7b due to the field enhancement in the gap and thus larger electromagnetic coupling between the QE exciton and the plasmonic resonances (see the following subsection for further details). In Chapter 3 and Chapter 5, we study the impact of several quantum-mechanical phenomena in the optical response of QE–MNPs coupled systems.

1.4.3 Coupled harmonic-oscillator model

The self-interaction Green's function formalism explained in the previous subsection is generic and, in principle, can be applied to obtain the optical response of a QE interacting with any plasmonic nanostructure of arbitrary shape. However, using Eq. (1.57) requires the computation of the optical response of the plasmonic nanostructure (e.g. using numerical methods [112–115]), which can be difficult in many situations. Moreover, the exact numerical solution of the electromagnetic interaction between QEs and MNPs is usually difficult to interpret. In contrast, a simpler model based on coupled harmonic oscillators, explained in this subsection, can provide physical insight into such exciton–plasmon electromagnetic interaction [42, 175–178].

In this model, the LSPP in the MNP and the exciton in the QE are each described as damped harmonic oscillators [42]. These oscillators represent, for example, the dipole moment induced at the MNP and at the QE, respectively, and are coupled through the electric near field induced by each structure. The equations of motion of the QE induced dipole moment, $\mathbf{p}_{\mathrm{QE}}(t)$, and that of the MNP, $\mathbf{p}_{\mathrm{MNP}}(t)$, are given under external plane-wave excitation $\mathrm{E}^{\mathrm{ext}}(t) = \mathrm{Re}\left\{\mathrm{E}_0 e^{-i\omega t}\right\}$ in time domain by [42, 178]

$$\begin{aligned}
\ddot{\mathbf{p}}_{\mathrm{QE}}(t) + \gamma_{\mathrm{QE}}\dot{\mathbf{p}}_{\mathrm{QE}}(t) + \omega^2_{\mathrm{QE}}\mathbf{p}_{\mathrm{QE}}(t) &= \alpha^0_{\mathrm{QE}}\Big(\mathbf{E}^{\mathrm{ext}}(t) + \beta_{\mathrm{MNP}}\mathbf{p}_{\mathrm{MNP}}(t)\Big) \\
\ddot{\mathbf{p}}_{\mathrm{MNP}}(t) + \gamma_{\mathrm{MNP}}\dot{\mathbf{p}}_{\mathrm{MNP}}(t) + \omega^2_{\mathrm{MNP}}\mathbf{p}_{\mathrm{MNP}}(t) &= \alpha^0_{\mathrm{MNP}}\Big(\mathbf{E}^{\mathrm{ext}}(t) + \beta_{\mathrm{QE}}\mathbf{p}_{\mathrm{QE}}(t)\Big),
\end{aligned} \tag{1.59}$$

where ω_{MNP}, γ_{MNP} and α^0_{MNP} are the resonant frequency, intrinsic loss rate and oscillator strength associated with the single LSPP mode of the MNP, respectively. Only a single LSPP mode is considered in the MNP, so that a generalization of the model would be required to simultaneously account for the electromagnetic coupling between the exciton and multiple LSPPs, such as the BDP and BQP resonances supported by the metallic dimer shown in Figure 1.7. In Eq. (1.59), the exciton–plasmon coupling is introduced *via* the electric near field induced by the

MNP (QE), $\beta_{\mathrm{MNP}}\mathbf{p}_{\mathrm{MNP}}$ ($\beta_{\mathrm{QE}}\mathbf{p}_{\mathrm{QE}}$), at the position of the QE (MNP).

The direct excitation of the QE by the plane wave is usually much weaker than the excitation by the electric near field of the MNP, and thus one can consider $\alpha^0_{\mathrm{QE}}\mathbf{E}^{\mathrm{ext}}(t) = 0$ in Eq. (1.59) [42]. Moreover, $\mathbf{p}_{\mathrm{MNP}}(t)$ is expected to be much stronger than $\mathbf{p}_{\mathrm{QE}}(t)$. Under these assumptions, the expression of the approximated polarizability of the coupled system can be obtained in the frequency domain (using $\mathbf{p}_{\mathrm{MNP}}(t) = \mathrm{Re}\left\{\mathbf{p}_{\mathrm{MNP}}(\omega)e^{-i\omega t}\right\}$ and $\mathbf{p}_{\mathrm{QE}}(t) = \mathrm{Re}\left\{\mathbf{p}_{\mathrm{QE}}(\omega)e^{-i\omega t}\right\}$)

$$\alpha(\omega) \approx \frac{\alpha^0_{\mathrm{MNP}}\left(\omega^2_{\mathrm{QE}} - \omega^2 - i\omega\gamma_{\mathrm{QE}}\right)}{\left(\omega^2_{\mathrm{MNP}} - \omega^2 - i\omega\gamma_{\mathrm{MNP}}\right)\left(\omega^2_{\mathrm{QE}} - \omega^2 - i\omega\gamma_{\mathrm{QE}}\right) - 4g^2\omega^2}, \tag{1.60}$$

where we define the coupling strength g such that $4g^2\omega^2 = \alpha^0_{\mathrm{QE}}\alpha^0_{\mathrm{MNP}}\beta_{\mathrm{QE}}\beta_{\mathrm{MNP}}$. The factor 4 is introduced so that g can be directly compared to the coupling strength used in cavity quantum-electrodynamics models [179]. This definition implies a dependence of g on ω, $g \propto 1/\omega$. However, in practice we consider g to be a constant (see below), consistent with the procedure adopted in the literature [42]. We expect that an alternative assumption for the definition of g would not substantially modify the results.

The expression given by Eq. (1.60) can be useful e.g. to estimate the value of the coupling strength g between a QE exciton and a specific LSPP in the MNP. This can be done by fitting the exact polarizability $\alpha(\omega)$ of the QE–MNPs system rigorously obtained by using e.g. the methodology explained in Subsection 1.4.2 to the approximated result obtained from Eq. (1.60). We follow this procedure in Chapter 5, which allows us to identify whether the studied QE–MNPs system is in the strong-coupling regime. In fact, the criteria adopted in the literature to identify the strong-coupling regime are intimately related to the value of g [180]. In brief, the less demanding criterion states that $g > |\gamma_{\mathrm{MNP}} - \gamma_{\mathrm{QE}}|/4$ has to be fulfilled. Other criteria often used are $g > (\gamma_{\mathrm{MNP}} + \gamma_{\mathrm{QE}})/4$ and the more restrictive $g > (\gamma_{\mathrm{MNP}} + \gamma_{\mathrm{QE}})/2$.

Figure 1.8 shows the absorption spectra $\sigma_{\mathrm{abs}}(\omega)$ [Eq. (1.49)] of a QE–MNPs system obtained by solving Eq. (1.57) within the self-interaction Green's function formalism (blue line) and the approximated value of $\sigma_{\mathrm{abs}}(\omega)$ obtained from Eq. (1.60) using the coupled harmonic-oscillator model (red dotted line). The parameters characterizing the system are the same as in Figure 1.7. In the case of the individual MNP (Figure 1.8a), the coupling strength g between the DP and the exciton is $g = 18$ meV $< (\gamma_{\mathrm{MNP}} - \gamma_{\mathrm{QE}})/4 < (\gamma_{\mathrm{MNP}} + \gamma_{\mathrm{QE}})/4 < (\gamma_{\mathrm{MNP}} + \gamma_{\mathrm{QE}})/2$, which indicates that the system is in the weak-coupling regime (here $\gamma_{\mathrm{MNP}} = \gamma_p$). For the metallic dimer (Figure 1.8b), the coupling strength g between the BDP and the exciton is $g = 45$ meV $\approx (\gamma_{\mathrm{MNP}} - \gamma_{\mathrm{QE}})/4 \approx (\gamma_{\mathrm{MNP}} + \gamma_{\mathrm{QE}})/4$, thus the system is nearly in the strong-coupling regime.

For situations of strong coupling, the coupled harmonic-oscillator model depicted in this subsection can also be used to calculate the frequencies of the two polaritons resulting from the electromagnetic interaction between the exciton and the LSPP. Once the values of the coupling strength g is determined, as explained above, the

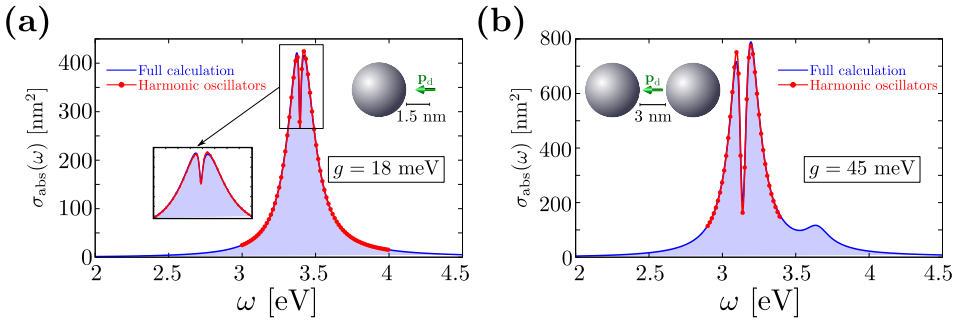

Figure 1.8: **(a)** Absorption cross-section spectra $\sigma_{\rm abs}(\omega)$ of a QE–MNP coupled system obtained by using the self-interaction Green's function formalism explained in Subsection 1.4.2 (blue line) and a fit to a coupled harmonic-oscillator model (Eq. (1.60), red dotted line). The MNP has a radius $a = 5$ nm, and it is characterized by a Drude dielectric function with $\omega_p = 5.89$ eV and $\gamma_p = 0.21$ eV. Within the coupled-oscillator model $\omega_{\rm MNP} = \omega_{\rm DP} = 3.4$ eV is used. The QE, located at 1.5 nm from the surface of the MNP, is characterized by an oscillator strength $\alpha^0_{\rm QE} = 2$ au, an intrinsic loss rate $\gamma_{\rm QE} = 10$ meV, and a transition frequency $\omega_{\rm QE} = \omega_{\rm DP}$ in resonance with the DP of the MNP. The coupling strength is $g = 18$ meV, and it is obtained by fitting the exact result obtained from Eq. (1.57) to the expression given by Eq. (1.60). **(b)** Same as in panel (a) but for a MNP dimer characterized by a gap separation $D = 3$ nm. Within the coupled-oscillator model $\omega_{\rm MNP} = \omega_{\rm BDP} = 3.15$ eV is used. The QE emitter is at resonance with the BDP mode of the dimer, $\omega_{\rm QE} = \omega_{\rm BDP}$, and the coupling strength is $g = 45$ meV. In both panels, $\gamma_{\rm MNP} = \gamma_p$ is used within the coupled-oscillator model.

frequencies of the upper (ω_+) and the lower (ω_-) polaritons can be obtained by solving the eigenmodes of Eq. (1.59) [179]

$$\omega_\pm = \frac{1}{2}(\omega_{\rm MNP} + \omega_{\rm QE}) \pm \frac{1}{2}{\rm Re}\left\{\sqrt{4g^2 + \left[\omega_{\rm MNP} - \omega_{\rm QE} + i\frac{\gamma_{\rm QE} - \gamma_{\rm MNP}}{2}\right]^2}\right\}. \tag{1.61}$$

According to Eqs. (1.61), in a resonant exciton–plasmon system ($\omega_{\rm MNP} \approx \omega_{\rm QE}$), ω_+ and ω_- are separated by a factor $2\sqrt{g^2 - (\gamma_{\rm QE} - \gamma_{\rm MNP})^2/16}$ as long as $g > |\gamma_{\rm QE} - \gamma_{\rm MNP}|/4$, which justifies the less demanding criterion of strong coupling mentioned above. Moreover, for situations where $g >> |\gamma_{\rm QE} - \gamma_{\rm MNP}|/4$, the separation is $2g$, leading to the so-called Rabi splitting between the upper and lower polaritons in strongly coupled systems [181–183]. In contrast, in the weak-coupling regime, where $g < |\gamma_{\rm QE} - \gamma_{\rm MNP}|/4$, there is no splitting between ω_+ and ω_-, indicating that no polaritonic (hybrid) modes are created as a consequence of the electromagnetic interaction between the exciton and the LSPP.

1.5 Summary

In summary, we have presented in this chapter the classical viewpoint of plasmonic excitations supported by MNPs and their electromagnetic coupling to QE excitons. First, we have reviewed Maxwell's equations in the linear-response regime, and focused on the local-response approximation (LRA) that neglects the spatial nonlocality of the optical response. Next, we have introduced the nonretarded approximation adopted in this thesis and presented a method to obtain the optical response of spherical individual nanoparticles and dimers. Then, after briefly describing bulk and surface plasmons, we have paid special attention to the excitation of LSPPs in plasmonic nanostructures of finite geometry such as spherical MNPs and dimers. We have also introduced a simple model to understand the nonlinear optical response from MNPs. Finally, we have presented the theoretical approaches used in this thesis to describe the electromagnetic interaction between QEs and MNPs within a classical linear-response framework. The concepts explained in this chapter thus provide the grounds of classical light–matter interaction and serve as a reference to study quantum phenomena that are out of the reach of classical descriptions. In this thesis, quantum effects arising in the light–matter interaction are studied within TDDFT as explained in the following Chapter 2.

CHAPTER 2

QUANTUM MANY-BODY DESCRIPTION OF LIGHT–MATTER INTERACTION

The classical theoretical framework introduced in Chapter 1 can be used to accurately describe light–matter interaction when the characteristic dimensions of the system, such as the size of the MNP or the gap separation in MNP ensembles, are relatively large. However, when small MNPs ($\lesssim$ 10 nm) or ultra-narrow gaps ($\lesssim$ 1 nm) are considered, the quantum nature of the electrons dynamics becomes important and classical descriptions are no longer valid. In this context, a methodology capable of describing the electronic structure from a quantum many-body perspective is required, which is a considerable challenge [184]. For example, to describe the ground state of a small sodium MNP containing 1000 atoms (with 11 electrons per atom), one would have to solve the Schrödinger equation for a wave function depending on 33000 spatial variables (three spatial variables per electron without considering spin degeneracy and neglecting the degrees of freedom of the nuclei). Solving this tremendously complex problem is out of current computational capabilities [185].

To reduce the computational complexity of this many-body problem, one can use density-functional theory (DFT), a rigorous formalism that deals with the ground-state electron density rather than with the many-electron wave function. DFT can be applied only to study ground-state electronic properties, so that to determine electronic excitations in metals (and other materials) resulting from light–matter interaction it is necessary to adopt the time-dependent extension of DFT, the so-called time-dependent density functional theory (TDDFT). This approach addresses the time evolution of the electron density when the system is subjected to a time-dependent external potential. On the other hand, a semiclassical

approach referred to as the surface-response formalism (SRF) which incorporates the parameters $d_\perp(\omega)$ and $d_\parallel(\omega)$ (first introduced by Peter Feibelman in the 1980s [98]), has prompted great interest and practical use in the Nanophotonics community over the last few years to account for certain quantum many-body effects in the optical response of metals. The advantage of using the SRF is that it is much simpler computationally as compared to TDDFT, and thus allows for studying quantum effects in larger plasmonic nanostructures. However, the SRF is a cruder approximation than TDDFT, and cannot account for all quantum many-body phenomena.

In Sections 2.1 and 2.2, we briefly recall the fundamentals of DFT and TDDFT, and describe the corresponding quantum many-body algorithms based on the wave-packet propagation (WPP) method employed in this thesis to address the dynamics of the electron density in time domain. We apply this TDDFT framework in Sections 2.3 and 2.4 to introduce some of the main quantum many-body phenomena manifested in the linear and nonlinear optical response of canonical plasmonic systems such as individual spherical and cylindrical MNPs and their dimers. Finally, we explain in Section 2.5 the fundamentals of the SRF used in this thesis (complementary to TDDFT) to provide additional insights on the study of particular quantum surface effects on the optical response.

2.1 Fundamentals of density functional theory (DFT)

Density-functional theory (DFT) allows us to determine the ground-state electronic properties of an interacting many-electron system by only calculating the ground-state (or *equilibrium*) electron density $n_0(\mathbf{r})$, i.e., without the need of the exact wave function satisfying the many-electron Schrödinger equation. According to the work by Hohenberg and Kohn [186], $n_0(\mathbf{r})$ completely determines the ground-state energy, $\mathcal{E}_0$, and all other electronic properties of the many-electron system subjected to an external time-independent potential. This potential can be, for example, the attractive Coulomb potential $V_{\text{ion}}(\mathbf{r})$ created by the positively charged ions in a metal, as we consider here. In this case, the ground-state energy $\mathcal{E}_0$ of a metal can be expressed as a unique functional of $n_0(\mathbf{r})$ (denoted by the square brackets),

$$\mathcal{E}_0[n_0(\mathbf{r})] = \int d\mathbf{r}\; n_0(\mathbf{r}) V_{\text{ion}}(\mathbf{r}) + \frac{1}{2}\int\int d\mathbf{r}\; d\mathbf{r}'\; \frac{n_0(\mathbf{r}) n_0(\mathbf{r}')}{|\mathbf{r}-\mathbf{r}'|} + \mathcal{G}[n_0(\mathbf{r})], \qquad (2.1)$$

where the first and second terms on the right-hand side (RHS) are the energy due to electron–ion and electron–electron Coulomb interaction in a metal, and $\mathcal{G}[n_0(\mathbf{r})]$ is a universal functional of the density $n_0(\mathbf{r})$ valid for any number of electrons and any potential $V_{\text{ion}}(\mathbf{r})$. $\mathcal{G}[n_0(\mathbf{r})]$ accounts for the kinetic energy and exchange–correlation energy (associated e.g. with the Pauli exclusion principle) of the interacting many-electron system. If $\mathcal{G}[n_0(\mathbf{r})]$ were known, determining the ground-state energy $\mathcal{E}_0$ and electron density $n_0(\mathbf{r})$ of a many-electron system could

be directly obtained by minimizing $\mathcal{E}_0[n_0(\mathbf{r})]$ relative to $n_0(\mathbf{r})$ according to the variational principle [186]. Thus, the work by Hohenberg and Kohn completely changes the paradigm of the electronic many-body problem, since dealing with the electron density $n_0(\mathbf{r})$ as the fundamental quantity instead of the the many-electron wave function allows the study of electronic properties of many-electron systems intractable in the past. Notice that Eq. (2.1) is formally exact. Unfortunately, the universal functional $\mathcal{G}[n_0(\mathbf{r})]$ is generally unknown and, therefore, DFT becomes in practice an approximation. Considerable effort has been devoted over the years to find suitable approximations for $\mathcal{G}[n_0(\mathbf{r})]$ [187–189].

Kohn and Sham [190] proposed to express $\mathcal{G}[n_0(\mathbf{r})]$ as a sum of two functionals,

$$\mathcal{G}[n_0(\mathbf{r})] = T_s[n_0(\mathbf{r})] + \mathcal{E}_{\text{xc}}[n_0(\mathbf{r})], \tag{2.2}$$

where

$$T_s[n_0(\mathbf{r})] = \sum_{j\in\text{occ}} \int d\mathbf{r} \left(\Psi_j^0(\mathbf{r})\right)^* \hat{T}\ \Psi_j^0(\mathbf{r}) \tag{2.3}$$

is the kinetic energy of an auxiliary system of non-interacting electrons[6] and $\mathcal{E}_{\text{xc}}[n_0(\mathbf{r})]$ is the exchange–correlation energy that contains all remaining many-body interactions. In Eq. (2.3), $\hat{T} = -\frac{1}{2}\nabla^2$ is the kinetic-energy operator, and the summation runs over the occupied ($j \in$ occ) time-independent Kohn–Sham (KS) orbitals $\Psi_j^0(\mathbf{r})$ that determine the equilibrium electron density $n_0(\mathbf{r})$ of the many-body system,

$$n_0(\mathbf{r}) = \sum_{j\in\text{occ}} \chi_j |\Psi_j^0(\mathbf{r})|^2, \tag{2.4}$$

with the statistical factors χ_j accounting for both spin and symmetry degeneracy. Note that, according to the definition of Eq. (2.4), $n_0(\mathbf{r})$ is considered to be positive.

The application of the variational principle to Eq. (2.1) using the functionals given by Eqs. (2.2) and (2.3) results in the following equation [191]:

$$\underbrace{\left(\hat{T} + V_{\text{ion}}(\mathbf{r}) + \int d\mathbf{r}'\ \frac{n_0(\mathbf{r}')}{|\mathbf{r}-\mathbf{r}'|} + \frac{\delta\mathcal{E}_{\text{xc}}[n_0(\mathbf{r})]}{\delta n_0(\mathbf{r})}\right)}_{\hat{H}^0[n_0(\mathbf{r})]} \Psi_j^0(\mathbf{r}) = \epsilon_j \Psi_j^0(\mathbf{r}), \tag{2.5}$$

where $\Psi_j^0(\mathbf{r})$ and ϵ_j are the time-independent KS orbitals and energies[7].

Thus, the equilibrium electronic density $n_0(\mathbf{r})$ [Eq. (2.4)] of the true many-body system can be obtained within the KS scheme from the solutions of the Schrödinger equation [Eq. (2.5)] of an auxiliary system of non-interacting electrons using an

[6] T_s is thus an *explicit* functional of the Kohn–Sham orbitals $\Psi_j^0(\mathbf{r})$, but an *implicit* functional of $n_0(\mathbf{r})$ according to Eq. (2.4) [72].

[7] Note that $\Psi_j^0(\mathbf{r})$ and ϵ_j in Eq. (2.5) are the eigenfunctions and eigenvalues of the auxiliary non-interacting electron system used to construct the exact electron density $n_0(\mathbf{r})$, and therefore, ϵ_j and $\Psi_j^0(\mathbf{r})$ have no direct physical interpretation [192, 193]. An exception is made for the energy of the highest occupied KS orbital, which can be used e.g. to estimate the work function of a metal [194].

effective time-independent Hamiltonian

$$\hat{H}^0[n_0(\mathbf{r})] = \hat{T} + V_{\text{eff}}[n_0(\mathbf{r})], \tag{2.6}$$

where $V_{\text{eff}}[n_0]$ is the effective one-electron potential given by

$$V_{\text{eff}}[n_0(\mathbf{r})] = V_{\text{ion}}(\mathbf{r}) + \int d\mathbf{r}' \, \frac{n_0(\mathbf{r}')}{|\mathbf{r} - \mathbf{r}'|} + V_{\text{xc}}[n_0(\mathbf{r})]. \tag{2.7}$$

In Eq. (2.7), the second term on the RHS is the electron–electron potential due to Coulomb interaction in the single-electron picture, and $V_{\text{xc}}[n_0(\mathbf{r})]$ is the exchange–correlation potential obtained from $\mathcal{E}_{\text{xc}}[n_0(\mathbf{r})]$ through the relationship

$$V_{\text{xc}}[n_0(\mathbf{r})] = \frac{\delta \mathcal{E}_{\text{xc}}[n_0(\mathbf{r})]}{\delta n_0(\mathbf{r})}, \tag{2.8}$$

which accounts for all many-body interactions that are not present in $\hat{T}$ and in the second term of Eq. (2.7), but exist in the true interacting many-electron system. According to the previous discussion about $\mathcal{G}[n_0(\mathbf{r})]$, the exchange–correlation energy functional $\mathcal{E}_{\text{xc}}[n_0]$ is not known exactly. We explain in Subsection 2.1.1 the approximation adopted in this thesis to calculate $\mathcal{E}_{\text{xc}}[n_0(\mathbf{r})]$.

Equations (2.4) and (2.5) are referred to as the time-independent KS equations, and have to be solved self-consistently: one can start with an assumed electron density $n_0(\mathbf{r})$, then construct $V_{\text{eff}}[n_0(\mathbf{r})]$ from Eq. (2.7), and finally obtain a new value of $n_0(\mathbf{r})$ using Eqs. (2.5) and (2.4). This procedure is repeated until convergence of the results is achieved. In the following Subsections 2.1.1 and 2.1.2, we describe the approximations used in this thesis to compute the potentials $V_{\text{xc}}[n_0(\mathbf{r})]$ and $V_{\text{ion}}(\mathbf{r})$.

2.1.1 The local-density approximation (LDA)

The simplest way to determine the exchange–correlation energy functional $\mathcal{E}_{\text{xc}}[n_0(\mathbf{r})]$ in Eq. (2.8) is to adopt the local-density approximation (LDA). If we assume that $n_0(\mathbf{r})$ does not change rapidly, the variation of $\mathcal{E}_{\text{xc}}[n_0(\mathbf{r})]$ with respect to the gradient of $n_0(\mathbf{r})$ can be neglected, and $\mathcal{E}_{\text{xc}}[n_0(\mathbf{r})]$ can be expressed as [62]

$$\mathcal{E}_{\text{xc}}[n_0(\mathbf{r})] = \int d\mathbf{r} \; n_0(\mathbf{r}) \; \epsilon_{\text{xc}}(\overline{n} = n_0(\mathbf{r})), \tag{2.9}$$

where $\epsilon_{\text{xc}}(\overline{n})$ is the exchange and correlation energy per electron of a homogeneous electron gas with average electron density $\overline{n}$ [190]. Thus, within the LDA, the exchange–correlation energy per particle located at position $\mathbf{r}$ in an inhomogeneous system with density $n_0(\mathbf{r})$ is approximated by the exchange–correlation energy per particle of a uniform electron gas with the same density, $\overline{n} = n_0(\mathbf{r})$. The LDA has been widely used to determine the electronic properties of many systems, including atoms and solids where the density does not vary slowly. For metallic surfaces,

the LDA is found to provide accurate results, which might be surprising since the equilibrium density $n_0(\mathbf{r})$ varies rapidly near the metal surface [62].

Using Eq. (2.8), we obtain the exchange–correlation potential within the LDA[8],

$$V_{\mathrm{xc}}[n_0(\mathbf{r})] = \frac{\partial\Big(n_0(\mathbf{r})\ \epsilon_{\mathrm{xc}}(\overline{n}=n_0(\mathbf{r}))\Big)}{\partial n_0(\mathbf{r})} = \epsilon_{\mathrm{xc}}(\overline{n}=n_0(\mathbf{r})) + n_0(\mathbf{r})\frac{\partial\epsilon_{\mathrm{xc}}(\overline{n})}{\partial\overline{n}}\bigg|_{\overline{n}=n_0(\mathbf{r})}, \tag{2.10}$$

which requires an analytical expression of $\epsilon_{\mathrm{xc}}(\overline{n})$. Several approximations have been proposed to that end [191, 195–197], and throughout this thesis, we use the exchange–correlation energy-density functional $\epsilon_{\mathrm{xc}}(\overline{n})$ given by Gunnarsson and Lundquist [198][9]:

$$\epsilon_{\mathrm{xc}}(\overline{n}) = -\frac{1}{2}\Big(0.916/r_s + 0.0666(1+x^3)\ln(1+1/x) - x^2 + \frac{x}{2} - 1/3)\Big), \tag{2.11}$$

with $r_s = \left(\frac{3}{4\pi\overline{n}}\right)^{1/3}$ the Wigner–Seitz radius [Eq. (1.11)], and $x = r_s/11.9$. Finally, according to Eq. (2.10), the exchange–correlation potential that we use in this thesis is given by [199]

$$V_{\mathrm{xc}}[n_0(\mathbf{r})] = -\frac{1}{2}\Big(1.222/r_s + 0.0666\ \ln(1+11.4/r_s)\Big)\bigg|_{\overline{n}=n_0(\mathbf{r})}. \tag{2.12}$$

2.1.2 The jellium model of free-electron metals

To obtain the potential $V_{\mathrm{ion}}(\mathbf{r})$ in Eq. (2.7), we adopt in this thesis the jellium model of free-electron metals [194, 200, 201], where the ions at the lattice sites are modeled as a uniform positive background charge with density

$$n_+(\mathbf{r}) = \begin{cases} \overline{n} & \text{inside the metal} \\ \\ 0 & \text{outside the metal} \end{cases}. \tag{2.13}$$

Thus, within the jellium model, $\overline{n}$ (or, equivalently, r_s [Eq. (1.11)]) is the only parameter needed to characterize the metal. For example, Al is modeled with $r_s = 2.07$ $\mathrm{a_0}$, Na with $r_s = 4$ $\mathrm{a_0}$, and K with $r_s = 4.96$ $\mathrm{a_0}$ [62].

This positive charge density $n_+(\mathbf{r})$ creates an attractive Coulomb potential

$$V_{\mathrm{ion}}(\mathbf{r}) = -\int d\mathbf{r}'\frac{n_+(\mathbf{r}')}{|\mathbf{r}-\mathbf{r}'|}. \tag{2.14}$$

[8] It can be shown that, for a functional $F[\rho(\mathbf{r})]$ of the form $F[\rho(\mathbf{r})] = \int d\mathbf{r}\ f\Big(\mathbf{r},\rho(\mathbf{r})\Big)$, the functional derivative is given by $\frac{\delta F}{\delta\rho(\mathbf{r})} = \frac{\partial f}{\partial\rho}$. A demonstration can be found in https://www.youtube.com/watch?v=_ntUQ_WBp0U.

[9] We consider the spin-unpolarized case with $\xi = 0$. Moreover, note that in ref. 198 the expression for $\epsilon_{\mathrm{xc}}(\overline{n})$ is given in *Rydberg* atomic units (while we use *Hartree* atomic units) and thus it differs from our Eq. (2.11) by a factor $\frac{1}{2}$.

Combining Eq. (2.14) with the second term on the RHS of Eq. (2.7), we can define the Hartree potential as

$$V_{\mathrm{H}}[n_0(\mathbf{r})] = \int d\mathbf{r}' \frac{n_0(\mathbf{r}') - n_+(\mathbf{r}')}{|\mathbf{r} - \mathbf{r}'|}, \tag{2.15}$$

which represents the part of the effective one-electron potential $V_{\mathrm{eff}}[n_0(\mathbf{r})]$ associated with electron–electron and electron–ion Coulomb interaction. In practice, in this thesis we obtain $V_{\mathrm{H}}[n_0(\mathbf{r})]$ by solving Poisson's equation,[10]

$$\nabla^2 V_{\mathrm{H}}[n_0(\mathbf{r})] = -4\pi\big(n_0(\mathbf{r}) - n_+(\mathbf{r})\big). \tag{2.16}$$

The effective one-electron potential can thus be written as [see Eq. (2.7)]

$$V_{\mathrm{eff}}[n_0(\mathbf{r})] = V_{\mathrm{xc}}[n_0(\mathbf{r})] + V_{\mathrm{H}}[n_0(\mathbf{r})], \tag{2.17}$$

with $V_{\mathrm{xc}}[n_0(\mathbf{r})]$ and $V_{\mathrm{H}}[n_0(\mathbf{r})]$ obtained from Eqs. (2.12) and (2.16), respectively.

As compared to fully atomistic *ab-initio* descriptions that take into account the precise spatial position of each nucleus forming the MNP [202], the jellium model presented in this subsection allows us to tackle MNPs of larger size (with a comparatively low computational complexity) so that the collective plasmonic excitations can be well developed [203]. The standard jellium model is found to semi-quantitatively predict general quantum effects in plasmonic systems, such as electronic spill-out, electron tunneling, nonlocal dynamical screening, nonlinear optical response, or photo-assisted electron transport [58, 67, 68, 77, 204–213]. Many of these effects have been also confirmed by experimental studies and by atomistic *ab-initio* calculations [79, 86, 214]. As a more technical note, in some situations the standard jellium model does not describe accurately the interaction between conduction electrons and ionic charges, resulting e.g. in an inadequate value of the work function of the metal [215]. A simple method to overcome this effect is to adopt the *stabilized* jellium model, where a constant (*structureless*) potential is added to the effective one-electron potential inside the metal so that the correct work function is obtained [216]. Moreover, the jellium model does not describe excitations involving electrons from the inner shells, as it is the case of *d*-band electronic transitions that are shown to substantially influence the optical response of noble metals such as Au or Ag [217, 218]. To mimic the influence of these inner shells, it is possible to use a polarizable medium which extends up to a certain distance from the MNP surface [219].

In general, these sophistications to the jellium model have not been implemented in this thesis[11], since we mainly focus on sodium MNPs whose electronic structure is sufficiently well described within the standard jellium model. Considering sodium MNPs allows us to study quantum effects, within the frequency range close to that

[10] Notice that solving Eq. (2.15) and Eq. (2.16) is equivalent since $G(\mathbf{r}, \mathbf{r}') = -\frac{1}{4\pi|\mathbf{r}-\mathbf{r}'|}$ is the Green's function that satisfies $\nabla^2 G(\mathbf{r}, \mathbf{r}') = \delta(\mathbf{r} - \mathbf{r}')$.

[11] As an exception, to describe the electronic structure of the cylindrical metallic nanowires in Section 2.3 we introduce a stabilizing potential to impose the value of the work function of gold.

of typical plasmonic materials such as gold, using a relatively simplified description.

2.2 Fundamentals of time-dependent density functional theory (TDDFT)

In this section, we describe the time-dependent density functional theory (TDDFT) used in this thesis to address optical excitations in metals. TDDFT is the time-dependent extension of DFT, and it is based on the work by Runge and Gross [69], which shows that an external time-dependent potential $V_{\text{ext}}(\mathbf{r},t)$ completely determines the time evolution of a given electron density $n(\mathbf{r},t)$. Moreover, this time-dependent electron density determines all the time-dependent properties of the many-electron system.

The work by Runge and Gross [69] allows for establishing a time-dependent KS scheme, where the dynamics of the electron density $n(\mathbf{r},t)$ of an interacting many-electron system (initially in the ground state) subjected to a time-dependent potential $V_{\text{ext}}(\mathbf{r},t)$ is addressed using an effective one-electron potential V_{eff} of the equivalent non-interacting system. The dynamics of the time-dependent KS orbitals $\Psi_j(\mathbf{r},t)$ starting from the ground state,

$$\Psi_j(\mathbf{r},t=0)=\Psi_j^0(\mathbf{r}), \tag{2.18}$$

can be obtained from the time-dependent KS equation,

$$i\frac{\partial}{\partial t}\Psi_j(\mathbf{r},t)=\underbrace{\left(\hat{T}+V_{\text{eff}}[n(\mathbf{r},t)]+V_{\text{ext}}(\mathbf{r},t)\right)}_{\hat{H}[n(\mathbf{r},t)]}\Psi_j(\mathbf{r},t) \tag{2.19}$$

with the time-dependent electron density $n(\mathbf{r},t)$ given by

$$n(\mathbf{r},t)=\sum_{j\in\text{occ}}\chi_j|\Psi_j(\mathbf{r},t)|^2=\sum_{j\in\text{occ}}\chi_j\Psi_j^*(\mathbf{r},t)\Psi_j(\mathbf{r},t). \tag{2.20}$$

Similarly to the equilibrium electron density $n_0(\mathbf{r})$ [Eq. (2.4)], the summation in Eq. (2.20) runs over the occupied time-dependent KS orbitals, and $n(\mathbf{r},t)$ is considered to be positive.

Equation (2.19) is an analogue of the time-dependent Schrödinger equation for a time-dependent one-electron Hamiltonian,

$$\hat{H}[n(\mathbf{r},t)]=\hat{T}+V_{\text{eff}}[n(\mathbf{r},t)]+V_{\text{ext}}(\mathbf{r},t), \tag{2.21}$$

where, similar to the time-independent KS equations used for the ground state [Eq. (2.5)], $\hat{T}=-\frac{1}{2}\nabla^2$ is the kinetic-energy operator, $V_{\text{eff}}[n(\mathbf{r},t)]$ is the effective time-dependent one-electron potential,

$$V_{\text{eff}}[n(\mathbf{r},t)]=V_{\text{xc}}[n(\mathbf{r},t)]+V_{\text{H}}[n(\mathbf{r},t)], \tag{2.22}$$

and $V_{\text{ext}}(\mathbf{r},t)$ is an arbitrary time-dependent potential that drives the system. In Eq. (2.22), $V_{\text{H}}[n(\mathbf{r},t)]$ is the time-dependent Hartree potential obtained from Poisson's equation [see Eq. (2.16)],

$$\nabla^2 V_{\text{H}}[n(\mathbf{r},t)] = -4\pi\big(n(\mathbf{r},t) - n_+(\mathbf{r})\big), \tag{2.23}$$

and $V_{\text{xc}}[n(\mathbf{r},t)]$ is the time-dependent exchange-correlation potential. In this thesis, we adopt the adiabatic local-density approximation (ALDA) for the exchange–correlation potential, which assumes that $V_{\text{xc}}[n(\mathbf{r},t)]$ is local not only in space but also in time. Following a similar approach as for the DFT calculations [see Eq. (2.10)], it is possible to write

$$V_{\text{xc}}[n(\mathbf{r},t)] = \epsilon_{\text{xc}}(\overline{n} = n(\mathbf{r},t)) + n(\mathbf{r},t)\frac{\partial \epsilon_{\text{xc}}}{\partial \overline{n}}\bigg|_{\overline{n}=n(\mathbf{r},t)}. \tag{2.24}$$

Therefore, in this thesis no memory effects are considered in V_{xc} an thus no losses are introduced directly in the TDDFT calculations [220, 221] (see further details in Subsection 2.2.1 to know how losses are introduced in the system). We use within TDDFT the exchange–correlation energy-density functional $\epsilon_{\text{xc}}(\overline{n})$ given by Gunnarsson and Lundquist [198], i.e., the same as used in the static DFT calculations.

To obtain the time evolution of the many-body electron density $n(\mathbf{r},t)$, the time-dependent KS equations given by Eqs. (2.19) and (2.20) need to be solved self-consistently using the initial conditions of Eq. (2.18). Formally, Eq. (2.19) is a nonlinear partial differential equation because the effective potential $V_{\text{eff}}[n(\mathbf{r},t)]$ [Eq. (2.22)] is a functional of the density $n(\mathbf{r},t)$ [Eq. (2.20)], which is nonlinear with respect to the KS orbitals $\Psi_j(\mathbf{r},t)$. Note, however, that very commonly Eqs. (2.19) and (2.20) are solved in the frequency domain to obtain the *linear* optical response of a system by assuming that the external potential $V_{\text{ext}}(\mathbf{r},t)$ is a weak perturbation [80].

In this thesis, we use a real-time implementation of TDDFT based on the wave-packet propagation (WPP) method and solve Eqs. (2.19) and (2.20) in the time domain [222, 223], which allows for obtaining both the linear and the nonlinear optical response of the system subjected to an arbitrary external field of weak or strong intensity. We explain in the following Subsection 2.2.1 the WPP method [224–227] adopted in this thesis.

2.2.1 The wave-packet propagation (WPP) method

Given a KS orbital $\Psi_j(\mathbf{r},t_1)$ at an instant of time $t = t_1$, the value of $\Psi_j(\mathbf{r},t_2)$ at another instant of time $t_2 > t_1$ is determined from the solution of Eq. (2.19), which can be written as [228]

$$\Psi_j(\mathbf{r},t_2) = \hat{U}(t_2,t_1)\Psi_j(\mathbf{r},t_1), \tag{2.25}$$

where the time-evolution operator $\hat{U}(t_2, t_1)$ is given by [229]

$$\hat{U}(t_2, t_1) = \hat{\mathcal{P}}_t \exp\left\{-i \int_{t_1}^{t_2} dt\ \hat{H}[n(\mathbf{r}, t)]\right\}, \tag{2.26}$$

with $\hat{\mathcal{P}}_t$ the time-ordering operator. If $\hat{H}[n(\mathbf{r}, t)$ [Eq. (2.21)] did not depend upon the time t, the integral of Eq. (2.26) would be trivial and Eq. (2.25) would become $\Psi_j(\mathbf{r}, t_2) = e^{-i\hat{H}(t_2 - t_1)}\Psi_j(\mathbf{r}, t_1)$. However, $\hat{H}[n(\mathbf{r}, t)]$ is a time-dependent functional due to the external time-dependent potential $V_{\text{ext}}(\mathbf{r}, t)$. In this case, one can use a short time propagation and consider that the time interval $t_2 - t_1$ is short enough so that the Hamiltonian does not significantly vary between t_1 and $t_2 = t_1 + \Delta t$ (with Δt a short time step). Then, we split the time propagation of $\Psi_j(\mathbf{r}, t)$ within the entire time interval into several short-time intervals, where Eq. (2.26) is approximated as

$$\hat{U}(t_1 + \Delta t, t_1) \approx \exp\left\{-i\Delta t\ \hat{H}[n(\mathbf{r}, t_1 + \Delta t/2)]\right\}. \tag{2.27}$$

The time-evolution operator $\hat{U}(t_1 + \Delta t, t_1)$ given by Eq. (2.27) uses the value of the Hamiltonian $\hat{H}[n(\mathbf{r}, t)]$ at an intermediate instant of time $t = t_1 + \Delta t/2$ to guarantee the time-reversal symmetry of the method and thus to preserve the norm of the KS orbitals, $\frac{d}{dt}\int d^3\mathbf{r}\ |\Psi_j(\mathbf{r}, t)|^2 = 0$ [230, 231]. In principle, $V_{\text{ext}}(\mathbf{r}, t)$ in Eq. (2.21) can be known at any arbitrary time since we typically know its explicit time dependence, however we do not know the value of V_{eff} [Eq. (2.22)] at $t = t_1 + \Delta t/2$ and therefore cannot directly estimate the value of $\hat{H}[n(\mathbf{r}, t = t_1 + \Delta t/2)]$. To overcome this issue, we use the following iterative procedure [75]

$$V_{\text{eff}}[n(\mathbf{r}, t_1 + \Delta t/2)] = \begin{cases} V_{\text{eff}}[n(\mathbf{r}, t_1)] & \text{first iteration} \\ \\ \frac{1}{2}\left\{V_{\text{eff}}[n(\mathbf{r}, t_1)] + V_{\text{eff}}[n(\mathbf{r}, t_1 + \Delta t)]\right\} & \text{otherwise} \end{cases}, \tag{2.28}$$

where $V_{\text{eff}}[n(\mathbf{r}, t_1 + \Delta t)]$ is obtained in the previous iteration by solving Eqs. (2.20)-(2.25) and (2.27), using the updated value of $V_{\text{eff}}[n(\mathbf{r}, t_1 + \Delta t/2)]$. We typically use 3 iterations to achieve convergence.

In addition, applying the time-evolution operator $\hat{U}(t_1 + \Delta t, t_1)$ given by Eq. (2.27) to propagate $\Psi_j(\mathbf{r}, t)$ from $t = t_1$ to $t = t_1 + \Delta t$ requires the application of the exponential of the kinetic-energy operator $\hat{T} = -\frac{1}{2}\nabla^2$ [Eq. (2.21)], which is nonlocal on $\mathbf{r}$. As an example, we first consider the implementation of the method in 3D Cartesian coordinates[12]. Then, it is convenient to further approximate

[12] The exact procedure used to apply $e^{-i\Delta t\hat{T}}$ depends on specific issues related to the coordinate system chosen to propagate the KS orbitals, and in this section we only discuss the general aspects [75]. Specific details of the algorithm in other coordinate systems are given in Subsections 2.3.1, 2.3.2, and 2.3.3.

$\hat{U}(t_1+\Delta t,t_1)$ using the split-operator technique [232–234][13],

$$\hat{U}(t_1+\Delta t,t_1)\approx e^{-i\Delta t V_{\rm tot}(\mathbf{r},t)/2}e^{-i\Delta t\hat{T}}e^{-i\Delta t V_{\rm tot}(\mathbf{r},t)/2}, \tag{2.29}$$

where

$$V_{\rm tot}(\mathbf{r},t)=V_{\rm eff}[n(\mathbf{r},t)]+V_{\rm ext}(\mathbf{r},t). \tag{2.30}$$

The advantage of using the split operator given by Eq. (2.29) is that $\hat{U}(t_1+\Delta t,t_1)$ is separated into (i) two identical operators $e^{-i\Delta t V_{\rm tot}(\mathbf{r},t)/2}$ that are local on $\mathbf{r}$ since $V_{\rm eff}[n(\mathbf{r},t)]$ is local within the ALDA, and (ii) another operator $e^{-i\Delta t\hat{T}}$ that is nonlocal on $\mathbf{r}$ because it involves second spatial derivatives. The operator $e^{-i\Delta t V_{\rm tot}(\mathbf{r},t)/2}$ is diagonal in a real-space grid representation and therefore can be directly applied to $\Psi_j(\mathbf{r},t)$ in real space [235]. On the other hand, the operator $e^{-i\Delta t\hat{T}}$ is diagonal in the reciprocal (k-momentum) space, since the kinetic-energy operator is $\hat{T}_k=\frac{1}{2}k^2$ in this representation [236–238]. Thus, $e^{-i\Delta t\hat{T}_k}$ can be directly applied to $\Psi_j(\mathbf{r},t)$ in the reciprocal space.

As a consequence, $\Psi_j(\mathbf{r},t)$ can be propagated from $t=t_1$ to $t=t_1+\Delta t$ according to Eq. (2.29) by employing space-to-momentum Fourier transforms, $\tilde{\mathcal{F}}_k$, and momentum-to-space inverse Fourier transforms, $\tilde{\mathcal{F}}_k^{-1}$. Using these techniques, Eq. (2.25) reads

$$\Psi_j(\mathbf{r},t_1+\Delta t)=e^{-i\Delta t V_{\rm tot}(\mathbf{r},t)/2}\tilde{\mathcal{F}}_k^{-1}\left\{e^{-i\Delta t\hat{T}_k}\tilde{\mathcal{F}}_k\{e^{-i\Delta t V_{\rm tot}(\mathbf{r},t)/2}\Psi_j(\mathbf{r},t_1)\}\right\}, \tag{2.31}$$

where the exponential of local potentials is directly multiplied by $\Psi_j(\mathbf{r},t_1)$ on each grid point in real space, and the application of the exponential of the kinetic-energy operator $\hat{T}_k$ is performed in the reciprocal space [227]. In this thesis, we use the fast Fouirer transform to compute $\tilde{\mathcal{F}}_k$ and $\tilde{\mathcal{F}}_k^{-1}$ within the WPP algorithm.

Last, to obtain the value of the KS orbital $\Psi_j(\mathbf{r},t)$ at any time t we can apply the time-evolution operator given by Eq. (2.29) several times using the procedure of Eq. (2.31) recursively [239],

$$\begin{aligned}\Psi_j(\mathbf{r},t)&=\hat{U}(t,t-\Delta t)\hat{U}(t-\Delta t,t-2\Delta t)\ldots\hat{U}(\Delta t,0)\Psi_j(\mathbf{r},t=0)\\&=\prod_{s=1}^{s_{\rm max}}\hat{U}(s\Delta t,(s-1)\Delta t)\Psi_j(\mathbf{r},t=0),\end{aligned} \tag{2.32}$$

where $s_{\rm max}$ is an integer number such that $t=s_{\rm max}\Delta t$, and the initial conditions at $t=0$ are given by the ground-state KS orbital [Eq. (2.18)].

[13] Note that, for two operators $\hat{A}$ and $\hat{B}$, $e^{\hat{A}+\hat{B}}\neq e^{\hat{A}}e^{\hat{B}}$ unless $[\hat{A},\hat{B}]=0$. The kinetic-energy operator $\hat{T}$ does not commute with $V_{\rm tot}(\mathbf{r},t)=V_{\rm eff}[n(\mathbf{r},t)]+V_{\rm ext}(\mathbf{r},t)$, and thus $e^{-i\Delta t(\hat{T}+V_{\rm tot}(\mathbf{r},t))}$ is not strictly $e^{-i\Delta t V_{\rm tot}(\mathbf{r},t)/2}e^{-i\Delta t\hat{T}}e^{-i\Delta t V_{\rm tot}(\mathbf{r},t)/2}$. The resulting error in Eq. (2.29) scales as $(\Delta t)^3$ [229].

Calculation of physical observables in time and frequency domains within the WPP method

The WPP explained in this subsection allows us to retrieve the real-space and real-time dynamics of the occupied KS orbitals $\Psi_j(\mathbf{r},t)$, which determine the evolution of the electron density $n(\mathbf{r},t)$ [Eq. (2.20)] and all other physical quantities of interest. In this thesis, we typically study the optoelectronic response of different plasmonic systems by analyzing the dipole moment $\mathbf{p}(t)$, the electric near field $\mathbf{E}^{\text{ind}}(\mathbf{r},t)$, and the electron-current density $\mathbf{j}(\mathbf{r},t)$ induced in response to different external potentials $V_{\text{ext}}(\mathbf{r},t)$[14].

The induced dipole moment $\mathbf{p}(t)$ is given in time domain by

$$\mathbf{p}(t) = -\int_V \delta n(\mathbf{r},t)\ \mathbf{r}\ d\mathbf{r}, \tag{2.33}$$

where $\delta n(\mathbf{r},t) = n(\mathbf{r},t) - n_0(\mathbf{r})$ is the induced electron density [Eqs. (2.4) and (2.20)], and the integral extends over the whole volume V of the studied nanostructure.

The induced electric near field $\mathbf{E}^{\text{ind}}(\mathbf{r},t)$ can be obtained in time domain from the Hartree potential $V_{\text{H}}[n(\mathbf{r},t)]$ [Eq. (2.23)] using

$$\mathbf{E}^{\text{ind}}(\mathbf{r},t) = \nabla V_{\text{H}}[n(\mathbf{r},t)]. \tag{2.34}$$

Note that the minus sign in Eq. (2.33) and the absence of negative sign in Eq. (2.34) is because $n(\mathbf{r},t)$ is a positive-valued electron density [Eq. (2.20)], which changes the standard sign convention of the potential $V_{\text{H}}[n(\mathbf{r},t)]$ [Eq. (2.23)]. In contrast, the electric field $\mathbf{E}^{\text{ind}}(\mathbf{r},t)$ given by Eq. (2.34) is defined, as usual, as the force that a test unitary positive charge $q = +1$ would experience from the field, and therefore is related to $V_{\text{H}}[n(\mathbf{r},t)]$ through $\mathbf{E}^{\text{ind}}(\mathbf{r},t) = -\nabla\left(-V_{\text{H}}[n(\mathbf{r},t)]\right) = \nabla V_{\text{H}}[n(\mathbf{r},t)]$.

Finally, based on the continuity equation, $\frac{\partial}{\partial t} n(\mathbf{r},t) = \nabla \cdot \mathbf{j}(\mathbf{r},t)$, the induced electron-current density $\mathbf{j}(\mathbf{r},t)$ can be calculated from [240]

$$\mathbf{j}(\mathbf{r},t) = -\sum_{j\in\text{occ}} \chi_j \text{Im}\{\Psi_j^*(\mathbf{r},t)\nabla\Psi_j(\mathbf{r},t)\}. \tag{2.35}$$

Very often, it is interesting to analyze the optoelectronic response of the system in the frequency domain, ω. The frequency-resolved quantities are then obtained from the time-to-frequency Fourier transform $\mathcal{F}$ [Eq. (1.3)],

[14] In addition, higher-order multipole moments of cylindrical and spherical nanostructures are also analyzed in Chapter 4 and Chapter 6.

$$\mathbf{p}(\omega) = \int_0^{\mathrm{T_f}} dt\ \mathbf{p}(t)\ e^{i\omega t}\ \mathfrak{F}(t), \tag{2.36a}$$

$$\mathbf{E}^{\mathrm{ind}}(\mathbf{r},\omega) = \int_0^{\mathrm{T_f}} dt\ \mathbf{E}^{\mathrm{ind}}(\mathbf{r},t)\ e^{i\omega t}\ \mathfrak{F}(t), \tag{2.36b}$$

$$\mathbf{j}(\mathbf{r},\omega) = \int_0^{\mathrm{T_f}} dt\ \mathbf{j}(\mathbf{r},t)\ e^{i\omega t}\ \mathfrak{F}(t), \tag{2.36c}$$

where $\mathrm{T_f}$ is the total propagation time used in our simulations, which must be long enough to achieve convergence.

Importantly, the time-dependent function $\mathfrak{F}(t)$ (or *filter*) in Eq. (2.36) is introduced to attenuate the collective time-dependent charge-density oscillations (losses), since the ALDA-TDDFT scheme adopted in this thesis does not account for decay and dephasing processes related to the scattering of electrons with phonons, nor for the intrinsic losses due to inelastic electron–electron interactions. This is a well-known failure of the ALDA used for the exchange–correlation potential $V_{\mathrm{xc}}[n(\mathbf{r},t)]$ [72, 220, 241, 242], and thus a filter $\mathfrak{F}(t)$ has to be applied to mimic such intrinsic losses in the system. In practice, in this thesis we employ two different filters $\mathfrak{F}(t)$ depending on the external excitation, as described in Sections 2.3 and 2.4.

Calculation of the projected density of electronic states (PDOS) within the WPP method

Given an equilibrium electron density $n_0(\mathbf{r})$ and a ground-state effective potential $V_{\mathrm{eff}}(\mathbf{r})$ of a system [Eq. (2.17)], it is possible to access the energies of both the *occupied* and *unoccupied* KS one-electron states of the system by analyzing the projected density of electronic states (PDOS), $\Sigma(\omega)$. Importantly, the PDOS can be obtained within the WPP method described here by propagating an initial wave packet $\Phi(\mathbf{r},t=0) = \Phi_0(\mathbf{r})$ of a particular symmetry according to the time-dependent Schrödinger equation under the (time-independent) one-electron Hamiltonian $\hat{H} = \hat{T} + V_{\mathrm{eff}}(\mathbf{r})$. This Hamiltonian corresponds to the Hamiltonian of a single electron subjected to the effective ground-state potential $V_{\mathrm{eff}}(\mathbf{r})$ of the nanostructure under study. In this case, using the WPP method to obtain the PDOS we do not apply any external potential $V_{\mathrm{ext}}(\mathbf{r},t)$, and $V_{\mathrm{eff}}(\mathbf{r})$ does not vary in time. However, the PDOS provides information about the occupied and unoccupied electronic states that will be involved in electronic transitions excited optically when an external time-dependent potential is applied.

The PDOS $\Sigma(\omega)$ projected onto the initial wave packet $\Phi_0(\mathbf{r})$ is given by

$$\Sigma(\omega) = \sum_{j=1}^{\infty} |c_j|^2 \delta(\omega - \epsilon_j), \tag{2.37}$$

with $\delta(\omega-\epsilon_j)$ the Dirac delta, ϵ_j the eigenenergies of the one-electron Hamiltonian

$\hat{H} = \hat{T} + V_{\text{eff}}(\mathbf{r})$, and

$$c_j = \langle \phi_j(\mathbf{r}) | \Phi_0(\mathbf{r}) \rangle \tag{2.38}$$

the complex coefficients corresponding to the expansion of the initial wave packet $\Phi_0(\mathbf{r})$ into the eigenfunctions $\phi_j(\mathbf{r})$ of the Hamiltonian $\hat{H}$,

$$\Phi_0(\mathbf{r}) = \sum_{j=1}^{\infty} c_j \phi_j(\mathbf{r}). \tag{2.39}$$

The eigenfunctions $\phi_j(\mathbf{r})$ are not known a priori, and we apply the WPP method to obtain $\Sigma(\omega)$ [Eq. (2.37)] without the need to calculate $\phi_j(\mathbf{r})$.

The PDOS $\Sigma(\omega)$ given by Eq. (2.37) represents the number of one-electron states of a particular spatial symmetry that the nanostructure sustains at a given energy level ω and spatial region. The PDOS includes the contribution of both the occupied and the unoccupied states, and it gives information about the degree of localization of a particular electronic state at a certain spatial region (determined by the initial wave packet $\Phi_0(\mathbf{r})$ used in the propagation). Notice that, since the PDOS shows the one-electron energy states available in a (fictitious) non-interacting KS electron system (see Section 2.1), the resonant energies optically excited at the interacting many-electron system will be renormalized with respect to the non-interacting one *via* Hartree and exchange–correlation potentials [192, 193]. However, the PDOS still provides useful insights into the properties of the electronic structure of the system. For example, we study in Chapter 5 the PDOS in the electronically coupled QE–MNPs system to quantify the degree of electronic hybridization of the occupied and unoccupied electronic states.

In order to calculate $\Sigma(\omega)$ [229, 243], we choose an initial wave packet $\Phi(\mathbf{r}, t = 0) = \Phi_0(\mathbf{r})$ of a particular symmetry and propagate it according to the time-dependent Schrödinger equation corresponding to $\hat{H} = \hat{T} + V_{\text{eff}}(\mathbf{r})$,

$$\Phi(\mathbf{r}, t) = e^{-i\left(\hat{T} + V_{\text{eff}}(\mathbf{r})\right)} \Phi_0(\mathbf{r}), \tag{2.40}$$

by using the WPP algorithm described above [Eqs. (2.31) and (2.32)]. Note that no external perturbation is used in the WPP calculations of the PDOS, $V_{\text{ext}}(\mathbf{r}, t) = 0$, and that the self-consistent procedure is not applied so that $V_{\text{eff}}(\mathbf{r})$ remains constant in time.

Once the time evolution of the initial wave packet $\Phi(\mathbf{r}, t)$ is obtained by solving Eq. (2.40), to calculate $\Sigma(\omega)$ we first apply the time-to-frequency Laplace transform $\hat{\mathcal{L}}_\omega$ to $\Phi(\mathbf{r}, t)$,

$$\hat{\mathcal{L}}_\omega \Phi(\mathbf{r}, t) = \int_0^\infty dt\, e^{i(\omega + i\zeta)t} \Phi(\mathbf{r}, t) = \int_0^\infty dt\, e^{i(\omega - \hat{H} + i\zeta)t} \Phi_0(\mathbf{r}) = \frac{i}{(\omega - \hat{H} + i\zeta)} \Phi_0(\mathbf{r}), \tag{2.41}$$

where $\zeta \to 0^+$ is a small positive number. Using Eq. (2.39), Eq. (2.41) can be

written as

$$\hat{\mathcal{L}}_\omega \Phi(\mathbf{r},t) = i\sum_{j=1}^{\infty} \frac{c_j \phi_j(\mathbf{r})}{(\omega - \epsilon_j + i\zeta)}. \tag{2.42}$$

Then, projecting Eq. (2.42) onto the initial wave packet $\Phi_0(\mathbf{r})$ one obtains

$$\langle \Phi_0(\mathbf{r}) | \hat{\mathcal{L}}_\omega \Phi(\mathbf{r},t)\rangle = i\sum_{j=1}^{\infty} \frac{|c_j|^2}{(\omega - \epsilon_j + i\zeta)}. \tag{2.43}$$

Finally, applying the Sokhotski–Plemelj theorem to Eq. (2.43), the PDOS $\Sigma(\omega)$ given by Eq. (2.37) can be expressed as

$$\begin{aligned} \Sigma(\omega) &= \frac{1}{\pi} \lim_{\zeta\to 0^+} \mathrm{Re}\{\langle \Phi_0(\mathbf{r}) | \hat{\mathcal{L}}_\omega \Phi(\mathbf{r},t)\rangle\}, \\ &= \frac{1}{\pi} \lim_{\zeta\to 0^+} \mathrm{Re}\{\hat{\mathcal{L}}_\omega \underbrace{\langle \Phi_0(\mathbf{r}) | \Phi(\mathbf{r},t)\rangle}_{\mathrm{A}(t)}\}, \end{aligned} \tag{2.44}$$

where $\mathrm{A}(t) = \langle \Phi_0(\mathbf{r}) | \Phi(\mathbf{r},t)\rangle$ is the autocorrelation function that can be calculated in time domain using the WPP method. Notice that c_j are the coefficients of $\Phi_0(\mathbf{r})$ decomposed into the eigenfunctions $\phi_j(\mathbf{r})$ of the Hamiltonian $\hat{H}$ [Eq. (2.38)], so that choosing different initial wave packets $\Phi_0(\mathbf{r})$ leads to a different PDOS $\Sigma(\omega)$ [244]. This can be useful to focus on specific electronic states with a special symmetry or spatial distribution (as we do in Chapter 5), since only these states of the system that are not orthogonal to the initial wave packet $\Phi_0(\mathbf{r})$ can be accessed by the WPP method used to calculate the PDOS.

2.3 Linear optical response of canonical plasmonic nanostructures addressed within TDDFT

In this section, we analyze TDDFT results of canonical systems to illustrate the general properties of the linear optical response of plasmonic nanostructures. In particular, we discuss in Subsection 2.3.1 the influence of the nanoparticle size in the optical response of spherical MNPs described within the jellium model, and introduce the quantum-mechanical concepts of Friedel oscillations, electron spill out, and surface-enabled Landau damping. In Subsection 2.3.2, we analyze the effect of the size and the gap separation in the *optoelectronic* response of spherical MNP dimers, and introduce the concept of electron tunneling. Finally, we study in Subsection 2.3.3 the linear optical response of individual cylindrical metallic nanowires and their dimers, which allows us to study larger nanostructures than the spherical MNPs because the symmetry of the system reduces the computational demands.

2.3.1 Individual spherical metallic nanoparticles

In this subsection, we consider individual spherical MNPs surrounded by vacuum. The electronic structure of the system is described within the jellium model of free-electron metals (see Subsection 2.1.2) using a Wigner–Seitz radius $r_s = 4$ a$_0$ that corresponds to sodium. We consider closed-shell MNPs, and the number of conduction electrons N_e is varied to study the influence of the MNP size in the optical response. The radius of the MNPs, a, is determined from

$$a = N_e^{1/3} r_s. \tag{2.45}$$

Before showing the results, we provide the main numerical details to carry out the TDDFT simulations.

Numerical implementation

To obtain the ground-state KS orbitals of individual spherical MNPs containing N_e conduction electrons using DFT, we take advantage of the spherical symmetry of the problem and solve the time-independent KS equations given by Eqs. (2.4) and (2.5) in a spherical coordinate system $\mathbf{r} = \{r, \theta, \varphi\}$ (Figure 1.2a). We write the time-independent KS orbitals as

$$\Psi^0_{j_r,\ell,m}(\mathbf{r}) \equiv \Psi^0_{j_r,\ell,m}(r,\theta,\varphi) = \frac{1}{r}\psi^0_{j_r,\ell}(r) Y^m_\ell(\theta,\varphi), \tag{2.46}$$

where the sequence of the radial ($j_r = 1, 2, \dots$) and angular ($\ell = 0, 1, \dots$) quantum numbers is limited by the condition $\epsilon_{j_r,\ell} \leq E_\mathrm{F}$, where $\epsilon_{j_r,\ell}$ is the energy of the ground-state KS orbital (see below) and E_F is the Fermi energy. The magnetic quantum number can take the values $m = (-\ell, \dots, 0, \dots, \ell)$. In Eq. (2.46), the radial part $\psi^0_{j_r,\ell}(r)$ satisfies the following one-dimensional Schrödinger-like equation [see Eqs. (2.5) and (1.24)]:

$$\underbrace{\left(-\frac{1}{2}\frac{d^2}{dr^2} + \frac{\ell(\ell+1)}{2r^2} + V_\mathrm{eff}[n_0(r)]\right)}_{\hat{H}^0[n_0(r)]} \psi^0_{j_r,\ell}(r) = \epsilon_{j_r,\ell}\psi^0_{j_r,\ell}(r), \tag{2.47}$$

with $V_\mathrm{eff}[n_0(r)]$ given by Eq. (2.17), and the equilibrium electron density $n_0(r)$ is given by

$$n_0(r) = 2\sum_{j_r,\ell\in\mathrm{occ}} \frac{1}{4\pi}\frac{2\ell+1}{r^2}|\psi^0_{j_r,\ell}(r)|^2. \tag{2.48}$$

In Eq. (2.48), the factor 2 is due to the spin, and $(2\ell+1)$ due to the degeneracy of the KS orbitals with the same angular quantum number, ℓ, and different magnetic quantum number, m. Because of the spherical symmetry of the problem, $n_0(r)$ and $V_\mathrm{eff}[n_0(r)]$ depend only on the radial coordinate r.

The Hartree potential $V_\mathrm{H}[n_0(r)]$ contained in $V_\mathrm{eff}[n_0(r)]$ [Eq. (2.17)] is calculated from Poisson's equation [Eq. (2.16)] by defining $\tilde{V}_\mathrm{H}[n_0(r)] = rV_\mathrm{H}[n_0(r)]$. This

definition allows us to obtain the Hartree potential from

$$\frac{d^2}{dr^2}\tilde{V}_{\rm H}[n_0(r)] = -r\ 4\pi\left(n_0(r) - n_+(r)\right), \tag{2.49}$$

which can be solved by directly applying the inverse matrix of operator $\frac{d^2}{dr^2}$ to the RHS of Eq. (2.49) using space-to-momentum Fourier sine transform.

As described in Section 2.1, the time-independent KS equations given by Eqs. (2.47) and (2.48) are solved self-consistently using an iterative procedure based on the diagonalization of the Fourier grid Hamiltonian (FGH) [237] obtained from $H^0[n_0(r)]$ [Eq. (2.47)], where the KS orbitals $\psi^0_{j_r,\ell}(r)$ are represented in a real-space mesh of equidistant points in the coordinate r, and the space-to-momentum Fourier sine transform is used to compute the operator $\frac{d^2}{dr^2}$ [230, 232]. At the first iteration, the effective potential is initialized to

$$V_{\rm eff}(r) = V^0_{\rm eff}\frac{e^{-(r-a-1)}}{1+e^{-(r-a-1)}}, \tag{2.50}$$

where $V^0_{\rm eff}$ is a (negative-valued) parameter that determines the depth of the potential. More details on the self-consistent procedure can be found in ref. 245.

Once the ground-state KS orbitals are calculated using DFT, we obtain the linear optical response of the spherical MNP within TDDFT by applying the WPP method described in Subsection 2.2.1. We consider here the following time-dependent external potential,

$$V_{\rm ext}(\mathbf{r},t) = \delta(t)\ {\rm E}_0\Delta t\ r\cos\theta, \tag{2.51}$$

which represents a perturbation at the initial time $t = 0$ within the dipole approximation corresponding to a plane-wave electric field polarized along the z-axis. In Eq. (2.51), $\delta(t)$ is the Dirac delta function, $\rm E_0$ is the amplitude of the external perturbation (we typically use ${\rm E}_0 \sim 10^{-5}$ au, weak enough so that the linear-response approximation holds), and Δt is the propagation time step used in our simulations, typically $\Delta t\ \sim 0.25-0.1$ au (1 au $\approx 2.419\times10^{-2}$ fs, see Appendix A).

The external potential given by Eq. (2.51) breaks the spherical symmetry of the system but preserves the rotational symmetry with respect to the z-axis (azimuthal symmetry), and therefore the magnetic quantum number m is still a good quantum number. It is thus convenient to express the time-dependent KS orbitals as[15]

$$\Psi_{j,m}(r,\theta,\varphi,t) = \frac{1}{r}\psi_{j,m}(r,\theta,t)\frac{1}{\sqrt{2\pi}}e^{im\varphi}, \tag{2.52}$$

where, here, the quantum number j replaces the pair $\{j_r,\ell\}$ defining the ground-

[15] In this thesis, all the considered external potentials $V_{\rm ext}(\mathbf{r},t)$ acting on spherical MNPs preserve the rotational symmetry of the system and thus we can always write the KS orbitals of spherical MNPs using Eq. (2.52) and follow the procedure described in this subsection.

state KS orbital. The orbitals $\psi_{j,m}(r,\theta,t)$ in Eq. (2.52) are obtained from the time-dependent KS equations [Eq. (2.19)], with the kinetic-energy operator $\hat{T}$ taking the form [Eq. (1.24)]

$$\hat{T} = -\frac{1}{2}\left[\frac{\partial^2}{\partial r^2} + \frac{1}{r^2}\left\{\frac{1}{\sin\theta}\frac{\partial}{\partial\theta}\left(\sin\theta\frac{\partial}{\partial\theta}\right) - \frac{m^2}{\sin^2\theta}\right\}\right]. \tag{2.53}$$

The time evolution of $\psi_{j,m}(r,\theta,t)$ and $\psi_{j,-m}(r,\theta,t)$ is identical, and therefore we only propagate $\psi_{j,m}(r,\theta,t)$ for $m \geq 0$. We can thus express the time-dependent electron density as

$$n(r,\theta,t) \sum_{\{j,m\geq 0\}\in \mathrm{occ}} \frac{1}{2\pi}\chi_m \frac{1}{r^2}|\psi_{j,m}(r,\theta,t)|^2, \tag{2.54}$$

with

$$\chi_m = \begin{cases} 2 & \text{for } m = 0 \\ \\ 4 & \text{for } m > 0 \end{cases} \tag{2.55}$$

accounting for both the spin and $\pm m$ degeneracy. The orbitals $\psi_{j,m}(r,\theta,t)$ are propagated in time by adapting the WPP scheme given by Eq. (2.32) to the use of spherical coordinates. We represent the KS orbitals $\psi_{j,m}(r,\theta,t)$ in a meshgrid extending in radial direction up to $25-35$ a_0 from the jellium edge, using a constant radial spacing of $\Delta r \sim 0.35 - 0.5$ a_0. The angular variable θ is discretized from 0 to π using $60-120$ points. In particular, the operator

$$e^{-i\Delta t\left[-\frac{1}{2}\frac{\partial^2}{\partial r^2}\right]}$$

linked to the first term on the RHS of Eq. (2.53) is applied to $\psi_{j,m}(r,\theta,t)$ in the reciprocal space using space-to-momentum Fourier sine transforms. On the other hand, the operator

$$e^{-i\Delta t\left[-\frac{1}{2r^2}\left\{\frac{1}{\sin\theta}\frac{\partial}{\partial\theta}\left(\sin\theta\frac{\partial}{\partial\theta}\right)-\frac{m^2}{\sin^2\theta}\right\}\right]}$$

linked to the second and third terms on the RHS of Eq. (2.53) is applied in real space by expanding $\psi_{j,m}(r,\theta,t)$ in a basis of associated Legendre polynomials $P_\ell^m(\cos\theta)$, taking advantage of the fact that $P_\ell^m(\cos\theta)$ are the eigenfunctions of the operator $\left\{\frac{1}{\sin\theta}\frac{\partial}{\partial\theta}\left(\sin\theta\frac{\partial}{\partial\theta}\right) - \frac{m^2}{\sin^2\theta}\right\}$. This procedure is described in detail in ref. 75.

The linear optical response of the MNP is analyzed by calculating its absorption cross-section spectrum, $\sigma_{\mathrm{abs}}(\omega) = \frac{4\pi}{c}\mathrm{Im}\{\alpha(\omega)\}$ [Eq. (1.49)], with $\alpha(\omega)$ the polarizability of the system calculated from $\alpha(\omega) = \frac{1}{\mathrm{E}_0\Delta t}\mathrm{p}(\omega)$[16]. $\mathrm{p}(\omega)$ is obtained using the time-to-frequency Fourier transform given by Eq. (2.36a) by considering

[16] $\mathrm{p}(\omega)$ is the frequency-dependent dipole moment induced along the z-axis, obtained according to Eqs. (2.33) and (2.36a).

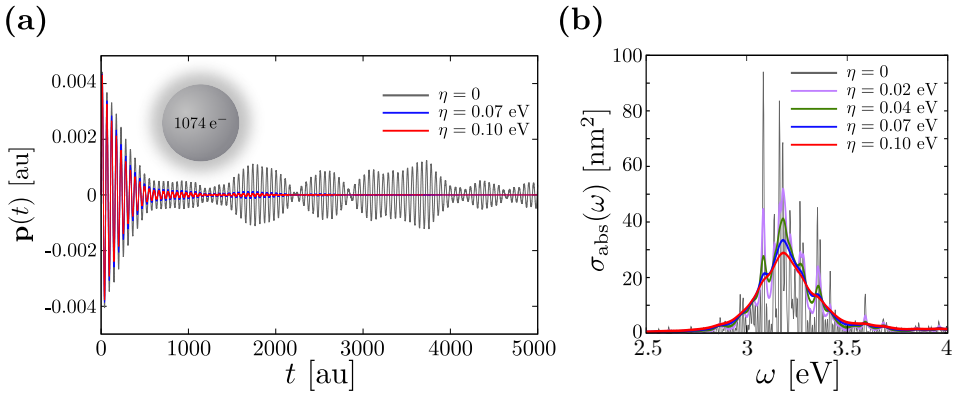

Figure 2.1: **(a)** Time evolution of the dipole moment $\mathbf{p}(t)$ induced at a spherical sodium MNP ($r_s = 4$ a$_0$) containing $N_e = 1074$ electrons in response to the external excitation given by Eq. (2.51). The results directly obtained from TDDFT within the WPP method (gray line) are damped by using different values of the attenuation factor η [Eq. (2.56)], as indicated in the legend. **(b)** Absorption cross-section spectra $\sigma_{\rm abs}(\omega)$ of the same MNP as in panel (a) obtained for different values of the attenuation factor η. Using different values of the factor η (with $\eta < \kappa$) leads to very similar widths of the DP resonance, κ. The results corresponding to $\eta = 0$ are divided by 2 for clarity.

in this case the filter

$$\mathfrak{F}(t) = e^{-\eta/2t}, \tag{2.56}$$

with an attenuation factor $\eta \sim 0.05 - 0.2$ eV smaller than the typical plasmon resonance width (as determined e.g. through the classical calculations in Chapter 1, γ_p in Eq. (1.10)).

We show in Figure 2.1a the effect of the filter $\mathfrak{F}(t)$ given by Eq. (2.56) in the result of the time-dependent dipole moment $\mathbf{p}(t)$ induced at a spherical MNP containing $N_e = 1074$ conduction electrons. Without applying the filter ($\eta = 0$, gray line), $\mathbf{p}(t)$ oscillates in time showing revivals because, as discussed in Subsection 2.2.1, the ALDA-TDDFT model adopted in this thesis does not include intrinsic dissipation processes in the free-electron gas. When an attenuation factor $\eta > 0$ is applied, $\mathbf{p}(t)$ is exponentially damped, thus accounting for the losses of the metal phenomenologically. This attenuation factor η also affects dramatically the absorption cross-section spectrum $\sigma_{\rm abs}(\omega)$ of the system as illustrated in Figure 2.1b. Indeed, for $\eta = 0$ the plasmon peak in $\sigma_{\rm abs}(\omega)$ at around $\omega = 3.2$ eV is fragmented into a set of discrete lines associated with the single electron–hole excitations that build up the plasmon[17] (see below) [206, 246]. The inclusion of η broadens these single electron–hole excitation peaks and allows us to retrieve the broad and smooth Lorentzian-like profile of the plasmon resonance similarly to the

[17] The width of the peaks associated to single electron–hole excitations in Figure 2.1b for $\eta = 0$ is due to the finite calculation time T_f, where in this case we use $T_f \sim 13000$ au. However, we typically use $T_f \sim 3000 - 4000$ au in this thesis for linear-response calculations, enough to achieve convergence when using $\eta = 0.05 - 0.2$ eV.

classical prediction shown in Figure 1.4d. We employ the filter given by Eq. (2.56) in Chapter 3, Chapter 4, and Chapter 5, where we study the linear optical response of different plasmonic systems.

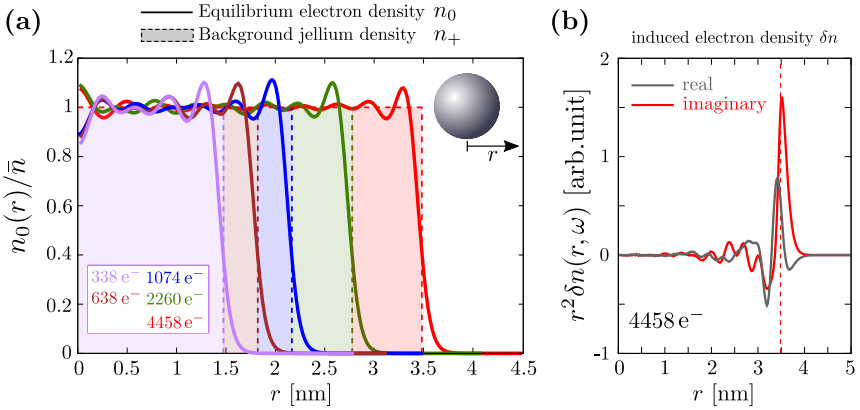

Figure 2.2: **(a)** Equilibrium electron density $n_0(r)$ (solid lines) and background jellium denisty $n_+(r)$ (dashed filled lines) as a function of the radial coordinate, r, for spherical MNPs characterized by a Wigner–Seitz radius $r_s = 4$ a$_0$ (sodium) and containing different numbers of conduction electrons: $N_e = 338$ electrons (purple), 638 electrons (brown), 1074 electrons (blue), 2260 electrons (green), and 4458 electrons (red). Results are normalized to the average electron density $\bar{n} = \left(\frac{4}{3}\pi r_s^3\right)^{-1}$ [Eq. (1.11)]. **(b)** Induced electron density $\delta n(\mathbf{r},\omega)$ (multiplied by r^2) along the radial axis r ($\theta = 0$) at the DP frequency $\omega = \omega_{\mathrm{DP}} = 3.25$ eV for a sodium MNP containing 4458 electrons in response to the external plane-wave excitation given by Eq. (2.51). The dashed red line represents the position of the jellium edge of the MNP. An attenuation factor $\eta = 0.2$ eV [Eq. (2.56)] is used to perform the Fourier transform.

Influence of the size of small spherical nanoparticles on their optical response

We show in Figure 2.2a the equilibrium electron density profile $n_0(r)$ obtained for spherical MNPs containing different number of conduction electrons within the range $N_e = 338 - 4458$, resulting in a radius $a \sim 1.5 - 3.5$ nm [Eq. (2.45)]. Quantum-mechanical phenomena such as electron spill-out [247] and Friedel oscillations [248, 249] of the equilibrium electron density $n_0(r)$ are observed. The electron spill out of $n_0(r)$ is a consequence of the finite potential barrier at the MNP surface that allows electrons to spread outside the background jellium edge located at $r = a$. Moreover, Friedel oscillations are due to electron reflection at $r = 0$ and at the MNP boundary, and can be understood as a manifestation of the Gibbs phenomenon occurring in the Fourier series of step-like functions: the electron density $n_0(r)$ is given by a summation of a finite number of $\psi^0_{j_r,\ell}(r)$ orbitals [Eq. (2.48)] and thus exhibits oscillations along the radial coordinate r. In addition, $n_0(r)$ in Figure 2.2a features either a peak or a dip at $r = 0$ depending on the number of conduction electrons. While for $N_e = 338$ electrons (purple), 638 electrons (brown) and 1074

electrons (blue) there is a dip at $r = 0$, for $N_e = 2260$ electrons (green) and 4458 electrons (red) there is a peak. This behavior is related to the relative contribution of the $\psi^0_{j_r,\ell}(r)$ orbitals with $\ell = 0$ (which depends upon the number of occupied closed shells), since only those with $\ell = 0$ can contribute to the electron density $n_0(r)$ precisely at $r = 0$ and only low-ℓ orbitals $\psi^0_{j_r,\ell}(r)$ contribute close to the center of the MNP because of the centrifugal potential $\ell(\ell+1)/r^2$ [Eq. (2.47)] that forbids electrons with high angular quantum number ℓ to approach the center of the MNP.

Figure 2.2b shows the electron density $\delta n(\mathbf{r}, \omega)$ induced at the dipolar plasmon (DP) frequency $\omega_{\rm DP} = 3.25$ eV in a spherical MNP ($N_e = 4458$ is considered as an example) in response to an external plane-wave excitation. The induced density $\delta n(\mathbf{r}, \omega)$ is predominantly located near the surface of the MNP as expected from classical descriptions. However, due to the nonlocal dynamical screening of conduction electrons described within the jellium model [58, 126], $\delta n(\mathbf{r}, \omega)$ spreads beyond the limits of the classical sharp edge at $r = a$ (not to be confused with the spill out of the *equilibrium* electron density $n_0(r)$ shown in Figure 2.2a).

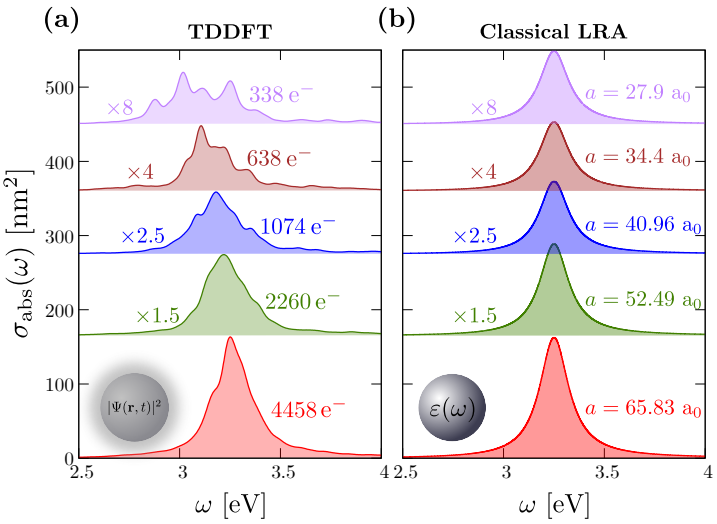

Figure 2.3: **(a)** TDDFT results of the absorption cross-section spectra $\sigma_{\rm abs}(\omega)$ of spherical MNPs with different number of conduction electrons, $N_e = 338$ (purple), 638 (brown), 1074 (blue), 2260 (green), and 4458 (red). The electronic structure of the MNPs is described within the jellium model using a Wigner–Seitz radius $r_s = 4$ a$_0$ that corresponds to sodium. An attenuation parameter $\eta = 0.07$ eV is used [Eq. (2.56)]. **(b)** Classical LRA results of $\sigma_{\rm abs}(\omega)$ for spherical MNPs with different radius a, as obtained from Eq. (1.45). a = 27.9 a$_0$ (purple), 34.4 a$_0$ (brown), 40.96 a$_0$ (blue), 52.49 a$_0$ (green), and 65.83 a$_0$ (red). The value of the radius a is determined according to Eq. (2.45). A Drude dielectric function [Eq. (1.10)] with $\omega_p = 5.63$ eV and $\gamma_p = 0.175$ eV is used for all MNP sizes, which reproduces the TDDFT data for the largest MNP (red curve).

We next show in Figure 2.3 the absorption cross-section spectra $\sigma_{\rm abs}(\omega)$ of the spherical sodium MNPs. The TDDFT results (panel a) illustrate that quantum

finite-size effects [250–252] break the invariance with particle size of the spectral profile of $\sigma_{\rm abs}(\omega)$ predicted by classical (nonretarded) LRA calculations (panel b). First, decreasing the size of the MNP within TDDFT produces a redshift of the DP resonance[18] from $\omega_{\rm DP} \sim 3.25$ eV (red, lower spectrum) to $\omega_{\rm DP} \sim 3$ eV (purple, upper spectrum), in contrast to the size-invariant $\omega_{\rm DP} = \omega_p/\sqrt{3} \approx 3.25$ eV classical LRA value[19] (see Subsection 1.2.3). This redshift is a consequence of the spill out of the induced charges due to nonlocal dynamical screening shown in Figure 2.2b. One can interpret in an intuitive picture that the size of the MNP is effectively increased [194], which for the same number of electrons reduces the electron density and, thus, also the classical value of ω_p [Eq. (1.12)] and $\omega_{\rm DP}$. The impact of this spill out, and thus the redshift, is more significant the smaller the MNP is [96, 256, 257].

Further, the width of the DP resonances, κ, obtained with TDDFT increases with decreasing the size of the MNP [258]. For small-sized MNPs, as considered in Figure 2.3, the width of the plasmon resonance κ obtained within TDDFT is determined by surface-enabled Landau damping [64, 66, 194, 259–261], consisting in the plasmon decay into single electron–hole excitations caused by the scattering at the MNP surface (see also Figure 2.1b). Indeed, the MNP surface provides the momentum required for electrons to excite an intraband transition within the conduction band and create an electron–hole pair [262, 263], which is forbidden in the bulk due to momentum conservation. This quantum surface effect gains more importance with decreasing the radius a of the MNP. Indeed, the plamon resonance width associated with Landau damping scales as $\sim a^{-1}$ [264–267] (see Subsection 2.5.1). Finally, the fragmented shape of $\sigma_{\rm abs}(\omega)$ obtained for the smallest MNP considered in Figure 2.3a (purple, $N_e = 338$ electrons) is also a consequence of surface-enabled Landau damping. For such small MNPs the energy difference between different single electron–hole transitions is larger than the broadening $\eta = 0.07$ eV [Eq. (2.56)] accounting for dissipation processes in the system [268]. These single-electron features gradually disappear with increasing the number of conduction electrons, because the spectrally close electron–hole transitions merge with each other. In this situation, a Lorentzian resonance profile of $\sigma_{\rm abs}$ is obtained, and thus the system is said to exhibit a "better-developed" plasmonic behavior with increasing size [203, 269].

2.3.2 Dimers of spherical metallic nanoparticles

We next consider a dimer composed by two identical spherical metallic nanoparticles (MNPs) of radius a, as schematically shown in Figure 2.4. The electronic structure of the MNPs is described within the jellium model by considering a closed-shell configuration as introduced in Subsection 2.3.1. The gap separation between the

[18] This is not the case for noble metals such as Au or Ag, where interband transitions involving d-band electrons give rise to a blueshift of $\omega_{\rm DP}$ instead of a redshift with decreasing size of the MNP [80, 253–255].

[19] In Figure 2.3b we use $\omega_p = 5.63$ eV so that the value of $\omega_{\rm DP}$ obtained classically coincides with that obtained in Figure 2.3a within TDDFT for the largest MNP.

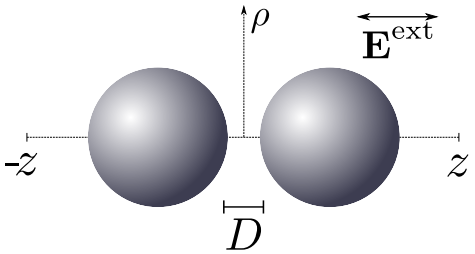

Figure 2.4: Sketch of a MNP dimer consisting of two spherical MNPs separated by a gap distance D. Cylindrical coordinates $\mathbf{r} = \{\rho, z, \varphi\}$ are adopted to perform the calculations. The origin of coordinate axes z and ρ is at the middle of the gap formed by the two MNPs. The z-axis also corresponds to the dimer axis.

two MNPs, D, is defined as the distance between the two closest jellium edges of each MNP. We study in this subsection the influence of the MNP size and gap separation distance D in the optoelectronic response of MNP dimers. The methodology to perform the calculations is based on the WPP method introduced in Subsection 2.2.1 using cylindrical coordinates $\mathbf{r} = \{\rho, z, \varphi\}$ (see coordinate system in Figure 2.4). We briefly describe below the specific aspects of the WPP method related to the cylindrical coordinate system adopted here.

Numerical implementation

We consider z-polarized illumination exciting the MNP dimer, so that the rotational symmetry of the system with respect to the z-axis is preserved (cylindrical symmetry). It is thus convenient to express the time-dependent Kohn–Sham (KS) orbitals $\Psi_{j,m}(\rho, z, \varphi, t)$ using cylindrical coordinates $\mathbf{r} = \{\rho, z, \varphi\}$ as

$$\Psi_{j,m}(\rho, z, \varphi, t) = \frac{1}{\sqrt{2\pi}} \psi_{j,m}(\rho, z, t) e^{im\varphi}, \tag{2.57}$$

where the quantum numbers $\{j, m\}$ define the KS state. In particular, here the magnetic quantum number m is also a good quantum number (similarly as for the individual MNP in Subsection 2.3.1), i.e., during the time propagation each KS orbital $\Psi_{j,m}(\rho, z, \varphi, t)$ preserves the initial value of m given by that of the ground-state KS orbital, $\Psi_{j,m}(\rho, z, \varphi, t = 0) = \Psi^0_{j,m}(\rho, z, \varphi)$.

For relatively large gap separation, $D \gtrsim 20$ a$_0$, the ground state KS orbitals $\Psi^0_{j,m}(\rho, z, \varphi)$ can be obtained from those of the individual MNP [$\Psi^0_{j_r,\ell,m}(r, \theta, \varphi)$, Eq. (2.46)] since, in this case, KS orbitals corresponding to different MNPs do not spatially overlap.[20] Thus, $\Psi^0_{j,m}(\rho, z, \varphi)$ are straightforwardly obtained from the values of $\Psi^0_{j_r,\ell,m}(r, \theta, \varphi)$ by direct interpolation between the spherical and cylindrical coordinate systems, where the displacement $\pm(a + D/2)$ of the center of each MNP in the z-axis is taken into account (see geometry in Figure 2.4). For

[20] The quantum number j defining the KS state in cylindrical coordinates replaces the pair $\{j_r, \ell\}$ in spherical coordinates.

smaller gap separation, $D \lesssim 20$ a$_0$, the ground-state KS orbitals $\Psi^0_{j,m}(\rho, z, \varphi)$ are obtained within the WPP method introduced in Subsection 2.2.1, where the gap separation D determining the position of the positive background jellium density $n_+(\mathbf{r})$ [Eq. (2.13)] is slowly reduced starting from a large value $D \approx 20$ a$_0$. The gap separation $D \to D - v_0 t$ decreases with velocity v_0 of the order of $v_0 \sim 0.002$ au, which guarantees that the equilibrium electron density $n_0(\mathbf{r})$ adiabatically follows the motion of the positive background density $n_+(\mathbf{r})$, and thus the ground-state KS orbitals of the desired value of D can be obtained. In this adiabatic process performed within the WPP method, no external excitation is applied. A detailed description of the ground-state calculation of the MNP dimer is reported in ref. 125.

The time evolution of the KS orbital $\psi_{j,m}(\rho, z, t)$ in $\{\rho, z\}$-space [Eq. (2.57)] under a general external excitation $V_{\text{ext}}(\rho, z, t)$ is governed by the time-dependent KS equation [Eq. (2.19)] for a time-dependent Hamiltonian expressed as

$$\hat{H}[n(\rho, z, t)] = \hat{T} + V_{\text{eff}}[n(\rho, z, t)] + V_{\text{ext}}(\rho, z, t), \tag{2.58}$$

where the effective potential $V_{\text{eff}}[n(\rho, z, t)]$ is obtained from Eq. (2.7), and the kinetic-energy operator is expressed in cylindrical coordinates as

$$\hat{T} = \underbrace{-\frac{1}{2}\frac{\partial^2}{\partial z^2}}_{\hat{T}_z} \underbrace{-\frac{1}{2\rho}\frac{\partial}{\partial \rho}\rho\frac{\partial}{\partial \rho} + \frac{m^2}{2\rho^2}}_{\hat{T}_\rho}. \tag{2.59}$$

Owing to the cylindrical symmetry, the time evolution is identical for KS orbitals with magnetic quantum number $\pm m$, and thus only the orbitals with $m \geq 0$ are propagated. In this case, the time-dependent electron density is given by

$$n(\rho, z, t) = \sum_{\{j, m \geq 0\} \in \text{occ}} \chi_m |\psi_{j,m}(\rho, z, t)|^2, \tag{2.60}$$

where χ_m is given by Eq. (2.55) and accounts for spin and $\pm m$ degeneracy ($\chi_m = 2$ for $m = 0$ and $\chi_m = 4$ for $m > 0$).

As a technical detail, the radial coordinate ρ is not expressed in equidistant spatial points, but using a non-uniform meshgrid. This procedure allows us to use a tighter meshgrid close to $\rho = 0$ than at larger radial distances, thus improving the accuracy of the method [229]. In particular, we use the following function to express the coordinate ρ in the calculations

$$\rho(\tilde{\rho}) = \tilde{\rho} - \frac{b}{\sqrt{a}} \text{atan}\left(\frac{\tilde{\rho}}{\sqrt{a}}\right), \tag{2.61}$$

where $a = 700$, $b = 595$, and the variable $\tilde{\rho}$ is expressed in an equidistant uniform meshgrid.

The kinetic-energy operator $\hat{T}$ given by Eq. (2.59) can be then written as

$$\hat{T} = \underbrace{-\frac{1}{2}\frac{\partial^2}{\partial z^2}}_{\hat{T}_z} \underbrace{-\frac{1}{2\rho\rho'}\frac{\partial}{\partial\tilde{\rho}}\frac{\rho}{\rho'}\frac{\partial}{\partial\tilde{\rho}} + \frac{m^2}{2\rho^2}}_{\hat{T}_{\tilde{\rho}}}, \tag{2.62}$$

with $\rho' = \frac{\partial\rho}{\partial\tilde{\rho}}$. Further, by redefining the time-dependent KS orbital as [Eq. (2.57)]

$$\phi_{j,m}(\tilde{\rho}, z, t) = \sqrt{\rho\rho'}\psi_{j,m}(\tilde{\rho}, z, t), \tag{2.63}$$

the time-dependent KS equation [Eq. (2.19)] to be solved finally transforms into

$$i\frac{\partial}{\partial t}\phi(\tilde{\rho}, z, t) = \left(\hat{T} + V_{\text{eff}}[n(\tilde{\rho}, z, t)] + V_{\text{ext}}(\tilde{\rho}, z, t)\right)\phi(\tilde{\rho}, z, t), \tag{2.64}$$

with

$$\hat{T} = \underbrace{-\frac{1}{2}\frac{\partial^2}{\partial z^2}}_{\hat{T}_z} \underbrace{-\frac{1}{2\sqrt{\rho\rho'}}\frac{\partial}{\partial\tilde{\rho}}\frac{\rho}{\rho'}\frac{\partial}{\partial\tilde{\rho}}\frac{1}{\sqrt{\rho\rho'}} + \frac{m^2}{2\rho^2}}_{\hat{T}_{\tilde{\rho}}}. \tag{2.65}$$

As described in Subsection 2.2.1, the most-involved part of the WPP algorithm is the application of the operator $e^{i\Delta t\hat{T}}$ [Eq. (2.31)], where in this case $\hat{T} = \hat{T}_z + \hat{T}_{\tilde{\rho}}$ is given by Eq. (2.65). Using the coordinate system and change of variables employed in this subsection, the operator $e^{i\Delta t\hat{T}_z}$ is diagonal in the momentum-space representation, and thus it can be applied by representing $\phi(\tilde{\rho}, z, t)$ in a real-space meshgrid of equidistant points in the z-coordinate and employing the direct and inverse space-to-momentum Fourier transforms, as introduced in Subsection 2.2.1. On the other hand, the operator $e^{i\Delta t\hat{T}_{\tilde{\rho}}}$ is diagonal neither in real space nor in momentum space. To apply this operator, we employ the Cayley transform such that [130, 229]

$$e^{i\Delta t\hat{T}_{\tilde{\rho}}}\phi(\tilde{\rho}, z, t) = \left(1 + \frac{1}{2}i\Delta t\hat{T}_{\tilde{\rho}}\right)^{-1}\left(1 - \frac{1}{2}i\Delta t\hat{T}_{\tilde{\rho}}\right)\phi(\tilde{\rho}, z, t) + \mathcal{O}(\Delta t^3), \tag{2.66}$$

where the operator $\hat{T}_{\tilde{\rho}}$ [Eq. (2.65)] is represented in a matrix form using finite differences with equidistant points in $\tilde{\rho}$ to express the derivatives [225, 226]. Further details on the numerical procedure used in this thesis to apply the WPP method in cylindrical coordinates can be found in ref. 75.

Influence of the particle size and gap separation in the optoelectronic response of spherical-nanoparticle dimers

We illustrate in Figure 2.5 the TDDFT results of the optical response of sodium dimers consisting of two identical spherical MNPs ($r_s = 4$ a$_0$) of radius a, obtained

using the following external potential [see Eq. (2.51)]

$$V_{\text{ext}}(\rho, z, t) = \delta(t)\ \mathrm{E}_0\ \Delta t\ z, \tag{2.67}$$

corresponding to plane-wave illumination $\mathbf{E} = \mathrm{E}_0\ \hat{\mathbf{z}}$ polarized along the dimer z-axis. The radius of the MNPs is determined from the number of conduction electrons N_e according to Eq. (2.45). We consider $N_e = 638$ electrons ($a = 34.4$ a$_0$, panels a,d,g,j), $N_e = 1074$ electrons ($a = 40.96$ a$_0$, panels b,e,h,k), and $N_e = 4458$ electrons ($a = 65.83$ a$_0$, panels c,f,i,l).

We first analyze the absorption spectra $\sigma_{\text{abs}}(\omega)$ shown in Figures 2.5a,b,c, where the gap separation distance, D, is varied from $D = 16$ a$_0$ to $D = 40$ a$_0$ ($D \approx 0.85 - 2.1$ nm). For all the MNP sizes considered, the excitation of the bonding dipolar plasmon (BDP) resonance at $\omega_{\text{BDP}} \sim 2.7 - 3$ eV, mainly formed due to the electromagnetic interaction between the DP resonances ($\ell = 1$) of the individual MNPs (see Figure 1.5b), dominates the absorption spectra $\sigma_{\text{abs}}(\omega)$. This BDP redshifts with decreasing D for all MNP sizes, consistent with the classical LRA prediction displayed in Figure 1.5a. Despite the overall similarity of the results obtained within TDDFT for different sizes of the MNPs, there are remarkable differences arising from the quantum finite-size effects that we introduced in Subsection 2.3.1 [126]. Similarly to the results of individual MNPs, the width of the BDP resonance is narrower for $N_e = 4458$ than for $N_e = 638$, and the shallow spectral features associated with single electron–hole transitions present for the smallest MNPs disappear with increasing the size of the MNPs. Further, the spectrum for $N_e = 4458$ in panel (c) shows a second peak at $\omega_{\text{BQP}} \sim 3.3 - 3.4$ eV that corresponds to the bonding quadrupolar plasmon (BQP) formed due to the optical hybridization between the plasmonic modes of the individual constituents (mainly a mixture of $\ell = 1$ and $\ell = 2$, see Figure 1.5b). This BQP mode, however, is not developed for $N_e = 638$ (panel a) because surface-enabled Landau damping hinders the formation of high-order plasmonic modes (see details in Chapter 3). In general, for relatively large gap separation, $D = 16 - 40$ a$_0$, the same quantum surface effects observed in Figure 2.3a for individual MNPs are also present in the optical response of MNP dimers.

Significantly, quantum many-body phenomena are more relevant for smaller gap separation, $D \lesssim 10$ a$_0$ ($\lesssim 0.5$ nm), where electron tunneling becomes an important process [50, 68, 202, 270–272]. Electron tunneling affects both the absorption cross-section spectra $\sigma_{\text{abs}}(\omega)$ (Figures 2.5d,e,f) and the enhancement of the electric field $|\mathbf{E}|^{\text{ind}}/\mathrm{E}_0$ (Figures 2.5g,h,i), but its influence is clearer on the latter. In contrast to the monotonous increase of the resonant $|\mathbf{E}|^{\text{ind}}/\mathrm{E}_0$ with reducing D expected from classical LRA calculations (Figure 1.5c), the TDDFT results in Figures 2.5g,h,i reveal that the maximum field enhancement is reached for $D \sim 0.5$ nm irrespective of the size of the MNPs that form the dimer. For smaller gap distances, $D \lesssim 0.5$ nm, the induced electric field in the middle of the gap gets quenched since the net electron transfer caused by electron tunneling tends to neutralize the high charge densities of opposite sign localized at the MNP surfaces across the junction [67, 83, 86, 126]. The effect of electron tunneling for small

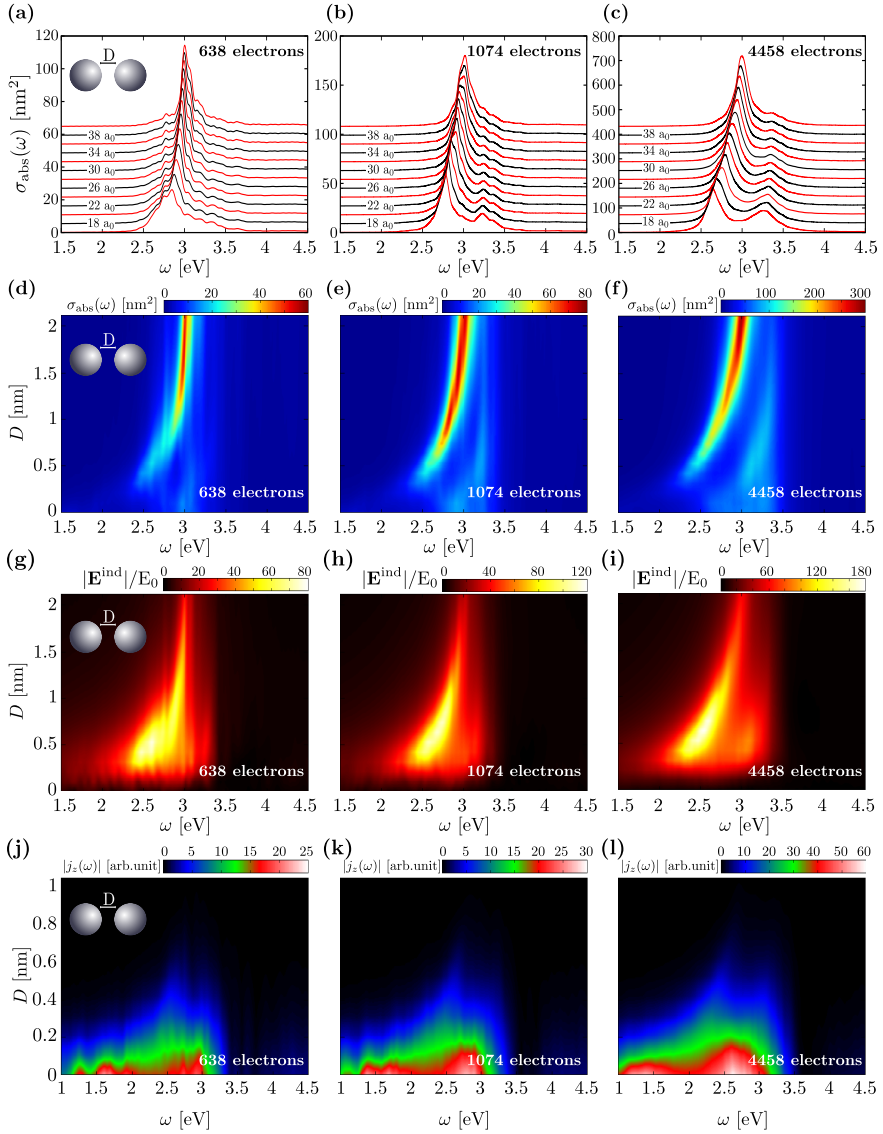

Figure 2.5: TDDFT study of the linear optical response of spherical MNP dimers of different size and gap separation, D. **(a,b,c)** Waterfall plot of the absorption spectra $\sigma_{\rm abs}(\omega)$ of spherical MNP dimers with a different number of conduction electrons N_e for gap separation ranging from $D = 16$ a$_0 \approx 0.85$ nm (bottom) to $D = 40$ a$_0 \approx 2.1$ nm (top) in steps of 2 a$_0$. **(d,e,f)** Color maps of $\sigma_{\rm abs}(\omega)$ as a function of the gap separation distance, D, and the frequency of the external excitation, ω. Smaller gaps than in panels (a,b,c) are considered. **(g,h,i)** Induced electric-field enhancement $|\mathbf{E}|^{\rm ind}/\mathrm{E}_0$ in the middle of the gap formed by two MNPs as a function of ω and D. **(j,k,l)** z-component of the induced electron-current density $|\mathbf{j}(\mathbf{r},\omega)|$ in the middle of the gap [Eq. (2.35)] as a function of ω and D. Panels (a,d,g,j) correspond to $N_e = 638$ conduction electrons, (b,e,h,k) to $N_e = 1074$ electrons, and (c,f,i,l) to $N_e = 4458$ electrons. In all the panels, the external plane-wave electric field is polarized along the dimer z-axis. An attenuation parameter $\eta = 0.07$ eV is used in Eq. (2.56) to obtain the spectral response.

junctions is further corroborated by analyzing the z-component of the induced electron-current density $|\mathbf{j}(\mathbf{r},\omega)|$ in the middle of the gap [Eq. (2.35)], as shown in Figures 2.5j,k,l. For $D \sim 0.5$ nm, i.e., prior to the direct geometrical contact ($D = 0$) between the two MNP surfaces, an electron current at optical frequencies $\omega \sim 1 - 3.5$ eV is established across the nanogap which increases when closing the gap distance D.

We thus find that electron tunneling dramatically influences the optical properties of MNP dimers with small gap separation, $D \lesssim 0.5$ nm, an effect that cannot be captured using standard classical theories [83, 86]. For larger separation distances, $D \gtrsim 0.5$ nm, electron tunneling does not play a significant role, but other quantum surface effects such as the spill out of the induced charges and surface-enabled Landau damping also influence the optical properties [58]. We show in Subsection 2.5.1 that the semiclassical SRF can be used to predict the optical properties of MNP dimers with relatively large gap separation successfully. Importantly, we also show that the SRF cannot be used to describe sub-nanometric junctions since this approach is not designed to account for electron tunneling.

2.3.3 Cylindrical metallic nanowires

We next use TDDFT to study the optical response of an individual cylindrical nanowire of radius R_c and that of a dimer composed by two identical nanowires. The nanowires are infinite along the z-axis, and thus translationally invariant with respect to the z-axis (see the geometry of the systems in Figure 2.6a). The individual nanowire is also rotationally invariant with respect to the azimuthal angle φ. The radius R_c of the nanowire is given by [126]

$$R_c = \sqrt{\frac{4}{3}\tilde{N}_e\, r_s^3}, \tag{2.68}$$

where $\tilde{N}_e$ is the number of conduction electrons per unit length in the z-direction. We use the methodology described below to obtain the optical response of individual nanowires and nanowire dimers and, in Chapter 4, this methodology allows us to obtain the Feibelman parameter $d_\perp(\omega, k_\parallel)$ as a function of both the frequency of the external excitation, ω, and of the wavenumber parallel to the metal surface, $k_\parallel$.

Numerical implementation

To derive the Kohn–Sham (KS) equations (Section 2.1) used to calculate the ground state of an infinite individual nanowire, we first consider the case of a cylinder with a spatial periodicity L in the z-direction (the infinite nanowire will be the case for $L \to \infty$) [128]. Applying the periodic boundary conditions in the z-direction, and due to the azimuthal symmetry of the system, the ground-state KS orbitals of the cylinder can be represented in a cylindrical coordinate system (ρ, z, φ) as [128]

$$\Psi^0_{j,m,q}(\rho, z, \varphi) = \frac{1}{\sqrt{2\pi}}\, \psi^0_{j,m}(\rho) e^{im\varphi} \frac{1}{\sqrt{L}} e^{i\frac{2\pi}{L}qz}, \tag{2.69}$$

with $\{j,m,q\}$ the quantum (integer) numbers that define a KS state. The time-independent KS equation is given in these coordinates by [Eq. (2.5)]

$$\left(\hat{H}[n_0(\rho)] - \frac{1}{2}\frac{\partial^2}{\partial z^2}\right)\Psi^0_{j,m,q}(\rho,z,\varphi) = \left(\epsilon_{j,m} + \frac{1}{2}\left(\frac{2\pi}{L}q\right)^2\right)\Psi^0_{j,m,q}(\rho,z,\varphi), \tag{2.70}$$

where $\epsilon_{j,m}$ are the eigenvalues of the radial part of the Hamiltonian $\hat{H}[n_0(\rho)]$,

$$\underbrace{\left(\hat{T} + V_{\mathrm{H}}[n_0(\rho)] + V_{\mathrm{xc}}[n_0(\rho)]\right)}_{\hat{H}[n_0(\rho)]}\psi^0_{j,m}(\rho) = \epsilon_{j,m}\psi^0_{j,m}(\rho), \tag{2.71}$$

and the ρ-space kinetic-energy operator $\hat{T}$ is expressed as

$$\hat{T} = -\frac{1}{2}\left(\frac{1}{\rho}\frac{\partial}{\partial\rho}\left(\rho\frac{\partial}{\partial\rho}\right) - \frac{m^2}{\rho^2}\right). \tag{2.72}$$

The equilibrium electron density $n_0(\rho)$ is given by

$$\begin{aligned} n_0(\rho) &= 2\sum_{\{j,m,q\}\in\mathrm{occ}} |\Psi^0_{j,m,q}(\rho,z,\varphi)|^2 \\ &= 2\sum_{\{j,m,q\}\in\mathrm{occ}} \frac{1}{2\pi}|\psi^0_{j,m}(\rho)|^2\frac{1}{L}\sum_q \Theta\left(E_{\mathrm{F}} - \left(\epsilon_{j,m} + \frac{1}{2}\left(\frac{2\pi}{L}q\right)^2\right)\right), \end{aligned} \tag{2.73}$$

where E_{F} is the Fermi energy, Θ represents the Heaviside step function, and the factor 2 is due to the spin degeneracy. Because of the cylindrical symmetry, the $\pm m$ states are degenerate so that we only solve Eqs. (2.70) and (2.71) for $m \geq 0$.

The case of the infinite cylindrical nanowire can be obtained by taking $L \to \infty$ in Eqs. (2.69)-(2.73). In such a situation, the summation over the quantum number q in Eq. (2.73) can be transformed into an integral over the continuous variable $k_z = \frac{2\pi}{L}q$, and $n_0(\rho)$ can be expressed as

$$n_0(\rho) = \sum_{\{j,m\geq 0\}\in\mathrm{occ}} \chi_{j,m}|\psi^0_{j,m}(\rho)|^2, \tag{2.74}$$

with the statistical factor $\chi_{j,m}$ accounting for spin and $\pm m$ degeneracy (see Subsection 2.3.1), as well as for the degeneracy due to the electron motion along the z-axis,

$$\chi_{j,m} = \begin{cases} \frac{1}{\pi^2}\sqrt{2(E_{\mathrm{F}} - \epsilon_{j,m})} & \text{for } m = 0 \\ \\ \frac{2}{\pi^2}\sqrt{2(E_{\mathrm{F}} - \epsilon_{j,m})} & \text{for m>0} \end{cases}. \tag{2.75}$$

Similarly to the equilibrium density for spherical MNPs in Subsection 2.3.1 [Eq. (2.48)], $n_0(\rho)$ of the cylindrical nanowire, given by Eq. (2.74), only depends upon the radial coordinate ρ. The orbitals $\psi^0_{j,m}(\rho)$ of the individual nanowire are therefore obtained from Eqs. (2.71) and (2.74) using a self-consistent procedure

based on the KS scheme described in Subsection 2.3.1, where the Hamiltonian $\hat{H}[n_0(\rho)]$ in Eq. (2.71) is diagonalized by expressing $\hat{T}$ [Eq. (2.72)] in real space with finite differences [75, 130].

Once the time-independent KS orbitals $\psi^0_{j,m}(\rho)$ of the individual nanowire are obtained from Eqs. (2.71) and (2.74), we use the WPP method described in Subsection 2.2.1 and propagate in real time the KS orbitals ψ_p subjected to an external time-dependent potential. The time-dependent potential $V_{\text{ext}}(x, y, t)$ only depends on the (x, y)-coordinates so that the translational invariance of the system along the z-axis is preserved. For the time propagation, we discretize ψ_p on an equidistant mesh in Cartesian coordinates, $\psi_p \equiv \psi_p(x, y, t)$, where the initial conditions $\psi_p(x, y, t = 0) \equiv \psi^0_{j,m}(\rho, \varphi)$ are given by the KS orbitals of the ground state. Note that when expressing the time-dependent KS orbitals in Cartesian coordinates, the quantum number p replaces the pair $\{j, m\}$ used in cylindrical coordinates for the ground state. One of the advantages of using Cartesian coordinates $\psi_p \equiv \psi_p(x, y, t)$ for the time propagation is that it is possible to directly apply the same algorithm as for the individual nanowire to study e.g. the optical response of a pair of parallel nanowires (nanowire dimer, Figure 2.6a) under the influence of any external potential $V_{\text{ext}}(x, y, t)$ depending on (x, y). This algorithm basically consists in applying the pseudospectral FGH method [230, 236, 237] to calculate the kinetic-energy operator $\hat{T}$ as well as the Hartree potential $V_{\text{H}}[n(x, y, t)]$ [Eq. (2.23)].

We obtain the optical response of nanowires to a spatially-constant x-polarized external electric field of amplitude E_0, corresponding to the following external potential [see Eq. (2.51)]:

$$V_{\text{ext}}(x, y, t) = \delta(t)\ \text{E}_0 \Delta t\ x. \tag{2.76}$$

Mesh steps of the order of $\Delta x = \Delta y \sim 0.5\ \text{a}_0$ and a time step of $\Delta t \sim 0.1$ au are typically used in this thesis for the cylindrical geometry. The KS orbitals $\psi_p(x, y, t)$ evolve in time according to the time-dependent KS equations [Eq. (2.19)], with the time-dependent electron density $n(x, y, t)$ expressed in Cartesian coordinates as

$$n(x, y, t) = \sum_{k \in \text{occ}} \chi_p \left|\psi_p(x, y, t)\right|^2. \tag{2.77}$$

In Eq. (2.77), the statistical factors χ_p are now given by

$$\chi_p = \frac{2}{\pi}\sqrt{2(E_{\text{F}} - \epsilon_p)}, \tag{2.78}$$

where ϵ_p is the eigenenergy of the ground-state KS orbital $\psi_p(x, y, t = 0)$.

Optical response of individual cylindrical metallic nanowires and dimers

We show here the TDDFT results for the linear optical response of an individual metallic nanowire and nanowire dimers [59, 119, 273–276] consisting of $\tilde{N} = 240\ \text{a}_0^{-1}$

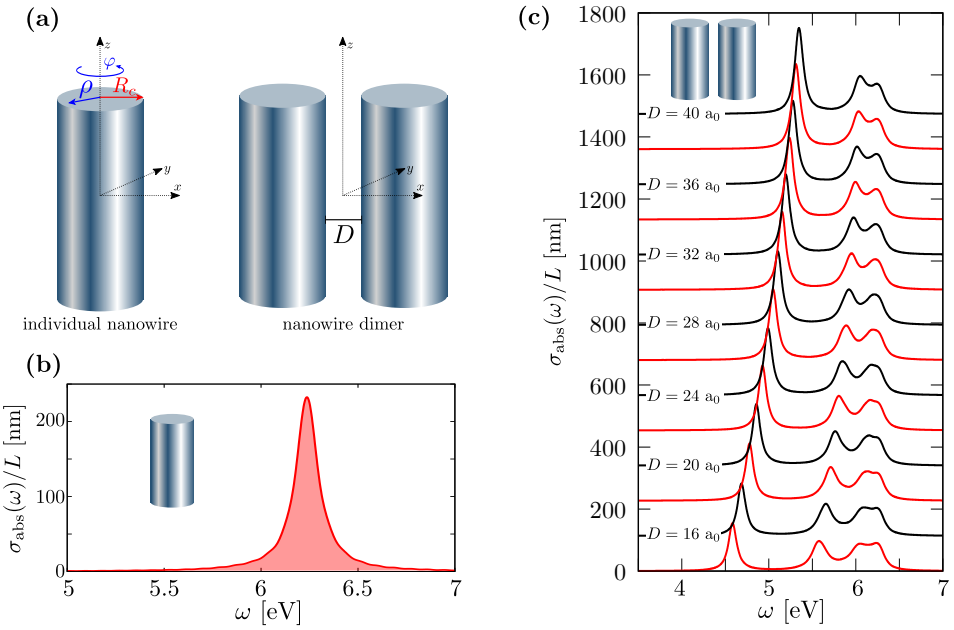

Figure 2.6: **(a)** Geometry of the individual cylindrical nanowire (left) and the dimer composed by two parallel nanowires (right). The radius of the nanowires is R_c, which is determined by the number of conduction electrons $\tilde{N}$ per unit length in the z-direction according to Eq. (2.68). The cylinders are infinite along the z-axis (translationally invariant), and are separated by a gap distance D along the x-axis in the dimer configuration. **(b)** Absorption cross-section spectrum $\sigma_{\rm abs}(\omega)/L$ per unit length L in the z-direction of an individual nanowire characterized by a Wigner–Seitz radius $r_s = 3.02$ a$_0$ and $\tilde{N} = 240$ a$_0^{-1}$ ($R_c \approx 94.3$ a$_0$). **(c)** Same as in **(b)** but for the dimer configuration where the gap separation is varied from $D = 14$ a$_0$ to $D = 40$ a$_0$. An attenuation parameter $\eta = 0.07$ eV [Eq. (2.56)] is used to perform the Fourier transform.

electrons per unit length in the z-direction (radius $R_c \approx 94.3$ a$_0$). We use a jellium model with a Wigner–Seitz radius $r_s = 3.02$ a$_0$ ($\omega_p \approx 8.98$ eV) characteristic of the conduction electron density of gold. In addition, we introduce a stabilizing potential[21] [216] inside the metal so that the work function $W_{\rm F} = 5.5$ eV of gold is retrieved [277]. Note that, since the jellium model does not account for optical transitions involving localized d-band electrons (see Subsection 2.1.2), the plasmonic response obtained here presents important differences with respect to the results that would be obtained for a more exact model of gold. However, this description of the metallic nanowires still allows one to predict electron transport properties of gold junctions in off-resonant excitation conditions, as implemented in recent works [77, 210, 278] when studying the electron-currents dynamics induced by ultrafast

[21] Applying a stabilizing potential simply consists in introducing a constant potential inside the metal in the effective potential given by Eq. (2.17) both in the ground-state and in the time-dependent calculations. This procedure does not introduce any additional computational difficulty.

electromagnetic fields in plasmonic gaps. Here we are interested in the general trends of the optical response of these systems, where similar physical effects as described in Subsections 2.3.1 and 2.3.2 for spherical MNPs are also expected to be present.

Figure 2.6b shows the absorption cross-section spectrum $\sigma_{\rm abs}(\omega)/L$ per unit length L in the z-direction of an individual metallic nanowire of radius $R_c \approx 94.3$ a$_0$ (≈ 5 nm). Due to the relatively large size of the nanowire, $\sigma_{\rm abs}(\omega)/L$ does not exhibit single electron–hole transition features and the plasmonic response is well developed. A single peak associated with the DP resonance ($m = 1$) of the nanowire emerges at $\omega_{\rm DP} = 6.24$ eV, slightly below the classical nonretarded prediction, $\omega_{\rm DP} = \omega_{\rm SP} = \omega_p/\sqrt{2} = 6.35$ eV[22] [22], as a consequence of the spill out of the induced charges (see Subsection 2.3.1).

On the other hand, Figure 2.6c displays the absorption spectrum $\sigma_{\rm abs}(\omega)/L$ of a dimer formed by two parallel nanowires, identical to that discussed in Figure 2.6b. The gap separation, D, ranges from $D = 14$ a$_0$ to $D = 40$ a$_0$ ($D \sim 0.75 - 2.1$ nm). The overall qualitative behavior of $\sigma_{\rm abs}(\omega)/L$ with reducing gap distance D is almost identical to either the classical LRA (Figure 1.5a) or TDDFT (Figure 2.5c) results of the spherical MNP dimers, and can be understood using the electromagnetic hybridization picture introduced in Subsection 1.2.3 [150, 151]. Note that, due to the azimuthal symmetry of the individual nanowires, here the magnetic quantum number m plays a similar role as the multipole order ℓ in spherical MNPs. For the largest gap separation, $D = 40$ a$_0$ ($D \sim 2.1$ nm), two distinct modes emerges: a BDP at $\omega_{\rm DP} \sim 5.35$ eV formed from the hybridization of the DP modes ($m = 1$) of the individual nanowires, and a broad pseudomode at $\omega_{\rm PSM} \sim 6.2$ eV formed by the hybridization of nearly-degenerated higher-order modes ($m > 1$). This pseudomode is slightly redshifted with respect to the surface plasmon frequency. For smaller gap separations, $D \sim 28$ a$_0$, $\sigma_{\rm abs}(\omega)/L$ exhibits three well-defined peaks because another distinct resonance corresponding to the BQP at $\omega_{\rm BQP} \sim 5.9$ eV emerges. The BDP and the BQP resonances redshift with reducing D because of the increasing attractive interaction between the charges of opposite sign across the junction [126].

2.4 Nonlinear effects in the optical response of spherical plasmonic nanoparticles addressed within TDDFT

In previous sections, we focused on the linear optical response of MNPs, which are shown to strongly enhance the strength of the incident electric field at optical frequencies because of the excitation of plasmon resonances. However, plasmonic nanostructures also exhibit an efficient nonlinear optical response to

[22] While the DP resonance in spherical MNPs ($\ell = 1$) is classically at $\omega_{\rm DP} = \omega_{\ell=1} = \omega_p/\sqrt{3}$ within the nonretarded approximation, the DP resonance in cylindrical nanowires ($m = 1$) is at the surface plasmon frequency, $\omega_{\rm DP} = \omega_{m=1} = \omega_{\rm SP} = \omega_p/\sqrt{2}$ [22].

strong illumination intensities, thus being good candidates for the fabrication of nanodevices based on nonlinear optics [36]. One manner to theoretically study the nonlinear optical response of MNPs is to adopt the classical scheme introduced in Section 1.3 with the use of the nonlinear hyperpolarizabilities $\alpha^{(n)}$, *ad hoc* parameters that characterize the nonlinear optical response of the system. In this section, we show that the real-time TDDFT approach based on the WPP method, employed in previous sections to study the linear optical response of plasmonic structures, can also be used to analyze nonlinear effects in the optical response without using *ad hoc* parameters.

As an example, we consider the nonlinear optical response of an individual spherical MNP. We describe the electronic structure of the MNP within the jellium model introduced in Subsection 2.1.2 using a Wigner–Seitz radius $r_s = 4$ a$_0$ of sodium. We address a spherical MNP that contains 1074 conduction electrons, with a radius $a = 40.96$ a$_0$ (≈ 2.2 nm). The numerical implementation is almost identical to the one used in Subsection 2.3.1. The only difference is that for this study of nonlinear effects, instead of using the external potential $V_{\text{ext}}(\mathbf{r}, t)$ given by Eq. (2.51), here we use the following one:

$$V_{\text{ext}}(\mathbf{r}, t) = \text{E}_0 \; r \cos\theta \cos(\omega(t - t_0)) \; e^{-\left(\frac{t-t_0}{\sigma}\right)^2}, \tag{2.79}$$

which corresponds to the potential experienced by an electron interacting with an incident Gaussian laser pulse polarized along the z-axis. The fundamental frequency of the external illumination $\omega = 1.585$ eV in this section is half of the DP frequency $\omega_{\text{DP}} = 3.17$ eV (see Figure 2.3a), the duration of the pulse is $\sigma = 5 \times 2\pi/\omega$, and the arrival time of the pulse t_0 is $t_0 = 5\sigma$.

In order to analyze the nonlinear optical response of the individual MNP, we calculate within TDDFT the time evolution of the induced electron density $\delta n(\mathbf{r}, t)$ and obtain the time-dependent induced dipole moment, $\mathbf{p}(t)$ [Eq. (2.33)], as well as the electric near field (induced field), $\mathbf{E}^{\text{ind}}(\mathbf{r}, t)$ [Eq. (2.34)], created by the MNP in response to an incident electromagnetic pulse. The frequency-resolved quantities are then obtained from the time-to-frequency Fourier transform given by Eq. (2.36),

$$\begin{aligned}
\delta n(\mathbf{r}, \Omega) &= \int dt \; \delta n(\mathbf{r}, t) \; e^{i\Omega t} \; e^{-\left(\frac{t-t_0}{\sigma}\right)^2}, \\
\mathbf{p}(\Omega) &= \int dt \; \mathbf{p}(t) \; e^{i\Omega t} \; e^{-\left(\frac{t-t_0}{\sigma}\right)^2}, \\
\mathbf{E}^{\text{ind}}(\mathbf{r}, \Omega) &= \int dt \; \mathbf{E}^{\text{ind}}(\mathbf{r}, t) \; e^{i\Omega t} \; e^{-\left(\frac{t-t_0}{\sigma}\right)^2},
\end{aligned} \tag{2.80}$$

where in this case the filter $\mathfrak{F}(t)$ is given by

$$\mathfrak{F}(t) = e^{-\left(\frac{t-t_0}{\sigma}\right)^2}. \tag{2.81}$$

The Gaussian filter $\mathfrak{F}(t)$ introduced in Eq. (2.81) partially accounts for decay and dephasing processes of the collective density oscillations that are not included in

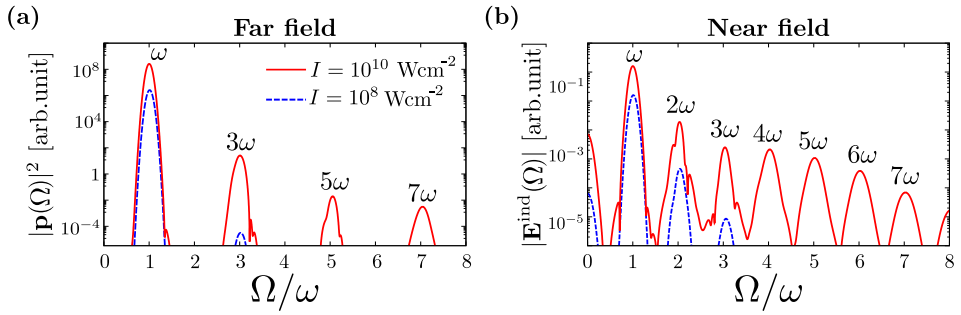

Figure 2.7: Nonlinear optical response of the individual spherical MNP as calculated within TDDFT for an incident z-polarized Gaussian electromagnetic pulse with fundamental frequency $\omega = 1.585$ eV (half of the frequency of the MNP dipolar plasmon $\omega_{\rm DP} = 3.17$ eV).The intensity is $I_0 = 10^8$ W cm^{-2} (dashed blue line) or $I_0 = 10^{10}$ W cm^{-2} (red line). Panel **(a)** shows the square of the induced dipole moment $|\mathbf{p}(\Omega)|^2$, and panel **(b)** the absolute value of the spectrum of the electric near field $|\mathbf{E}^{\rm ind}(\mathbf{r}, \Omega)|$ induced at the z-axis at 18 a$_0$ (≈ 0.95 nm) from the MNP surface. The symbol Ω represents the frequency of the induced electromagnetic fields in response to the incident illumination with fundamental frequency ω.

the present ALDA-TDDFT approach [72, 241, 242] (see Section 2.2), and allows us to reach convergent spectral response at high-harmonic frequencies. This approach is justified because the fundamental frequency is strongly detuned from the DP resonance of the MNP, so that no electron-density oscillation and high-harmonic generation is expected when the laser is switched off. Consistently, we apply a Gaussian filter given by the envelope of the incident pulse. Moreover, in Eq. (2.80) we use the symbol Ω (compare Eq. (2.80) with Eq. (2.36)) to refer to the oscillation frequency of the electromagnetic fields (and dipole moments) induced by the MNP due to the nonlinear optical response to the external excitation oscillating at ω.

The nonlinear optical response of the individual spherical MNP is displayed in Figure 2.7. In panel (a), we show the intensity spectrum of the induced dipole moment $|\mathbf{p}(\Omega)|^2$, which is proportional to the power of light emitted to the far field [Eq. (1.46)]. In panel (b), we show the spectrum of the induced near field $|\mathbf{E}^{\rm ind}(\mathbf{r}, \Omega)|$ at the z-axis, at 18 a$_0$ (≈ 0.95 nm) from the MNP surface. Results are obtained for an incident Gaussian electromagnetic pulse with intensity $I_0 = 10^8$ W cm^{-2} ($\mathrm{E}_0 = 4.8 \times 10^{-5}$ au, dashed blue line) and $I_0 = 10^{10}$ W cm^{-2} ($\mathrm{E}_0 = 4.8 \times 10^{-4}$ au, red line), averaged over the duration of the pulse σ. The corresponding energy per incident pulse is well below the documented damage threshold of small MNPs [279–281]. The induced dipole moment $|\mathbf{p}(\Omega)|^2$ in Figure 2.7a exhibits only odd harmonics $n = 1, 3, 5 \ldots$. Thus, only odd multiples $\Omega = \omega,\ 3\omega,\ 5\omega, \ldots$ of the incoming frequency ω are emitted by the system into the far field, consistently with the inversion symmetry of the MNP that prevents even-harmonic generation [152, 282] (see Section 1.3). Overall, the nonlinear response $|\mathbf{p}(\Omega)|^2$ for $I_0 = 10^{10}$ W cm^{-2} is several orders of magnitude larger than that for $I_0 = 10^8$ W cm^{-2}. This large increase is in accordance with the I_0^n dependence of $|\mathbf{p}(\Omega = n\omega)|^2$, expected from the standard theory of nonlinear optics as described in Section 1.3 [152].

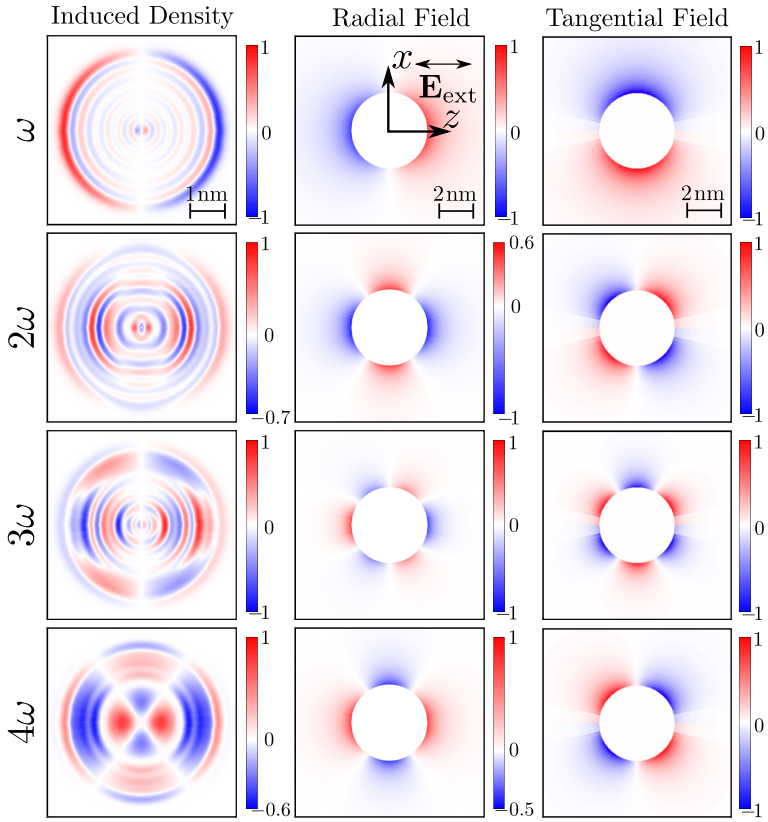

Figure 2.8: Color maps of the real part of the induced electron density $\delta n(\mathbf{r}, \Omega)$ (left), of the radial component of the electric near field $\mathbf{E}^{\mathrm{ind}}(\mathbf{r}, \Omega)$ (center), and of the tangential component of $\mathbf{E}^{\mathrm{ind}}(\mathbf{r}, \Omega)$ (right) induced at the fundamental, second, third, and fourth-harmonic frequency by a z-polarized Gaussian electromagnetic pulse with fundamental frequency $\omega = 1.585$ eV and intensity $I_0 = 10^{10}$ W cm^{-2} incident at the individual spherical MNP. Results are rotationally symmetric with respect to the z-axis, and they are shown in the (x, z)-plane normalized to unity.

In contrast to the far-field response, both odd and even harmonics are present in the spectrum of the electric near field induced by the individual MNP (Figure 2.7b). Indeed, at the metal–vacuum interface the inversion symmetry is locally broken, and short-range even-harmonic electric fields can be induced close to the MNP surface [283–287]. As expected, the induced field $|\mathbf{E}^{\mathrm{ind}}(\mathbf{r}, \Omega)|$ is orders of magnitude larger for $I_0 = 10^{10}$ W cm^{-2} (red line) than for $I_0 = 10^{8}$ W cm^{-2} (blue).

The color maps of the induced electron density $\delta n(\mathbf{r}, \Omega)$ and of the electric near field $\mathbf{E}^{\mathrm{ind}}(\mathbf{r}, \Omega)$ induced by the incident z-polarized Gaussian electromagnetic pulse are shown in Figure 2.8 for the fundamental, second, third, and fourth harmonics. The induced charge density $\delta n(\mathbf{r}, \Omega = n\omega)$ of the n-th harmonic and the corresponding near field $\mathbf{E}^{\mathrm{ind}}(\mathbf{r}, \Omega = n\omega)$ are shown in the (x, z)-plane.

Because of the symmetry of the configuration, the calculated color maps are independent of a rotation around the z-axis. At odd harmonics ($n = 1, 3$), the induced charge densities are antisymmetric with respect to the (x, y)-plane, $\delta n(x, y, z, n\omega) = -\delta n(x, y, -z, n\omega)$, which results in a net dipole moment (see Figure 2.7a). In contrast, a quadrupolar-like near field and symmetric charge-density, $\delta n(\mathbf{r}, n\omega) = \delta n(\text{-}\mathbf{r}, n\omega)$, are induced at even harmonics ($n = 2, 4$) [288–294]. The dipole moment $\mathrm{p}(\Omega)$ is zero in this case, and thus there is no emission into the far field at even harmonics. Thus, despite the second harmonic being at resonance with the dipolar plasmon of the MNP, the latter can not be excited because of the symmetry selection rules. Another consequence of the symmetry selection rules is that, for any point located in the (x, y)-plane, the even-harmonic near field in that point is oriented perpendicularly to the z-polarized incident pulse. We use in Chapter 6 the insights obtained in this section to study nonlinear effects when the spherical MNP is coupled to a QE located nearby, demonstrating that the presence of the QE enables the emission into the far field at the second-harmonic frequency, otherwise forbidden because of the inversion symmetry of the MNP.

2.5 Semiclassical surface-response formalism (SRF)

In this section, we introduce the semiclassical surface-response formalism (SRF) employed in this thesis, which allows one to account for quantum surface effects using much less computationally-demanding calculations as compared to the TDDFT methodology. In brief, the SRF is an extension of the classical LRA (Chapter 1) that incorporates surface-response corrections at the metal–dielectric interface in the solution of Maxwell's equations (Section 1.1) by means of the so-called Feibelman parameters obtained from quantum-mechanical calculations [95–98]. These parameters, commonly denoted as $d_\perp$ and $d_\parallel$, were first introduced by Peter Feibelman in the 1980s [98], and have received renewed attention during the last years [97, 124, 129, 276, 295–302] due to their usefulness to study systems that have recently become experimentally feasible. Indeed, the semiclassical SRF based on the Feibelman parameters allows us to account for the gradual variation of the induced electron density across the metal–vacuum interface (see Figure 2.2b), in contrast to the classical LRA described in Chapter 1 that considers the polarization charges to be located strictly at the metal boundary of infinitesimal width.

The Feibelman parameters $d_\perp$ and $d_\parallel$ are usually defined by considering a semi-infinite metal surface [54, 55, 62, 98], although the expressions for $d_\perp$ and $d_\parallel$ have been also proposed for other geometries such as spherical MNPs [95][23]. To our knowledge, the Feibelman parameters have been so far computed in the literature within the long-wavelength approximation, which consists in neglecting the nonlocality of the optical response in the direction parallel to the metal–dielectric interface. Thus, within the long-wavelength approximation, $d_\perp \equiv d_\perp(\omega)$

[23] In Chapter 4 we analyze the Feibelman parameter $d_\perp$ for a cylindrical metallic nanowire.

and $d_\parallel \equiv d_\parallel(\omega)$ solely depend on the excitation frequency, ω, and not on the wavenumber parallel to the metal surface, $k_\parallel$. In this thesis we thus refer to the $k_\parallel$-independent $d_\perp(\omega)$ and $d_\parallel(\omega)$ as the *nondispersive* Feibelman parameters. We adopt the long-wavelength approximation in this section and in Chapter 3, where we identify situations where this approximation becomes inaccurate. In Chapter 4, we calculate the Feibelman parameters as a function of both ω and $k_\parallel$ and propose a *dispersive* SRF that overcomes the shortcomings of the long-wavelength approximation.

The nondispersive Feibelman parameters defined for a semi-infinite planar metal–vacuum interface at $z = 0$ (Figure 1.3a) are usually expressed as [62, 81, 124, 296]:

$$d_\perp(\omega) = \frac{\int dz\ z\ \delta n(z,\omega)}{\int dz\ \delta n(z,\omega)}, \tag{2.82a}$$

$$d_\parallel(\omega) = \frac{\int dz\ z\ \frac{\partial}{\partial z} j_\parallel(z,\omega)}{\int dz\ \frac{\partial}{\partial z} j_\parallel(z,\omega)}, \tag{2.82b}$$

with $\delta n(z,\omega)$ the quantum-mechanical (complex-valued) electron density induced in response to the external excitation, and $j_\parallel(z,\omega)$ the parallel-to-the-surface component of the associated induced electron current density. Other definitions equivalent to Eq. (2.82) that express the parameters in terms of the electromagnetic fields and nonlocal dielectric functions have been also used [62, 98, 296, 303]. In Eq. (2.82), the real part of $d_\perp(\omega)$ ($\mathrm{Re}\{d_\perp(\omega)\}$) corresponds to the position of the centroid of the induced charge density with respect to the positive background edge of the metals (see schematic representation in Figure 2.9a), while the imaginary part ($\mathrm{Im}\{d_\perp(\omega)\}$) is related to surface-enabled Landau damping [62] (see below). On the other hand, $\mathrm{Re}\{d_\parallel(\omega)\}$ represents the position of the centroid of the normal derivative of the electron current parallel to the metal surface.

The Feibelman parameters $d_\perp(\omega)$ and $d_\parallel(\omega)$ are surface-response functions inherent to a specific metal, but also dependent on the surrounding material [62]. Importantly, $d_\parallel(\omega)$ given by Eq. (2.82b) vanishes for charge-neutral planar surfaces [62, 304], and it is also expected to be much less important than $d_\perp(\omega)$ for curved surfaces [95]. In this thesis we thus consider $d_\parallel(\omega) = 0$, consistent with the approximation adopted in other studies [81, 124, 296, 300]. We show in Figure 2.9b the nondispersive Feibelman parameter $d_\perp(\omega)$ used in this section and in Chapter 3, obtained in ref. 296 for a sodium planar surface ($r_s = 4\ \mathrm{a_0}$) surrounded by vacuum[24]. The Feibelman parameter $d_\perp(\omega)$ in Figure 2.9b shows a resonance at $\omega \sim 4.7$ eV, associated with the excitation of the Bennet plasmon at $\omega \sim 0.8\omega_p$ [79, 305], also referred to as the multipole *surface* plasmon [62, 306] (not to be confused with localized multipole plasmons supported e.g. by spherical MNPs). Kramers-Kronig relations connect the real (blue line) and imaginary (red line) parts of $d_\perp(\omega)$ [307].

[24] Ref. 124 provides the parametrization to express the data of $d_\perp(\omega)$ obtained in ref. 296 within TDDFT as a sum of Lorentzian functions.

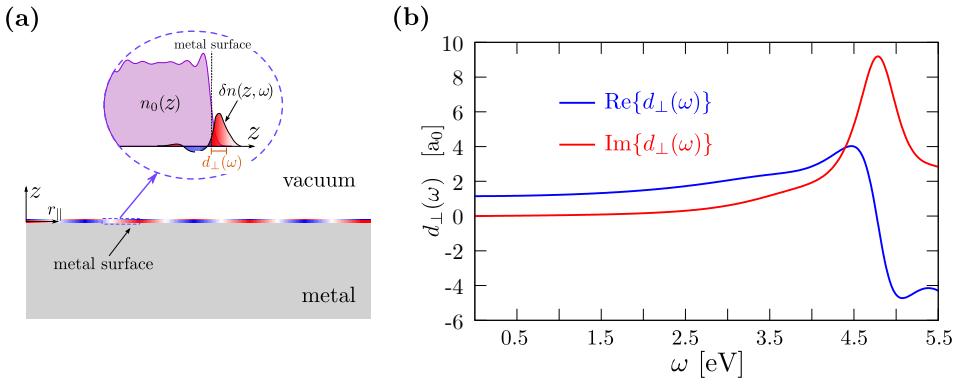

Figure 2.9: **(a)** Schematic representation of the nondispersive Feibelman parameter $d_\perp(\omega)$ in a planar metal–vacuum interface. $\mathrm{Re}\{d_\perp(\omega)\}$ corresponds to the position of the centroid of the induced charge $\delta n(z,\omega)$ with respect to the classical metal surface located at $z=0$. **(b)** Real (blue) and imaginary (red) parts of the nondispersive Feibelman parameter $d_\perp(\omega)$ obtained in ref. 296 for a planar sodium–vacuum interface. The parameter shown in panel (b) is used in this section and in Chapter 3, where we study quantum surface phenomena in the interaction between QEs and MNPs.

The advantage of the SRF is that, once the Feibelman parameters are obtained for a planar surface of a given material using quantum-mechanical methods, these parameters can in principle be applied to account semiclassically for quantum surface effects in the optical response of arbitrary-shaped MNPs. Within the semiclassical SRF, the electromagnetic problem is addressed by solving Maxwell's equations [Eq. (1.5)] with the use of local dielectric functions (e.g. a Drude dielectric function, Eq. (1.10)), and introducing a set of modified boundary conditions at the metal–dielectric interfaces that differ from those used within the classical LRA [Eqs. (1.16) and (1.18)]. $d_\perp(\omega)$ and $d_\parallel(\omega)$ can be related, respectively, to a surface polarization oriented perpendicularly to the interface and to a parallel surface current [97, 296] leading to the following modified boundary conditions (see also ref. 124):

$$\hat{\mathbf{n}}\times\left(\mathbf{E}_{\mathrm{out}}^{\mathrm{SRF}}-\mathbf{E}_{\mathrm{in}}^{\mathrm{SRF}}\right)=-d_\perp(\omega)\;\hat{\mathbf{n}}\times\nabla\left[\hat{\mathbf{n}}\cdot\left(\mathbf{E}_{\mathrm{out}}^{\mathrm{SRF}}-\mathbf{E}_{\mathrm{in}}^{\mathrm{SRF}}\right)\right], \tag{2.83a}$$

$$\hat{\mathbf{n}}\cdot\left(\mathbf{D}_{\mathrm{out}}^{\mathrm{SRF}}-\mathbf{D}_{\mathrm{in}}^{\mathrm{SRF}}\right)=d_\parallel(\omega)\;\nabla\cdot\left[\hat{\mathbf{n}}\times\left(\mathbf{D}_{\mathrm{out}}^{\mathrm{SRF}}-\mathbf{D}_{\mathrm{in}}^{\mathrm{SRF}}\right)\times\hat{\mathbf{n}}\right], \tag{2.83b}$$

$$\hat{\mathbf{n}}\times\left(\mathbf{H}_{\mathrm{out}}^{\mathrm{SRF}}-\mathbf{H}_{\mathrm{in}}^{\mathrm{SRF}}\right)=i\omega d_\parallel(\omega)\;\left[\hat{\mathbf{n}}\times\left(\mathbf{D}_{\mathrm{out}}^{\mathrm{SRF}}-\mathbf{D}_{\mathrm{in}}^{\mathrm{SRF}}\right)\times\hat{\mathbf{n}}\right], \tag{2.83c}$$

$$\hat{\mathbf{n}}\cdot\left(\mathbf{B}_{\mathrm{out}}^{\mathrm{SRF}}-\mathbf{B}_{\mathrm{in}}^{\mathrm{SRF}}\right)=0, \tag{2.83d}$$

where $\hat{\mathbf{n}}$ is the normal unit vector pointing outwards from the metal boundary, and the superscript "SRF" denotes that the fields are calculated within the semiclassical SRF. Note that, as mentioned above, we consider $d_\parallel(\omega)=0$, so that in practice we only consider the modifications introduced by Eq. (2.83a) into the boundary

conditions. The rest of the boundary conditions remain the same as in the classical LRA [Eqs. (1.16) and (1.18)].

In the following Subsection 2.5.1, we explain how we implement in this thesis the semiclassical SRF within the nonretarded approximation to obtain the optical response of spherical MNPs and their dimers.

2.5.1 Optical response of spherical nanostructures using the SRF

Within the nonretarded approximation, the semiclassical SRF can be straightforwardly implemented to obtain the optical response of spherical MNPs using the numerical method introduced in Subsection 1.1.3 with very little modifications. The optical response of the spherical MNPs of radius a is determined by the potential $\phi^{\text{ind}}_{\text{SRF}}(\mathbf{r},\omega)$ induced in response to an external potential $\phi^{\text{ext}}(\mathbf{r},\omega)$. According to Eq. (1.26), $\phi^{\text{ind}}_{\text{SRF}}(\mathbf{r},\omega)$ can be written in a spherical harmonic basis set $Y^m_\ell(\theta,\varphi)$,

$$\phi^{\text{ind}}_{\text{SRF}}(\mathbf{r},\omega)=\sum_{\ell=0}^{\infty}\sum_{m=-\ell}^{\ell} b^{\text{SRF}}_{\ell m}(\omega)Y^m_\ell(\theta,\varphi)\begin{cases} r^\ell/a^\ell & r\leq a \\ a^{\ell+1}/r^{\ell+1} & r\geq a \end{cases}. \tag{2.84}$$

The only difference between Eq. (2.84) and the one used within the classical LRA [Eq. (1.26)] is that the coefficients $b^{\text{SRF}}_{\ell m}(\omega)$ and $b_{\ell m}(\omega)$ are different. In this case, $b^{\text{SRF}}_{\ell m}(\omega)$ within the SRF are determined by applying the modified boundary conditions given by Eq. (2.83a) and Eq. (2.83b). For $d_\parallel(\omega)=0$, as considered in this thesis, Eqs. (2.83a) and (2.83b) can be written within the nonretarded approximation in terms of the total potential $\phi^{\text{SRF}}(\mathbf{r},\omega)=\phi^{\text{ext}}(\mathbf{r},\omega)+\phi^{\text{ind}}_{\text{SRF}}(\mathbf{r},\omega)$ [see Eq. (1.23)],

$$\nabla_\parallel\left(\phi^{\text{SRF}}_{\text{out}}-\phi^{\text{SRF}}_{\text{in}}\right)=-d_\perp(\omega)\,\nabla_\parallel\left[\hat{\mathbf{n}}\cdot\nabla\left(\phi^{\text{SRF}}_{\text{out}}-\phi^{\text{SRF}}_{\text{in}}\right)\right], \tag{2.85a}$$

$$\hat{\mathbf{n}}\cdot\nabla\phi^{\text{SRF}}_{\text{out}}=\varepsilon(\omega)\,\hat{\mathbf{n}}\cdot\nabla\phi^{\text{SRF}}_{\text{in}}, \tag{2.85b}$$

with $\nabla_\parallel$ the surface gradient operator [124]. Using Eq. (2.84) and Eq. (2.85) (here $\hat{\mathbf{n}}=\hat{\mathbf{r}}$) results in

$$b^{\text{SRF}}_{\ell m}(\omega)=\xi(\ell,\omega)\int d\tilde{\Omega}\,[Y^m_\ell(\theta,\varphi)]^*\frac{\partial}{\partial r}\phi^{\text{ext}}(\mathbf{r},\omega)\Big|_{r=a}, \tag{2.86}$$

where the integral extends over the solid angle $\tilde{\Omega}=\{\theta,\varphi\}$ and

$$\xi(\ell,\omega)=\frac{-a(\varepsilon(\omega)-1)(1+\ell d_\perp(\omega)/a)}{(\ell+1)(1+\ell d_\perp(\omega)/a)+\ell\varepsilon(\omega)(1-(\ell+1)d_\perp(\omega)/a)}. \tag{2.87}$$

Once the coefficients $b^{\text{SRF}}_{\ell m}(\omega)$ are determined from Eqs. (2.86) and (2.87), one can calculate the induced potential within the SRF using Eq. (2.84) and thus obtain the

optical response of the spherical MNP. In a similar way, the optical response of a spherical MNP dimer within the SRF can be obtained using the coupled-multipole method described in Subsection 1.1.3 but replacing Eq. (1.34) by Eq. (2.87).

As explained in Subsection 1.2.3, for plane-wave illumination $\phi^{\rm ext}(\mathbf{r},\omega) = -\mathrm{E}_0\, r\cos\theta$ [Eq. (1.43)] the integral in Eq. (2.86) has an analytical solution (which is non-null only for $\ell = 1$), and the polarizability $\alpha_{\rm SRF}(\omega)$ of the individual MNP within the SRF results in [see Eq. (1.45)]:

$$\alpha_{\rm SRF}(\omega) = a^3 \frac{(\varepsilon(\omega)-1)\,(1+d_\perp(\omega)/a)}{\varepsilon(\omega)+2-2\,(\varepsilon(\omega)-1)\,d_\perp(\omega)/a}. \tag{2.88}$$

We show in Figure 2.10a the absorption cross-section spectra $\sigma_{\rm abs}(\omega) = \frac{4\pi\omega}{c}\mathrm{Im}\{\alpha_{\rm SRF}(\omega)\}$ obtained within the semiclassical SRF [Eq. (2.88)] for individual spherical MNPs with different radius ranging from $a = 27.9$ a_0 (purple) to $a = 65.83$ a_0 (red). These MNPs sizes correspond to the ones considered in Figure 2.3 using TDDFT (panel a) and classical LRA (panel b) calculations. A single Lorentzian-like peak emerges for all MNP sizes considered in Figure 2.10a, associated with the excitation of the DP resonance. Importantly, the semiclassical SRF predicts a redshift of the frequency of the DP resonance $\omega_{\rm DP}^{\rm SRF}$ with decreasing size of the MNP, as well as an increase of the DP resonance width, $\kappa^{\rm SRF}$. These predictions are in agreement with the TDDFT results shown in Figure 2.3a, and can be directly inferred from the analytical expression of $\alpha_{\rm SRF}(\omega)$ given by Eq. (2.88): the frequency of the DP resonance $\omega_{\rm DP}^{\rm SRF}$ is determined from the poles of $\alpha_{\rm SRF}(\omega)$, while $\kappa^{\rm SRF}$ is given by the full width at half maximum (FWHM) [267],

$$\omega_{\rm DP}^{\rm SRF} = \frac{\omega_p}{\sqrt{3}}\left(1 - \mathrm{Re}\{d_\perp(\omega=\omega_{\rm DP}^{\rm SRF})\}/a\right), \tag{2.89a}$$

$$\kappa^{\rm SRF} = \gamma_p + 2\omega_{\rm DP}^{\rm SRF}\mathrm{Im}\{d_\perp(\omega=\omega_{\rm DP}^{\rm SRF})\}/a. \tag{2.89b}$$

The second term on the RHS of Eq. (2.89a) introduces a redshift of $\omega_{\rm DP}^{\rm SRF}$ due to the spill out of the induced charges that increases with reducing a as long as $\mathrm{Re}\{d_\perp(\omega=\omega_{\rm DP})\}$ is positive (Figure 2.9b, blue line). Moreover, the second term on the RHS of Eq. (2.89b) introduces an additional broadening produced by surface-enabled Landau damping that increases with reducing a, consistent with TDDFT results (see Subsection 2.3.1). However, the semiclassical SRF presented in this section is not designed to capture the discrete electronic levels of the small-sized quantum system, and thus the features associated with single electron–hole transitions naturally manifested within TDDFT for the smallest MNPs are not present in the SRF results (compare purple and brown curves in Figures 2.3a and 2.10a).

We analyze next the optical response of a spherical MNP dimer obtained within the semiclassical SRF. Figure 2.10b illustrates the absorption cross-section spectra $\sigma_{\rm abs}(\omega)$ of a dimer formed by two spherical MNPs of radius $a = 34.4$ a_0, where the gap separation is varied from $D = 16$ a_0 to $D = 40$ a_0. Taking the TDDFT results for $N_e = 638$ electrons as a reference (shown in Figure 2.5a), the semiclassical

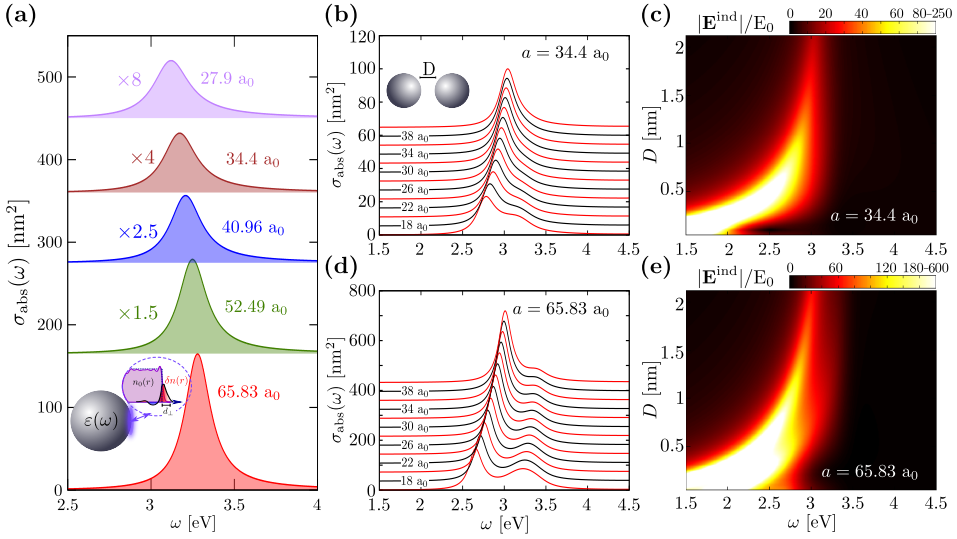

Figure 2.10: Semiclassical SRF study of the optical response of spherical MNPs and their dimers. **(a)** Absorption cross-section spectra, $\sigma_{\rm abs}(\omega)$, of individual spherical MNPs with different radius a obtained within the semiclassical SRF according to Eq. (1.49) and Eq. (2.88). $a = 27.9$ a$_0$ (purple), 34.4 a$_0$ (brown), 40.96 a$_0$ (blue), 52.49 a$_0$ (green), and 65.83 a$_0$ (red). **(b)** Absorption cross-section spectra $\sigma_{\rm abs}(\omega)$ of spherical MNP dimers with radius $a = 34.4$ a$_0$ for different size of the gap, D, ranging from $D = 16$ a$_0$ to $D = 40$ a$_0$. The external electric field is polarized along the dimer z-axis. **(c)** Induced electric-field enhancement $|\mathbf{E}|^{\rm ind}/\mathrm{E}_0$ in the middle of the gap formed by two MNPs with radius $a = 34.4$ a$_0$. Results are shown as a function of the frequency of the external plane-wave illumination, ω, and the surface-to-surface gap distance, D. **(d, e)** Same as in panels (b,c) but for larger MNPs with radius $a = 65.83$ a$_0$. In all the panels, we use the SRF with the nondispersive Feibelman parameter $d_\perp(\omega)$ obtained in ref. 296 for a planar sodium–vacuum interface. A plasma frequency $\omega_p = 5.89$ eV and a damping parameter $\gamma_p = 0.1$ eV are used to characterize sodium within the Drude model [Eq. (1.10)]. In **(c)** and **(d)**, the upper range of values in the color bar denote saturation.

SRF correctly reproduces the overall broadening of the spectra as well as the redfshift of the BDP resonance with decreasing D. Moreover, the BQP is hardly formed within the SRF due to surface-enabled Landau damping as predicted by TDDFT calculations (see further details in Chapter 3). However, the single-particle excitation features present in the TDDFT results are again absent in the SRF description. The agreement between SRF (Figure 2.10d) and TDDFT (Figure 2.5c) improves when considering larger MNPs with radius $a = 65.83$ a$_0$, since in this case $\sigma_{\rm abs}(\omega)$ within TDDFT does not exhibit single-particle excitation features associated with the finite size of the MNPs. The BQP is well developed within the two approaches in this case.

Finally, we show in Figures 2.10c and 2.10e that the SRF correctly describes the electric-field enhancement $|\mathbf{E}|^{\rm ind}/\mathrm{E}_0$ for relatively large junctions but that it fails for very narrow gaps $D \lesssim 0.5$ nm. For $D \gtrsim 0.5$ nm, i.e., for distances where electron tunneling does not play a significant role, the results obtained in Figures

2.10c,e within the SRF are qualitatively in good agreement with the TDDFT results shown in Figures 2.5g,i: both approaches predict an increase of the resonant field enhancement $|\mathbf{E}|^{\mathrm{ind}}/\mathrm{E}_0$ with reducing the gap down to $D \sim 0.5$ nm. However, for smaller gaps $D \lesssim 0.5$ nm, the semiclassical SRF (incorrectly) predicts a continuous enhancement of $|\mathbf{E}|^{\mathrm{ind}}/\mathrm{E}_0$ at the plasmon resonance when further reducing D because the SRF does not account for electron tunneling that neutralizes the large charge densities at the surfaces of both MNPs [83]. Thus, the semiclassical SRF cannot be used to simulate the optical response of plasmonic systems with subnanometric gap separations where electron tunneling becomes important. In this situations, fully quantum TDDFT calculations or other semiclassical descriptions such as the quantum-corrected model are needed [83–87].

2.6 Summary

In summary, we have described in this chapter the methodologies employed in this thesis to account for quantum many-body effects in the optical response of plasmonic nanostructures. First, we have reviewed the fundamentals of DFT and TDDFT, and focused on the WPP method used to obtain the dynamics of the electron density in real time under external time-dependent excitation. Next, we have briefly described the numerical implementation of the WPP-TDDFT algorithms for the specific geometries considered here, namely individual spherical MNPs and nanowires, as well as their dimers. Then, by analyzing the linear optical response of the studied nanostructures, we have introduced the main quantum many-body effects present in the interaction between light and MNPs, namely Friedel oscillations, electron spill out, surface-enabled Landau damping, and electron tunneling, which are found to dramatically modify the optical properties of the systems. We have also shown that the use of the TDDFT methodology in time domain allows us to directly address the nonlinear optical response of a system without using any *ad-hoc* parameter such as the nonlinear hyperpolarizabilities $\alpha^{(n)}$ introduced in Section 1.3. Finally, we have introduced the semiclassical SRF, a methodology capable of incorporating quantum surface phenomena such as electron spill out and surface-enabled Landau damping using computationally less-demanding calculations as compared to TDDFT, but incapable of accounting for other quantum effects such as electron tunneling in subnanometric gap separations. The methodologies and concepts explained in this chapter thus provide the basis of the quantum many-body approach to light–matter interaction and serve as a reference to study in the next chapters novel quantum many-body phenomena arising from the optical and electronic coupling between MNPs and QEs.

CHAPTER 3

QUANTUM SURFACE EFFECTS IN THE ELECTROMAGNETIC COUPLING BETWEEN QUANTUM EMITTERS AND METALLIC NANOPARTICLES

As discussed in Section 1.4, the absorption and emission rates of quantum emitters (QEs) are greatly increased due to their electromagnetic interaction with MNPs located nearby, leading to a plethora of interesting phenomena [182, 183, 308–311]. For example, the spontaneous decay rate and exciton energy of the QE are drastically modified, and hybrid plasmon–exciton polaritonic states can be created in the strong-coupling regime [180, 312–316]. As pointed out in previous chapters, the coupling between QEs and MNPs has been extensively used in a variety of applications, such as in surface-enhanced fluorescence [25–27], biosensing [317, 318], or single-molecule detection [28, 29], among others.

Together with the experimental progress, considerable theoretical effort has been devoted to accurately describing the electromagnetic QE–MNPs interaction, and several models at different levels of approximation have been adopted [105, 145, 169, 319–323]. In this chapter, we use the point-dipole approximation described in Subsection 1.4.1 to model the exciton dynamics of a QE [40, 45, 324, 325], and thus consider that the spatial extent of the QE is much smaller than the effective field localization of the plasmonic resonance [144, 172, 326–328], and that the electronic orbitals of the QE and those of the metal atoms forming the MNPs do not spatially overlap [107, 109, 329].

As described in Subsection 1.4.2, the electromagnetic QE–MNPs interaction can be described within the point-dipole approximation using the formalism of the *self-interaction* dyadic Green's function, $\hat{\mathbb{G}}(\mathbf{r}_{\mathrm{QE}}, \mathbf{r}_{\mathrm{QE}}, \omega)$ [40, 104, 169–172],

which in the weak-coupling regime determines the Purcell factor [101, 102] and Lamb shift [103, 104] in the emission by the QE produced by the plasmonic environment. Typically, a local dielectric function obtained experimentally or from simple theoretical approaches, such as the Drude model (Subsection 1.1.1), can be used to characterize the MNPs. However, such a dielectric function does not account for quantum phenomena relevant in MNPs of small characteristic dimensions such as electron spill-out, surface-enabled Landau damping, or nonlocal dynamical screening [10, 61, 64, 66, 96, 126, 209, 212, 219], introduced in Section 2.3 when analyzing the linear optical response of MNPs. These nonclassical phenomena, inherent to the quantum nature of electrons in metals, are also expected to influence the QE–MNPs electromagnetic interaction when small MNPs and QE–MNPs distances are considered [65, 124, 300, 330–336].

In this chapter, we use the TDDFT approach [58, 79, 80, 202, 210, 214, 337–341] based on the WPP method introduced in Chapter 2 to provide a fundamental description of the electromagnetic coupling between QEs and canonical MNPs. The QE–MNP separations are set sufficiently large so that electron tunneling is negligible and thus the electromagnetic interaction mainly determines the optical properties of the system. However, we consider QE–MNP separations small enough for the aforementioned quantum surface effects to be important. We first use TDDFT to calculate the self-interaction Green's function $\hat{\mathbb{G}}(\mathbf{r}_{\rm QE}, \mathbf{r}_{\rm QE}, \omega)$ that governs the QE–MNPs coupling. A comparison with classical LRA results (Subsection 1.1.1) reveals the importance of quantum effects. Further, we compare TDDFT results and the semiclassical nondispersive SRF (Section 2.5) that incorporates quantum surface-response corrections *via* the Feibelman parameter $d_\perp(\omega)$ obtained in the long-wavelength approximation, which allows us to identify surface-enabled Landau damping and spill-out of the induced electron density as the dominant quantum mechanisms dramatically influencing the electromagnetic QE–MNPs interaction.

TDDFT also provides a benchmark to establish the validity range of the (standard) *nondispersive* SRF to adequately account for the dominant quantum phenomena arising in the electromagnetic interaction between QEs and MNPs. The nondispersive SRF, as used in this chapter, neglects the nonlocal optical response in the direction parallel to the metal surface (long-wavelength limit), enabling a very efficient implementation of nonlocality in nanoscale geometries [97]. In this chapter, we identify situations of very small QE–MNP distances where the nondispersive implementation of the SRF eventually fails, indicating that the dispersion of the Feibelman parameters with respect to the wavenumber parallel to the surface needs to be considered (see Chapter 4).

3.1 System and methods

We analyze the electromagnetic coupling between a point-like QE and two different canonical plasmonic nanostructures. First, we consider in Subsections 3.2.1, 3.2.2, and 3.2.3 the case of an individual spherical MNP, where the QE is placed at a distance d from the MNP surface (Figure 3.1a). Then, in Subsection 3.2.4, we

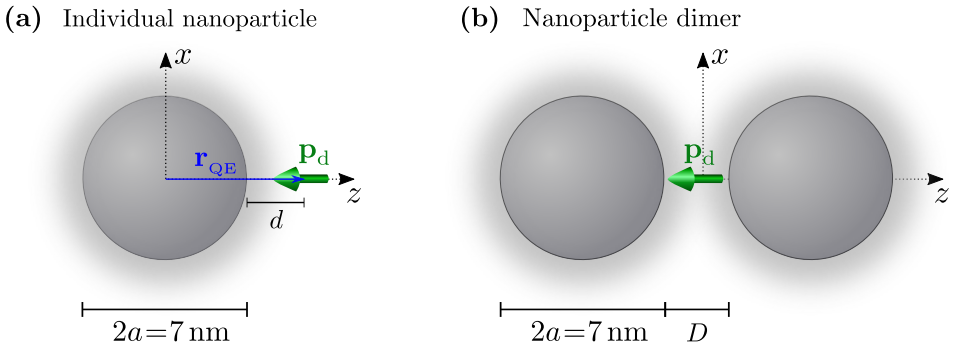

Figure 3.1: Sketch of the systems studied in this chapter, consisting of a QE modeled as a point dipole $\mathbf{p}_\mathrm{d}$ placed **(a)** at a distance d from the surface of an individual spherical MNP, and **(b)** at the center of a gap of size D formed by two identical spherical MNPs. The point dipole is oriented along the z-axis, which is also the axis of the dimer. Each MNP is represented within the free-electron jellium model using a Wigner–Seitz radius $r_s = 4$ a$_0$ that corresponds to sodium, and contains $N_e = 4458$ conduction electrons resulting in a radius $a = 65.83$ a$_0$ (≈ 3.5 nm).

analyze a dimer composed by two identical spherical MNPs separated by a gap distance D (Figure 3.1b), with the QE situated at the center of the gap ($z = 0$). We define the coordinates in the same way as in Subsections 2.3.1 and 2.3.2, such that the center of the nanoparticle(s) and the QE is at the z-axis. The entire system is surrounded by vacuum.

We consider closed-shell jellium MNPs of radius $a = 65.83$ a$_0$ (≈ 3.5 nm), which results in a well-developed plasmonic response [203] in the TDDFT simulations. The surface-to-emitter distance is sufficiently large to ensure that the electron densities of the MNPs at the position of the QE are negligible, and therefore there is no electron tunneling [43, 67, 68, 83, 86, 342]. Specifically, we consider surface-to-emitter distances d in the range of $d = 10 - 42$ a$_0$ ($\approx 0.5 - 2.2$ nm) for the case of the individual MNP, and gap separations of $D = 2d = 20 - 45$ a$_0$ ($\approx 1.1 - 2.4$ nm) for the dimer structure. We use the point-dipole approximation described in Subsection 1.4.1 to model the QE and thus neglect its spatial extent.

We focus on the study of the self-interaction Green's function $\hat{\mathbb{G}}(\mathbf{r}_\mathrm{QE}, \mathbf{r}_\mathrm{QE}, \omega)$ defined according to Eq. (1.56), which provides the electric field $\mathbf{E}^\mathrm{self}(\mathbf{r}_\mathrm{QE}, \omega)$ created by the metallic nanostructure at a position $\mathbf{r}_\mathrm{QE}$ in response to a point dipole $\mathbf{p}_\mathrm{d}$ located at the same position and oscillating at a frequency ω. Importantly, $\hat{\mathbb{G}}(\mathbf{r}_\mathrm{QE}, \mathbf{r}_\mathrm{QE}, \omega)$ determines the total decay rate (Γ) and the Lamb shift ($\Delta\omega_\mathrm{QE}$) of a QE that interacts weakly with the plasmonic nanostructure [104, 170–172],

$$\Gamma = \gamma_0 + \gamma_\mathrm{QE}^\mathrm{nr} + 2|\mu_\mathrm{QE}|^2 \mathrm{Im}\{\hat{\mathbf{k}} \cdot \hat{\mathbb{G}}(\mathbf{r}_\mathrm{QE}, \mathbf{r}_\mathrm{QE}, \omega = \omega_\mathrm{QE}) \cdot \hat{\mathbf{k}}\}, \tag{3.1a}$$

$$\Delta\omega_\mathrm{QE} = -|\mu_\mathrm{QE}|^2 \mathrm{Re}\{\hat{\mathbf{k}} \cdot \hat{\mathbb{G}}(\mathbf{r}_\mathrm{QE}, \mathbf{r}_\mathrm{QE}, \omega = \omega_\mathrm{QE}) \cdot \hat{\mathbf{k}}\}, \tag{3.1b}$$

with γ_0, $\gamma_\mathrm{QE}^\mathrm{nr}$ and μ_QE the spontaneous decay rate in vacuum, the non-radiative intrinsic loss rate, and the transition dipole moment of the QE along the $\hat{\mathbf{k}}$-direction,

respectively [22]. The self-interaction Green's function $\hat{\mathbb{G}}(\mathbf{r}_{\rm QE}, \mathbf{r}_{\rm QE}, \omega)$ in Eq. (3.1a) and Eq. (3.1b) is evaluated at the transition frequency of the QE, $\omega = \omega_{\rm QE}$. The unit vector $\hat{\mathbf{k}}$ defines the orientation of $\mathbf{p}_{\rm d}$. We note that the enhancement of the decay rate due to the QE–MNPs coupling is often normalized by γ_0, which gives the Purcell factor

$$\mathrm{F_P} = \frac{\Gamma - \gamma_{\rm QE}^{\rm nr}}{\gamma_0} = 1 + \frac{3c^3}{2\omega_{\rm QE}^3} \mathrm{Im}\{\hat{\mathbf{k}} \cdot \hat{\mathbb{G}}(\mathbf{r}_{\rm QE}, \mathbf{r}_{\rm QE}, \omega = \omega_{\rm QE}) \cdot \hat{\mathbf{k}}\}, \tag{3.2}$$

c being the speed of light in vacuum [102, 343].

We restrict our analysis to the case of a point dipole oriented along the z-axis, $\mathbf{p}_{\rm d} = \mathrm{p_d}\ \hat{\mathbf{z}}$, where $\hat{\mathbf{z}}$ is the unit vector along the z-axis. Moreover, we use $\mathbf{r}_{\rm QE} = r_{\rm QE}\ \hat{\mathbf{z}}$, so that $\hat{\mathbb{G}}(\mathbf{r}_{\rm QE}, \mathbf{r}_{\rm QE}, \omega)$ can be considered as a scalar, $\hat{\mathbb{G}}(\mathbf{r}_{\rm QE}, \mathbf{r}_{\rm QE}, \omega) \equiv G(\mathbf{r}_{\rm QE}, \mathbf{r}_{\rm QE}, \omega)$, because of the symmetry of our system. In the upcoming subsections, we briefly summarize the key aspects of the three different models used in this chapter to obtain $G(\mathbf{r}_{\rm QE}, \mathbf{r}_{\rm QE}, \omega)$, namely the TDDFT, the classical LRA, and the semiclassical SRF based on the nondispersive Feibelman parameters. Further details on the methodologies adopted in this chapter are provided in Chapters 1 and 2.

3.1.1 Time-dependent density functional theory (TDDFT)

In the TDDFT calculations we describe the MNPs within the jellium model of free-electron metals [194, 200] as introduced in Subsection 2.1.2. We use a Wigner–Seitz radius equal to that of sodium, $r_s = 4\ \mathrm{a_0}$, which allows us to use the values of the nondispersive Feibelman parameters obtained in ref. 296 (Figure 2.9b) to calculate $G(\mathbf{r}_{\rm QE}, \mathbf{r}_{\rm QE}, \omega)$ within the SRF and make the comparison between the TDDFT and SRF results. Note also that the DP resonance of sodium MNPs lies at optical frequencies ($\omega_{\rm DP} \sim 3$ eV, see Figure 2.3), very close to that of gold MNPs, thus placing the results within the frequency range relevant for actual applications in plasmonics. The closed-shell MNPs contain $N_e = 4458$ conduction electrons, which sets the radius of the background jellium edge to $a = 65.83\ \mathrm{a_0}$ (≈ 3.5 nm).

In order to obtain the self-interaction Green's function within TDDFT, $G_{\rm TDDFT}(\mathbf{r}_{\rm QE}, \mathbf{r}_{\rm QE}, \omega)$, we use the WPP method explained in Subsection 2.2.1 to solve the time-dependent KS equations given by Eqs. (2.19) and (2.20) in time domain, and to calculate the time evolution of the electron density $n(\mathbf{r}, t)$. Instead of Eq. (2.51) used to model plane-wave illumination in Chapter 2, the external potential $V_{\rm ext}(\mathbf{r}, t)$ that drives the system [Eq. (2.21)] is given in this chapter by an impulsive potential created by a point dipole,

$$V_{\rm ext}(\mathbf{r}, t) = -\mathrm{p_d}\ \Delta t\ \hat{\mathbf{z}} \cdot \frac{\mathbf{r} - \mathbf{r}_{\rm QE}}{|\mathbf{r} - \mathbf{r}_{\rm QE}|^3} \delta(t), \tag{3.3}$$

with $\delta(t)$ the Dirac delta function and the amplitude $\mathrm{p_d}$ sufficiently small to ensure a linear response. $V_{\rm ext}(\mathbf{r}, t)$ appears with a minus sign in Eq. (3.3) because it is acting on electrons with charge $q_{\rm e} = -1$. For the individual MNP, we employ

the method described in Subsection 2.3.1 and represent the occupied KS orbitals $\Psi_j(\mathbf{r},t)$ using a meshgrid in spherical coordinates, whereas for the dimer we adopt cylindrical coordinates as introduced in Subsection 2.3.2. The propagation time-step is $\Delta t \sim 0.05$ au.

The Hartree potential $V_{\mathrm{H}}[n(\mathbf{r},t)]$ [Eq. (2.23)] is calculated for the individual spherical MNP by expressing $V_{\mathrm{H}}[n(\mathbf{r},t)]$ as a sum of Legendre polynomials $P_\ell(\cos\theta)$,

$$V_{\mathrm{H}}[n(\mathbf{r},t)] = \sum_{\ell=0}^{\infty} \frac{1}{r} V_\ell(r,t) P_\ell(\cos\theta), \tag{3.4}$$

since the system subjected to the external potential $V_{\mathrm{ext}}(\mathbf{r},t)$ given by Eq. (3.3) possesses rotational symmetry with respect to the z-axis, and therefore the response is independent of the azimuthal angle φ. Using the Laplace operator ∇^2 in spherical coordinates [Eq. (1.24)], Poisson's equation given by Eq. (2.23) can be expressed as:

$$\sum_{\ell=0}^{\infty} \frac{1}{r} \underbrace{\left(\frac{d^2}{dr^2} - \frac{\ell(\ell+1)}{r^2} \right)}_{\mathbb{A}_\ell} V_\ell(r,t) P_\ell(\cos\theta) = -4\pi \sum_{\ell=0}^{\infty} n_\ell(r,t) P_\ell(\cos\theta), \tag{3.5}$$

where

$$n_\ell(r,t) = \frac{2}{2\ell+1} \int_{-1}^{1} \left(n(\mathbf{r},t) - n_+ \right) P_\ell(\cos\theta) d(\cos\theta), \tag{3.6}$$

and we express the operator $\mathbb{A}_\ell = \left(\frac{d^2}{dr^2} - \frac{\ell(\ell+1)}{r^2} \right)$ in matrix form using the method of the Fourier grid Hamiltonian with sine basis functions [344]. From Eq. (3.5), $V_\ell(r,t)$ can then be directly obtained from

$$V_\ell(r,t) = -4\pi \mathbb{A}_\ell^{-1} \Big(r \; n_\ell(r,t) \Big). \tag{3.7}$$

For the dimer geometry we obtain $V_{\mathrm{H}}[n(\mathbf{r},t)]$ following the procedure described in Subsection 2.3.2 [75].

Finally, we calculate the time-dependent electric field $\mathbf{E}^{\mathrm{ind}}(\mathbf{r} = \mathbf{r}_{\mathrm{QE}}, t)$ induced by the metallic nanostructure at the position $\mathbf{r}_{\mathrm{QE}}$ of the QE using $V_{\mathrm{H}}[n(\mathbf{r},t)]$ according to Eq. (2.34). The time-to-frequency Fourier transform [Eq. (2.36)] finally leads to the frequency-resolved self-interaction Green's function [compare to Eq. (1.56)],

$$G_{\mathrm{TDDFT}}(\mathbf{r}_{\mathrm{QE}}, \mathbf{r}_{\mathrm{QE}}, \omega) = \frac{1}{\mathrm{p_d} \Delta t} \underbrace{\int_0^{\mathrm{T_f}} dt \; \mathbf{E}^{\mathrm{ind}}(\mathbf{r}_{\mathrm{QE}}, t) \; e^{i(\omega + i\eta/2)t}}_{\mathbf{E}^{\mathrm{self}}(\mathbf{r}_{\mathrm{QE}}, \omega)}, \tag{3.8}$$

where $\mathrm{T_f} = 3500$ au is the total propagation time used in our simulations (enough to achieve convergence), and $\eta = 0.07$ eV accounts for relaxation processes beyond

the ALDA-TDDFT description [241, 242] of the many-body dynamics such as the interaction of excited electrons with phonons and many-body inelastic electron–electron scattering events (see Sections 2.2 and 2.3).

3.1.2 Classical local-response approximation (LRA)

The classical self-interaction Green's function, $G_{\mathrm{LRA}}(\mathbf{r}_{\mathrm{QE}}, \mathbf{r}_{\mathrm{QE}}, \omega)$, is obtained within the (nonretarded) local-response approximation (LRA) using the methodology described in Subsection 1.1.3 for the external potential given by Eq. (1.53), $\phi_{\mathrm{QE}}(\mathbf{r}) = \mathrm{p}_{\mathrm{QE}}\hat{\mathbf{z}} \cdot \frac{\mathbf{r}-\mathbf{r}_{\mathrm{QE}}}{|\mathbf{r}-\mathbf{r}_{\mathrm{QE}}|^3}$. The specific details to obtain $G_{\mathrm{LRA}}(\mathbf{r}_{\mathrm{QE}}, \mathbf{r}_{\mathrm{QE}}, \omega)$ for both the individual spherical MNP and the dimer are given in Subsection 1.4.2. In this chapter, we use a Drude-type local dielectric function $\varepsilon(\omega)$ to characterize the metal [Eq. (1.10)], with a plasma frequency $\omega_p = \sqrt{\frac{3}{r_s^3}} = 5.89$ eV and intrinsic damping parameter $\gamma_p = 0.1$ eV. The value of parameter γ_p is obtained from the comparison of the absorption spectrum $\sigma_{\mathrm{abs}}(\omega)$ of the individual spherical MNP calculated with TDDFT and with the SRF, as detailed in the following Subsection 3.1.3.

In the case of a point-like QE at position $\mathbf{r}_{\mathrm{QE}}$ oriented in the radial direction and exciting the individual MNP of radius a, the self-interaction Green's function is given by Eq. (1.58a) [145]

$$G_{\mathrm{LRA}}(\mathbf{r}_{\mathrm{QE}}, \mathbf{r}_{\mathrm{QE}}, \omega) = \sum_{\ell=1}^{\infty} (\ell+1)^2 \frac{a^{2\ell+1}}{R^{2\ell+4}} \frac{\varepsilon(\omega)-1}{\varepsilon(\omega)+\frac{\ell+1}{\ell}}, \tag{3.9}$$

with R the distance between the position $\mathbf{r}_{\mathrm{QE}}$ of the QE and the center of the MNP, and ℓ the multipole order of the plasmonic resonance.

3.1.3 Semiclassical surface-response formalism (SRF)

The semiclassical SRF employed in this chapter is based on the nondispersive Feibelman parameter $d_\perp(\omega)$ given by Eq. (2.82a) [95, 98], a (frequency-dependent) complex-valued function that allows for incorporating quantum surface effects into an otherwise classical description. Indeed, $\mathrm{Re}\{d_\perp(\omega)\}$ determines the position of the centroid of the induced charge density with respect to the positive jellium edge of the metal, and $\mathrm{Im}\{d_\perp(\omega)\}$ accounts for surface-enabled Landau damping [62]. As explained in Section 2.5, in this chapter we consider $d_\parallel(\omega) = 0$ [Eq. (2.82b)] and use the nondispersive parameter $d_\perp(\omega)$ obtained by Christensen *et al.* [296] within the jellium model (Figure 2.9b) for a semi-infinite planar metal surface with $r_s = 4$ a_0 (see also ref. 124). Using the parameter $d_\perp(\omega)$ obtained for planar surfaces is a reasonable approximation when the radius of curvature of the nanostructure or the typical length of the variation of the external potential along the surface is much larger than the Feibelman parameter. One of the objectives of this chapter is indeed to test the validity of this approximation for situations where the radius of curvature of the system is small and the external potential along the metal surface

(here created by the point-dipole QE) varies rapidly.

Similarly to the classical LRA, within the semiclassical SRF one can obtain an analytical solution of the nonretarded self-interaction Green's function in the present system, $G_{\mathrm{SRF}}(\mathbf{r}_{\mathrm{QE}}, \mathbf{r}_{\mathrm{QE}}, \omega)$. The expression for $G_{\mathrm{SRF}}(\mathbf{r}_{\mathrm{QE}}, \mathbf{r}_{\mathrm{QE}}, \omega)$ can be obtained from Eq. (2.86) and Eq. (2.87) considering the external potential $\phi^{\mathrm{ext}}(\mathbf{r}, \omega) \equiv \phi_{\mathrm{QE}}(\mathbf{r})$ of a point dipole given by Eq. (1.53), which results in (for $d_{\parallel}(\omega) = 0$) [95, 124]:

$$G_{\mathrm{SRF}}(\mathbf{r}_{\mathrm{QE}}, \mathbf{r}_{\mathrm{QE}}, \omega) = \sum_{\ell=1}^{\infty} (\ell+1)^2 \frac{a^{2\ell+1}}{R^{2\ell+4}} \frac{(\varepsilon(\omega)-1)\left(1+\frac{\ell}{a} d_{\perp}(\omega)\right)}{\varepsilon(\omega) + \frac{\ell+1}{\ell} - (\varepsilon(\omega)-1)\frac{\ell+1}{a} d_{\perp}(\omega)}. \quad (3.10)$$

For $d_{\perp}(\omega)/a \to 0$, i.e., for situations where the radius of the MNP a is much larger than the surface-response correction $d_{\perp}(\omega)$, Eq. (3.10) reduces to the classical LRA expression of $G_{\mathrm{LRA}}(\mathbf{r}_{\mathrm{QE}}, \mathbf{r}_{\mathrm{QE}}, \omega)$ given by Eq. (3.9).

The value of the damping parameter γ_p used in the Drude-type dielectric function $\epsilon(\omega)$ [Eq. (1.10)] for the classical LRA as well as for the SRF results is obtained from the fitting of the absorption cross-section spectrum $\sigma_{\mathrm{abs}}(\omega)$ of the individual MNP calculated within TDDFT to the result obtained within the nondispersive SRF. The absorption cross section $\sigma_{\mathrm{abs}}(\omega)$ within TDDFT is calculated using the methodology described in Subsection 2.3.1 for plane-wave illumination [given by Eq. (2.51)], and the SRF value is obtained using the polarizability $\alpha_{\mathrm{SRF}}(\omega)$ given by Eq. (2.88). Figure 3.2 shows very good agreement between the TDDFT results (solid blue line) and the nondispersive SRF (dashed red line) when using $\gamma_p = 0.1$ eV, thus justifying the value of γ_p used in this chapter.

For simplicity, in the following we generically use $G(\mathbf{r}_{\mathrm{QE}}, \mathbf{r}_{\mathrm{QE}}, \omega)$ to refer to any of $G_{\mathrm{TDDFT}}(\mathbf{r}_{\mathrm{QE}}, \mathbf{r}_{\mathrm{QE}}, \omega)$, $G_{\mathrm{LRA}}(\mathbf{r}_{\mathrm{QE}}, \mathbf{r}_{\mathrm{QE}}, \omega)$, and $G_{\mathrm{SRF}}(\mathbf{r}_{\mathrm{QE}}, \mathbf{r}_{\mathrm{QE}}, \omega)$. The methodology used to calculate $G(\mathbf{r}_{\mathrm{QE}}, \mathbf{r}_{\mathrm{QE}}, \omega)$ will be clear in the context of each subsection.

3.2 Results and discussion

In this section, we present the results for the electromagnetic coupling between a QE and spherical metallic nanostructures. First, in Subsection 3.2.1, we focus on the role of quantum phenomena by comparing quantum TDDFT and classical LRA results for a QE in proximity to an individual spherical MNP. Then, in Subsection 3.2.2, we compare results of TDDFT and the semiclassical nondispersive SRF for the same system. In Subsection 3.2.3, we use the nondispersive SRF to analyze the origin of the observed quantum effects, and discuss the validity range and shortcomings of the long-wavelength Feibelman paramater $d_{\perp}(\omega)$ that neglects the nonlocality of the optical response in the direction parallel to the metal surface. Finally, in Subsection 3.2.4, we extend the analysis to the case of a dimer of two identical spherical MNPs, showing that the quantum surface effects observed for the individual MNP are also manifested in the dimer configuration and that the

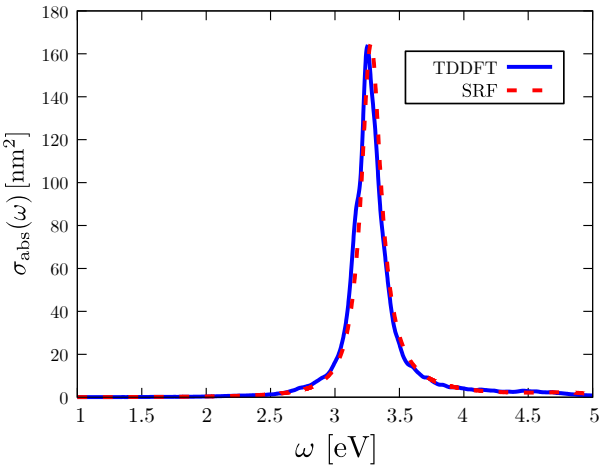

Figure 3.2: Comparison between the absorption cross-section spectra $\sigma_{\rm abs}$ obtained from TDDFT calculations within the jellium model using a Wigner–Seitz radius $r_s = 4$ a$_0$ (solid blue line), and from the nondispersive SRF using a plasma frequency $\omega_p = 5.89$ eV and intrinsic damping parameter $\gamma_p = 0.1$ eV in the Drude dielectric function given by Eq. (1.10) (dashed red line). The nondispersive SRF results are obtained from Eq. (2.88), and the TDDFT results are obtained following the procedure described in Subsection 2.3.1. An attenuation factor $\eta = 0.07$ eV [Eq. (2.56)] is used to perform the Fourier transform within TDDFT.

nondispersive SRF does not describe accurately situations of gap distances narrower than $D \sim 1.5$ nm for the present dimer geometry.

3.2.1 Quantum TDDFT vs. classical LRA

We first analyze the quantum effects that influence the self-interaction Green's function $G(\mathbf{r}_{\rm QE}, \mathbf{r}_{\rm QE}, \omega)$ obtained for a QE placed in front of an individual spherical MNP. The QE is oriented in the radial direction perpendicular to the MNP surface (see sketch in Figure 3.1a). To identify the quantum effects, we first compare in Figure 3.3 the classical LRA (panels a,b) and the TDDFT (panels c,d) results. We plot both the imaginary (a,c) and real (b,d) parts of $G(\mathbf{r}_{\rm QE}, \mathbf{r}_{\rm QE}, \omega)$ which are related to the Purcell factor and Lamb shift, respectively [Eqs. (3.1a) and (3.1b)]. Results are shown as a function of the oscillation frequency of the QE, ω, and the distance d between the QE and the surface of the spherical MNP, $d = R - a$.

The classical LRA calculations predict a dependence of $G(\mathbf{r}_{\rm QE}, \mathbf{r}_{\rm QE}, \omega)$ on frequency determined by various multipolar plasmon modes excited by the QE, resulting in several peaks in the spectra of $\mathrm{Im}\{G(\mathbf{r}_{\rm QE}, \mathbf{r}_{\rm QE}, \omega)\}$ (Figure 3.3a). The three lower-frequency sharp resonances are associated with the dipolar (DP, $\ell = 1$), quadrupolar (QP, $\ell = 2$), and octupolar (OP, $\ell = 3$) plasmons of the spherical MNP. Their frequencies ω_ℓ are given by the poles of Eq. (3.9), $\mathrm{Re}\left\{\epsilon(\omega_\ell) + \frac{\ell+1}{\ell}\right\} = 0$. As

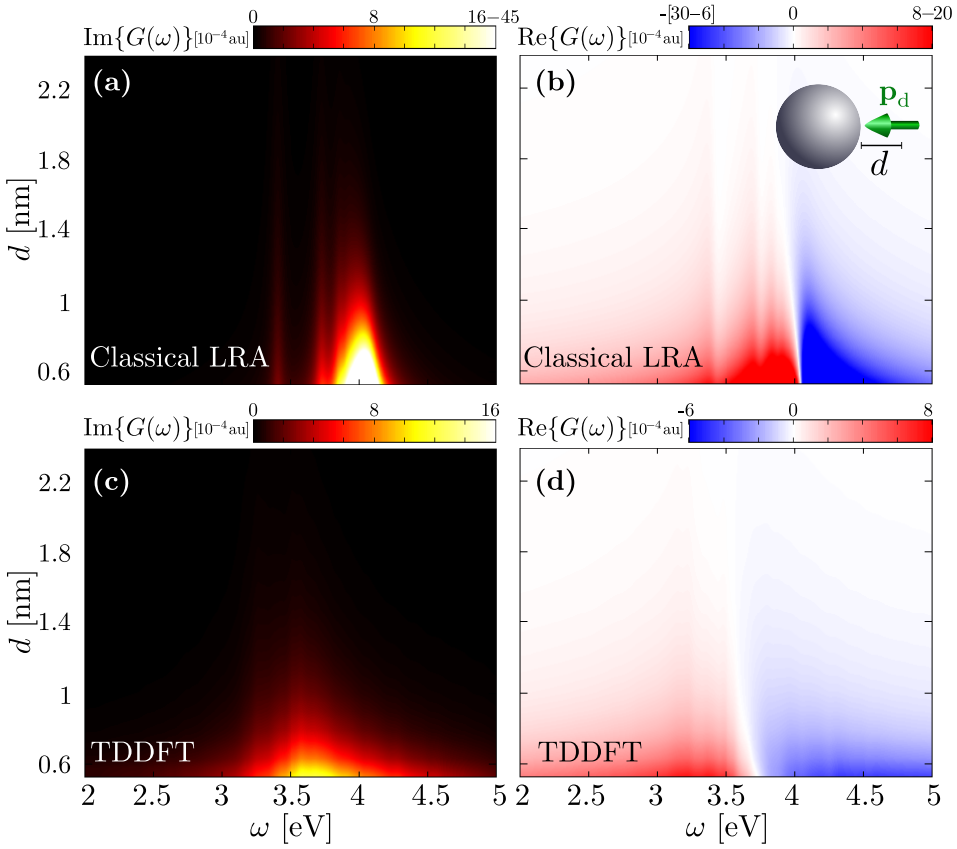

Figure 3.3: **(a)** Classical LRA result of the **(a)** imaginary part ($\mathrm{Im}\{G(\mathbf{r}_{\mathrm{QE}}, \mathbf{r}_{\mathrm{QE}}, \omega)\}$), and **(b)** real part ($\mathrm{Re}\{G(\mathbf{r}_{\mathrm{QE}}, \mathbf{r}_{\mathrm{QE}}, \omega)\}$) of the self-interaction Green's function $G(\mathbf{r}_{\mathrm{QE}}, \mathbf{r}_{\mathrm{QE}}, \omega)$ obtained for a point-like QE placed in front of an individual spherical MNP of radius $a = 65.83$ a$_0$ (≈ 3.5 nm). Results are shown as a function of the frequency ω of the oscillating QE and the surface-to-emitter distance, d. Panels **(c)** and **(d)** correspond to the results obtained with TDDFT simulations. In **(a)** and **(b)**, the upper and lower range of values in the color bar denote saturation.

we consider a metal described with a Drude dielectric function, this results in

$$\omega_\ell = \omega_p \sqrt{\frac{\ell}{2\ell + 1}}. \tag{3.11}$$

From Eq. (3.11) it follows that the frequencies of the DP, QP and OP are respectively $\omega_{\mathrm{DP}} \approx 3.4$ eV, $\omega_{\mathrm{QP}} \approx 3.7$ eV, and $\omega_{\mathrm{OP}} \approx 3.85$ eV. The high-frequency broad peak at $\omega_{\mathrm{PSM}} \sim 4$ eV (i.e., close to the surface plasmon frequency $\omega_{\mathrm{SP}} = \omega_p/\sqrt{2} \approx 4.16$ eV) corresponds to the so-called *pseudomode* [143], which is composed by a pilling up of several overlapping high-order plasmonic modes ($\ell = 4, 5, 6, \dots$) with closely-spaced resonant frequencies.

At small $d \approx 0.53 - 1$ nm, $\mathrm{Im}\{G(\mathbf{r}_{\mathrm{QE}}, \mathbf{r}_{\mathrm{QE}}, \omega)\}$, as calculated within the classical LRA, is dominated by the pseudomode excitation. As the distance between the QE and the MNP increases, $\mathrm{Im}\{G(\mathbf{r}_{\mathrm{QE}}, \mathbf{r}_{\mathrm{QE}}, \omega)\}$ decreases, and the relative contribution of different plasmon modes changes in favor of the low ℓ resonances (this behavior can be seen more clearly in Figure 3.4). Thus, for large $d \sim 1.6-1.8$ nm, the values of $\mathrm{Im}\{G(\mathbf{r}_{\mathrm{QE}}, \mathbf{r}_{\mathrm{QE}}, \omega)\}$ attained within the pseudomode frequency range become comparable to those at the sharp DP and QP resonances. The faster decrease of the resonances associated with high-order plasmon modes with increasing d can be inferred from Eq. (3.9), where $R = a+d$. We also note that the value of $\mathrm{Im}\{G(\mathbf{r}_{\mathrm{QE}}, \mathbf{r}_{\mathrm{QE}}, \omega)\}$ obtained for a QE resonant with the pseudomode at $\omega_{\mathrm{PSM}} = 4.05$ eV and located at $d = 0.58$ nm corresponds to a Purcell factor $\mathrm{F_P} \approx 5.2 \times 10^6$ [Eq. (3.2)]. This very large value is explained by the small volume of the MNP (and the resulting strong field localization).

In contrast to the classical results, $\mathrm{Im}\{G(\mathbf{r}_{\mathrm{QE}}, \mathbf{r}_{\mathrm{QE}}, \omega)\}$ as calculated with TDDFT (Figure 3.3c) mainly reveals a single broad feature [345] for the range of distances considered in this chapter. At small separation $d \approx 0.53 - 1$ nm, the maximum value of $\mathrm{Im}\{G(\mathbf{r}_{\mathrm{QE}}, \mathbf{r}_{\mathrm{QE}}, \omega)\}$ is reached within the frequency interval $\omega \sim 3.6 - 3.7$ eV, i.e., it is redshifted with respect to the classical pseudomode peak. As d increases, the resonant feature slightly shifts to lower frequencies. Moreover, the overall profile somewhat sharpens, albeit, in sheer contrast with the classical theory, the contributions of different plasmon modes remain spectrally broader and are barely resolved. Consistent with the strong broadening of the plasmon resonances due to quantum effects, the TDDFT results show smaller values of $\mathrm{Im}\{G(\mathbf{r}_{\mathrm{QE}}, \mathbf{r}_{\mathrm{QE}}, \omega)\}$ at resonance, and thus lower QE decay rates, as compared to the classical LRA prediction. For example, for a QE placed at a distance $d = 0.58$ nm, the resonant Purcell factor $\mathrm{F_P}$ calculated within TDDFT is $\mathrm{F_P} \approx 1.5 \times 10^6$. This is more than three times smaller than the maximum LRA value. On the other hand, the broadening of the spectra leads to a larger off-resonant $\mathrm{Im}\{G(\mathbf{r}_{\mathrm{QE}}, \mathbf{r}_{\mathrm{QE}}, \omega)\}$ obtained with TDDFT as compared to classical LRA predictions.

We next compare the classical LRA and quantum TDDFT results for the real part of the self-interaction Green's function, $\mathrm{Re}\{G(\mathbf{r}_{\mathrm{QE}}, \mathbf{r}_{\mathrm{QE}}, \omega)\}$, which determines the Lamb shift $\Delta\omega_{\mathrm{QE}}$ of the QE transition frequency [Eq. (3.1b)]. As depicted in Figure 3.3b, and consistent with the results obtained for the imaginary part of the Green's function (Figure 3.3a), the frequency dependence of $\mathrm{Re}\{G(\mathbf{r}_{\mathrm{QE}}, \mathbf{r}_{\mathrm{QE}}, \omega)\}$ obtained from classical LRA calculations features a rich resonance profile. For an individual plasmonic mode, the Kramers-Kronig relations would lead to a sign change of $\mathrm{Re}\{G(\mathbf{r}_{\mathrm{QE}}, \mathbf{r}_{\mathrm{QE}}, \omega)\}$ at the resonance frequency. In the full calculations, $\mathrm{Re}\{G(\mathbf{r}_{\mathrm{QE}}, \mathbf{r}_{\mathrm{QE}}, \omega)\}$ does not show the sign change at resonance for low ℓ modes and small distances, because of the off-resonant contribution associated with neighboring plasmon modes with larger ℓ. It is only at the pseudomode frequency that the contribution of the nearly degenerate resonances leads to a change of sign of $\mathrm{Re}\{G(\mathbf{r}_{\mathrm{QE}}, \mathbf{r}_{\mathrm{QE}}, \omega)\}$ from positive values at frequencies below $\omega_{\mathrm{PSM}} \sim 4$ eV to negative values above this frequency. When d increases, the contribution from off-resonant neighboring modes is reduced so that, in addition to the pseudomode

resonance, the sign change of $\mathrm{Re}\{G(\mathbf{r}_{\mathrm{QE}}, \mathbf{r}_{\mathrm{QE}}, \omega)\}$ can be observed at the DP and QP resonances. This appears particularly clear in Figure 3.4 discussed below, where we show the frequency dependence of the Green's function calculated for a set of fixed separations, d, between the QE and the MNP surface.

Similarly to the results obtained for the imaginary part, the TDDFT calculations in Figure 3.3d show smaller absolute values of $\mathrm{Re}\{G(\mathbf{r}_{\mathrm{QE}}, \mathbf{r}_{\mathrm{QE}}, \omega)\}$ (Lamb shift) and a broader structure at the resonant plasmon frequency $\omega \sim 3.3 - 3.7$ eV as compared to the classical LRA. This holds for the entire distance d range considered in this chapter. Notably, a single broad resonance is appreciated in the TDDFT results, and $\mathrm{Re}\{G(\mathbf{r}_{\mathrm{QE}}, \mathbf{r}_{\mathrm{QE}}, \omega)\}$ changes its sign from positive to negative only at the resonant frequency $\omega \sim 3.3 - 3.7$ eV, i.e. at lower frequency than within the classical LRA. As a consequence, for QEs with transition frequencies within the range of $\omega_{\mathrm{QE}} \sim 3.7 - 4$ eV, each model predicts a photonic Lamb shift $\Delta\omega_{\mathrm{QE}} \propto \mathrm{Re}\{G(\mathbf{r}_{\mathrm{QE}}, \mathbf{r}_{\mathrm{QE}}, \omega = \omega_{\mathrm{QE}})\}$ of opposite sign [Eq. (3.1b)]. For example, according to the LRA, a QE located at $d = 0.58$ nm and characterized by a transition dipole moment $\mu_{\mathrm{QE}} = 0.1\ e$ nm and resonant frequency $\omega_{\mathrm{QE}} = 4$ eV experiences a redshift of $\Delta\omega_{\mathrm{QE}} \approx -130$ meV. In contrast, TDDFT predicts a blueshift of $\Delta\omega_{\mathrm{QE}} \approx 34$ meV under the same conditions.

3.2.2 Quantum TDDFT vs. semiclassical nondispersive SRF

After identifying the main quantum-mechanical effects in Figure 3.3, we can use the nondispersive SRF to dissect the role of nonlocality and the spill-out of the induced charges that can be behind the differences between the classical LRA and TDDFT results of $G(\mathbf{r}_{\mathrm{QE}}, \mathbf{r}_{\mathrm{QE}}, \omega)$ discussed above. To this end, we compare in Figure 3.4 the real part (upper panels a-e) and the imaginary part (lower panels f-j) of $G(\mathbf{r}_{\mathrm{QE}}, \mathbf{r}_{\mathrm{QE}}, \omega)$ as calculated using the three different approaches (TDDFT, LRA, and SRF). Results are shown as a function of the oscillation frequency of the QE, for selected values of the surface-to-emitter distance d. The solid and dashed blue lines show the reference TDDFT results and those obtained using the nondispersive SRF, respectively. The classical LRA results are plotted by gray-dotted lines. The overall good agreement between the TDDFT and the nondispersive SRF in Figure 3.4 establishes the validity of the latter and allows us to use the framework of the SRF to analyze the role of the quantum phenomena manifested in $G(\mathbf{r}_{\mathrm{QE}}, \mathbf{r}_{\mathrm{QE}}, \omega)$, as we discuss below.

We first focus on the results at relatively large distance $d = 1.38 - 2.22$ nm (panels a-c and f-h), where the agreement between the nondispersive SRF and TDDFT is particularly good. The semiclassical SRF accurately reproduces the TDDFT results of the spectral position and resonance profile of $G(\mathbf{r}_{\mathrm{QE}}, \mathbf{r}_{\mathrm{QE}}, \omega)$, thus correctly accounting for the redshift and larger broadening of the peaks as compared to the classical LRA. On the other hand, for distances below $d \leq 0.95$ nm (panels d,e and i,j), the nondispersive SRF results are redshifted with respect to those of TDDFT, i.e., the semiclassical model based on the long-wavelength approximation of $d_{\perp}(\omega)$ overestimates the redshift of the plasmonic modes from

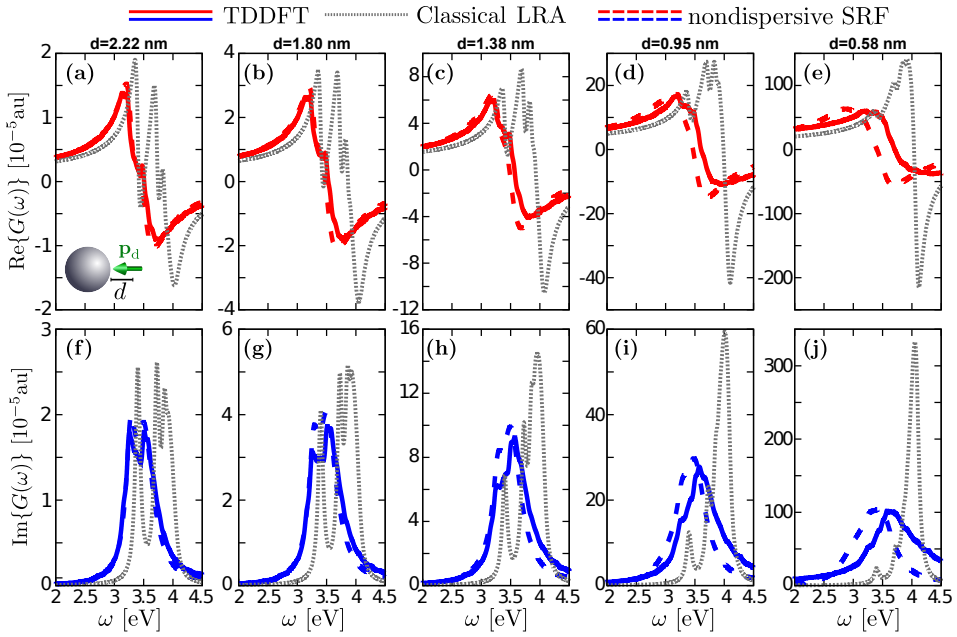

Figure 3.4: Real part (upper panels **a-e**) and imaginary part (lower panels **f-j**) of the self-interaction Green's function obtained for a point-like dipole in proximity to an individual spherical MNP of radius $a = 65.83$ a$_0$ (≈ 3.5 nm) made of sodium, as calculated from TDDFT (solid lines), within the nondispersive SRF (dashed lines) and within the classical LRA (dotted gray lines). Each panel corresponds to a selected surface-to-emitter distance d, ranging from $d = 0.58$ nm (rightmost panels) to $d = 2.22$ nm (leftmost panels), according to the labels on top.

the resonant frequencies obtained within the LRA as d decreases. The differences between the TDDFT and nondispersive SRF increase when reducing surface-to-emitter distance, d. Thus, based on this comparison, we conclude that for small d the calculations based on the long-wavelength Feibelman parameters provide a qualitative agreement with TDDFT, but not quantitative accuracy.

3.2.3 Interpretation of the quantum effects within the nondispersive SRF and its limitations

The overall good agreement as well as the discrepancy for small separation between the TDDFT and SRF results can be understood from the analytical SRF expression of $G(\mathbf{r}_{\rm QE}, \mathbf{r}_{\rm QE}, \omega)$. The resonant frequencies ω_ℓ can be found from the poles of Eq. (3.10),

$$\mathrm{Re}\left\{\varepsilon(\omega_\ell) + \frac{\ell+1}{\ell} - (\varepsilon(\omega_\ell) - 1)\frac{\ell+1}{a} d_\perp(\omega_\ell)\right\} = 0, \tag{3.12}$$

so that, for a Drude-type dielectric function [Eq. (1.10)], ω_ℓ can be obtained from the following expression:

$$\omega_\ell^2 \approx \omega_p^2 \frac{\ell}{2\ell+1}\Big(1 - \underbrace{\frac{(\ell+1)}{a}\mathrm{Re}\left\{d_\perp(\omega_\ell)\right\}}_{\substack{\text{spill-out of the}\\ \text{induced electron density}}}\Big), \tag{3.13}$$

where $\omega_\ell >> \gamma_p$ is assumed. For the sodium jellium material considered here, where interband transitions are negligible, the finite electrostatic potential barrier at the jellium surface allows for the induced electron density to spill out of the metal boundary, giving rise to positive values of $\mathrm{Re}\left\{d_\perp(\omega)\right\}$ in the frequency range of interest [296]. The positive $\mathrm{Re}\left\{d_\perp(\omega)\right\}$ decreases the value of ω_ℓ in Eq. (3.13), and one can thus conclude that the spill-out of the induced electron density is responsible for the redshift of all the resonant frequencies ω_ℓ, as compared to the LRA values given by Eq. (3.11). This redshift is larger for plasmonic modes of higher order ℓ.

To illustrate this discussion, we show in Figure 3.5a the resonant frequencies ω_ℓ of the first ten plasmonic modes ($\ell = 1-10$) of the individual spherical MNP as obtained from the LRA (Eq. (3.11), red dots), the TDDFT (orange dots) and the nondispersive SRF (Eq. (3.13), blue dots). For simplicity, we calculate the SRF values of ω_ℓ as the frequency at which the imaginary part of the corresponding ℓ-contribution to $G(\mathbf{r}_{\mathrm{QE}}, \mathbf{r}_{\mathrm{QE}}, \omega)$, $G_\ell(\mathbf{r}_{\mathrm{QE}}, \mathbf{r}_{\mathrm{QE}}, \omega)$, is maximum [Eq. (3.10)], and we have checked that the results are consistent with Eq. (3.13). The TDDFT results of the resonant frequency ω_ℓ are defined here as the mean value between the two frequencies at which $\mathrm{Im}\{G_\ell(\mathbf{r}_{\mathrm{QE}}, \mathbf{r}_{\mathrm{QE}}, \omega)\}$ is half of the maximum value.

The results in Figure 3.5a show good agreement between the TDDFT and the nondispersive SRF for the first four resonant frequencies ω_ℓ ($\ell \leq 4$), which explains the match in the spectral position of $G(\mathbf{r}_{\mathrm{QE}}, \mathbf{r}_{\mathrm{QE}}, \omega)$ obtained by the two models for relatively large distance $d = 1.38 - 2.22$ nm, where the response is mostly dominated by these low-order modes (panels a-c and f-h in Figure 3.4). However, for higher-order plasmonic modes $\ell \gtrsim 5$, the values of ω_ℓ within the SRF start to decrease with increasing ℓ, instead of getting larger as occurs for small ℓ and for the TDDFT results. Thus, the nondispersive SRF results in considerably lower values of ω_ℓ as compared to the TDDFT predictions. As a consequence, since the relative contribution of these high-order modes $\ell \gtrsim 5$ becomes important only for very small d, the nondispersive SRF calculations produce an additional redshift of $G(\mathbf{r}_{\mathrm{QE}}, \mathbf{r}_{\mathrm{QE}}, \omega)$ as compared to TDDFT for small separation distances $d \leq 0.95$ nm. This effect can be clearly identified in panels d,e and i,j in Figure 3.4. As discussed in Chapter 4, the mismatch between the nondispersive SRF and the TDDFT values of ω_ℓ for $\ell \gtrsim 5$ is a consequence of the approximation adopted to implement the calculation of $d_\perp(\omega)$. Indeed, the $d_\perp(\omega)$ parameter is obtained by considering the long-wavelength limit (small wavenumber in the direction parallel to the surface) [98] in a planar metal–vacuum interface [124, 296], which translates, in the case of a spherical MNP, into the condition $\ell d_\perp(\omega)/a << 1$. Thus, for a given radius a of a MNP, large values of ℓ, above a threshold value, do not fulfill this condition. Indeed, for small QE–MNP separation, large ℓ values are required to capture the full response, and thus the nondispersive SRF based on the long-wavelength limit

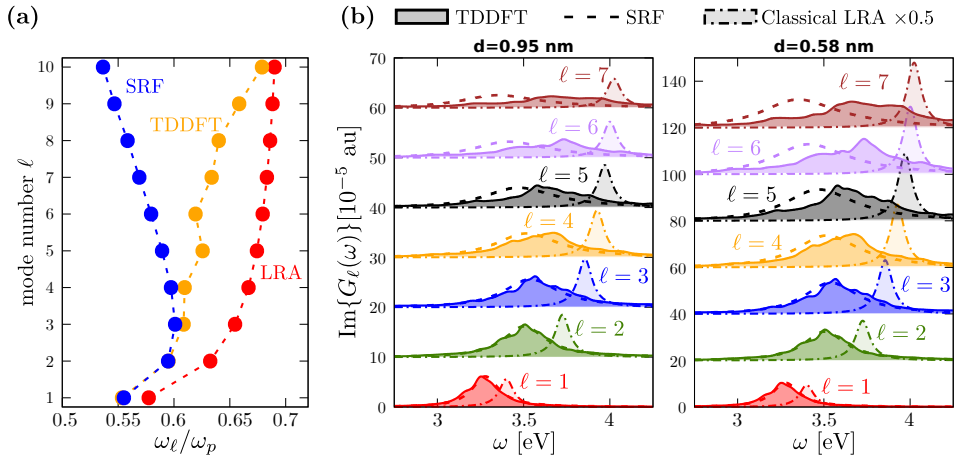

Figure 3.5: **(a)** Resonant energies ω_ℓ of the first ten plasmonic modes ($\ell = 1-10$) as obtained from the LRA (red dots), TDDFT (orange) and nondispersive SRF (blue), measured in units of the plasma frequency $\omega_p = 5.89$ eV. **(b)** Contribution of the first seven plasmonic modes $G_\ell(\mathbf{r}_{\rm QE}, \mathbf{r}_{\rm QE}, \omega)$ ($\ell = 1-7$) to the imaginary part of the self-interaction Green's function $G(\mathbf{r}_{\rm QE}, \mathbf{r}_{\rm QE}, \omega)$, as obtained from TDDFT calculations (solid lines), within the nondispersive SRF (dashed lines) and within the classical LRA (dashed-dotted lines). Panel on the left corresponds to a surface-to-emitter distance $d = 0.95$ nm, and panel on the right to $d = 0.58$ nm. The spectra in panel **(b)** are shifted vertically for visibility.

of $d_\perp(\omega)$ becomes inaccurate in such a situation.

Additionally, the SRF can also be used to explain the broad resonance profile of $G(\mathbf{r}_{\rm QE}, \mathbf{r}_{\rm QE}, \omega)$ shown by the TDDFT results in Figure 3.3 and Figure 3.4. From Eq. (3.10), we infer that the broadening κ_ℓ of the ℓ-resonance, $G_\ell(\mathbf{r}_{\rm QE}, \mathbf{r}_{\rm QE}, \omega)$, is given within the SRF by

$$\kappa_\ell \approx \gamma_p + \underbrace{\omega_\ell \frac{\ell+1}{a} \mathrm{Im}\left\{d_\perp(\omega_\ell)\right\}}_{\text{surface-enabled Landau damping}} , \tag{3.14}$$

which expresses an enhancement of the total damping κ_ℓ produced by surface-enabled Landau damping because $\mathrm{Im}\left\{d_\perp(\omega_\ell)\right\}$ is positive [124]. As a consequence, most plasmonic ℓ-modes within TDDFT spectrally overlap, giving rise to the generally broad profile of the total $G(\mathbf{r}_{\rm QE}, \mathbf{r}_{\rm QE}, \omega)$, which includes the contributions $G_\ell(\mathbf{r}_{\rm QE}, \mathbf{r}_{\rm QE}, \omega)$ from all ℓ-modes (Figures 3.3 and 3.4) [345].

In order to illustrate the consequences of surface-enabled Landau damping, we show in Figure 3.5b the contribution of the first seven plasmonic modes $G_\ell(\mathbf{r}_{\rm QE}, \mathbf{r}_{\rm QE}, \omega)$ ($\ell = 1-7$) to the spectra of the imaginary part of the self-interaction Green's function $G(\mathbf{r}_{\rm QE}, \mathbf{r}_{\rm QE}, \omega)$, as obtained from the three different models employed in this chapter. Results are shown for $d = 0.95$ nm (left-hand side panel in b) and $d = 0.58$ nm (right-hand side panel in b). As expected, within the classical LRA (dashed-dotted lines) all the multipoles have the same broadening,

with full width at half maximum (FWHM) equal to γ_p. In contrast, both TDDFT (solid lines) and the nondispersive SRF (dashed lines) predict an increasing FWHM with increasing plasmonic order ℓ, as given by Eq. (3.14). Finally, the comparison of the results obtained for $d = 0.95$ nm and $d = 0.58$ nm in Figure 3.5b corroborates that the relative contribution of higher-order plasmonic resonances increases with decreasing surface-to-emitter distance d within the three models employed in this chapter (LRA, TDDFT and SRF).

3.2.4 Quantum TDDFT vs. nondispersive SRF in a nanoparticle dimer

In this subsection, we extend the analysis of the calculation of the Green's function to a dimer comprising two identical spherical MNPs, where the QE is placed at the center of the gap of size D, as sketched in Figure 3.1b. This configuration has received special attention due to its capability to strongly enhance the amplitude of the incident electric field within the nanogap [23], leading to very efficient QE–MNPs interaction. Thus, the study of nonclassical effects in the dimer configuration appears particularly interesting.

Figure 3.6 shows the real (right-hand side panels) and imaginary (center panels) parts of the self-interaction Green's function $G(\mathbf{r}_{\rm QE}, \mathbf{r}_{\rm QE}, \omega)$ calculated for the dimer configuration, as obtained with classical LRA calculations (top), TDDFT (middle), and the nondispersive SRF (bottom). The QE is oriented along the dimer axis (the z-axis). Results are shown as a function of the oscillation frequency of the QE, ω, and the size of the gap, D. Thus, the distance d between the QE and the surface of each MNP forming the nanogap is $d = D/2$.

Both the imaginary part (Figure 3.6b) and real part (Figure 3.6c) of $G(\mathbf{r}_{\rm QE}, \mathbf{r}_{\rm QE}, \omega)$ calculated within the classical LRA show similar behavior for the dimer configuration as for the individual MNP. For the range of gap sizes $D = 20 - 45$ a$_0$ ($\approx 1.06 - 2.4$ nm) covered in Figure 3.6, the classical LRA results show a rich resonance profile with at least three well-defined resonances, namely the bonding dipolar plasmon (BDP, $\omega_{\rm BDP} \sim 3$ eV), the bonding quadrupolar plasmon (BQP, $\omega_{\rm BQP} \sim 3.5$ eV) and the broad dimer pseudomode ($\omega_{\rm PSM} \sim 3.75 - 4.1$ eV). These BDP, BQP and pseudomode are the results of the optical hybridization between the plasmonic ℓ-order modes of the individual MNPs [151]. For all the D values considered, the BDP and BQP resonances are narrow, while the pseudomode is broad because it originates from the hybridization of high-order plasmonic modes $\ell \geq 3$ of the isolated MNPs with closely-spaced resonant frequencies. The spectral weight of the pseudomode within the classical LRA considerably increases for small gap separations, and it becomes dominant for gaps smaller than $D \lesssim 36$ a$_0$ ($D \lesssim 1.9$ nm).

In contrast to these classical LRA predictions, the TDDFT results (panels e,f) show only two distinct resonant features: a BDP at $\omega_{\rm BDP} \sim 2.75$ eV and a pseudomode at $\omega_{\rm PSM} \sim 3.25 - 3.5$ eV, i.e., the distinct BQP mode does not split from the broad pseudomode due to Landau damping. Within TDDFT, the BDP is the dominant resonance for the whole range of gap sizes covered in this chapter,

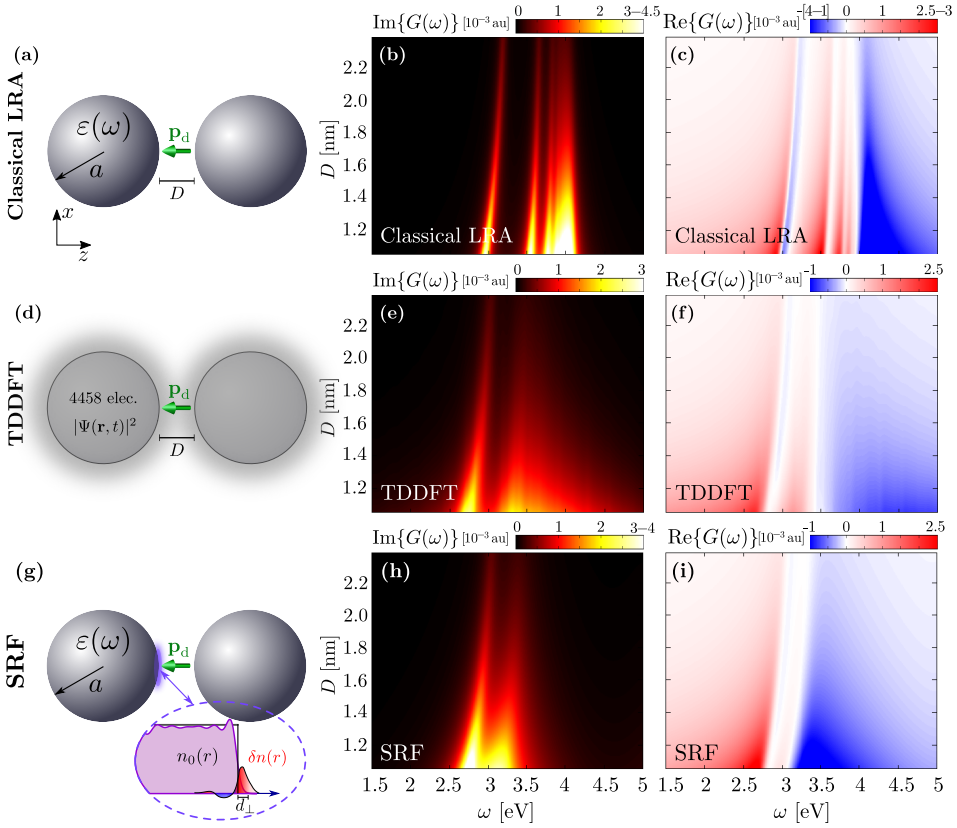

Figure 3.6: Self-interaction Green's function $G(\mathbf{r}_{\rm QE}, \mathbf{r}_{\rm QE}, \omega)$ obtained for a point-like QE placed at the center of the gap of size D formed by two identical Na spherical MNPs of radius $a = 65.83$ a$_0$ (≈ 3.5 nm). The QE is oriented along the dimer z-axis. **a-d-g** Sketches of the system studied within the three models employed in this chapter: **(a)** classical LRA, where the dielectric response of the metal is described by a local dielectric function $\varepsilon(\omega)$ and standard hard-wall boundary conditions are applied at the metal–vacuum interface, **(d)** TDDFT, where the time evolution of the electron density $n(\mathbf{r}, t) = \sum_{j\in \rm occ} \chi_j |\Psi_j(\mathbf{r}, t)|^2$ is obtained from the time-dependent KS equations and **(g)** Nondispersive SRF, which uses the local dielectric function $\varepsilon(\omega)$ to describe the bulk response of the metals but incorporates quantum surface-response corrections at the metal–vacuum interface by means of the $d_\perp(\omega)$ parameter. Imaginary part (panels b,e,h) and real part (c,f,i) of the self-interaction Green's function $G(\mathbf{r}_{\rm QE}, \mathbf{r}_{\rm QE}, \omega)$ as obtained from the classical LRA (**b-c**), TDDFT (**e-f**) and nondispersive SRF (**h-i**). Results are shown as a function of the oscillation frequency of the QE, ω, and the size of the gap, D. In **(b)**, **(c)**, and **(h)**, the upper and lower range of values in the color bar denote saturation.

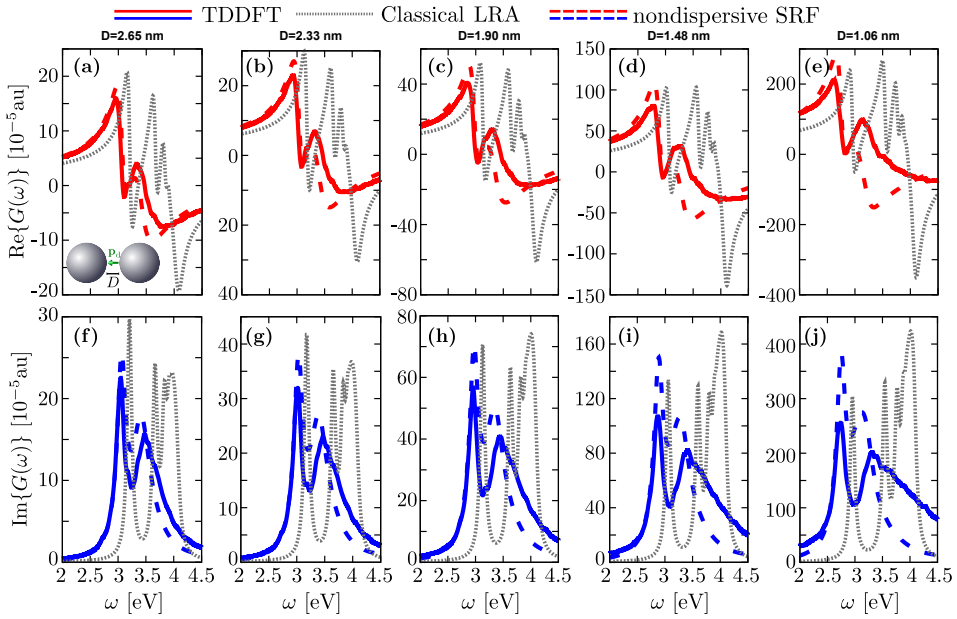

Figure 3.7: Real part (upper panels **a-e**) and imaginary part (lower panels **f-j**) of the self-interaction Green's function obtained for a point-like dipole placed at the center of a gap of size D formed by two identical Na spherical MNPs of radius $a = 65.83$ a$_0$ (≈ 3.5 nm), as calculated from TDDFT (solid lines), within the nondispersive SRF (dashed lines), and within the classical LRA (dotted gray lines). Each panel corresponds to selected gap sizes D ranging from $D = 1.06$ nm (rightmost panels) to $D = 2.65$ nm (leftmost panels). Gap separation distances are indicated on the top panels.

and its spectral weight increases as the gap separation D becomes larger. The nondispersive SRF (panels h,i in Figure 3.6) accurately reproduces the TDDFT spectra when comparing the strength and the spectral position of the BDP and the pseudomode. The broadening of the BDP resonance is also well reproduced by the SRF. However, we note that the pseudomode obtained from the nondispersive SRF calculations is sharper (albeit still substantially broader than the LRA prediction) than the one obtained within TDDFT. This effect is directly related to the redshift of the high-order modes $\ell \gtrsim 5$ with increasing ℓ shown by the nondispersive SRF in Figure 3.5 for an individual MNP, which is expected to be reflected also in the dimers results. Since the high-ℓ resonances of the individual MNP have lower frequency, they cannot contribute to the broadening of the pseudomode in the large frequency range $\omega_{\rm PSM} \sim 3.5$ eV.

For the sake of a quantitative comparison between the classical LRA, TDDFT and nondispersive SRF results, we show in Figure 3.7 the frequency dependence of $G(\mathbf{r}_{\rm QE}, \mathbf{r}_{\rm QE}, \omega)$ calculated for a set of fixed gap separations D, as obtained from a cut of Figure 3.6. Although there are quantitative discrepancies between the TDDFT and the SRF results for narrow gaps $D \sim 1 - 1.5$ nm (panels d,e,i,j in

Figure 3.7), the overall good agreement between the two approaches indicates that the spill-out of the induced charges and surface-enabled Landau damping, already discussed in the individual MNP results, are also the main quantum mechanisms influencing $G(\mathbf{r}_{\rm QE}, \mathbf{r}_{\rm QE}, \omega)$ in the dimer configuration. Moreover, these results corroborate the validity of the long-wavelength limit implementation of the SRF to adequately describe the electromagnetic interaction between a QE and a plasmonic gap nanostructure for situations where the gap separation is larger than $D \sim 1.5$ nm (panels a,b,c,f,g,h in Figure 3.7). However, similarly to the case of the individual MNP in Subsections 3.2.2 and 3.2.3, for smaller gap separations in a dimer, $D < 1.5$ nm, the limitations of the approximation used to obtain the Feibelman parameter $d_\perp(\omega)$ (neglecting the nonlocality of optical response in the direction parallel to the metal surface) affects the accuracy of the results, since in such a case, high-order plasmonic ℓ-modes are also relevant in the response of the system.

3.3 Summary

In this chapter, we study the influence of quantum phenomena on the electromagnetic interaction between a point-like quantum emitter (QE) and canonical metallic nanostructures. We focus on the study of the self-interaction dyadic Green's function $\hat{\mathbb{G}}(\mathbf{r}_{\rm QE}, \mathbf{r}_{\rm QE}, \omega)$ obtained for an individual spherical MNP and a dimer comprising two identical spherical MNPs, with the QE oriented perpendicular to the metal surfaces. In the case of the dimer, the QE is located in the middle of the gap. We consider sufficiently large QE–MNP separations so that charge-transfer processes related to electron tunneling do not play a role.

We first calculate $\hat{\mathbb{G}}(\mathbf{r}_{\rm QE}, \mathbf{r}_{\rm QE}, \omega)$ in the presence of an individual sodium MNP using time-dependent density functional theory (TDDFT), and then employ analytical expressions derived from a semiclassical model (referred to as the nondispersive SRF) in order to identify the origin of the quantum effects that influence the QE–MNP coupling. This nondispersive SRF incorporates surface quantum-response corrections by means of the Feibelman $d_\perp(\omega)$ parameter obtained under the long-wavelength approximation. The overall good agreement between TDDFT and the nondispersive SRF for both the individual and the dimer configurations confirms that surface-enabled Landau damping and the spill-out of the induced electron density drastically affect the electromagnetic QE–MNPs interaction. These mechanisms explain why the resonances of $\hat{\mathbb{G}}(\mathbf{r}_{\rm QE}, \mathbf{r}_{\rm QE}, \omega)$ obtained from TDDFT are redshifted and broader as compared to those obtained from a classical calculation using the local-response approximation (LRA) of the optical response of the metals.

We find that these quantum effects become more significant with increasing order ℓ of the plasmonic resonance. The analysis of the TDDFT calculations indicates that the higher the value of ℓ, the larger the broadening κ_ℓ produced by surface-enabled Landau damping as well as the redshift produced by the spill-out of the dynamical screening charges. Thus, the quantum phenomena explored in

this chapter show a considerable influence in the optical response for very small distance between a QE and a metallic surface, and when the QE is coupled to high-order plasmonic modes of the nanostructure.

We also find that the nondispersive SRF calculations based on the long-wavelength limit of the Feibelman parameter $d_\perp(\omega)$ describe more accurately the Green's function of a dipolar emitter when considering QEs coupled to low-order plasmonic modes. However, these calculations are not accurate when the contribution from high-order modes ($\ell \gtrsim 5$) of the nanostructure is large, as occurs when the distance d between the QE and the MNP is very small, $d \sim 0.6$ nm. As a consequence, in the dimer configuration the nondispersive SRF calculations underestimate the broadening of the pseudomode and become inaccurate for gap separations of the order of $D \sim 1 - 1.5$ nm. The shortcomings of the nondispersive SRF are due to the limitations to address the parallel nonlocality of the response when using a $d_\perp(\omega)$ parameter where the dependence on the wavenumber $k_\parallel$ parallel to the metal surface (or, equivalently, the angular momentum ℓ for spherical MNPs) is neglected. For more accurate results, it is necessary to go beyond the long-wavelength limit of $d_\perp(\omega)$ to properly account for the nonlocality of the surface response in the direction parallel to the surface, as this impacts the results in situations where the QE–MNP distance is small (high-order ℓ modes involved). The extension of the SRF to a *dispersive* model that takes into account the $k_\parallel$-dependence of $d_\perp$ is proposed in Chapter 4.

This chapter thus provides a fundamental description of the quantum phenomena influencing the electromagnetic interaction between a QE and plasmonic nanostructures for surface-to-emitter distances as small as ≈ 0.5 nm. For even smaller separation, charge-transfer processes between the QE and the MNPs can influence the optoelectronic response of the system, so that a many-body treatment based on TDDFT of both the QE and the MNPs is necessarily required to naturally account for any quantum effect in those extreme situations, including also charge-transfer processes. We adopt this strategy in Chapter 5.

CHAPTER 4

DISPERSIVE SURFACE-RESPONSE FORMALISM TO ADDRESS OPTICAL NONLOCALITY IN SITUATIONS OF EXTREME PLASMONIC FIELD CONFINEMENT

As shown in Chapter 3, the surface-response formalism (SRF) based on the Feibelman parameter $d_\perp$ allows us to capture quantum effects such as the spill in/out of the induced charges, surface-enabled Landau damping, and nonlocal dynamical screening in a computationally simple manner. To the best of our knowledge, $d_\perp$ has been so far computed using the long-wavelength approximation [98], which consists in neglecting the nonlocality of the optical response in the direction parallel to the metal–dielectric interface. The *nondispersive* Feibelman parameter is then a function of the excitation frequency, $d_\perp \equiv d_\perp(\omega)$, and it does not depend on the wavenumber $k_\parallel$ parallel to the metal surface. Considering the long-wavelength limit reduces the computational effort to obtain $d_\perp(\omega)$ from quantum calculations. Moreover, it simplifies the implementation of the SRF in existing numerical tools that solve Maxwell´s equations in Nanophotonics as employed in a number of recent studies [97, 124, 129, 296, 299, 300].

Using the long-wavelength limit of $d_\perp$ (i.e., considering $k_\parallel \sim 0$) is a reasonable approximation when the nonlocality of the optical response in the direction perpendicular to the surface dominates, i.e., when the characteristic scale Δ_s of the optical field variation along the surface is large as compared to that of the surface-response correction, $\Delta_s >> d_\perp$. This is the case of e.g. typical individual metallic nanoparticles (MNPs) subjected to plane-wave illumination. However, in

Chapter 3 we demonstrate that using the long-wavelength approximation of $d_\perp(\omega)$ within the nondispersive SRF is not accurate when describing situations involving multipole plasmon modes characterized by localized surface charges that rapidly vary along the MNPs surface. This is analogous to exciting plasmons with large transverse wavenumber $k_\parallel$, and therefore requires to go beyond the long-wavelength limit of $d_\perp$.

In this chapter, we demonstrate that accounting explicitly for the nonlocality of the optical response in the direction parallel to the surface lifts the shortcomings of the nondispersive SRF. Using a *dispersive* Feibelman parameter $d_\perp \equiv d_\perp(\omega, k_\parallel)$ that is a function of ω and $k_\parallel$ allows for correctly predicting the optical response of plasmonic structures in extreme situations where plasmon-induced charges characterized by high $k_\parallel$ can be excited, such as in structures with small radius or small gaps, for instance. We first study in Subsection 4.2.1 the energy dispersion of localized multipolar plasmon resonances sustained by a cylindrical metallic nanowire using TDDFT, and show that the energies of multipolar plasmon modes in such a nanowire are governed by a universal parameter m/R_c equivalent to the wavenumber $k_\parallel$ of surface plasmons at planar interfaces (here m is the magnetic quantum number, and R_c is the nanowire radius). Consistent with this statement, we demonstrate that the energy dispersion of localized multipolar plasmon modes relative to m/R_c in cylindrical nanowires follows the previously-studied $k_\parallel$-dispersion of nonretarded surface plasmons at planar metal surfaces [62, 306, 346]. Thus, TDDFT calculations of the cylindrical nanowire are used in Subsection 4.2.2 to obtain the Feibelman parameter $d_\perp \equiv d_\perp(\omega, k_\parallel = m/R_c)$, which reveals a strong dependence on $k_\parallel$. We show in Subsection 4.2.3 that the dispersive ($k_\parallel$-dependent) SRF accurately reproduces the energy dispersion of plasmon resonances obtained from TDDFT for the cylindrical nanowire. Furthermore, we demonstrate that the same set of $d_\perp(\omega, k_\parallel)$ can be used to address optical nonlocality in the parallel direction in metallic nanostructures of different shapes. To this end, we apply the dispersive SRF to small spherical MNPs as well as to nanometer-gap dimers coupled to quantum emitters (QEs), obtaining a good agreement between the dispersive SRF and TDDFT results. This chapter thus provides a significant advance toward the implementation of a SRF that adequately accounts for quantum effects in the optical response of plasmonic systems exhibiting extreme optical nonlocality.

4.1 System and methods

Three different plasmonic nanostructures are considered in this chapter to show the generality of the dispersive SRF: (i) an infinite cylindrical nanowire of radius R_c extended along the z-axis, as described in Subsection 2.3.3, which is used to calculate $d_\perp(\omega, k_\parallel)$, (ii) an individual spherical MNP of radius a, as described in Subsection 2.3.1, and (iii) a dimer consisting of two identical spherical MNPs with a QE located in the middle of the gap. The dimer considered here is the same as the one considered in Chapter 3. All the nanostructures considered in this chapter are described within the jellium model of free-electron metals (see

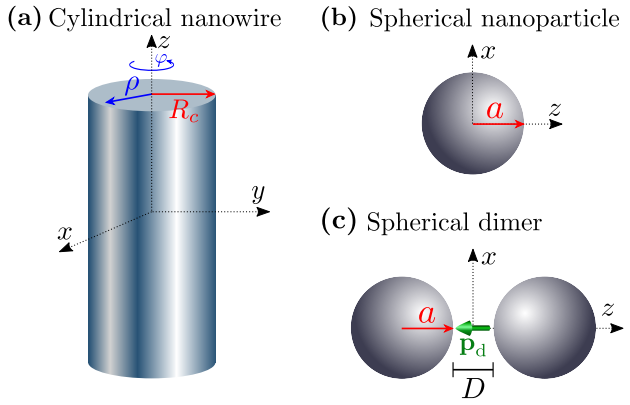

Figure 4.1: Sketch of the systems studied in this chapter. **(a)** Cylindrical Na nanowire with radius R_c, infinite along the z-axis. ρ is the radial coordinate, and φ the azimuthal angle. The system possesses rotational symmetry with respect to the z-axis. We consider three different values of the radius: $R_c = 75$ a$_0$, 100 a$_0$, and 150 a$_0$. **(b)** Spherical Na nanoparticle with radius $a = 65.83$ a$_0$. **(c)** A point-like quantum emitter (QE) with a dipole moment $\mathbf{p}_d$ placed at the middle of the gap formed by two identical spherical Na nanoparticles. The QE is represented by the green arrow. The gap separation distance is denoted as D. In all the structures, Na is characterized by a Wigner–Seitz radius $r_s = 4$ a$_0$.

Subsection 2.1.2) using a Wigner–Seitz radius $r_s = 4$ a$_0$ that corresponds to sodium. The classical bulk plasma frequency is therefore $\omega_p = \sqrt{\frac{3}{r_s^3}} = 5.89$ eV, the surface plasmon frequency $\omega_{\rm SP} = \omega_p/\sqrt{2} = 4.16$ eV, and the localized dipolar plasmon (DP) frequency $\omega_{\rm DP} = \omega_p/\sqrt{3} = 3.4$ eV. We choose this material because it allows for a direct comparison between our results and those obtained in Chapter 3 using the long-wavelength approximation. The schematic representation of the nanostructures studied in this chapter is depicted in Figure 4.1.

The optical response of individual spherical MNPs and dimers has been studied in detail in previous chapters, and thus here we focus on the numerical procedure used to obtain the energy dispersion of localized multipolar plasmon resonances sustained by the cylindrical nanowire. We address cylindrical nanowires with large radii R_c (as compared to that of spherical MNPs) within the range $R_c = 75-150$ a$_0$ ($\approx 4-8$ nm) characterized by well-developed multipolar plasmons, thus allowing us to span a large range of periods $2\pi R_c/m$ of the spatial variation of plasmon-induced charges along the nanowire surface. Here, owing to the cylindrical symmetry of the system, the multipolar plasmon modes can be characterized by the magnetic number m related to the $e^{im\varphi}$ dependence on the azimuthal angle φ of the potentials, fields and induced charges.

In the frequency domain, the potential $V_{\rm ind}(\rho, \varphi, \omega)$ induced at $\rho > R_c$ in response to an external excitation $V_{\rm ext}(x, y, t)$ can be expressed as

$$V_{\rm ind}(\rho,\varphi,\omega) = 2\sum_{m=1}^{m_{\rm max}} \left(\frac{R_c}{\rho}\right)^m \mathrm{Q}_m(\omega)\cos(m\varphi), \tag{4.1}$$

where $\mathrm{Q}_m(\omega)$ is the frequency-resolved multipole moment of order m per unit length along the z-axis. Our aim is to determine the frequency and width of these multipolar resonances.

With this purpose, we use the Kohn–Sham scheme (KS) of TDDFT introduced in Section 2.2. We employ the same numerical implementation as described in Subsection 2.3.3 but, instead of considering a x-polarized plane-wave excitation given by Eq. (2.76), here we consider the following impulsive external potential $V_{\rm ext}(x,y,t)$:

$$V_{\rm ext}(x,y,t) = \xi\ \delta(t)\ \sum_{m=1}^{m_{\rm max}} \left(\frac{\rho}{R_c}\right)^m \cos(m\varphi), \tag{4.2}$$

where $x=\rho\cos\varphi$ and $y=\rho\sin\varphi$, $\delta(t)$ is the Dirac delta function, the amplitude ξ is sufficiently weak to ensure a linear response, and $m_{\rm max}=30$ is the highest multipole order considered in the simulation. In Eq. (4.2), we write explicitly the dependence of $V_{\rm ext}(x,y,t)$ on the spatial variables (x,y) to stress that we use Cartesian coordinates as described in Subsection 2.3.3. Due to the excitation used here, multipolar plasmon excitations are localized at the (x,y)-plane, and do not propagate along the z-axis. The term *localized* referring to plasmons excited at the nanowire is often omitted but implicitly assumed. Because of the cylindrical symmetry of the system, m is a good quantum number, i.e., an external potential with angular dependence $\cos(m\varphi)$ excites localized multipolar plasmon modes at the nanowire characterized by induced charges with the same angular dependence $\cos(m\varphi)$.

Using the real-time ALDA-TDDFT methodology in Cartesian coordinates as introduced in Subsection 2.3.3, we calculate the time-dependent multipole moment $\mathrm{Q}_m(t)$ induced at the nanostructure per unit length along the z-axis, defined as[25]

$$\mathrm{Q}_m(t) = -\frac{1}{m}\iint dx\ dy\ \left(\frac{\rho}{R_c}\right)^m \cos(m\varphi)\ \delta n(x,y,t), \tag{4.3}$$

where the electron density $\delta n(x,y,t)$ induced by $V_{\rm ext}(x,y,t)$ in Eq. (4.2) is given by [Eq. (2.77)]

$$\delta n(x,y,t) = n(x,y,t) - n(x,y,t=0). \tag{4.4}$$

The frequency-resolved spectrum of the multipole moment $\mathrm{Q}_m(\omega)$ is finally obtained from the time-to-frequency Fourier transform,

$$\mathrm{Q}_m(\omega) = \int dt\ \mathrm{Q}_m(t) e^{(i\omega-\eta/2)t}, \tag{4.5}$$

[25] The $1/(R_c)^m$ factor of the definition of the cylindrical multipole moment in Eq. (4.3) (and consistently the factor $(R_c)^m$ in Eq. (4.1)) simplifies the comparison between the results of the calculations performed for nanowires of different radius R_c.

where an attenuation factor $\eta = 0.15$ eV is used [Eq. (2.56)] to mimic dissipation processes beyond the reach of the ALDA-TDDFT scheme adopted here (see details in Section 2.2).

It is worth mentioning that, for $m_{\max} = 1$, Eq. (4.2) expresses the nonretarded potential corresponding to a plane-wave illumination polarized along the x-axis. Such illumination is typically used in linear-response TDDFT calculations to obtain the dipolar polarizability of the system, as described in Subsection 2.3.3.

4.2 Results and discussion

4.2.1 TDDFT study of the energy dispersion of multipolar plasmon resonances in a metallic nanowire

Figure 4.2 shows the intensity spectrum of the multipole moments, $|\mathrm{Q}_m(\omega)|^2$, obtained for a cylindrical nanowire of radius $R_c = 150$ a$_0$ (panel a) and $R_c = 100$ a$_0$ (panel b) in response to the external potential given by Eq. (4.2). The results for different values of m are plotted, ranging from $m = 1$ (top) to $m = m_{\max}$ (bottom). For the largest nanowire $m_{\max} = 30$ is considered, whereas for the smallest one $m_{\max} = 23$. The general behavior of multipolar plasmon resonances $|\mathrm{Q}_m(\omega)|^2$ is independent of the size of the nanostructure: first, for a given m, a well-defined resonance centered at a frequency ω_m is obtained associated with the excitation of the multipolar plasmon mode of order m. The width of the multipolar plasmon resonance for the two nanowires increases with increasing m because of the enhancement of surface-enabled Landau damping, where the plasmon decays into electron–hole pair excitations at the surface region, as discussed in Chapter 3 for spherical MNPs for increasing ℓ. Moreover, regardless of the specific value of the radius R_c, ω_m first redshifts with increasing m and, after reaching a minimum, it continuously blueshifts. However, the multipolar plasmon resonances of a given order m are broader for the smaller nanowire, and do not emerge at the same frequency ω_m for the two sizes. For example, the dipolar plasmon resonance ($m = 1$) emerges at $\omega_1 \sim 4.1$ eV for $R_c = 150$ a$_0$ (extremely close to the classical long-wavelength limit of the surface plasmon frequency, $\omega_{\mathrm{SP}} = 4.16$ eV), while for $R_c = 100$ a$_0$ it appears at $\omega_1 \sim 4.06$ eV. Moreover, for the largest nanowire the minimum value of ω_m is reached at $m = 10$ ($\omega_{10} \sim 3.8$ eV), whereas for the smallest nanowire the minimum is obtained at $m = 8$. The differences in the results obtained for the two nanowires are particularly apparent when comparing ω_m for $m = 20$: in this case, there is a mismatch in ω_m of the order of ~ 0.5 eV.

The results shown in Figure 4.2a,b are closely related to the dispersion relation of *surface* plasmon resonances supported by planar metal–vacuum interfaces as a function of the parallel wavenumber $k_\parallel$, as we discuss below. Indeed, the induced fields and surface charge densities of localized multipolar plasmons considered in this chapter have a dependence of $\exp(im\varphi)$ on the azimuthal angle φ. By introducing the coordinate $r_\parallel$ along the surface of the nanowire cross-section, $r_\parallel = R_c\ \varphi$, the angular dependence transforms into $\exp(im\varphi) \to \exp(i\frac{m}{R_c}\ r_\parallel)$.

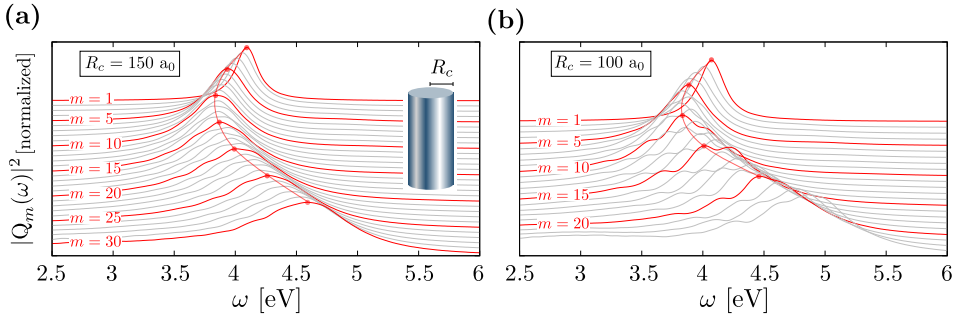

Figure 4.2: **(a)** Intensity spectrum of the multipole moment $|Q_m(\omega)|^2$ induced at an infinitely long cylindrical Na nanowire ($r_s = 4$ a$_0$) of radius $R_c = 150$ a$_0$ (≈ 8 nm). Results are shown as a function of the frequency of the external excitation, ω, for different values of the magnetic quantum number m, ranging from $m = 1$ (top) to $m = 30$ (bottom), as indicated in the insets. All $|Q_m(\omega)|^2$ are normalized to their corresponding maximum value. **(b)** Same as in **(a)** but for a smaller nanowire of radius $R_c = 100$ a$_0$ (≈ 5.3 nm) and magnetic number within the range $m = 1 - 23$. Results are displaced in the vertical axis for clarity.

For $R_c \to \infty$, the cylindrical geometry tends to the planar-surface geometry with $r_\parallel$ being the coordinate parallel to the surface, so that setting $\frac{m}{R_c} \to k_\parallel$ recovers the standard dependence $\exp(ik_\parallel r_\parallel)$ of a surface plasmon propagating along the surface [see Eq. (1.38)]. Thus, we interpret $\frac{m}{R_c}$ in the following as an "effective" wavenumber $k_\parallel$ by considering that localized multipolar plasmons in the nanowire correspond to *confined* surface plasmons with a quantized wavelength $\lambda_\parallel = 2\pi R_c/m$ [347]. To support this correspondence, we compare in Figure 4.3 the intensity spectra $|Q_m(\omega)|^2$ obtained for nanowires with radius $R_c = 75$ a$_0$ (dahsed lines), 100 a$_0$ (dotted lines), and 150 a$_0$ (solid lines). Results are shown for selected values of m such that $k_\parallel = m/R_c = 0.013,\ 0.02,\ 0.04,\ 0.067$, and 0.1 a$_0^{-1}$. Whenever the ratio m/R_c is fixed, the intensity spectrum of the multipole moment $|Q_m(\omega)|^2$ obtained for nanowires of different size shows near perfect match with each other, thus confirming that an effective wavenumber $k_\parallel = m/R_c$ determines the optical response of the system.

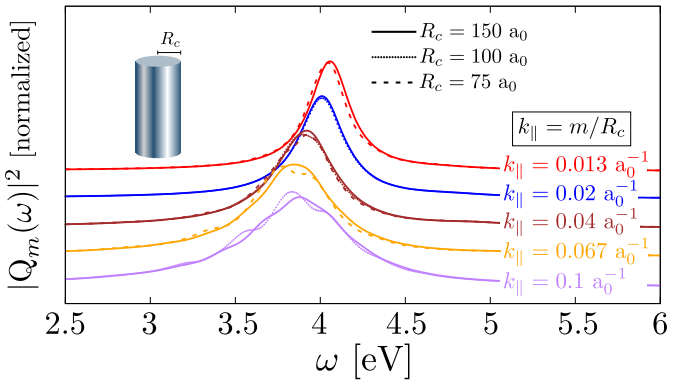

Figure 4.3: Intensity spectrum of the multipole moments $|Q_m(\omega)|^2$ obtained for cylindrical nanowires of different radii R_c and selected values of the magnetic number m. Solid lines: $R_c = 150$ a$_0$. Dotted lines: $R_c = 100$ a$_0$. Dashed lines: $R_c = 75$ a$_0$. The selected values of m are such that $k_\parallel = m/R_c = 0.013$ a$_0^{-1}$ (red), $k_\parallel = 0.02$ a$_0^{-1}$ (blue), $k_\parallel = 0.04$ a$_0^{-1}$ (brown), $k_\parallel = 0.067$ a$_0^{-1}$ (orange), and $k_\parallel = 0.1$ a$_0^{-1}$ (purple) for the three values of R_c. The spectra $|Q_m(\omega)|^2$ corresponding to a specific wavenumber $k_\parallel = m/R_c$ are normalized to the maximum value obtained for the case of $R_c = 150$ a$_0$. Results are displaced in the vertical axis for clarity.

4.2.2 Calculation of the dispersive Feibelman parameter $d_\perp(\omega, k_\parallel)$

The results presented in the previous section allow us to calculate $d_\perp \equiv d_\perp(\omega, k_\parallel)$ as a function of both the excitation frequency ω and the effective wavenumber parallel to the surface, $k_\parallel = m/R_c$, using the cylindrical geometry. In this subsection, we first obtain the expression of the Feibelman parameter $d_\perp$ for a cylindrical metallic nanowire within the SRF, and then discuss the TDDFT results of $d_\perp \equiv d_\perp(\omega, k_\parallel)$ calculated for the present system following the methodology employed in the previous subsection.

Expression of the Feibelman parameter $d_\perp$ for a cylindrical nanowire

To obtain the expression of the Feibelman parameter $d_\perp$ for a cylindrical nanowire infinite along the z-axis, we focus on the SRF solution of the electrostatic potential $\phi^{\text{ind}}(\rho, \varphi, \omega)$ induced at the nanowire (in the nonretarded approximation). Due to the translational invariance of the system with respect to the z-axis, ϕ^{ind} only depends upon the spatial variables (ρ, φ). The induced potential $\phi^{\text{ind}}(\rho, \varphi, \omega)$ can thus be expressed as:

$$\phi^{\text{ind}}(\rho, \varphi, \omega) = \sum_{m=-\infty}^{m=\infty} \phi_m(\rho, \omega)\, e^{im\varphi}, \tag{4.6}$$

where formally the sum extends from $m = -\infty$ to $m = \infty$.

The radial part of the induced potential, $\phi_m(\rho, \omega)$, is given by the solution of

Poisson's equation,

$$\left[\frac{1}{\rho}\frac{\partial}{\partial\rho}\left(\rho\frac{\partial}{\partial\rho}\right)-\frac{m^2}{\rho^2}\right]\ \phi_m(\rho,\omega)=4\pi\delta n_m(\rho,\omega), \tag{4.7}$$

where $\delta n_m(\rho,\omega)$ are the moments of the induced electron density $\delta n(\rho,\varphi,\omega)$ satisfying

$$\delta n(\rho,\varphi,\omega)=\sum_{m=-\infty}^{m=\infty}\delta n_m(\rho,\omega)\ e^{im\varphi}. \tag{4.8}$$

To solve Eq. (4.7), we first consider the Green's function $G_m(\rho,\rho')$ that satisfies the following equation

$$\left[\frac{1}{\rho}\frac{\partial}{\partial\rho}\left(\rho\frac{\partial}{\partial\rho}\right)-\frac{m^2}{\rho^2}\right]\ G_m(\rho,\rho')=\frac{1}{\rho}\delta(\rho-\rho'), \tag{4.9}$$

so that

$$\phi_m(\rho,\omega)=4\pi\int_0^\infty\rho' d\rho' G_m(\rho,\rho')\delta n_m(\rho',\omega). \tag{4.10}$$

The solution of Eq. (4.9) for $m\neq 0$ is given by

$$G_m(\rho,\rho')=\begin{cases}-\frac{1}{2m}\left(\frac{\rho}{\rho'}\right)^m & \text{for } \rho<\rho'\\ \\ -\frac{1}{2m}\left(\frac{\rho'}{\rho}\right)^m & \text{for } \rho>\rho'\end{cases}. \tag{4.11}$$

Thus, according to Eq. (4.10), the radial part of the induced potential is given by

$$\phi_m(\rho,\omega)=-2\frac{\pi}{m}\left[\int_0^\rho\rho'\ d\rho'\left(\frac{\rho'}{\rho}\right)^m\delta n_m(\rho',\omega)+\int_\rho^\infty\rho'\ d\rho'\left(\frac{\rho}{\rho'}\right)^m\delta n_m(\rho',\omega)\right]. \tag{4.12}$$

For example, within the (piecewise-constant) local-response approximation (LRA), where the induced charge density $\delta n_m(\rho,\omega)=\sigma_m(\omega)\delta(\rho-R_c)$ is strictly located at the jellium edge of the nanowire of radius R_c, Eq. (4.12) leads to the classical LRA solution of the induced potential

$$\phi_m^{\mathrm{LRA}}(\rho,\omega)=\begin{cases}-2\frac{\pi}{m}\sigma_m(\omega)\frac{\rho^m}{R_c^{m-1}} & \text{for } \rho<R_c\\ \\ -2\frac{\pi}{m}\sigma_m(\omega)\frac{R_c^{m+1}}{\rho^m} & \text{for } \rho>R_c\end{cases}. \tag{4.13}$$

However, when quantum surface effects are considered within the SRF, $\delta n_m(\rho,\omega)$ is not strictly located at the jellium edge of the nanowire but it has a finite extension near the metal surface. In what follows, we assume that $\delta n_m(\rho,\omega)$ is nonzero only in the small region $\pm\Delta$ (with $\Delta\ll R_c$) inside and outside the jellium edge located at $\rho=R_c$. Further, we introduce the variable $\delta\rho$ such that $\rho'=R_c+\delta\rho$,

so that $\delta\rho$ varies within the interval $\pm\Delta$. We can thus develop $\left(\frac{\rho}{\rho'}\right)^m$ and $\left(\frac{\rho'}{\rho}\right)^m$ in Eq. (4.12) into a Taylor series around R_c with respect to $\delta\rho$, which results in

$$\left(\frac{\rho}{\rho'}\right)^m = \frac{\rho^m}{R_c^m} - m\frac{\rho^m}{R_c^{m+1}}\delta\rho + \mathcal{O}\left(\frac{\delta\rho^2}{R_c^2}\right) \approx \frac{\rho^m}{R_c^m}\left[1 - m\frac{\delta\rho}{R_c}\right], \tag{4.14}$$

and

$$\left(\frac{\rho'}{\rho}\right)^m = \frac{R_c^m}{\rho^m} + m\frac{R_c^{m-1}}{\rho^m}\delta\rho + \mathcal{O}\left(\frac{\delta\rho^2}{R_c^2}\right) \approx \frac{R_c^m}{\rho^m}\left[1 + m\frac{\delta\rho}{R_c}\right]. \tag{4.15}$$

Using Eqs. (4.14) and (4.15), the radial part of the potential $\phi_m(\rho,\omega)$ outside the surface region $R_c \pm \Delta$ can be expressed within the SRF [Eq. (4.12)] as

$$\phi_m(\rho,\omega) = \begin{cases} -2\frac{\pi}{m}\left(\frac{\rho}{R_c}\right)^m \int_{R_c-\Delta}^{R_c+\Delta} \rho'\, d\rho' \delta n_m(\rho',\omega)\left[1 - m\frac{\rho'-R_c}{R_c}\right] & \text{for } \rho < R_c - \Delta \\ -2\frac{\pi}{m}\left(\frac{R_c}{\rho}\right)^m \int_{R_c-\Delta}^{R_c+\Delta} \rho'\, d\rho' \delta n_m(\rho',\omega)\left[1 + m\frac{\rho'-R_c}{R_c}\right] & \text{for } \rho > R_c + \Delta \end{cases}. \tag{4.16}$$

By comparing the potential $\phi_m(\rho,\omega)$ within the SRF [Eq. (4.16)] and the classical LRA result $\phi_m^{\mathrm{LRA}}(\rho,\omega)$ [Eq. (4.13)], one can define the surface charge $q^{\mathrm{cyl}}(\omega,m)$ per unit length in the z-coordinate and per 2π in φ

$$q^{\mathrm{cyl}}(\omega,m) \equiv \int_{R_c-\Delta}^{R_c+\Delta} \rho\, d\rho\, \delta n_m(\rho,\omega), \tag{4.17}$$

and the Feibelman parameter for a cylindrical nanowire,

$$d_\perp^{\mathrm{cyl}}(\omega,m) \equiv \frac{\int_{R_c-\Delta}^{R_c+\Delta} \rho\, d\rho\, (\rho - R_c)\, \delta n_m(\rho,\omega)}{q^{\mathrm{cyl}}(\omega,m)}, \tag{4.18}$$

so that the induced potential $\phi_m(\rho,\omega)$ within the SRF outside the surface region $R_c \pm \Delta$ is given by

$$\phi_m(\rho,\omega) = \begin{cases} -2\frac{\pi}{m}\left(\frac{\rho}{R_c}\right)^m q^{\mathrm{cyl}}(\omega,m)\left[1 - \frac{m}{R_c} d_\perp^{\mathrm{cyl}}(\omega,m)\right] & \text{for } \rho < R_c - \Delta \\ -2\frac{\pi}{m}\left(\frac{R_c}{\rho}\right)^m q^{\mathrm{cyl}}(\omega,m)\left[1 + \frac{m}{R_c} d_\perp^{\mathrm{cyl}}(\omega,m)\right] & \text{for } \rho > R_c + \Delta \end{cases}. \tag{4.19}$$

As expected, for $R_c \to \infty$ or $\Delta \to 0$, Eq. (4.19) reduces to the classical LRA solution $\phi_m^{\mathrm{LRA}}(\rho,\omega)$ given by Eq. (4.13) with $\sigma_m(\omega) = \frac{q(\omega,m)}{R_c}$. The numerator in the definition of the Feibelman parameter $d_\perp^{\mathrm{cyl}}(\omega,m)$ [Eq. (4.18)] is an analogue of the induced *surface* dipole moment [62] per unit length in the z-coordinate, while the denominator is an analogue of the induced surface charge per unit length in the

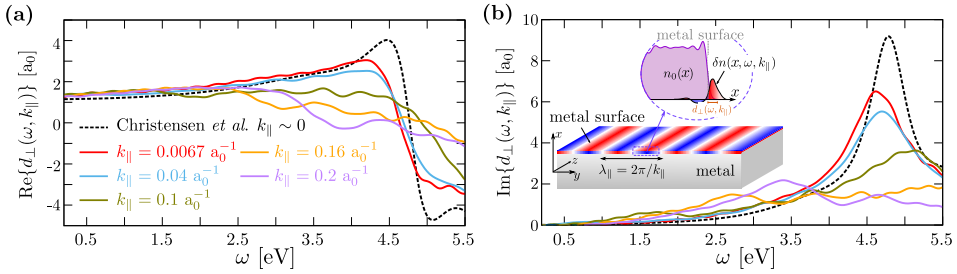

Figure 4.4: **(a)** Real part of the dispersive Feibelman parameter $d_\perp(\omega, k_\parallel = m/R_c)$ for selected values of $k_\parallel$ as obtained from TDDFT calculations performed for a cylindrical nanowire of radius $R_c = 150$ a$_0$. The parameter $d_\perp(\omega)$ obtained in ref. 296 under the long-wavelength approximation is shown by the dashed black line as a reference. Results are shown as a function of the frequency, ω. The values of $k_\parallel$ are indicated in the inset. **(b)** Same as in (a) for the imaginary part. The sketch in the inset represents the induced charge density $\delta n(x, \omega, k_\parallel)$ in a semi-infinite planar metal surface, with the Feibelman parameter $d_\perp(\omega, k_\parallel)$ accounting for the position of the centroid of $\delta n(x, \omega, k_\parallel)$ relative to the geometrical metal surface. n_0 represents the equilibrium electron density.

z-coordinate. In this respect, Eq. (4.18) is similar to the definition of the Feibelman parameter $d_\perp$ for a planar metal surface introduced in Eq. (2.82a), and thus, the real part of $d_\perp^{\text{cyl}}(\omega, m)$ provides the position of the centroid of the induced charges with respect to the jellium edge of the metal as a function of ω and m, and the imaginary part is related to the contribution of surface-enabled Landau damping.

TDDFT results of $d_\perp(\omega, k_\parallel)$

Once $d_\perp^{\text{cyl}}(\omega, m)$ is calculated for a given m and nanowire radius R_c according to Eq. (4.18) (using the WPP algorithm within TDDFT), $d_\perp \equiv d_\perp(\omega, k_\parallel)$ is obtained using $d_\perp^{\text{cyl}}(\omega, m)$ with $k_\parallel = m/R_c$. The integrals in Eq. (4.18) are calculated within a region extending $\Delta \sim 20$ a$_0$ inside and outside the metal surface in the radial direction.

We show in Figure 4.4 the real ($\text{Re}\{d_\perp(\omega, k_\parallel)\}$, panel a) and imaginary ($\text{Im}\{d_\perp(\omega, k_\parallel)\}$, panel b) parts of the dispersive Feibelman parameter obtained from TDDFT calculations using a cylindrical nanowire of radius $R_c = 150$ a$_0$. Results are shown as a function of ω for various values of the "effective" wavenumber $k_\parallel = m/R_c$. We show in Appendix D that the calculations performed for a different nanowire radius $R_c = 100$ a$_0$ with the same ratio m/R_c give very similar results.

The results shown in Figure 4.4 for $k_\parallel = 0.0067$ a$_0^{-1}$ (red line), corresponding to the smallest wavenumber considered, show a complex-valued Lorentzian-like resonance at $\omega \sim 4.6$ eV. This resonance is associated with the excitation of the Bennet plasmon at $\omega \sim 0.8\omega_p$ [62, 79, 305, 306], as discussed in Section 2.5. The results of $d_\perp(\omega, k_\parallel)$ for small $k_\parallel$ are consistent with the results of Christensen *et al.* [296] obtained for a flat surface of the same material in the long-wavelength limit ($k_\parallel = 0$, dashed black lines). However, with increasing $k_\parallel$, the Bennet plasmon

resonance in $d_\perp(\omega, k_\parallel)$ broadens and blueshifts [62]. Importantly, in the frequency range $\omega \sim 2.5 - 4.5$ eV relevant for plasmon excitations, the following trend is observed with increasing $k_\parallel$: first, $\mathrm{Re}\left\{d_\perp(\omega, k_\parallel)\right\}$ generally decreases and can even change its sign from positive to negative values, indicating that the centroid of the induced charge density shifts towards the inside of the metal for high $k_\parallel$. Further, $\mathrm{Im}\left\{d_\perp(\omega, k_\parallel)\right\}$ increases overall reflecting more efficient decay of the plasmon into electron–hole pair excitations *via* surface-enabled Landau damping. Additionally, in the low-frequency regime $\omega \lesssim 2$ eV, i.e., well away from any collective plasmon resonance, the optical response of the system is close to that of an ideal metal and becomes independent of $k_\parallel$. Thus, $\mathrm{Re}\left\{d_\perp(\omega, k_\parallel)\right\} \sim 1.2$ $\mathrm{a_0}$ indicates that the centroid of induced charge density approaches the position of the image potential plane with respect to the jellium edge [62].

4.2.3 Validation of the dispersive SRF

Once the Feibelman parameter $d_\perp(\omega, k_\parallel)$ is obtained from TDDFT calculations, we next establish the validity of the dispersive SRF proposed in this chapter to correctly account for quantum surface effects in nanoscale plasmonic systems. To that end, we first show that the dispersive SRF model correctly reproduces the TDDFT results of the energy dispersion of plasmon resonances in a cylindrical nanowire as a function of $k_\parallel = m/R_c$. We then extend the applicability of the dispersive SRF to obtain the optical response of individual spherical MNPs as well as their dimers.

Energy dispersion of plasmon resonances in a metallic nanowire as a function of $k_\parallel$

We show in Figure 4.5 the energy $\omega_s(k_\parallel)$ of plasmon resonances sustained by metallic nanowires of radius R_c. The TDDFT (blue), dispersive SRF (orange), and nondispersive SRF (red) results are shown as a function of the effective wavenumber $k_\parallel = m/R_c$. Within TDDFT, we obtain the resonant plasmon frequency ω_s as the mean value between the frequencies of the half-maximum of $|\mathrm{Q}_m(\omega)|^2$ displayed in Figure 4.2. As we detail in Appendix E, within the dispersive SRF, ω_s is determined from the following transcendental equation,

$$\omega_s(k_\parallel) = \omega_{\mathrm{SP}}\left(1 - \frac{k_\parallel}{2}\mathrm{Re}\{d_\perp(\omega_s, k_\parallel)\}\right), \tag{4.20}$$

which is solved self-consistently for a given wavenumber $k_\parallel = m/R_c$. The nondispersive SRF results are also obtained from Eq. (4.20) using the parameter $d_\perp(\omega)$ calculated by Christensen *et al.* [296] under the long-wavelength limit ($k_\parallel = 0$).

When $k_\parallel$ increases, the plasmon frequency $\omega_s(k_\parallel)$ in Figure 4.5 obtained from TDDFT first redshifts, reaches a minimum at $k_\parallel \sim 0.08$ $\mathrm{a_0^{-1}}$, and then continuously blueshifts. This shape of the plasmon energy dispersion is determined by the change of the location of the dynamically-induced screening charges from above to

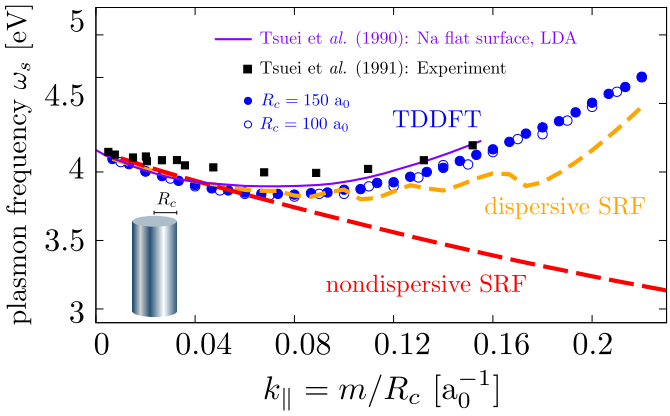

Figure 4.5: **(a)** Energy dispersion $\omega_s(k_\parallel)$ of the plasmon resonances sustained by a cylindrical nanowire of radius R_c as a function of the effective wavenumber parallel to the metal surface, $k_\parallel = m/R_c$. Here m stands for the magnetic quantum number. Results are obtained using three different models: TDDFT (blue); dispersive SRF (orange), where the Feibelman parameter $d_\perp(\omega, k_\parallel)$ depends on ω and $k_\parallel$; and nondispersive SRF (red), where $d_\perp(\omega)$ is a function of frequency exclusively. The TDDFT results are obtained for two cylindrical nanowires, R_c = 100 a_0 and 150 a_0, as indicated in the insert. We also show the experimental (black rectangles) and theoretical (purple line) results of the surface plasmon dispersion of a planar Na–vacuum interface [62, 306, 346].

below the classical image plane, i.e., a shift of the centroid of the induced charge density from outside the metal to inside [62, 306, 346]. Importantly, this change of the location of the dynamically-induced screening charges is well described by the dispersive Feibelman parameter $d_\perp(\omega, k_\parallel)$ shown in Figure 4.4a, and thus the dispersive SRF results in Figure 4.5 correctly reproduce the TDDFT values within the broad range of $k_\parallel$ considered. Notice that the dispersion of $\omega_s(k_\parallel)$ obtained here within TDDFT and within dispersive SRF for cylindrical nanowires closely matches the measured (black rectangles) and calculated (purple line) dispersion curve of the surface plasmon propagating at a planar Na–vacuum interface[26] [62, 306, 346], which further confirms the equivalence between the wavenumber $k_\parallel$ of propagating surface plasmons and the effective wavenumber m/R_c of localized multipolar plasmons sustained by the infinite metallic nanowire.

In contrast, the nondispersive SRF only predicts accurately the plasmon energy dispersion for small values of the parallel wavenumber, $k_\parallel \lesssim 0.06$ a_0^{-1}. Indeed, for small values of $k_\parallel$ where the long-wavelength approximation is well justified, Figure 4.5 shows an excellent agreement between the TDDFT and both dispersive and nondispersive SRF results. This good agreement occurs because we consider as a reference the nondispersive parameter $d_\perp(\omega)$ reported by Christensen *et al.* [296], which is very close to the dispersive parameter $d_\perp(\omega, k_\parallel)$ obtained in this chapter with the TDDFT methodology for small $k_\parallel$ within the frequency range of interest

[26] The results of ref. 346, originally presented in units of the bulk plasmon frequency, are rescaled using the value ω_p = 5.89 eV considered here.

(compare in Figure 4.4a the red and the blue lines with the reference dashed black line). However, for higher wavenumber, $k_\parallel \gtrsim 0.06\ \mathrm{a}_0^{-1}$, the nondispersive model fails to account for the change of the location of the dynamically-induced screening charges with increasing $k_\parallel$ and thus mistakenly predicts a continuous redshift of ω_s across the entire range of wavenumbers $k_\parallel$. Figure 4.5 thus demonstrates the necessity of considering the explicit dependence of $d_\perp$ on $k_\parallel$ to accurately describe the nonlocal plasmonic response for $k_\parallel \gtrsim 0.06\ \mathrm{a}_0^{-1}$.

Dispersive SRF applied to other geometries: individual spherical nanoparticle and nanoparticle dimer

We finally show that the dispersive SRF presented in this chapter can be used to treat nonlocality in a broad range of plasmonic systems using the dispersive Feibelman parameter $d_\perp(\omega, k_\parallel)$ that we obtained for a cylindrical nanowire (with $k_\parallel = m/R_c$). In particular, we demonstrate the applicability of the dispersive SRF proposed here to correctly account for quantum surface effects and nonlocality in the optical response of individual spherical MNPs and their dimers. To validate the results in these configurations, we compare a set of optical properties as obtained within the dispersive SRF with those obtained with TDDFT calculations.

As a first example of a canonical plasmonic system, we consider a spherical Na metal nanoparticle (MNP) with radius $a = 65.83\ \mathrm{a}_0$ (≈ 3.5 nm), as schematically depicted in Figure 4.1b. This spherical MNP is the same as the one considered in Chapter 3, where we showed that its size is sufficiently large to ensure a well-developed plasmonic response and, on the other hand, it is small enough for nonlocal effects to noticeably affect the optical response. As discussed in Subsection 1.2.3, individual spherical MNPs support (localized) multipole plasmon resonances characterized by the angular momentum ℓ. This symmetry parameter ℓ in spherical MNPs plays an analogous role to the magnetic quantum number m in cylindrical nanowires, and determines the spatial scale of the charge-density oscillations along the surface. Thus, we tentatively assign $k_\parallel = \ell/a$ for spherical MNPs. The spectrum of multipole plasmons is determined by the multipolar polarizabilities $\alpha_\ell(\omega)$, which are given within the SRF by [see Eq. (3.10)]:

$$\alpha_\ell(\omega) \propto \frac{(\varepsilon(\omega)-1)\left(1+k_\parallel d_\perp(\omega,k_\parallel)\right)}{\varepsilon(\omega)+\frac{\ell+1}{\ell}-(\varepsilon(\omega)-1)\frac{\ell+1}{a}d_\perp(\omega,k_\parallel)}. \tag{4.21}$$

In Eq. (4.21), $\varepsilon(\omega)$ is the dielectric function of the material described within the Drude model (using $\omega_p = 5.89$ eV and $\gamma_p = 0.1$ eV in Eq. (1.10)).

In Figure 4.6a, we compare the imaginary part of $\alpha_\ell(\omega)$, $\mathrm{Im}\{\alpha_\ell(\omega)\}$ (normalized to its maximum), obtained from TDDFT (solid filled curves), nondispersive SRF (left-hand side panel, short-dashed lines) and dispersive SRF (right-hand side panel, long-dashed lines) for different values of ℓ. The TDDFT results are obtained following the procedure described in Chapter 3, and for the nondispersive SRF results we use the parameter $d_\perp(\omega)$ calculated in ref. 296 within the long-wavelength approximation. A clear peak associated with the excitation of the multipolar ℓ

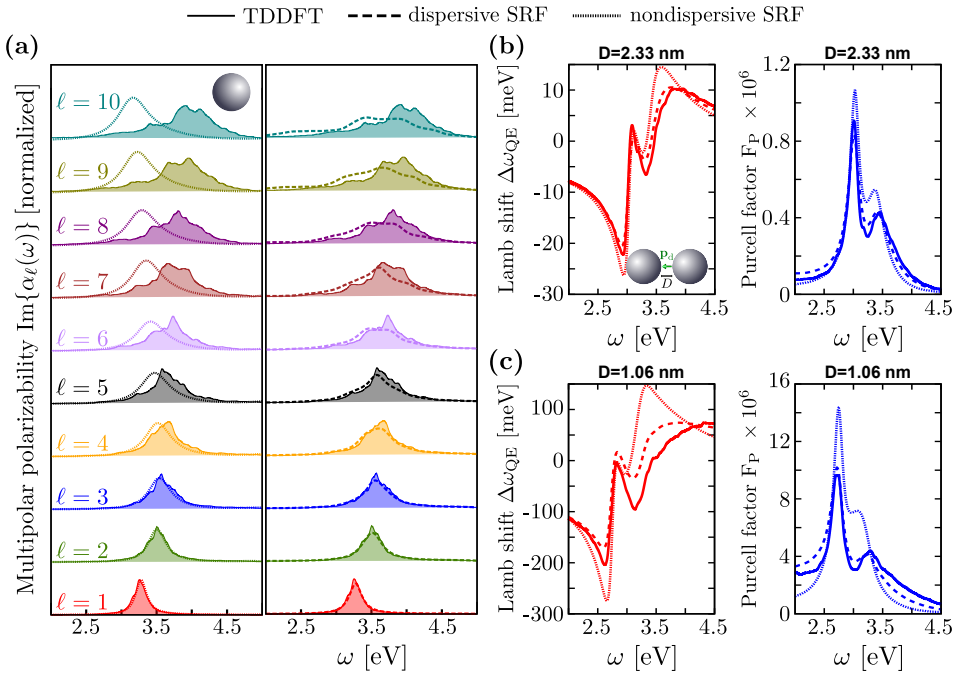

Figure 4.6: Comparison between the results obtained using TDDFT (solid lines), dispersive SRF (long-dashed lines), and nondispersive SRF (short-dashed lines). **(a)** Imaginary part of the first ten multipolar polarizabilities $\alpha_\ell(\omega)$ ($\ell = 1 - 10$). The left-hand side panel presents the comparison between TDDFT and *nondispersive* SRF results, whereas the right-hand side panel presents the comparison between TDDFT and *dispersive* SRF results. Each spectra is normalized to the corresponding maximum value obtained within TDDFT for each value of ℓ. The spectra corresponding to different ℓ are vertically displaced for visibility. The TDDFT results are represented by solid lines with hatched area. **(b,c)** Lamb shift $\Delta\omega_{QE}$ (left-hand side panels) and Purcell factor F_P (right-hand side panels) obtained within the three methods for a point-dipole quantum emitter (QE) at the center of a spherical MNP dimer of radius $a = 65.83$ a_0 (≈ 3.5 nm). The dipole is oriented along the dimer axis, and its transition dipole moment is $\mu = 0.1$ e nm (with e the electron charge). In **(b)**, the gap separation is $D = 2.33$ nm. In **(c)**, $D = 1.06$ nm.

plasmon mode appears in each spectrum of $\mathrm{Im}\{\alpha_\ell\}$, which allows for the discussion on their energies and widths.

The TDDFT results of $\mathrm{Im}\{\alpha_\ell(\omega)\}$ in Figure 4.6a show that the multipole plasmon resonances of order ℓ continuously blueshift with increasing ℓ in the considered range $\ell = 1 - 10$. The resonance broadens as ℓ increases due to the enhancement of surface-enabled Landau damping [64, 66, 194, 259–261]. As already discussed in Chapter 3, the nondispersive SRF accurately reproduces the TDDFT data of $\mathrm{Im}\{\alpha_\ell(\omega)\}$ for low values of $\ell \sim 1 - 4$, but fails to make correct predictions for $\ell \geq 5$. Indeed, for these large values of effective $k_\parallel = \ell/a$, the plasmonic resonances within the nondispersive SRF start to redshift with increasing ℓ in contrast to the continuous blueshift obtained from TDDFT calculations. Thus, the nondispersive SRF predicts multipole plasmon frequencies that deviate significantly from the TDDFT values. In sheer contrast, by accounting for the dependence of the Feibelman parameter $d_\perp$ on $k_\parallel$, the dispersive SRF correctly captures the energy blueshift and broadening of multipole plasmon resonances in $\mathrm{Im}\{\alpha_\ell(\omega)\}$ (see right-hand side panel in Figure 4.6a). Although some quantitative differences emerge for large multipole order $\ell = 7 - 10$, one can observe an overall good agreement between TDDFT and the dispersive SRF results over the entire range of ℓ values considered here. Thus, the dispersive SRF is useful to describe localized multipole plasmon resonances of large order ℓ sustained by small MNPs.

Finally, we address another canonical plasmonic system: a dimer of spherical MNPs. Specifically, we study the case of a point-dipole quantum emitter (QE) located at the center of the gap formed by two identical spherical MNPs with radius $a = 65.83$ $\mathrm{a_0}$ (≈ 3.5 nm), as sketched in Figure 4.1c. This system is identical to the one considered in Chapter 3. The QE is oriented along the axis of the MNP dimer (the z-axis). The gap separation distance, D, is in the nanometer scale, and thus nonlocality strongly influences the optical response of the system, as shown in Chapter 3. We focus on the enhancement of the QE total decay rate given by the Purcell factor $\mathrm{F_P}$ and the change of resonant frequency $\Delta\omega_{\mathrm{QE}}$ (Lamb shift) due to the self-interaction of the QE with the MNP dimer. The Lamb shift is calculated considering a transition dipole moment $\mu = 0.1$ e nm (with e the electron charge). The TDDFT and SRF results are obtained within the nonretarded approximation following the procedure described in Chapter 3, where for the dispersive SRF we use the Feibelman parameter $d_\perp(\omega, k_\parallel)$ obtained in this chapter.

Figure 4.6b shows the Lamb shift $\Delta\omega_{\mathrm{QE}}$ (left-hand side panel) and Purcell factor $\mathrm{F_P}$ (right-hand side panel) obtained for a gap separation $D = 2.33$ nm, as calculated with the three models employed in this chapter (TDDFT, dispersive SRF, and nondispersive SRF). The three approximations show qualitatively good agreement, although the nondispersive SRF results slightly deviate from the TDDFT and dispersive SRF predictions. For this relatively large gap, the excitation of low-ℓ multipole plasmon resonances dominates the response of the MNP dimer to the field created by the point-dipole QE (see Chapter 3), which validates the long-wavelength approximation behind the nondispersive SRF results. Nonetheless, the results obtained within the dispersive SRF are more accurate when compared to TDDFT.

The better performance of the dispersive SRF to describe the electromagnetic QE–MNPs interaction is more evident when considering a smaller gap, which naturally involves larger values of ℓ in the response. Figure 4.6c shows the Lamb shift $\Delta\omega_{\mathrm{QE}}$ and Purcell factor $\mathrm{F_P}$ for a gap separation $D = 1.06$ nm. In this situation, because of the higher spatial confinement of the induced charges at the metal surfaces across the gap, plasmon modes with large multipolar order ℓ become important. These large-ℓ modes have overlapping resonant frequencies and thus contribute to a single broad peak (referred to as the pseudomode, see Chapter 3) at $\omega \sim 3.4$ eV, as revealed by the TDDFT calculations. Since the nondispersive model does not accurately describe the energy of large-ℓ multipolar modes for the individual MNP (Figure 4.6a), it also fails to predict the energy and the width of the plasmon pseudomode obtained within TDDFT for the dimer of small gap. Moreover, the nondispersive SRF strongly overestimates the Purcell factor and the Lamb shift close to the bonding dipolar plasmon (BDP) resonance at $\omega \sim 2.75$ eV because of the contribution of high-ℓ multipolar modes near the BDP frequency within the nondispersive model (see Figure 4.6a). In contrast, the dispersive SRF provides accurate results even for this small gap separation, thus indicating that the dispersive SRF is well suited to correctly account for nonlocality in situations where plasmon-induced charges are characterized by a rapid variation in the direction parallel to the metal surface.

4.3 Summary

In summary, in this chapter we have proposed a *dispersive* SRF that explicitly accounts for the dependence of the Feibelman parameter $d_\perp$ on the wavenumber parallel to the metal surface, $k_\parallel$. Using TDDFT calculations as a reference, we have demonstrated that the *dispersive* SRF is much more accurate than the *nondispersive* SRF, usually implemented in the literature, in describing plasmonic systems characterized by extremely confined induced fields. The dispersive SRF proposed here thus overcomes the limitations of the nondispersive SRF identified in Chapter 3.

Using the analogy between localized multipolar plasmons in infinite cylindrical nanowires of radius R_c and propagating surface plasmons at planar metal–vacuum interfaces, we have demonstrated that m/R_c can be interpreted as a wavenumber parallel to the surface, $k_\parallel = m/R_c$ (here m is the magnetic quantum number). This study has allowed us to obtain the dispersive Feibelman parameter $d_\perp(\omega, k_\parallel = m/R_c)$ using cylindrical nanowires, which is incorporated into the SRF to complete the description based on the long-wavelength value $d_\perp(\omega, k_\parallel = 0)$, used in Chapter 3 and in other recent works [124, 129, 296, 299, 300].

Supported by the examples of cylindrical and spherical metallic nanostructures, we have demonstrated that, in contrast to the nondispersive model, the dispersive SRF accurately describes the nonlocal optical response in extreme situations where the induced charges are characterized by a rapid variation in the direction parallel

to the metal surface (large $k_{\parallel}$). The results shown in this chapter thus contribute to the development of a theoretical model that captures quantum nonlocal effects in extreme situations, while keeping the numerical efficiency and easy implementation into the framework of classical electromagnetic theories [348]. We thus believe that the dispersive SRF proposed in this chapter can be useful to correctly account for optical nonlocality in nanostructured systems with extreme plasmonic field confinement, as it can be the case of metallic nanostructures interacting with fast electrons, MNPs coupled to QEs in close proximity, or MNPs ensembles with extremely narrow junctions. The dispersive SRF substantially improves the perfomance of the nondispersive SRF to describe nonlocality in the optical response of narrow junctions, however it still lacks the description of charge-transfer processes. To account for such effects by using semiclassical models, it would be necessary to further develop the present framework combining the SRF with e.g. a quantum-corrected model [83–87].

CHAPTER 5

ELECTRONIC EXCITON–PLASMON COUPLING IN A NANOCAVITY BEYOND THE ELECTROMAGNETIC INTERACTION PICTURE

The main mechanism that controls the interaction between quantum emitters (QEs) and metallic nanoparticles (MNPs) is the excitation of the QE exciton by the local electric field associated to the MNP plasmon. In previous chapters, the plasmonic response of MNPs is described either classically (Chapter 1) or by using TDDFT simulations that capture nonlocal and quantum surface effects (Chapter 3), while the exciton dynamics of the QE is modeled within the point-dipole approximation. The success of the methodologies used in previous chapters to explain the main features of the optical response in plasmonic nanocavities is due to the dominance of the electromagnetic interaction in the QE–MNP coupling for separations as small as one nanometer [145, 349]. However, at even smaller separations between emitters and metal surfaces, of the order of Ångstroms, another quantum effect becomes important: electronic states localized at the QE and at the MNPs hybridize into "supermolecular" states which modify optical transitions, allowing for electron transfer between the QE and the MNP.

Despite its importance [166, 349–352], the effect of hybridization between the QE and the MNP electronic states as well as the corresponding electron-transfer processes remain largely unexplored in Nanophotonics, as the quantum theoretical treatment of the problem is challenging. It is only recently that such studies have become within the reach of theoretical efforts [107–109, 323, 329] enabling e.g. a better understanding of light emission in tunneling junctions [309–311]. Notably, it has been shown that a QE bridging two MNPs can trigger electron conductance

across subnanometric junctions, which strongly influences the optical and electronic (*optoelectronic*) response of the coupled system [107–109, 329, 353].

In this chapter, we apply a fully quantum many-body approach based on TDDFT to study the optoelectronic response and exciton dynamics in a QE–MNPs system where the QE is located at subnanometric separation from the metallic interfaces. In contrast to the methodologies employed in previous chapters, here we use a TDDFT treatment to describe the electronic structure of *both* the QE and the MNPs. We place particular emphasis on the role of electronic coupling and electron transfer between the QE and the MNPs to unveil the manifestation of these quantum effects in the optical response of the entire coupled system. Importantly, we demonstrate that the modification of the electronic structure of the hybrid QE–MNPs system as well as the broadening of the electronic states of the QE due to charge transfer lead to a breakdown of the classical electromagnetic description of plasmon–exciton interaction. We reveal important quantitative and qualitative differences between quantum TDDFT and classical LRA results of the linewidths and frequencies of the relevant optical modes. Moreover, we also observe the formation of a novel charge-transfer plasmon mode at low frequencies mediated by the emitter electronic structure.

5.1 System and methods

We consider a QE interacting with a plasmonic dimer formed by two spherical MNPs. As sketched in Figure 5.1a, the QE placed in the middle of a plasmonic nanogap is illuminated by a plane wave polarized along the dimer axis (z-axis). In this chapter, the gap separation D is varied to explore different regimes of electronic QE–MNPs coupling, ranging from electronically decoupled QE–MNPs (large D) to electronically coupled ones (small D). The calculation of the optical response is performed within the Kohn–Sham (KS) scheme of time-dependent density functional theory (TDDFT) [70–72, 189] as introduced in Section 2.2, which successfully incorporates quantum phenomena such as many-body and single electron–hole pair excitations, electronic spill-out, nonlocal screening or electron tunneling in (sub)-nanometric metallic cavities [79, 125, 202, 211, 212, 214, 337, 338, 342].

The electronic structure of the MNPs is described within the jellium model of free-electron metals [194, 200] introduced in Subsection 2.1.2, using a Wigner–Seitz radius of $r_s = 4$ $\mathrm{a_0}$ that corresponds to sodium. Each MNP contains 638 conduction electrons (radius $a = 34.4$ $\mathrm{a_0} \approx 1.8$ nm), and the Fermi level of the MNPs stands at $\mathrm{E_F} = -2.86$ eV below the vacuum level. In contrast to the point-dipole approximation employed in previous chapters to model the QE (e.g. in Chapter 3), here we consider a "more realistic" QE that has a finite spatial extension. The electronic structure of the QE is described as a two-level system using a model potential $V_{\mathrm{QE}}(\mathbf{r})$ (see below). The optical response of the coupled QE–MNPs is addressed using the wave-packet propagation (WPP) method in cylindrical coordinate system, as introduced in Subsection 2.3.2. To excite the system, we apply an external potential $V_{\mathrm{ext}}(\mathbf{r}, t) = \mathrm{E}_0\ \Delta t\ z\ \delta(t)$ [Eq. (2.67)], which

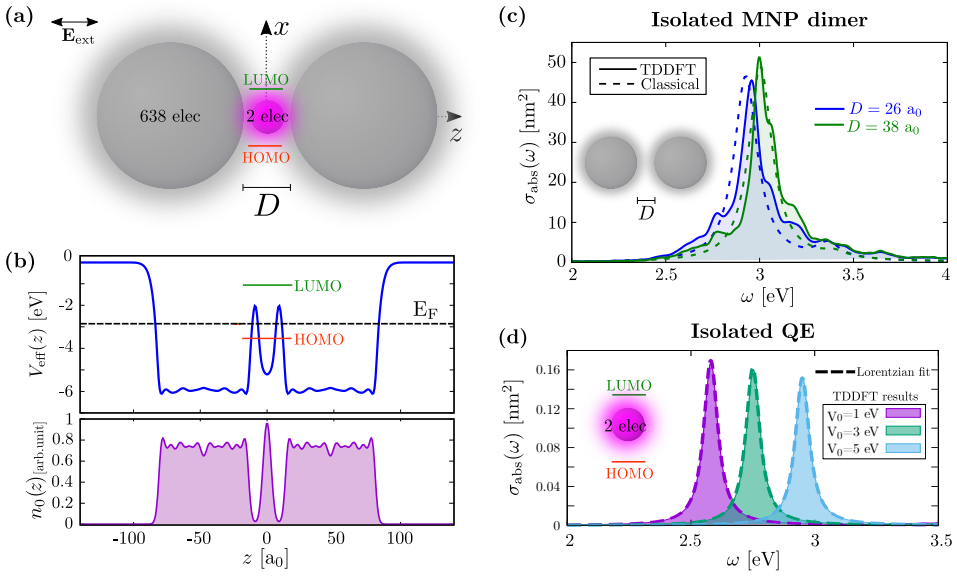

Figure 5.1: **(a)** Sketch of the system studied in this chapter. A QE with a single optically-allowed HOMO–LUMO transition is located in the middle of a gap of size D formed by two spherical MNPs. The QE and each MNP contain 2 and 638 conduction electrons, respectively. **(b)** Effective one-electron potential $V_{\text{eff}}(\mathbf{r})$ (top) and equilibrium electron density $n_0(\mathbf{r})$ (bottom) along the symmetry z-axis for the coupled QE–MNPs system with gap size $D = 26$ a$_0$. The HOMO and LUMO energy levels of the isolated QE are represented by red and green lines, respectively. The Fermi level $\text{E}_\text{F} = -2.86$ eV of the MNPs is shown by the black dashed line. **(c)** Absorption cross-section spectra $\sigma_{\text{abs}}(\omega)$ of the isolated MNP dimer for $D = 26$ a$_0$ (blue line) and $D = 38$ a$_0$ (green). Dashed and solid lines correspond to the results obtained with classical LRA and TDDFT simulations, respectively. **(d)** Absorption cross-section spectra $\sigma_{\text{abs}}(\omega)$ of the isolated QE for different values of the parameter V_0 [Eq. (5.3)] used to control optical and electronic properties of the QE.

corresponds to plane-wave illumination polarized along the z-axis.

Prior to studying the coupled QE–MNPs system, we summarize in Figure 5.1c the TDDFT results of the absorption spectra of the isolated MNP dimer of radius $a = 34.4$ a$_0$ ≈ 1.8 nm considered in this chapter (solid lines). Gap separation distance of $D = 38$ a$_0$ (green) and $D = 26$ a$_0$ (blue) are considered here. The optical response of the MNP dimer is characterized by a bonding dipolar plasmon (BDP) resonance at $\omega_{\text{BDP}} \sim 3$ eV. As expected from the results shown in Chapter 1 and Chapter 2, this BDP mode redshifts when reducing the gap separation because of the increased capacitive coupling between the two MNPs [354]. As a reference, in Figure 5.1c we also show the results from classical (nonretarded) LRA calculations (dashed lines) introduced in Section 1.1. The MNPs are described in this case with a Drude dielectric function [Eq. (1.10)] using an "effective" plasma frequency $\omega_p = 5.43$ eV and intrinsic damping parameter $\gamma_\text{p} = 0.15$ eV. These parameters are chosen to provide reasonably good agreement between the TDDFT and classical

LRA results of the absorption spectrum of the individual MNP (not shown) [125]. Using this value of $\omega_p = 5.43$ eV (i.e., slightly smaller than the nominal bulk plasma frequency $\omega_p = 5.89$ eV of sodium for $r_s = 4$ a_0, Eq. (1.12)) allows us to account for the redshift of the dipolar plasmon (DP) frequency of the small individual MNP because of the electron spill-out and dynamical screening introduced in Subsection 2.3.1. In addition, the damping parameter $\gamma_p = 0.15$ eV used in LRA in this chapter accounts for all the decay channels of the plasmon excitation including the contribution of surface-enabled Landau damping. Further, in all classical LRA calculations we also introduce a gap scaling of $\Delta = 3.4$ a_0 to (partially) account for the spill-out of the induced electron density with respect to the geometrical surface of the MNPs in the dimer configuration (correctly captured by the TDDFT simulations, as shown in Subsection 2.3.2). Introducing the gap scaling $\Delta = 3.4$ a_0 is similar to considering the Feibelman parameter $d_\perp(\omega)$ employed in Chapter 3 and Chapter 4, as reported in ref. 58. In this thesis we found that this procedure is valid to reproduce the redshift of the BDP of the MNP dimer, however it overstimates the strength of the higher-order plasmon modes such as the BQP. Thus, nonlocal and quantum effects are partially introduced in the classical LRA calculations of this chapter in an effective manner, which allows us to correctly reproduce the TDDFT spectra of the isolated MNP dimer.

We next introduce in Subsection 5.1.1 the TDDFT description adopted in this chapter to model the QE, which allows for studying the effect of the electronic interaction between the QE and MNPs states.

5.1.1 Characterization of the model quantum emitter (QE)

The electronic structure of the QE is described within the free-electron jellium model (Subsection 2.1.2), in a similar way as we model the MNPs. We consider a spherical QE of radius $R_{\mathrm{QE}} = 5$ a_0 (≈ 0.26 nm) containing two valence electrons. The spin-restricted case is considered [355]. In the ground-state configuration of the QE, the total spin is zero, and the 2 electrons with opposite spins occupy the same Kohn–Sham (KS) valence orbital. From the charge neutrality condition, the positive background density n_+ [Eq. (2.13)] representing the atomic cores of the QE and spreading over its spatial extent satisfies

$$\frac{4}{3}\pi R_{\mathrm{QE}}^3 n_+ = 2. \tag{5.1}$$

The occupied ($j = 1$) and unoccupied ($j = 2, 3, 4, \dots$) one-electron KS orbitals $\Psi^0_{\mathrm{QE},j}(\mathbf{r})$ of the QE and their energies $\epsilon_{\mathrm{QE},j}$ are obtained from the time-independent KS equation of DFT [Eq. (2.5)],

$$\hat{H}[n^0_{\mathrm{QE}}(\mathbf{r})]\Psi^0_{\mathrm{QE},j}(\mathbf{r}) = \epsilon_{\mathrm{QE},j}\Psi^0_{\mathrm{QE},j}(\mathbf{r}), \tag{5.2}$$

where $\epsilon_{\mathrm{QE},j}$ are the one-electron energy levels of the QE, and we use spherical coordinates as described in Subsection 2.3.1. The equilibrium electron density of the isolated QE, $n^0_{\mathrm{QE}}(\mathbf{r})$, is given in this case by $n^0_{\mathrm{QE}}(\mathbf{r}) = 2|\Psi^0_{\mathrm{QE},1}(\mathbf{r})|^2$, with the

factor 2 accounting for spin degeneracy.

Controlling the values of the one-electron energy levels $\epsilon_{\mathrm{QE},j}$ of the QE states allows us to study different situations of the QE–MNPs coupling, where the QE exciton can be either in resonance or out of resonance with the main BDP resonance of the MNP dimer at $\omega_{\mathrm{BDP}} \sim 3$ eV (see Figure 5.1c). To this end, we introduce in the Hamiltonian $\hat{H}[n^0_{\mathrm{QE}}(\mathbf{r})]$ [Eq. (5.2)] an additional attractive potential $V_{\mathrm{QE}}(\mathbf{r})$ [216]. This attractive potential $V_{\mathrm{QE}}(\mathbf{r})$ can be thought of as a pseudopotential due to the atomic cores, it is localized in the spatial region of the QE, and it is given by

$$V_{\mathrm{QE}}(\mathbf{r}) = -V_0 e^{-4|\mathbf{r}|^2/R^2_{\mathrm{QE}}}. \tag{5.3}$$

The one-electron energy levels $\epsilon_{\mathrm{QE},j}$ of the QE states can be thus modified by changing the parameter V_0.

In this chapter, we refer to $\Psi^0_{\mathrm{QE},1}(\mathbf{r})$ as the *highest occupied molecular orbital* (HOMO), which is a $1s$ ($\ell = 0, m = 0$) orbital with zero orbital momentum (ℓ) and magnetic quantum number (m). Thus, the electronic configuration of the QE is $1s^2$. The energy level of the HOMO is $\mathrm{E_{HOMO}} = \epsilon_{\mathrm{QE},1}$. For the values of V_0 [Eq. (5.3)] considered in this chapter, we find only three energy-degenerate unoccupied KS orbitals accessible for optical transitions from the ground state. These orbitals correspond to the $2p$-shell and are characterized by the orbital momentum $\ell = 1$ and magnetic quantum numbers $m = 0, \pm 1$. With $\psi_{\mathrm{QE},2p}(r)$ the radial part of the KS orbital of the isolated QE, we can define

$$\begin{aligned}
\Psi^0_{\mathrm{QE},2}(\mathbf{r}) &= Y^0_1(\theta,\varphi)\psi_{\mathrm{QE},2p}(r), \\
\Psi^0_{\mathrm{QE},3}(\mathbf{r}) &= Y^{-1}_1(\theta,\varphi)\psi_{\mathrm{QE},2p}(r), \\
\Psi^0_{\mathrm{QE},4}(\mathbf{r}) &= Y^1_1(\theta,\varphi)\psi_{\mathrm{QE},2p}(r),
\end{aligned} \tag{5.4}$$

where $Y^m_\ell(\theta,\varphi)$ are the spherical harmonics. Because of the symmetry of the system considered in this chapter (see Figure 5.1a), with an incident electromagnetic wave polarized along the z-axis, the electronic transitions preserve the magnetic quantum number m, and thus are effective between the ground-state $1s$ KS orbital and the $2p$ ($\ell = 1, m = 0$) KS orbital $\Psi^0_{\mathrm{QE},2}(\mathbf{r})$. Thus, the optical absorption of the QE is determined by the $1s \rightarrow 2p$ transition. For the sake of simplicity, in this chapter we refer to $\Psi^0_{\mathrm{QE},2}(\mathbf{r})$ as the *lowest unoccupied molecular orbital* (LUMO).

The free parameter V_0 of the potential $V_{\mathrm{QE}}(\mathbf{r})$ [Eq. (5.3)] is used to control the energy levels of the HOMO ($\mathrm{E_{HOMO}} = \epsilon_{\mathrm{QE},1}$) and the LUMO ($\mathrm{E_{LUMO}} = \epsilon_{\mathrm{QE},2}$) of the QE, as schematically depicted in Figure 5.1a by the red and green lines, respectively. As a consequence, the parameter V_0 also determines the oscillator strength α^0_{QE} and transition frequency ω_{QE} of the QE exciton [Eq. (1.54)] relevant in the optical response of the coupled QE–MNPs system. We show in Table 5.1 the energy levels $\mathrm{E_{HOMO}}$ and $\mathrm{E_{LUMO}}$, as well as the oscillator strength α^0_{QE} and transition frequency ω_{QE} of the QE exciton, obtained for the three different values of the background potential $V_0 = 1$ eV, 3 eV, and 5 eV [Eq. (5.3)] considered in this chapter. The values of $\mathrm{E_{HOMO}}$ and $\mathrm{E_{LUMO}}$ are directly obtained from time-independent DFT calculations following the procedure described in

Subsection 2.3.1, whereas the values of α^0_{QE} and ω_{QE} are estimated by fitting the absorption cross section spectrum $\sigma_{\mathrm{abs}}(\omega)$ of the isolated QE calculated within TDDFT to the classical value obtained from Eq. (1.55) and Eq. (1.49) using the point-dipole approximation (see Figure 5.1d). We use an intrinsic damping parameter $\gamma_{\mathrm{QE}} = 70$ meV in the classical LRA calculations for the three different situations determined by V_0 considered in this chapter. The value of $\gamma_{\mathrm{QE}} = 70$ meV corresponds to the attenuation parameter $\eta = 70$ meV used in the filter given by Eq. (2.56) to obtain the frequency-resolved response from real-time TDDFT simulations in this chapter.

	$\mathrm{E_{HOMO}}$ [eV]	$\mathrm{E_{LUMO}}$ [eV]	ω_{QE} [eV]	α^0_{QE} [au]
V_0 =1 eV	-3.29	-1.23	2.58	1.70
V_0 =3 eV	-3.40	-1.16	2.75	1.62
V_0 =5 eV	-3.57	-1.08	2.95	1.52

Table 5.1: Energy levels of the HOMO ($\mathrm{E_{HOMO}}$) and the LUMO ($\mathrm{E_{LUMO}}$) of the isolated QE of radius $R_{\mathrm{QE}} = 5$ $\mathrm{a_0}$ as obtained from time-independent DFT calculations for different values of V_0, together with the oscillator strength α^0_{QE} and resonant transition frequency ω_{QE} obtained by fitting the TDDFT results according to the classical value of the absorption cross section obtained obtained from Eq. (1.55) using the point-dipole approximation.

As shown in Table 5.1, the resonant transition frequency ω_{QE} of the QE does not match exactly the energy difference between the one-electron energy levels obtained from time-independent DFT calculations, i.e., $\omega_{\mathrm{QE}} \neq \mathrm{E_{LUMO}} - \mathrm{E_{HOMO}}$. Indeed, as pointed out in Chapter 2, when introducing the Kohn–Sham scheme of TDDFT adopted in this thesis (see Section 2.1), $\mathrm{E_{HOMO}}$ and $\mathrm{E_{LUMO}}$ represent the energy levels of a fictitious non-interacting electron system, so that the resonant frequencies of the interacting system will be renormalized with respect to the non-interacting one *via* Coulomb and exchange–correlation potentials [192, 193].

5.2 Results and discussion

5.2.1 Influence of the QE exciton quenching at optical frequencies

Once the optical response of the isolated constituents has been determined, we can analyze how the optical response of the hybrid system is affected by the optoelectronic coupling between the QE and the MNP dimer. To this end, we first compare in Figure 5.2 the classical LRA (panels a,c) and quantum TDDFT (panel b,d) results of the absorption cross section spectra $\sigma_{\mathrm{abs}}(\omega)$ of the QE–MNPs system as a function of gap separation D. The gap separation is varied from $D = 40$ $\mathrm{a_0}$ to $D = 16$ $\mathrm{a_0}$, which allows for covering different interaction regimes and for observing the onset of electronic hybridization in the system. We consider two different QEs in Figure 5.2, characterized by a transition frequency $\omega_{\mathrm{QE}} = 2.58$ eV in panels a,b ($V_0 = 1$ eV in Eq. (5.3), see Table 5.1), and $\omega_{\mathrm{QE}} = 2.75$ eV in panels c,d

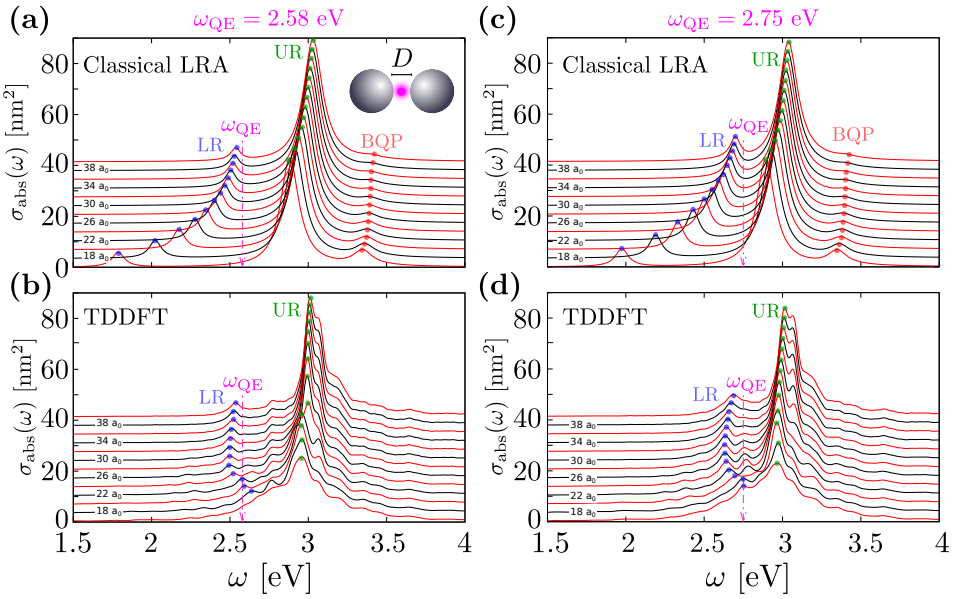

Figure 5.2: Optical absorption of the hybrid QE–MNPs system considered in this chapter. Waterfall plot of the absorption spectra as obtained from **(a,c)** classical LRA, and **(b,d)** TDDFT simulations for a gap separation distance ranging from $D = 16$ a$_0$ to $D = 40$ a$_0$ in steps of 2 a$_0$. The D value is indicated at each second spectra marked by the black line. Results are shown as a function of frequency, ω. The transition frequency ω_{QE} of the isolated QE is marked with a vertical magenta arrow in all the panels. The blue (LR), green (UR), and red (BQP) dots indicate the resonance frequencies of the main modes of the system. Panels **(a,b)** correspond to $\omega_{QE} = 2.58$ eV, and **(c,d)** to $\omega_{QE} = 2.75$ eV. Both situations represent a QE exciton out of resonance with the main BDP of the MNP dimer at $\omega_{BDP} \sim 3$ eV.

($V_0 = 3$ eV). The two situations correspond to a QE transition frequency ω_{QE} out of resonance with the BDP of the MNP dimer at $\omega_{BDP} \sim 3$ eV (see Figure 5.1c), and therefore the observed effects are qualitatively very similar in both cases. We thus discuss the two off-resonant QE–MNPs systems together, and will consider a resonant situation at the end of this subsection.

To make an intuitive link with the classical picture of the point-dipole QE in proximity to a MNP dimer, we first outline the classical results of the absorption spectra $\sigma_{abs}(\omega)$ of the coupled system shown in Figure 5.2a,c. Three resonant features are obtained within the framework of classical electromagnetic theory for the two off-resonant QEs considered: a lower resonance (LR; blue dots) considerably shifting to lower frequencies as the gap separation is reduced, an upper resonance (UR; green dots) at $\omega_{UR} \sim 3$ eV, and a bonding quadrupolar plasmon (BQP; red dots) at $\omega_{BQP} \sim 3.4$ eV, more pronounced for narrow gaps. The LR shifts from $\omega_{LR} \sim 2.5$ eV to ~ 1.8 eV in the case of $\omega_{QE} = 2.58$ eV (panel a), and from $\omega_{LR} \sim 2.7$ eV to ~ 2 eV in the case of $\omega_{QE} = 2.75$ eV (panel c).

For large interparticle distance, $D = 30 - 40$ a$_0$, the spectra in Figure 5.2b,d

obtained within the TDDFT approach are in good agreement with classical LRA results (Figure 5.2a,c). Indeed, in these situations, the electron densities of the individual nanoconstituents do not spatially overlap, thus avoiding the hybridization of the electronic orbitals. At these large separations, the assignment of the underlying modes can be performed using their asymptotic behavior. First, the LR can be associated with the QE exciton. This excitonic frequency is slightly redshifted with respect to the transition frequency ω_{QE} of the isolated QE due to the interaction with the MNPs (Lamb shift) [103]. The TDDFT calculations of the induced electron density confirm the excitonic nature of the LR branch, characterized by a strongly polarized QE, as observed in Figure 5.3a (the case of $\omega_{\mathrm{QE}} = 2.58$ eV is shown). On the other hand, the UR at $\omega_{\mathrm{UR}} \sim 3$ eV is associated with the BDP plasmon mode of the isolated MNP dimer. The induced electron density at the QE appears polarized in the direction opposite to the main dipole induced at the MNPs, since ω_{UR} is higher than the exciton frequency ω_{QE} of the isolated QE (see Figure 5.3b).

Upon decreasing the gap separation below $D = 26$ a$_0 \approx 1.4$ nm, the quantum nature of the electron dynamics strongly affects the overall shape of the absorption profile. The BQP mode shown by the classical LRA approach at $\omega_{\mathrm{BQP}} \sim 3.4$ eV is not developed in the TDDFT results. This is because, for these small particles, surface-enabled Landau damping prevents the formation of high-order plasmonic resonances [124, 336], as discussed in Section 2.3.2 and Chapter 3. Moreover, for small gap separations, the TDDFT simulations predict a smaller redshift and stronger broadening of the UR branch as compared to classical results. These effects can be mainly ascribed to quantum phenomena such as nonlocality and finite-size effects that are important for such small MNPs, but also to electron transport between the MNPs mediated by the electronic structure of the QE [329], as we further confirm in Subsection 5.2.2. The induced electron density shown in Figure 5.3d indicates that the BDP character of the UR mode is preserved for these small separations.

The most dramatic difference between quantum TDDFT and classical LRA results is observed for the LR branch with excitonic asymptotic character. Classical calculations predict a strong and continuous redshift of the LR with decreasing gap separation distance due to the electromagnetic interaction, i.e., the interaction between the QE exciton dipole and its induced screening charges at the surfaces of the MNPs across the gap. In sheer contrast to this classical prediction, within the fully quantum model, the LR branch blueshifts with decreasing gap size for $D \leq 26$ a$_0$, and gradually disappears loosing its excitonic character and evolving into a broad low-frequency shoulder of the UR for the smallest gap size considered in Figure 5.2b,d ($D = 16$ a$_0$). This can be observed in Figure 5.3c, where the loss of the exciton character can be identified through the spread of the induced electron density over the MNPs (compare panels a and c).

The blueshift of the LR branch with decreasing separation and its subsequent disappearance shown in Figure 5.2b,d are direct consequences of the hybridization between the electronic states of the QE and those of the MNPs. The excited electron initially localized on the $2p$ LUMO of the QE can tunnel through the potential

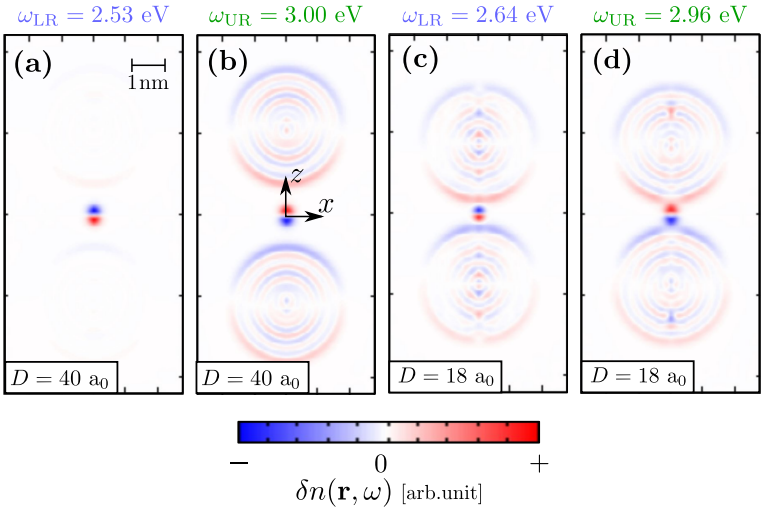

Figure 5.3: TDDFT results of the induced electron density $\delta n(\mathbf{r}, \omega)$ (red for positive and blue for negative sign) for different optical resonances of the QE–MNPs system for $\omega_{QE} = 2.58$ eV ($V_0 = 1$ eV in Eq. (5.3)). The resonance frequency is indicated at the top of each panel. Panels **(a)** and **(b)** correspond to a gap separation distance $D = 40$ a$_0$, and **(c)** and **(d)** to $D = 18$ a$_0$, as indicated. Each snapshot is taken at the instant of time t when the absolute value of the total dipole moment of the system is maximum. Results are plotted in the (x, z)-plane, and the system holds axial symmetry with respect to the z-axis.

barrier separating the QE from the MNPs. The electron transfer from the QE into the empty states of the MNPs above the Fermi level results in the quenching of the QE signature in the optical response [166]. This electronic interaction between the QE and the MNPs can be clearly observed in Figure 5.4, where we show the evolution of the projected density of electronic states (PDOS) [229] upon decreasing of the dimer gap separation D for the two off-resonant QEs considered so far (panel a: $V_0 = 1$ eV, $\omega_{QE} = 2.58$ eV, panel b: $V_0 = 3$ eV, $\omega_{QE} = 2.75$ eV). Due to the azimuthal symmetry of the system, the magnetic quantum number m is a preserved quantity, so that the HOMO can only couple to electronic states with $m = 0$. Consistently, the PDOS localized at the QE is calculated within the $m = 0$ symmetry subspace in the region of the QE using the WPP method as described in Subsection 2.2.1. To this end, we propagate a Gaussian-like initial wave packet $\Phi_0(\mathbf{r}) = Ce^{|\mathbf{r}-\mathbf{r}_0|^2/4}$ (C is a normalization constant) centered at the dimer z-axis at $\mathbf{r}_0 = \frac{1}{2} R_{QE}\, \hat{\mathbf{z}}$ (with the center of the QE at the origin of coordinates, and $R_{QE} = 5$ a$_0$ the radius of the QE).

For large separation distance, $D \sim 30 - 40$ a$_0$, the PDOS in Figure 5.4 shows two well-defined peaks corresponding to the HOMO and LUMO of the QE. Thus, the excitation of the HOMO–LUMO $1s \rightarrow 2p$ electronic transition leads to an induced dipole moment that can be correctly described within a classical point-dipole approximation. However, upon reducing D, the electronic states localized

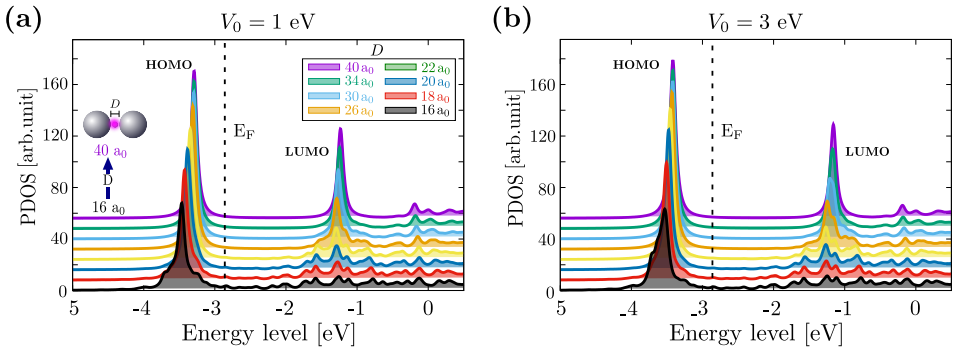

Figure 5.4: Projected density of electronic states (with $m = 0$ symmetry) localized at the QE. Results are shown as a function of the electron energy for different values of the gap size D ranging from $D = 16$ a_0 to $D = 40$ a_0 as displayed in the inset. The Fermi level $E_F = -2.86$ eV of the MNPs is depicted by a vertical dashed line. Panel **(a)** correspond to the results obtained for $V_0 = 1$ eV in Eq. (5.3) (resulting in $\omega_{QE} = 2.58$ eV), and panel **(b)** to $V_0 = 3$ eV ($\omega_{QE} = 2.75$ eV).

at the QE experience a broadening which reveals an increase of the rate of electron transfer between the QE and the MNPs [229]. The HOMO has higher binding energy and thus it is more localized in space as compared to the LUMO. For this reason, the coupling of the HOMO with the MNPs is smaller, and its resonance in the PDOS is well defined and preserved even for the smallest separation of the gap, $D = 16$ a_0, considered here. As D is decreased, the HOMO energy shifts to lower values owing to the increase of the Coulomb interaction with the MNPs. In contrast, the less bound and thus more spatially extended LUMO strongly hybridizes with the unoccupied states of the MNPs. As a consequence, the LUMO resonance in the PDOS dramatically broadens when narrowing the gap. Finally, for smaller gaps $D \sim 20$ a_0, the peak of the LUMO vanishes, revealing the absence of a well-defined unoccupied electronic state localized in the QE which could be optically accessible. We can describe this effect as the electronic quenching of the QE-localized dipole expressed in the optical excitation [166]. Indeed, in this situation the excited electron is shared between the LUMO of the QE and the MNPs electronic states.

The modifications of the HOMO and LUMO by the electronic interactions between the QE and the MNPs shown in Figure 5.4 drastically affect the coupling between the QE excitation and light as identified in Figure 5.2b,d, and lead to (i) the blueshift of the LR mode for gap sizes below $D \sim 26$ a_0, and (ii) the progressive transformation of the LR mode into a broad spectral feature appearing as a shoulder of the UR mode. The excitation in this case is built up by the hole localized in the HOMO of the QE and an excited electron delocalized over the QE–MNPs system.

Resonant situation

To demonstrate that the underlying physics owing to quantum effects holds irrespective of the detuning between ω_{QE} and ω_{BDP}, we analyze next in Figure 5.5 the situation where the exciton frequency of the isolated QE $\omega_{\mathrm{QE}} = 2.95$ eV ($V_0 = 5$ eV in Eq. (5.3), see Table 5.1) is in resonance with the main BDP of the MNP dimer at $\omega_{\mathrm{BDP}} \sim 3$ eV. In particular, this choice is convenient to analyze the regime of strong electromagnetic coupling (or, in short, strong coupling) between the exciton and the plasmon, where the coupling strength g overcomes the losses and hybrid polaritonic states are formed.

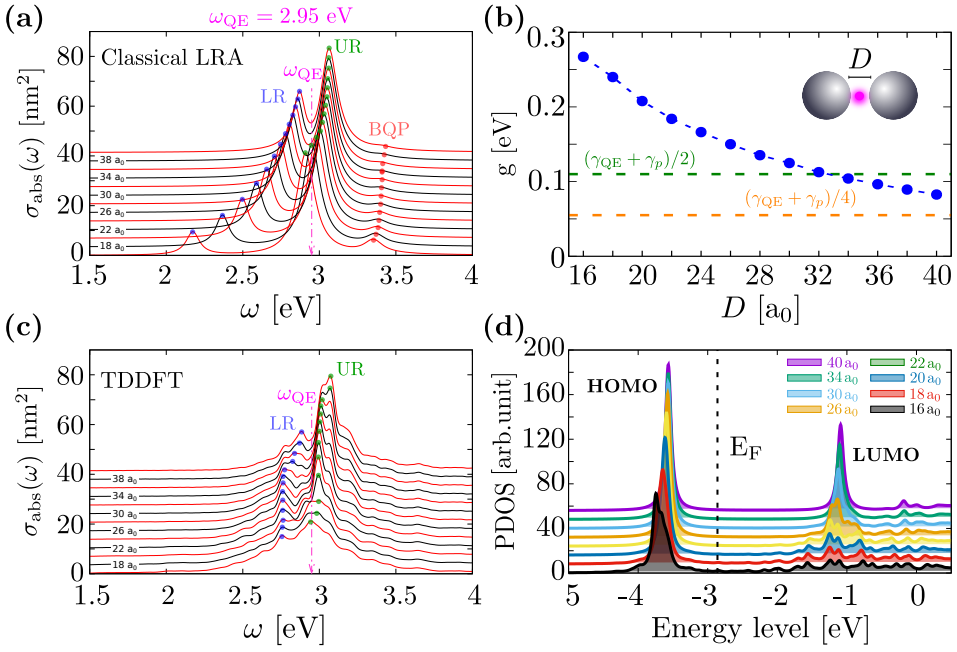

Figure 5.5: **(a)** Waterfall plots of the optical absorption spectra of the resonantly coupled QE–MNPs system obtained from classical LRA calculations. The incident electromagnetic plane wave is polarized along the dimer axis (z-axis). Results are shown as a function of the frequency ω for gap sizes ranging from $D = 16$ a$_0$ to $D = 40$ a$_0$ in steps of 2 a$_0$. The D value is indicated at each second spectra marked by the black lines. The blue (lower resonance, LR), green (upper resonance, UR), and red (bonding quadrupolar plasmon, BQP) dots indicate the main modes of the system. The exciton frequency of the isolated QE, $\omega_{\mathrm{QE}} = 2.95$ eV (marked with vertical magenta arrows), is close to the dominant BDP resonance of the MNP dimer. **(b)** Blue dashed line with dots: coupling strength g obtained for the resonant QE–MNPs system for different values of the gap size D [Eq. (1.60)]. The values $(\gamma_{\mathrm{QE}} + \gamma_p)/4$ and $(\gamma_{\mathrm{QE}} + \gamma_p)/2$ are drawn by orange and green lines, respectively. **(c)** Same as in panel (a) but for the results obtained within the TDDFT model. **(d)** PDOS (with $m = 0$ symmetry) localized at the QE for the resonant QE–MNPs system characterized by $V_0 = 5$ eV in Eq. (5.3). Results are shown as a function of the electron energy for different values of the gap size D ranging from $D = 16$ a$_0$ to $D = 40$ a$_0$ as displayed in the inset.

The classical LRA results of $\sigma_{\mathrm{abs}}(\omega)$ in Figure 5.5a show a splitting between the LR (blue dots) and the UR (green dots) with respect to the resonant frequency ω_{QE} of the isolated QE already for large gap separation distance $D = 40$ a$_0$. This LR–UR splitting is a signature of the strong coupling between the QE exciton and the BDP resonance of the MNP dimer, as we further confirm by analyzing in Figure 5.5b the coupling strength g. The coupling strength g is obtained by fitting the classical LRA results of $\sigma_{\mathrm{abs}}(\omega)$ to the spectra obtained from the coupled harmonic-oscillator model introduced in Section 1.4.3 [Eq. (1.60)]. Figure 5.5b shows that, for the largest distance considered ($D = 40$ a$_0$), the criterion $g > (\gamma_{\mathrm{MNP}} + \gamma_{\mathrm{QE}})/4$ often used to identify strong coupling is satisfied. With decreasing D, the LR–UR frequency difference in Figure 5.5a strongly increases within the classical LRA model owing to the stronger electromagnetic coupling between the exciton and the plasmon. This is consistent with the increase of g, observed in Figure 5.5b, which satisfies the more restrictive criterion $g > (\gamma_{\mathrm{MNP}} + \gamma_{\mathrm{QE}})/2$ for smaller gaps $D \leq 32$ a$_0$. Moreover, within the classical LRA framework, the higher-order plasmonic modes of the MNPs contribute to the electromagnetic interactions between the dimer and the QE for small gap separations. The effect of these higher-order modes, well documented for isolated dimer antennas [23], results here in an additional redshift of both the LR and UR branches, which explains why the UR branch can appear at lower frequencies than the exciton frequency $\omega_{\mathrm{QE}} = 2.95$ eV of the isolated QE. Results in Figure 5.5a,b thus demonstrate that the resonant QE–MNPs system would be in the strong-coupling regime according to the classical LRA description.

The TDDFT results of $\sigma_{\mathrm{abs}}(\omega)$ in Figure 5.5c also show a splitting between the LR and the UR with respect to ω_{QE} for large gap separation distance $D = 40$ a$_0$, although the strength of the LR is weaker than the one predicted by the classical model. This difference is a consequence of the nonlocality and finite-size effects (introduced in Section 2.3) that affect the optical response of the isolated MNP dimer, as confirmed by the analysis shown in Subsection 5.2.2 below. The general similarity between classical and TDDFT results for large separation occurs because there is no QE exciton quenching produced by electronic hybridization for such large separation. At those distances the electronic QE–MNPs coupling does not play a role. However, upon reducing the gap size D, the electronic orbitals of the QE hybridize with those of the MNPs. As shown in Figure 5.5d, the LUMO evolves into a broad structure reflecting the fast transfer of the excited electron between the LUMO of the QE and the conduction-band states of the MNPs quantized by the finite-size effect. This electronic interaction has an immediate consequence on the optical response of the strongly coupled QE–MNPs system since it hinders the energy transfer between the QE and the MNPs, thus attenuating the UR–LR splitting in exciton-plasmon polariton systems as well as producing a progressive merging of the LR and UR branches into a broad spectral feature when decreasing gap separation D. In this situation, strong electromagnetic coupling is, therefore, frustrated due to electronic QE–MNPs coupling.

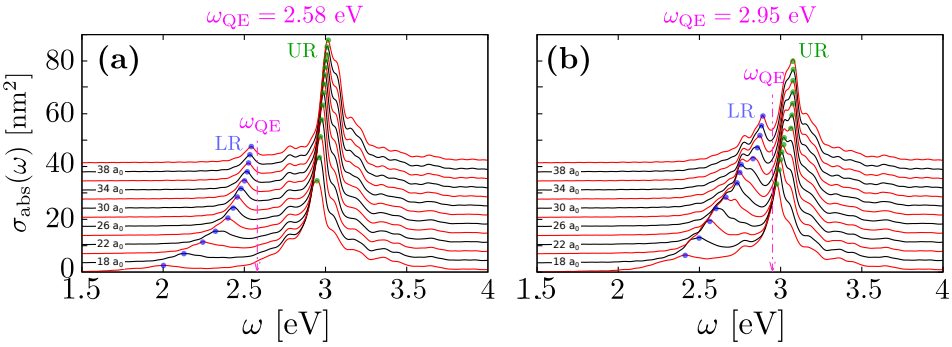

Figure 5.6: Absorption cross-section spectra $\sigma_{\mathrm{abs}}(\omega)$ of the studied QE–MNPs system, as obtained from the semiclassical model employed in this section. This semiclassical approach is based on the self-interaction Green's function [Eq. (1.57)] and considers that the QE is a classical point dipole, however $\hat{\mathbb{G}}(\mathbf{r}_{\mathrm{QE}}, \mathbf{r}_{\mathrm{QE}}, \omega)$, $\mathbf{E}^{\mathrm{ind}}(\mathbf{r} = \mathbf{r}_{\mathrm{QE}}, \omega)$, $\hat{\alpha}_{\mathrm{MNP}}(\omega)$ and $\hat{\alpha}^{\mathrm{QE}}_{\mathrm{MNP}}(\omega)$ are obtained from TDDFT simulations of the isolated MNP dimer. Results are shown as a function of the frequency ω for gap size ranging from $D = 16$ a$_0$ to $D = 40$ a$_0$ in steps of 2 a$_0$. Panel **(a)** corresponds to the results obtained for $\omega_{\mathrm{QE}} = 2.58$ eV, and panel **(b)** to $\omega_{\mathrm{QE}} = 2.95$ eV.

5.2.2 Quantum finite-size effects vs. electronic QE–MNPs coupling

In order to gain a better understanding of the role played by the electronic QE–MNPs coupling in the optical response, and to discard nonlocal and finite-size effects as studied in Chapter 3 in connection with QE exciton quenching, we apply here a *semiclassical*[27] approach to the current QE–MNPs system. This semiclassical approach adopts the self-interaction Green's function formalism (see Subsection 1.4.2), where the QE is introduced as a classical point dipole. The dipole moments induced at the MNPs and at the QE are then obtained from Eq. (1.57). However, the quantities $\hat{\mathbb{G}}(\mathbf{r}_{\mathrm{QE}}, \mathbf{r}_{\mathrm{QE}}, \omega)$, $\mathbf{E}^{\mathrm{ind}}(\mathbf{r} = \mathbf{r}_{\mathrm{QE}}, \omega)$, $\hat{\alpha}_{\mathrm{MNP}}(\omega)$ and $\hat{\alpha}^{\mathrm{QE}}_{\mathrm{MNP}}(\omega)$ are obtained from the TDDFT simulations of the MNP dimer, as described in Subsection 2.3.2 and Chapter 3. This semiclassical approach naturally includes finite-size effects on the response of the MNP dimer such as electron spill-out, nonlocality, surface-enabled Landau damping, and single electron–hole transitions. However, since the QE is introduced as a classical point dipole, the electronic coupling between the MNPs and the QE, as well as the actual electronic structure of the QE and the finite-size extension of its transition density are not accounted for. Thus, we expect that the differences between TDDFT and the semiclassical approach reveal the effect of electronic hybridization, only accounted for within the fully quantum TDDFT model.

We show in Figure 5.6 the absorption cross-section $\sigma_{\mathrm{abs}}(\omega)$ obtained within the semiclassical model employed in this subsection for $\omega_{\mathrm{QE}} = 2.58$ eV (panel a)

[27] The semiclassical approach employed in this chapter should not be confused with the semiclassical SRF employed in Chapter 3 and Chapter 4.

and $\omega_{QE} = 2.95$ eV (panel b). For large gap separation distances, $D \sim 30 - 40$ a_0, the semiclassical results shown in Figure 5.6 coincide with the results of TDDFT calculations displayed in Figure 5.2b ($\omega_{QE} = 2.58$ eV) and Figure 5.5c ($\omega_{QE} = 2.95$ eV). In particular, consistent with the discussion of the previous subsection, the LR calculated for the resonant case $\omega_{QE} = 2.95$ eV within both the semiclassical model and TDDFT is considerably weaker than the one predicted by the classical LRA approach (Figure 5.5a). Thus, the origin of the difference between the TDDFT and the classical LRA absorption spectra resides on quantum surface effects that are important for such small MNPs. Indeed, at large D there is no hybridization between the electronic states localized at the QE and at the MNPs.

As already discussed, the electronic QE–MNPs coupling strongly affects the absorption spectra of the system for D below $D \sim 26$ a_0, which is now further corroborated from the comparison between the semiclassical results in Figure 5.6, the TDDFT results in Figure 5.2b and Figure 5.5c, and the classical results in Figure 5.2a and Figure 5.5a. First, TDDFT shows substantial broadening and reduction of the amplitude for the UR evolving from the BDP of the MNP dimer as compared to both semiclassical and classical results. These effects, not captured by the semiclassical model, are attributed to the charge-transfer processes between the MNPs. In our system, electron transport can occur at larger gap separations as compared to typical vacuum junctions (see Subsection 2.3.2) because it is assisted by photoexcited electron transfer through the LUMO of the QE [356].

On the other hand, the semiclassical model in Figure 5.6 predicts a continuous redshift of the LR for the off-resonant case (panels a), and increasing LR–UR splitting for the resonant case (panel b) with decreasing gap size D, consistent with the classical LRA predictions. As compared to these classical results, the main difference is that the semiclassical model shows a weakening and a broadening of the LR upon decreasing D, which points toward the role of nonlocal optical effects that can also affect the electromagnetic response for such a small system [336] as discussed in detail in Chapter 3. Therefore, the comparison of the results obtained within the classical LRA, the semiclassical model, and the TDDFT approach as employed in this chapter allows us to conclude that the blueshift of the LR for decreasing D below $D \leq 26$ a_0 for the off-resonant QE–MNPs system, as well as the weakening of the LR–UR splitting for the resonant case, are only observed when the hybridization between the MNPs and the QE electronic orbitals is possible, i.e., when the (excited) electron can tunnel across the system.

5.2.3 Charge-transfer resonances at low frequencies

Finally, we discuss in Figure 5.7 the role of the QE in triggering electron transport between the two MNPs across the junction in response to external illumination. In the last years, several works have identified the emergence of charge-transfer plasmons (CTP) supported by metallic vacuum junctions for gap separations typically below ~ 0.4 nm and resonant frequencies of the order of a few electronvolts [43, 68, 83, 84, 86, 342, 357]. CTP are plasmonic resonances where a net electron transport occur between the MNPs that form the nanogap (see Subsection 2.3.2).

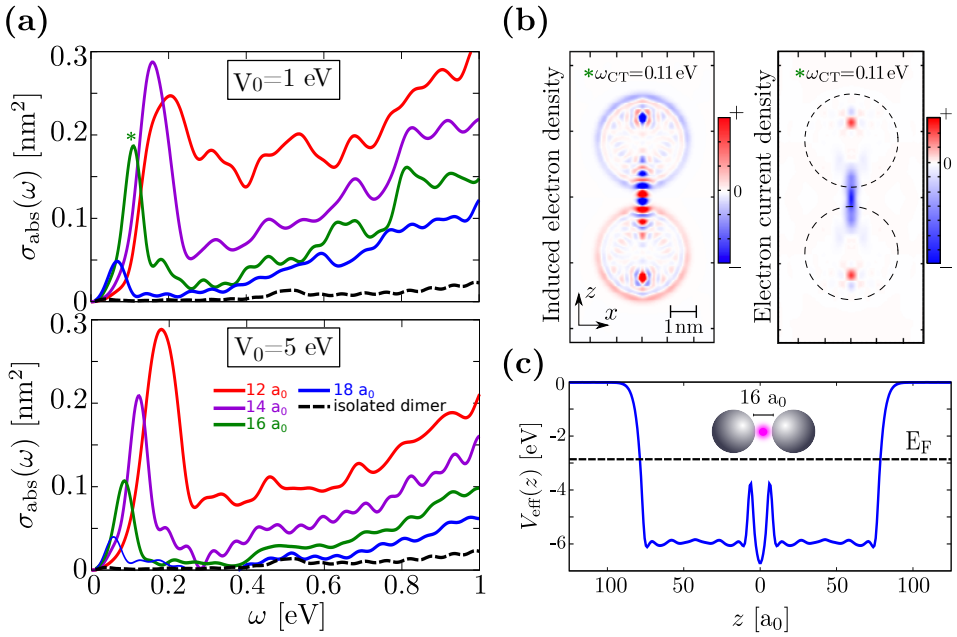

Figure 5.7: **(a)** Absorption spectra of the hybrid QE–MNPs system for low illumination frequencies $\omega = 0-1$ eV. Results are shown for a gap size D ranging from $D = 12$ a$_0$ to $D = 18$ a$_0$, as indicated in the inset. The reference absorption spectrum of the isolated MNP dimer for $D = 12$ a$_0$ is shown by the dashed black line. The situations for $V_0 = 1$ eV (top) and $V_0 = 5$ eV (bottom) in Eq. (5.3) are considered. **(b)** Color maps of the induced electron density (left) and the electron-current density along the z-direction (right) for an incident z-polarized electromagnetic plane wave of frequency $\omega_{CT} = 0.11$ eV. The gap distance is $D = 16$ a$_0$, and $V_0 = 1$ eV. On the right-hand side panel, the boundaries of the jellium edges of the MNPs are indicated by dashed lines. The snapshots are taken at the instants of time when the absolute value of the total dipole moment (left-hand side panel) and of the electron-current density in the middle of the junction (right-hand side panel) are maximum. **(c)** Ground-state potential V_{eff} along the symmetry z-axis of the hybrid QE–MNPs system for $D = 16$ a$_0$.

Moreover, as pointed out in previous works [107–109, 329, 353], the presence of a QE bridging a metallic nanogap substantially modifies the charge-transfer properties of the system and triggers out the emergence of low-frequency resonances associated with electron transport between the MNPs.

In our study, the absorption cross-section $\sigma_{abs}(\omega)$ shown in Figure 5.7a for two different QEs characterized by $V_0 = 1$ eV (top) and $V_0 = 5$ eV (bottom) reveals that a charge-transfer resonance emerges in the low-frequency region, $\omega_{CT} \sim 0.1 - 0.2$ eV, for gap sizes $D = 12$ a$_0$ $-$ 18 a$_0$ ($D \approx 0.6 - 0.95$ nm, thus larger than typical tunneling distances in metal–vacuum–metal junctions studied in Subsection 2.3.2). Our results are consistent with the findings reported in the literature [74, 107, 108, 353]. This new resonance is only activated due to the presence of the QE (see the response of the isolated dimer depicted by the dashed line), and it blueshifts and strengthens considerably when decreasing interparticle

distance. The charge-transfer character of the mode is clearly revealed by the induced electron density shown in Figure 5.7b (left-hand side panel), with each MNP exhibiting a monopolar electron density pattern of opposite sign, and it is further corroborated by the electron-current density along the z-direction (right-hand side panel), which clearly shows that electrons shuttle from one MNP to another. In the studied QE–MNPs system, the observed charge-transfer resonances at $\omega_{\mathrm{CT}} \sim 0.1 - 0.2$ eV emerge because for gap separations of $D \sim 18$ $\mathrm{a_0}$ and below, the QE gives rise to a decrease of the potential barrier close to the dimer axis below the Fermi level of the system (Figure 5.7c), so that even a classically-allowed over-the-barrier electron transport between the MNPs becomes possible. Thus, the low-frequency charge-transfer plasmon reported here can be understood as a consequence of the ballistic electron transport and does not require the tunneling mechanism aid by a localized state at the QE [109].

5.3 Summary

In summary, in this chapter we have identified the role played by *electronic coupling* in the optical response of a canonical hybrid system consisting in a two-level quantum emitter (QE) placed in a nanogap formed by two spherical metal nanoparticles (MNPs). Using a TDDFT description for *both* the QE and the MNPs, we have demonstrated the quenching of the QE exciton originated by the hybridization of the excited states localized at the QE and the electronic states of the MNPs. This exciton quenching drastically affects the optoelectronic response of the hybrid QE–MNPs system for small gap separations. For example, it gives rise to a blueshift of the lower resonance (LR) with decreasing gap separation distance below $D \lesssim 26$ $\mathrm{a_0}$ for situations where the QE transition frequency ω_{QE} is out of resonance with the main plasmonic mode of the MNP dimer, in contrast to the classical LRA calculations that predict a continuous redshift. Further, exciton quenching produced by the electronic interaction also leads to a drastic attenuation of the LR–UR splitting in resonant QE–MNPs systems, thus frustrating the strong coupling predicted by classical LRA simulations. On the other hand, depletion of the potential barrier within sub-nanometric gaps due to the presence of the QE gives rise to a low-frequency electron-transfer resonance at $\omega_{\mathrm{CT}} \sim 0.2$ eV, even for situations where the electronic states of the QE do not act as a gateway for electron transport between the MNPs. Our findings are expected to qualitatively apply for plasmon–exciton systems irrespective of the specific electronic structure of the nanoconstituents, since they are based on general and robust quantum-mechanical phenomena such as electron tunneling and electron transfer between the MNPs and the QE. Thus, the results obtained in this chapter stress the need to consider the QE–MNPs electronic coupling, in addition to the standard electromagnetic interaction, in order to unveil fundamental quantum effects related to charge transfer, often affecting practical implementation of nanoscale sources of photon emission and optoelectronic nanodevices.

CHAPTER 6

SECOND-HARMONIC GENERATION FROM A QUANTUM EMITTER COUPLED TO A METALLIC NANOPARTICLE

In previous chapters, we focused on the analysis of quantum effects emerging in the optical and electronic response of plasmonic systems in situations where the intensity of the external illumination is weak and thus the response is linear. However, when the intensity of the external illumination is strong, the excitation of plasmonic resonances in metallic nanoparticles (MNPs) can also lead to nonlinear effects that can be useful for (bio-)imaging [358–360] or for generation of extreme-ultraviolet attosecond laser pulses [361], among others [36, 37]. In particular, second-harmonic generation (SHG), whereby two photons at the fundamental frequency are absorbed to emit one photon at the second-harmonic frequency, is at the focus of very active research owing to its practical and fundamental interest [362–371]. In this context, it has been shown that plasmonic nanostructures resonant at the fundamental or at the second-harmonic frequency (or at both frequencies) can give rise to considerable enhancement of SHG [294, 367, 368, 372–383]. Recent experiments have also shown the polarization-resolved probing of the nonlinear near-field distribution of metallic nanostructures by using doubly resonant plasmonic antennas [384]. To achieve SHG, however, the symmetry of the system needs to be considered. For example, we showed in Section 1.3 and Section 2.4 that, for typical plane-wave incidence, SHG is forbidden from nanostructures that are centrosymmetric. This nonlinear response is thus very sensitive to the geometry of the system and to surface effects that may eventually break the symmetry constraints and lead to the emission of light at the second-harmonic frequency [37, 68, 154, 385–388].

In this chapter, we study SHG from a coupled system consisting of a quantum emitter (QE) placed in the vicinity of a spherical MNP [111, 389, 390], as sketched in Figure 6.1a. The small individual centrosymmetric MNP does not allow for second-harmonic emission into the far field, but it creates second-harmonic near fields in the proximity of the MNP surface. The presence of the QE lifts the symmetry constraints and allows for SHG. When the electronic transition frequency of the QE, ω_{QE}, is resonant with the second harmonic of the incident frequency, the QE plays the role of an optical resonator, which efficiently couples to the nonlinear electric near field induced close to the MNP (see Section 2.4), transduces this near field into the far field, and thus produces SHG [384]. This QE–MNP system thus enables frequency conversion and allows for its control. To calculate the nonlinear response of the coupled system and to reveal the physical mechanisms behind SHG in this situation, we use TDDFT calculations [70, 71] based on the wave-packet propagation (WPP) method introduced in Section 2.2. With the insights obtained from the TDDFT simulations, we develop a semi-analytical model that accurately reproduces the TDDFT results. This semi-analytical model also allows for addressing more general and complex situations beyond the reach of TDDFT, making possible a detailed study of the sensitivity of SHG to different parameters that characterize the system. In particular, we demonstrate the polarization conversion of the nonlinear signal, as well as the existence of various regimes of SHG determined by the intrinsic losses of the QE. The methodology and results presented in this chapter can pave the conceptual road for enhancing and optimizing SHG mediated by QEs coupled to plasmonic systems [391, 392].

6.1 System and methods

We consider a QE located in proximity to a spherical sodium MNP. The MNP is characterized as in Section 2.4 (Wigner–Seitz radius $r_s = 4$ a$_0$, $N_e = 1074$ conduction electrons, and radius $a = 40.96$ a$_0$). The dipolar plasmon (DP) resonance of the individual MNP is at $\omega_{\mathrm{DP}} = 3.17$ eV, and the quadrupolar plasmon (QP) resonance at $\omega_{\mathrm{QP}} = 3.4$ eV. A Gaussian-like external excitation $V_{\mathrm{ext}}(\mathbf{r}, t)$ given by Eq. (2.79) with fundamental frequency ω, duration $\sigma = 5 \times 2\pi/\omega$, and intensity $I_0 = 10^{10}$ W cm^{-2} (amplitude $\mathrm{E}_0 = 4.8 \times 10^{-4}$ au) is used within TDDFT in this chapter. Importantly, as discussed in Section 2.4, such spherical MNP cannot emit second-harmonic light into the far field due to symmetry constraints, however second-harmonic fields with a quadrupolar pattern are induced in the proximity of the MNP because the inversion symmetry is locally broken at the surface (right-hand side panel in Figure 6.1b). The transition frequency of the QE is set to be resonant with the second harmonic of the fundamental frequency of the external illumination, $\omega_{\mathrm{QE}} = 2\omega$, so that a variation of ω in our calculations implies simultaneous variation of ω_{QE}. The QE plays the role of an optical resonator, sensitive to the second-harmonic electric near field [384]. We model the QE as a point-like dipole as described in Subsection 1.4.1, using an oscillator strength $\alpha^0_{\mathrm{QE}} = 1$ au in Eq. (1.54). The value of the intrinsic damping parameter γ_{QE} is

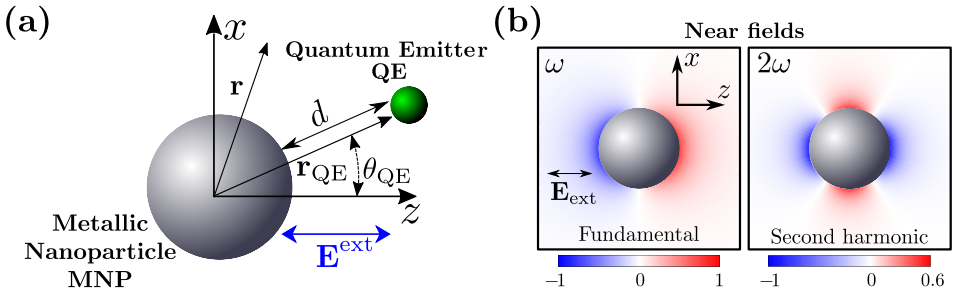

Figure 6.1: **(a)** Sketch of the system studied in this chapter: the radius of the spherical sodium MNP is $a = 40.96$ a$_0$ (≈ 2.2 nm), and the point-like QE is located at position $\mathbf{r}_{\rm QE}$, at a distance d from the MNP surface. A Wigner–Seitz radius $r_s = 4$ a$_0$ is used to characterize the MNP within the jellium model. **(b)** Color maps of the real part of the radial component of the electric near field $\mathbf{E}^{\rm ind}(\mathbf{r},\omega)$ induced at the fundamental (ω, left-hand side panel) and at the second-harmonic frequency (2ω, right-hand side panel) by a z-polarized Gaussian electromagnetic pulse with fundamental frequency $\omega = 1.585$ eV and intensity $I_0 = 10^{10}$ W cm^{-2} incident at the individual spherical MNP in the absence of the QE (same results are also shown in Figure 2.8). Results are rotationally symmetric with respect to the z-axis, and they are shown in the (x,z)-plane normalized to unity. Red and blue colors are used for positive and negative values, respectively (white for zero).

varied in this chapter within the range $\gamma_{\rm QE} = 0.1$ eV $- 10^{-7}$ eV.

The expectation value of the QE dipole moment, $\mathbf{p}_{\rm QE}(t)$, evolves in time according to [22] [see Eq. (1.54)]:

$$\ddot{\mathbf{p}}_{\rm QE}(t) + \gamma_{\rm QE}\dot{\mathbf{p}}_{\rm QE}(t) + \omega_{\rm QE}^2\mathbf{p}_{\rm QE}(t) = \alpha_{\rm QE}^0\mathbf{E}^{\rm tot}(\mathbf{r}_{\rm QE},t), \tag{6.1}$$

where the total electric field $\mathbf{E}^{\rm tot}(\mathbf{r}_{\rm QE},t)$ acting on the QE position $\mathbf{r}_{\rm QE}$ is given by the sum of the incident laser pulse (with amplitude E$_0$, duration $\sigma = 5\times 2\pi/\omega$, and arrival time $t_0 = 5\sigma$),

$$\mathbf{E}^{\rm ext}(t) = \hat{\mathbf{z}}\ \mathrm{E}_0\cos(\omega(t-t_0))\ e^{-\left(\frac{t-t_0}{\sigma}\right)^2}, \tag{6.2}$$

and the field $\mathbf{E}^{\rm ind}(\mathbf{r}_{\rm QE},t)$ induced by the MNP [Eq. (2.34)] at the position $\mathbf{r}_{\rm QE}$ of the QE, $\mathbf{E}^{\rm tot}(\mathbf{r}_{\rm QE},t) = \mathbf{E}^{\rm ext}(t) + \mathbf{E}^{\rm ind}(\mathbf{r}_{\rm QE},t)$. Note that $\mathbf{E}^{\rm ind}(\mathbf{r}_{\rm QE},t)$ includes the reaction of the MNP not only to the incident pulse, but also to the electric field induced by the QE. It thus also accounts for the QE self-interaction (see Subsection 1.4.2). We describe in Appendix C how we solve Eq. (6.1) in this thesis.

The QE dipole $\mathbf{p}_{\rm QE}(t)$ acts as a radiation source emitting into the far field as well as affecting the dynamics of the conduction electrons of the MNP. Because of the small size of the system, retardation effects can be neglected, so that the QE placed at a position $\mathbf{r}_{\rm QE}$ near the MNP creates an electrostatic potential given by [Eq. (3.3)]:

$$V_{\rm QE}(\mathbf{r},t) = -\mathbf{p}_{\rm QE}(t)\cdot\frac{\mathbf{r}-\mathbf{r}_{\rm QE}}{|\mathbf{r}-\mathbf{r}_{\rm QE}|^3}. \tag{6.3}$$

Thus, the Kohn–Sham Hamiltonian $\hat{H}[n(\mathbf{r},t)]$ within TDDFT [Eq. (2.19)] acting on the MNP conduction electrons is given by

$$\hat{H}[n(\mathbf{r},t)] = \hat{T} + V_{\mathrm{H}}[n(\mathbf{r},t)] + V_{\mathrm{xc}}[n(\mathbf{r},t)] + V_{\mathrm{ext}}(\mathbf{r},t) + V_{\mathrm{QE}}(\mathbf{r},t), \tag{6.4}$$

where, as discussed in Section 2.1 and Section 2.2, $n(\mathbf{r},t)$ is the time-dependent electron density [Eq. (2.20)], $\hat{T} = -\frac{1}{2}\nabla^2$ is the kinetic-energy operator, $V_{\mathrm{H}}[n(\mathbf{r},t)]$ is the Hartree potential [Eq. (2.23)], $V_{\mathrm{xc}}[n(\mathbf{r},t)]$ is the exchange–correlation potential [Eq. (2.12)] calculated using the kernel of Gunnarsson and Lundquist [198], and $V_{\mathrm{ext}}(\mathbf{r},t)$ is the external potential given by Eq. (2.79) that drives the QE–MNP system. We employ the WPP algorithm in spherical coordinates as described in Subsection 2.3.1. In this case, the time-dependent Kohn–Sham equations given by Eq. (2.19) and Eq. (2.20) are solved self-consistently together with Eq. (6.1), Eq. (6.3), and Eq. (6.4). These equations are solved in time domain, and the time-to-frequency Fourier transform given by Eq. (2.80) is used to obtain the frequency-resolved quantities of interest such as the nonlinear dipole moment induced at the MNP, $\mathbf{p}_{\mathrm{MNP}}(\Omega)$, and at the QE, $\mathbf{p}_{\mathrm{QE}}(\Omega)$. The total dipole moment $\mathbf{p}(\Omega)$ is given by the sum of both, $\mathbf{p}(\Omega) = \mathbf{p}_{\mathrm{MNP}}(\Omega) + \mathbf{p}_{\mathrm{QE}}(\Omega)$. Here, the symbol Ω is used to denote the frequency of the induced dipole moments, since we are considering the nonlinear regime where $\omega \neq \Omega$ in general. A Gaussian filter $\mathfrak{F}(t)$ given by Eq. (2.81) is used in the Fourier transforms to partially account for decay and dephasing processes of the collective density oscillations that are not included in the present ALDA-TDDFT approach (see Section 2.2).

6.2 Results and discussion

6.2.1 TDDFT results

We initially place the QE at the z-axis, corresponding to the direction of polarization of the incident laser pulse, at a distance $d = 18\ \mathrm{a_0}$ (≈ 0.95 nm) from the MNP surface. For this geometry, only z-polarized dipole moments are induced in the QE and in the MNP. The system then possesses cylindrical symmetry with respect to the z-axis, which greatly reduces the computational demands for the TDDFT calculations. The frequency of the external excitation $\omega = 1.585$ eV is first considered such that its second harmonic matches the DP frequency of the MNP, $2\omega = \omega_{\mathrm{DP}} = 3.17$ eV, and the intrinsic damping parameter of the QE is set to $\gamma_{\mathrm{QE}} = 0.1$ eV.

Figure 6.2 shows that the coupled QE–MNP system features strong emission at both odd and even harmonics, in contrast to the individual MNP that only emits at odd-harmonics due to the inversion symmetry of the system (see Section 2.4). In this figure, the intensity spectrum of the total induced dipole moment $|\mathbf{p}(\Omega)|^2$ calculated within TDDFT for the coupled QE–MNP structure is shown by the blue line, revealing clear peaks at even harmonics $\Omega = 2\omega,\ 4\omega$ and 6ω. The reference results obtained for the nonlinear response of the individual MNP (without QE) are shown by the dashed red line (only harmonics at $\Omega = \omega,\ 3\omega,\ 5\omega$ and 7ω are

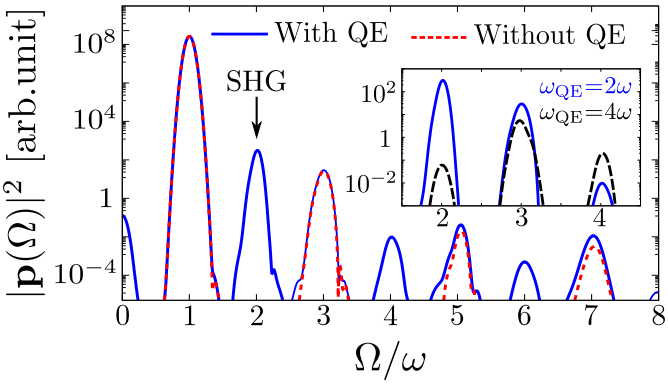

Figure 6.2: Intensity spectrum of the total dipole moment $|\mathbf{p}(\Omega)|^2$ of the coupled QE–MNP system (solid blue line) and of the individual MNP (dashed red line). Results are obtained for an incident z-polarized Gaussian electromagnetic pulse with fundamental frequency $\omega = 1.585$ eV and intensity $I_0 = 10^{10}$ W cm^{-2}. The QE is located at the z-axis, at a distance $d = 18$ a$_0$ (≈ 0.95 nm) from the MNP surface, and it is characterized by a transition frequency $\omega_{QE} = 2\omega$, an intrinsic damping parameter $\gamma_{QE} = 0.1$ eV, and oscillator strength $\alpha^0_{QE} = 1$ au, following Eq. (6.1). Results are shown as a function of the frequency measured in units of the fundamental frequency ω. In the inset, the solid blue line corresponds to the same result as in the main figure (with QE), and the dashed black line corresponds to the results obtained for the transition frequency of the QE resonant with the fourth harmonic of the incident light, $\omega_{QE} = 4\omega$, with $\omega = 0.79$ eV.

observed, as discussed in Figure 2.7). The even harmonics in the far field from the coupled QE–MNP system emerge because the QE breaks the reflection symmetry with respect to the (x, y)-plane, and thus the total inversion symmetry of the system [388]. Note that the spectra in Figure 6.2 are artificially broadened by application of the Gaussian filter given in Eq. (2.81) that allows for introducing losses in the system. We show in Figure 6.3 the effect of the Gaussian filter given by Eq. (2.81). While the nonfiltered spectrum of the hybrid MNP-QE system (blue line) appears quite noisy, the filtered one presents very well-defined high-harmonic peaks (red line). All the peaks are broadened by the filter, which results in an attenuation of the maximum value of the peaks as compared to the nonfiltered signal. Figure 6.3 thus illustrates how this filtering procedure allows us to reach convergent spectral response at high-harmonic frequencies. In Subsection 6.2.2, we develop a semi-analytical method that allows us to overcome the difficulties of the ALDA-TDDFT calculations to incorporate losses [72, 241, 242].

The resonance between the transition frequency of the QE, ω_{QE}, and the second harmonic of the incident pulse strongly enhances the intensity emitted by the system at 2ω. To illustrate this resonance effect, we show in the inset of Figure 6.2 the results obtained for a different situation. The QE transition frequency ω_{QE} in this case is set to be resonant with 4ω (dashed black line), and the system is illuminated by a Gaussian pulse with fundamental frequency ω such that the fourth harmonic matches the frequency of the MNP dipolar plasmon, $4\omega = \omega_{QE} = \omega_{DP} = 3.17$ eV.

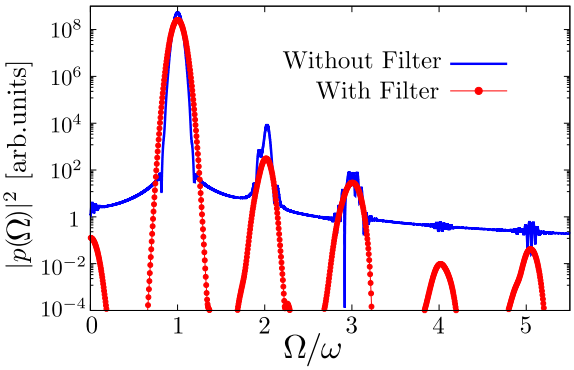

Figure 6.3: Intensity spectrum $|p(\Omega)|^2$ of the induced dipole moment of the coupled QE–MNP system considered in this chapter for the case when we apply the Gaussian filter (red dotted line) and without applying the filter (blue line). The QE is located at $d = 18$ a$_0$ from the MNP surface, and a Gaussian electromagnetic field with frequency $\omega = 1.585$ eV and average intensity $I_0 = 10^{10}$ W cm^{-2} is used. Results are shown as a function of the frequency measured in units of the fundamental frequency ω.

For this excitation frequency, the TDDFT results reveal that $|\mathbf{p}(\Omega)|^2$ at the second harmonic decreases by several orders of magnitude in favor of the emission at the fourth harmonic resonant with the QE transition. With the purpose of enhancing SHG, in the following we thus focus on the situation where $\omega_{\mathrm{QE}} = 2\omega$.

Physical mechanism behind SHG from the QE–MNP system

We next use TDDFT calculations to determine the physical mechanism behind the nonlinear second-harmonic response of the coupled QE–MNP system shown in Figure 6.2. The dipole moment of the QE, $\mathbf{p}_{\mathrm{QE}}(t)$, mainly oscillates at the fundamental frequency ω and at the second-harmonic frequency 2ω of the incident pulse. Indeed, the QE transition is resonant with the second harmonic, $\omega_{\mathrm{QE}} = 2\omega$, but the field acting on the QE at the fundamental frequency ω is orders of magnitude stronger than the near field induced by the MNP at 2ω (see Figure 2.7b). As a result, the off-resonant dipole moment of the QE at ω can be strong and, thus, two distinct channels might contribute to the second-harmonic dipole moment of the coupled QE–MNP system: (i) the excitation of the QE dipole moment at the resonant second-harmonic frequency 2ω induces a second-harmonic dipole moment at the MNP due to a *linear interaction*, and (ii) the off-resonant dipole moment of the QE at the fundamental frequency ω lifts the symmetry constraint of the entire system and allows for the second-harmonic dipole moment to be induced at the MNP via a *nonlinear process*.

In order to obtain the respective weight of the two different channels inducing a second-harmonic dipole at the MNP, we proceed as follows: using the Fourier analysis, we split the dipole moment $\mathbf{p}_{\mathrm{QE}}(t)$ of the QE obtained from the TDDFT

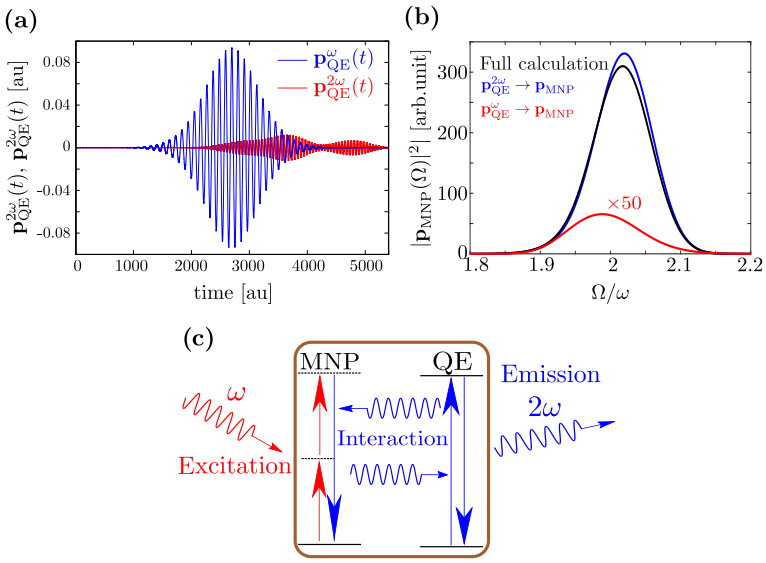

Figure 6.4: **(a)** Time evolution of the two main components of the QE dipole moment: (i) one oscillating at the second-harmonic frequency 2ω ($\mathbf{p}^{2\omega}_{\mathrm{QE}}(t)$, red line), and (ii) the other one oscillating mainly at the fundamental frequency ω ($\mathbf{p}^{\omega}_{\mathrm{QE}}(t)$, blue line). The QE is located at $d = 18$ a$_0$ from the MNP surface, and a Gaussian electromagnetic field with frequency $\omega = 1.585$ eV and average intensity $I_0 = 10^{10}$ W cm^{-2} is used [Eq. (6.2)]. **(b)** Second-harmonic dipole moment of the MNP, $|\mathbf{p}_{\mathrm{MNP}}(\Omega \sim 2\omega)|^2$, when interacting with the QE from a full calculation (black line), when interacting with the QE oscillating only at 2ω (blue line), and when interacting with the QE oscillating at ω (red line, amplified 50 times) for the same parameters as in panel a. For further details see the main text. **(c)** Sketch of the main physical process behind SHG in the present system. The MNP induces a near field at 2ω that excites the emitter. Then, the linear QE–MNP electromagnetic interaction at 2ω generates the emission into the far field at the second-harmonic frequency.

calculation of the coupled QE–MNP system into a sum of the two leading contributions, $\mathbf{p}_{\mathrm{QE}}(t) = \mathbf{p}^{\omega}_{\mathrm{QE}}(t) + \mathbf{p}^{2\omega}_{\mathrm{QE}}(t)$, one oscillating at the fundamental frequency, $\mathbf{p}^{\omega}_{\mathrm{QE}}(t)$, and the other one at the second-harmonic frequency, $\mathbf{p}^{2\omega}_{\mathrm{QE}}(t)$. $\mathbf{p}^{\omega}_{\mathrm{QE}}(t)$ and $\mathbf{p}^{2\omega}_{\mathrm{QE}}(t)$ are shown in Figure 6.4a by the blue and red lines, respectively. We then run two different TDDFT simulations, where the electron density of the MNP evolves in the following way:[28]

(i) solely under the action of the potential created by the point dipole oscillating at the second-harmonic frequency, $V^{2\omega}_{\mathrm{QE}}(\mathbf{r}, t) = -\mathbf{p}^{2\omega}_{\mathrm{QE}}(t) \cdot \frac{\mathbf{r}-\mathbf{r}_{\mathrm{QE}}}{|\mathbf{r}-\mathbf{r}_{\mathrm{QE}}|^3}$ [Eq. (6.3)], with no external laser pulse applied ($V_{\mathrm{ext}}(\mathbf{r}, t) = 0$), and

(ii) under the action of the external potential $V_{\mathrm{ext}}(\mathbf{r}, t)$ given by Eq. (2.79) (corresponding to the laser pulse) plus the potential created by the point dipole oscillating at the fundamental frequency, $V^{\omega}_{\mathrm{QE}}(\mathbf{r}, t) = -\mathbf{p}^{\omega}_{\mathrm{QE}}(t) \cdot \frac{\mathbf{r}-\mathbf{r}_{\mathrm{QE}}}{|\mathbf{r}-\mathbf{r}_{\mathrm{QE}}|^3}$.

[28] The self-consistency loop is stopped in both cases, in the sense that the MNP does not act back on the QE.

As shown in Figure 6.4b, the second-harmonic dipole moment $|\mathbf{p}_{\mathrm{MNP}}(\Omega \sim 2\omega)|^2$ of the MNP obtained in scenario (i) and shown with blue line, closely corresponds to the result of the complete self-consistent calculation (black line). On the other hand, the second-harmonic dipole moment $|\mathbf{p}_{\mathrm{MNP}}(\Omega \sim 2\omega)|^2$ obtained under scenario (ii) is more than 2 orders of magnitude weaker (red line) than the one obtained from the full calculation. These results point toward the following main physical mechanism underlying far-field SHG in the present system:

1. The interaction of the (strong) incident laser pulse with the conduction electrons of the MNP generates a second-harmonic near field.

2. The second harmonic of the near field of the MNP resonantly drives the QE at 2ω and induces a second-harmonic dipole moment at the QE.

3. The resulting QE dipole oscillating at 2ω radiates into the far field in the presence of the MNP.

The physical process revealed by TDDFT simulations is sketched in Figure 6.4c [111], and allows us to develop a practical semi-analytical approach in Subsection 6.2.2 which, by combining TDDFT and classical results, can be used to describe more complex situations involving the intrinsic losses of the QE as well as its position with respect to the MNP.

6.2.2 TDDFT vs. semi-analytical model

The understanding of the physical mechanism behind SHG established above using TDDFT calculations can be used to develop a semi-analytical model capable of reproducing the role of the QE in the second-harmonic response of the coupled QE–MNP system. As discussed below, this semi-analytical model goes beyond the TDDFT because it naturally incorporates the losses and the plasmon decay, and thus lifts the necessity of using artificial broadening of the spectral features [Eq. (2.81)]. Moreover, this approach allows us to analyze systems without axial symmetry, i.e., situations of arbitrary polarization of the incident pulse and position of the QE. Such analysis would be computationally out of reach for the TDDFT calculations.

This semi-analytical model is based on the self-interaction Green's function formalism described in Subsection 1.4.2, which addresses the QE–MNP electromagnetic coupling in frequency domain. The QE is excited by the incident laser pulse and by the nonlinear electric near field induced at the MNP, as obtained from the TDDFT calculations of the individual MNP, i.e., in the absence of the QE. The excited QE then radiates into the far field in the presence of the MNP. The last stage of the calculation, which involves the coupling of the QE with the MNP and the resulting light emission to the far field, is treated within the classical framework introduced in Chapter 1. Using the self-interaction Green's function formalism we obtain (see Subsection 1.4.2):

$$\mathbf{p}_{\mathrm{QE}}(\Omega) = \left(\mathbb{I} - \alpha_{\mathrm{QE}}(\Omega)\hat{\mathbb{G}}(\mathbf{r}_{\mathrm{QE}}, \mathbf{r}_{\mathrm{QE}}, \Omega)\right)^{-1} \alpha_{\mathrm{QE}}(\Omega)\mathbf{E}^{\mathrm{tot}}(\mathbf{r}_{\mathrm{QE}}, \Omega),$$
$$\mathbf{p}_{\mathrm{MNP}}(\Omega) = \mathbf{p}_{\mathrm{MNP}}^{\mathrm{TDDFT}}(\Omega) + \alpha_{\mathrm{MNP}}(\Omega)\hat{\mathbb{G}}_0\mathbf{p}_{\mathrm{QE}}(\Omega), \tag{6.5}$$

where $\mathbf{p}_{\mathrm{MNP}}^{\mathrm{TDDFT}}(\Omega)$ is the dipole moment of the individual MNP induced by the incident laser pulse, calculated with TDDFT in the absence of the QE (this contribution is zero for even harmonics $\Omega = 2\omega,\ 4\omega, \dots$). The electric field at the position $\mathbf{r}_{\mathrm{QE}}$ of the QE, $\mathbf{E}^{\mathrm{tot}}(\mathbf{r}_{\mathrm{QE}}, \Omega)$, is given by

$$\mathbf{E}^{\mathrm{tot}}(\mathbf{r}_{\mathrm{QE}}, \Omega) = \mathbf{E}_{\mathrm{ind}}^{\mathrm{TDDFT}}(\mathbf{r}_{\mathrm{QE}}, \Omega) + \mathbf{E}^{\mathrm{ext}}(\Omega), \tag{6.6}$$

where the field of the external laser pulse $\mathbf{E}^{\mathrm{ext}}(\Omega)$ (Fourier transform of Eq. (6.2)) is added to the electric field $\mathbf{E}_{\mathrm{ind}}^{\mathrm{TDDFT}}(\mathbf{r}_{\mathrm{QE}}, \Omega)$ created by the noninteracting MNP. $\mathbf{E}_{\mathrm{ind}}^{\mathrm{TDDFT}}(\mathbf{r}_{\mathrm{QE}}, \Omega)$ is obtained from TDDFT calculations for the individual MNP subjected to a Gaussian laser pulse (Section 2.4), and it introduces all the second-harmonic nonlinearity. The polarizability of the sodium MNP of radius a, $\alpha_{\mathrm{MNP}}(\Omega)$, and that of the QE, $\alpha_{\mathrm{QE}}(\Omega)$, are obtained from Eq. (1.45) and Eq. (1.55), respectively. Finally, in Eq. (6.5) $\hat{\mathbb{G}}(\mathbf{r}_{\mathrm{QE}}, \mathbf{r}_{\mathrm{QE}}, \Omega)$ is the self-interaction dyadic Green's function that provides the electric field created by the spherical MNP at position $\mathbf{r}_{\mathrm{QE}}$ in response to a point dipole located at the same position [Eq. (1.58)], and the vacuum Green's function $\hat{\mathbb{G}}_0$ provides the electric field at the center of the MNP produced by a unitary point dipole placed at position $\mathbf{r}_{\mathrm{QE}}$ [22].

Within this semi-analytical model, we use a Drude dielectric function $\varepsilon(\Omega)$ of the MNP given by Eq. (1.10), where the plasma frequency $\omega_p = 5.49$ eV and intrinsic damping parameter $\gamma_p = 0.218$ eV are determined from the fit to the linear optical absorption spectrum σ_{abs} of the individual MNP calculated within TDDFT (not shown). This parametrization allows us to partially account for quantum finite-size effects in the plasmonic response of the MNP [64, 194], as described in Section 2.3 and Chapter 3. Moreover, to mimic the effect of the spill-out of the induced charge density, naturally included within the TDDFT results, the semi-analytical model calculations are performed using a reduced "effective" QE–MNP separation $d_{\mathrm{eff}} = d - \Delta$, where $\Delta = 1.5$ a$_0$. As a result, e.g., the TDDFT data obtained for the QE located at $d = 18$ a$_0$ from the MNP surface are compared with semi-analytical model results obtained for $d_{\mathrm{eff}} = 16.5$ a$_0$. As pointed out in Chapter 5, introducing the distance scaling Δ is effectively similar to considering the Feibelman parameter $d_\perp$ to account for the spill-out of the induced electron density [58].

We analyze the performance of the semi-analytical approach by comparing the TDDFT and the semi-analytical results for the nonlinear response of the coupled QE–MNP system excited by a z-polarized Gaussian pulse with fundamental frequency $\omega = 1.585$ eV and intensity $I_0 = 10^{10}$ W cm^{-2}. We show in Figure 6.5a the intensity spectrum of the total dipole $|\mathbf{p}(\Omega)|^2$ as obtained from TDDFT (solid blue line)

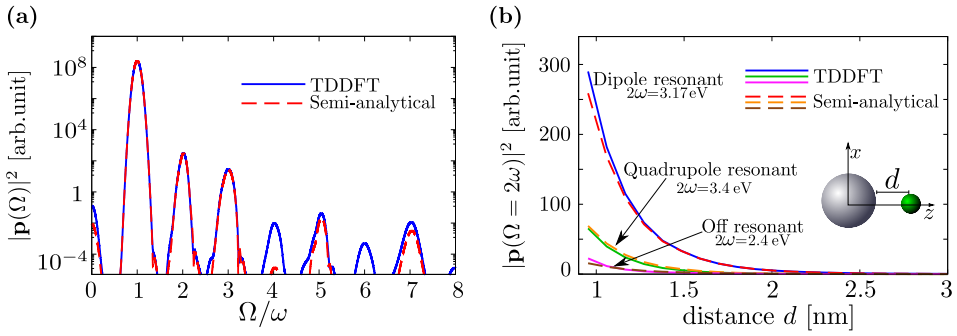

Figure 6.5: **(a)** Intensity spectrum of the induced total dipole moment $|\mathbf{p}(\Omega)|^2$ obtained from the TDDFT calculations (blue line) and from the semi-analytical model (dashed red line). Results are shown as a function of the frequency measured in units of the fundamental frequency $\omega = 1.585$ eV of the incident laser pulse. The QE is located at $d = 18$ a_0 (0.95 nm) from the MNP surface. **(b)** Second-harmonic dipole moment $|\mathbf{p}(\Omega = 2\omega)|^2$ calculated using the semi-analytical model (dashed lines) and TDDFT (solid lines). Results are shown as a function of the QE–MNP distance d for three different fundamental frequencies such that $2\omega = 2.4$ eV (off resonance), $2\omega = 3.17$ eV (at resonance with the MNP dipolar plasmon), and $2\omega = 3.4$ eV (at resonance with the MNP quadrupolar plasmon). In both panels a z-polarized Gaussian pulse of intensity $I_0 = 10^{10}$ W cm^{-2} is used [Eq. (6.2)].

and from the semi-analytical model (dashed red line) calculations. An excellent agreement between the two approaches is obtained for the nonlinear dipole moment at the second harmonic $\Omega = 2\omega$, which is at the focus of the present chapter.

On the other hand, for higher-order harmonics the agreement strongly worsens, specially for high-order even harmonics $\Omega = 4\omega$ and $\Omega = 6\omega$ that can be generated only due to the QE–MNP electromagnetic interaction. This indicates that other nonlinear processes beyond the scope of the present model become important for such low-intensity harmonic generation. It is worth noting that, for the sake of comparison between the two approaches, the Gaussian filters employed in the Fourier analysis of the time-dependent quantities in the TDDFT [Eq. (2.81)] are also introduced in the semi-analytical model calculations shown in Figure 6.5a,b [393].

The results shown so far are obtained for the second harmonic in resonance with the DP of the MNP, $2\omega = \omega_{\mathrm{DP}} = 3.17$ eV. One would expect that, under these conditions, SHG is very efficient because the emission of the QE resonantly excited by the near field of the MNP at 2ω is further enhanced by the DP of the MNP playing the role of a nanoantenna [367, 368, 378–384]. On the other hand, the second-harmonic near field of the MNP that drives the QE, $\mathbf{E}_{\mathrm{ind}}^{\mathrm{TDDFT}}(\mathbf{r}_{\mathrm{QE}}, \Omega = 2\omega)$, has a quadrupolar character [288–294, 394] (see right panel in Figure 6.1b), and therefore it should be stronger when the second-harmonic frequency matches the quadrupolar plasmon (QP) resonance of the MNP [394], i.e., when $2\omega = \omega_{\mathrm{QP}} = 3.4$ eV. This, in turn, could also lead to an efficient excitation of the QE and thus increase the emitted second-harmonic signal.

In order to find the optimal conditions for SHG from the coupled QE–MNP, we

use the TDDFT and the semi-analytical method to study how the second-harmonic emission into the far field depends on the fundamental frequency ω. In Figure 6.5b, the second-harmonic dipole intensity $|\mathbf{p}(\Omega = 2\omega)|^2$ is shown as a function of the distance d of the QE from the MNP surface for three different frequencies ω of the incident Gaussian laser pulse. First, the values of ω are set such that the second harmonic matches either the DP ($2\omega = 3.17$ eV, dipole resonant) or the QP ($2\omega = 3.4$ eV, quadrupole resonant) resonances of the MNP. We consider as well the reference case where both the fundamental frequency and the second harmonic are out of resonance with any of the plasmonic modes of the MNP ($2\omega = 2.4$ eV, off resonant). We recall that the transition frequency of the QE is always in resonance with the second harmonic, $\omega_{\mathrm{QE}} = 2\omega$.

Remarkably, the semi-analytical model in Figure 6.5b does an excellent job in reproducing the TDDFT results for the three situations. Both approaches show the strongest SHG when the second-harmonic frequency matches the DP resonance of the MNP, while the off-resonant conditions lead to the smallest SHG. Furthermore, for all three excitation frequencies $|\mathbf{p}(\Omega = 2\omega)|^2$ monotonically decreases with increasing distance d. This behavior reflects the decrease of the nonlinear near field created by the MNP at $\Omega = 2\omega$ (right panel in Figure 6.1b). However, as we show using the semi-analytical model in Subsection 6.2.3, the dependence of SHG on the frequency and distance is strongly affected by the intrinsic losses of the QE (determined by the damping parameter γ_{QE}). This aspect of the problem cannot be addressed within the present TDDFT because, as stated above, it lacks the description of the decay and dephasing processes [241, 242], forcing an artificial broadening of the spectral features using, e.g., the Gaussian filters applied to connect the time-resolved and the frequency-resolved quantities [Eq. (2.81)]. As a consequence, reliable information can only be obtained from TDDFT for the cases where the QE has large intrinsic losses.

6.2.3 Influence of the intrinsic losses and the position of the QE on the efficiency of SHG

The semi-analytical model introduced in the previous section can be used for a detailed study of SHG from the coupled QE–MNP structure in response to incident plane-wave illumination (in contrast to the electromagnetic Gaussian pulse, Eq. (6.2), considered previously). Moreover, the analysis of the dependence of SHG on experimentally relevant parameters, which was not computationally possible with TDDFT, becomes within reach. Namely, we are interested in the dependence of SHG on the fundamental frequency ω of the external laser, on the intrinsic losses of the QE (γ_{QE}), and on the position of the QE relative to the MNP.

The second-harmonic dipole $\mathbf{P}_{2\omega}$ induced in the coupled QE–MNP system by an incident plane wave with average intensity I_0 can be estimated from the frequency-resolved dipole $\mathbf{p}(\Omega)$ induced by the electromagnetic Gaussian pulse [Eq. (6.2)] as obtained from Eq. (6.5). The relationship between $\mathbf{P}_{2\omega}$ (induced under plane-wave excitation) and $\mathbf{p}(\Omega)$ (under electromagnetic Gaussian pulse) is

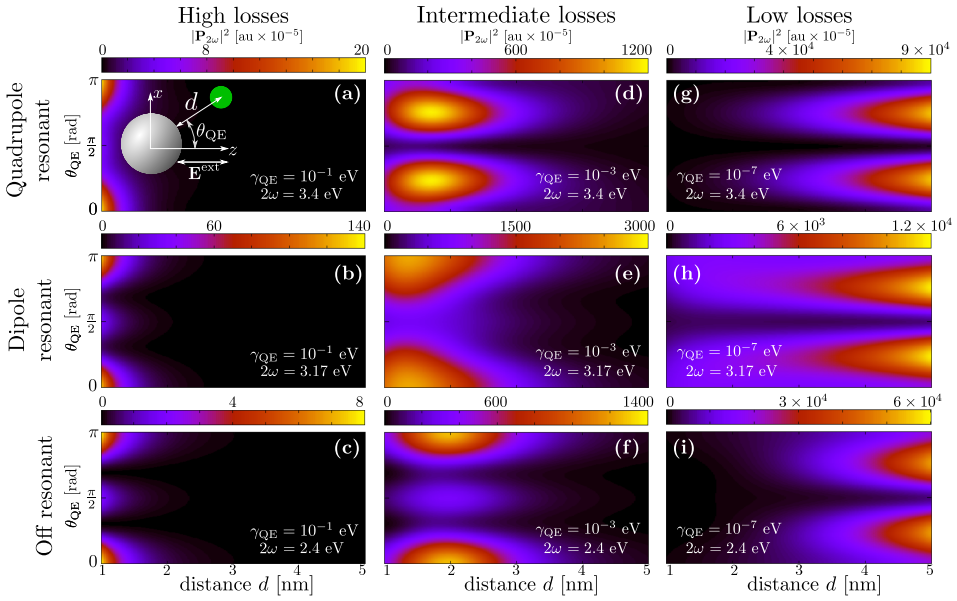

Figure 6.6: Second-harmonic response $|\mathbf{P}_{2\omega}|^2$ of the coupled QE–MNP system illuminated with an incident z-polarized plane wave with fundamental frequency ω and average intensity $I_0 = 10^{10}$ W cm^{-2} for different positions of the QE in the (x, z)-plane. The distance is measured from the surface of the MNP, and the QE is placed at a point given by (d, θ_{QE}). The polar angle θ_{QE} is measured with respect to the symmetry z-axis parallel to the electric field vector of the incident electromagnetic plane wave (see inset in panel a). Different panels correspond to the results obtained for different values of the fundamental frequency ω (rows) and intrinsic QE losses determined by γ_{QE} (columns). We set ω such that (i) the second harmonic is at resonance with the QP resonance of the MNP ($2\omega = 3.4$ eV, quadrupole resonant, top row), (ii) the second harmonic is at resonance with the DP resonance of the MNP ($2\omega = 3.17$ eV, dipole resonant, middle row), and (iii) the fundamental frequency and the second harmonic are out of resonance with respect to any mode of the MNP ($2\omega = 2.4$ eV, off resonant, bottom row). The choice of γ_{QE} illustrates situations with high ($\gamma_{QE} = 10^{-1}$ eV, left-hand side column), intermediate ($\gamma_{QE} = 10^{-3}$ eV, center column), and low ($\gamma_{QE} = 10^{-7}$ eV, right-hand side column) QE losses.

given by

$$\mathbf{P}_{2\omega} = \frac{8\sqrt{2\pi} I_0}{\sigma c \mathrm{E}_0^2} \mathbf{p}(\Omega = 2\omega), \tag{6.7}$$

where c is the speed of light in vacuum, and σ and E_0 are the duration and the amplitude of the electromagnetic Gaussian pulse used in the TDDFT simulations, respectively (see details in Appendix F). $\mathbf{p}(\Omega = 2\omega)$ is calculated using the semi-analytical model [Eq. (6.5)].

The color maps in Figure 6.6 show the second-harmonic response $|\mathbf{P}_{2\omega}|^2$ of the coupled QE–MNP structure subjected to an incident z-polarized plane wave with fundamental frequency ω and average intensity $I_0 = 10^{10}$ W cm^{-2} for different positions of the QE, defined by the distance d from the MNP surface and the polar angle θ_{QE} (see Figure 6.1a and the inset in Figure 6.6a for the geometry of the

system). The range of distances $d = 1 - 5$ nm considered in Figure 6.6 is set such that retardation effects can be neglected. The results are axially symmetric with respect to the z-axis, and without loss of generality, we consider that the QE is placed in the (x, z)-plane.

Each panel in Figure 6.6 shows the dependence of the SHG on the QE position for different fundamental frequency, ω, and intrinsic damping parameter of the QE, γ_{QE}. Specifically, we performed calculations for (i) high QE losses ($\gamma_{\mathrm{QE}} = 0.1$ eV), which often occur in experiments at room temperature, (ii) intermediate losses ($\gamma_{\mathrm{QE}} = 10^{-3}$ eV), and (iii) low losses ($\gamma_{\mathrm{QE}} = 10^{-7}$ eV), close to the spontaneous decay rate of the QE. Similarly to the discussion in Figure 6.5b, we consider fundamental frequencies ω corresponding to three different situations: (i) the second harmonic is at resonance with the DP resonance of the MNP ($2\omega = \omega_{\mathrm{DP}} = 3.17$ eV, dipole resonant), (ii) the second harmonic is at resonance with the QP of the MNP ($2\omega = \omega_{\mathrm{QP}} = 3.4$ eV, quadrupole resonant), and (iii) both the second harmonic and the fundamental frequency are off-resonance with respect to any plasmon mode of the MNP ($2\omega = 2.4$ eV, off resonant).

Some common features can be observed in Figure 6.6. First, the symmetry with respect to the position of the emitter given by the angle $\theta_{\mathrm{QE}} = \pi/2$, which reflects the symmetry of the system with respect to the (x, y)-plane. Second, SHG is generally higher for the QE placed around the z-axis ($\theta_{\mathrm{QE}} \approx 0$ and π), the region where the near field excited at 2ω is stronger (due to its quadrupolar spatial profile, see right panel in Figure 6.1b). Indeed, the near field resonantly excites the QE and partially imprints its spatial distribution into the dependence of the second-harmonic signal on the position of the QE. Another result common for large and intermediate QE losses is that the strongest SHG is obtained for the second-harmonic frequency at resonance with the DP of the MNP, $2\omega = \omega_{\mathrm{DP}}$, which corroborates the TDDFT results discussed in Subsection 6.2.2.

The most prominent feature revealed by the results in Figure 6.6 is however the key role played by the intrinsic losses of the QE in the efficiency of SHG and in its dependence on the QE position. In general, lower intrinsic losses allow us to obtain significantly larger SHG. Remarkably, with γ_{QE} ranging from high (10^{-1} eV) to intermediate (10^{-3} eV) and low (10^{-7} eV) losses, the character of SHG as a function of increasing distance d (within the studied distances) changes completely. While $|\mathbf{P}_{2\omega}|^2$ is monotonously decreasing for large QE losses in the range of distances considered (panels a,b,c), it is maximized at $d \sim 1.5 - 2$ nm for intermediate losses (panels d,e,f), and at $d \sim 15 - 20$ nm for low losses (this last result is not shown in the figure because it falls outside the validity limit of the nonretarded approximation used in the calculations). As a further striking result, for low intrinsic QE losses $\gamma_{\mathrm{QE}} = 10^{-7}$ eV, the resonant condition with the DP of the MNP in panel (h), $2\omega = \omega_{\mathrm{DP}}$, does not lead to the largest but to the smallest SHG. The maximum SHG is obtained in this case for the QE resonant with the QP resonance of the MNP (panel g) and for off-resonant conditions (panel i).

In order to understand these results, it is useful to consider the respective weights of the contributions to the total second-harmonic dipole from the QE, $\mathbf{P}_{2\omega}^{\mathrm{QE}}$, and from the MNP, $\mathbf{P}_{2\omega}^{\mathrm{MNP}}$, where $\mathbf{P}_{2\omega} = \mathbf{P}_{2\omega}^{\mathrm{QE}} + \mathbf{P}_{2\omega}^{\mathrm{MNP}}$. For simplicity, we discuss

the case of the QE located at the z-axis, but the same arguments are valid for other geometries. From Eq. (6.5) we obtain

$$\begin{aligned} \frac{|\mathbf{P}_{2\omega}^{\mathrm{QE}}|}{|\mathbf{P}_{2\omega}|} &= \frac{1}{|1+\alpha_{\mathrm{MNP}}(2\omega)\ \hat{\mathbf{z}}\ \hat{\mathbb{G}}_0\ \hat{\mathbf{z}}|}, \\ \frac{|\mathbf{P}_{2\omega}^{\mathrm{MNP}}|}{|\mathbf{P}_{2\omega}|} &= \frac{|\alpha_{\mathrm{MNP}}(2\omega)\ \hat{\mathbf{z}}\ \hat{\mathbb{G}}_0\ \hat{\mathbf{z}}|}{|1+\alpha_{\mathrm{MNP}}(2\omega)\ \hat{\mathbf{z}}\ \hat{\mathbb{G}}_0\ \hat{\mathbf{z}}|}. \end{aligned} \tag{6.8}$$

These expressions are very useful since they do not depend on the particular properties of the QE. As shown in Figure 6.7a, at large distance d, SHG is dominated by the dipole moment induced at the QE for the three excitation frequencies (dashed lines), while at short separation distances the dipole moment of the MNP provides the leading contribution (solid lines). Note that, given the scaling of the MNP polarizability with the particle radius, $\alpha_{\mathrm{MNP}} \sim a^3$ [Eq. (1.45)], and the dependence on the separation distance of the vacuum Green's dyadic in the near field, $\hat{\mathbf{z}}\ \hat{\mathbb{G}}_0\ \hat{\mathbf{z}} \sim 1/|a+d|^3$, the crossover region would move to larger distances d with increasing MNP radius.

Along with the relative contributions to SHG given by Eq. (6.8), the response of the QE at 2ω plays a key role in SHG from the coupled QE–MNP system. The self-interaction due to the presence of the MNP modifies the total decay rate of the QE, Γ, due to the Purcell effect. Therefore, it is useful to discuss how the decay rate of the QE changes due to this self-interaction with the MNP. The total decay rate Γ (or, equivalently, "effective" broadening) of the QE resonance is given by

$$\Gamma = \gamma_{\mathrm{QE}} + \alpha_{\mathrm{QE}}^0 \mathrm{Im}\{\hat{\mathbf{z}}\ \hat{\mathbb{G}}(\mathbf{r}_{\mathrm{QE}}, \mathbf{r}_{\mathrm{QE}}, 2\omega)\ \hat{\mathbf{z}}\}/2\omega, \tag{6.9}$$

where $\hat{\mathbf{z}}\ \hat{\mathbb{G}}(\mathbf{r}_{\mathrm{QE}}, \mathbf{r}_{\mathrm{QE}}, 2\omega)\ \hat{\mathbf{z}} \propto 1/|\mathbf{r}_{\mathrm{QE}}|^6 = 1/(a+d)^6$ can be adopted as an approximation ($\ell = 1$ in Eq. (1.58a)). The self-interaction contribution to Γ given by the second term on the RHS of Eq. (6.9) is shown in Figure 6.7b. Because of the frequency dependence of the self-interaction Green's function $\hat{\mathbb{G}}(\mathbf{r}_{\mathrm{QE}}, \mathbf{r}_{\mathrm{QE}}, 2\omega)$ [Eq. (1.58)], this is largest when the second-harmonic frequency is resonant with the DP or QP resonance of the MNP, and smallest for the off-resonance conditions. Notice that the broadening Γ of the QE transition determines the maximum nonlinear dipole moment of the QE that can be reached at resonance with the second-harmonic near field of the MNP, $\omega_{\mathrm{QE}} = 2\omega$.

We are now in a position to explain the main trends observed in Figure 6.6. Let us consider first the case of high intrinsic losses $\gamma_{\mathrm{QE}} = 10^{-1}$ eV dominating the decay of the QE over the extra losses introduced by the self-interaction, so that the "effective" broadening remains unchanged, $\Gamma \simeq \gamma_{\mathrm{QE}}$ (see Figure 6.7b). The QE dipole at the second-harmonic frequency can then be estimated from $\mathbf{P}_{2\omega}^{\mathrm{QE}} \propto \mathbf{E}_{\mathrm{ind}}^{\mathrm{TDDFT}}(\mathbf{r}_{\mathrm{QE}}, 2\omega)/\gamma_{\mathrm{QE}}$ [Eq. (6.5)]. The near field at the second-harmonic frequency induced by the MNP in response to the incident field is of quadrupolar character so that $\mathbf{E}_{\mathrm{ind}}^{\mathrm{TDDFT}} \propto 1/|\mathbf{r}_{\mathrm{QE}}|^4$, and correspondingly $\mathbf{P}_{2\omega}^{\mathrm{QE}} \propto 1/|\mathbf{r}_{\mathrm{QE}}|^4$. Further, the second-harmonic dipole of the MNP resulting from the interaction with

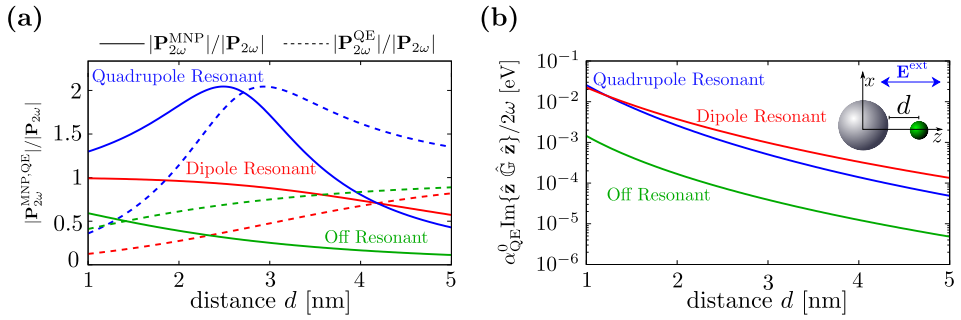

Figure 6.7: **(a)** Relative contributions of the MNP, $|\mathbf{P}^{\rm MNP}_{2\omega}|/|\mathbf{P}_{2\omega}|$ (solid lines), and of the QE, $|\mathbf{P}^{\rm QE}_{2\omega}|/|\mathbf{P}_{2\omega}|$ (dashed lines) to the total nonlinear dipole $\mathbf{P}_{2\omega}$ of the system at the second-harmonic frequency [Eq. (6.8)]. Results are shown as a function of the QE–MNP distance d. The QE is located at the z-axis ($\theta_{\rm QE} = 0$). **(b)** Additional broadening of the QE transition because of the interaction with the MNP. The quantity $\alpha^0_{\rm QE}{\rm Im}\{\hat{\mathbf{z}}\,\hat{\mathbb{G}}(\mathbf{r}_{\rm QE},\mathbf{r}_{\rm QE},2\omega)\,\hat{\mathbf{z}}\}/2\omega$ is shown as a function of the QE–MNP distance d. In the two panels we consider three different fundamental frequencies of the incident light, corresponding to $2\omega = 3.4$ eV (second harmonic at resonance with the QP resonance of the MNP, blue lines), $2\omega = 3.17$ eV (second harmonic at resonance with the DP resonance of the MNP, red lines), and $\omega = 2.4$ eV (off-resonant conditions, green lines).

the QE can be obtained from Eq. (6.5). This is given by $\mathbf{P}^{\rm MNP}_{2\omega} = \alpha_{\rm MNP}(2\omega)\hat{\mathbb{G}}_0\mathbf{P}^{\rm QE}_{2\omega}$, which results in $\mathbf{P}^{\rm MNP}_{2\omega} \propto 1/|\mathbf{r}_{\rm QE}|^7$. Therefore, the maximum total nonlinear dipole $\mathbf{P}_{2\omega}$ is reached for small d (the MNP dominating regime, see Figure 6.7a), and monotonically decreases with increasing d as a consequence of the drop-off of both the second-harmonic near field and the QE–MNP interaction. Since the emission is maximum for short distances where it is dominated by the nonlinear dipole moment of the MNP, the power emitted to the far field is enhanced when the second-harmonic matches the dipolar plasmon, i.e., when the MNP polarizability $\alpha_{\rm MNP}$ is largest.

We consider next the case of low intrinsic losses, $\gamma_{\rm QE} = 10^{-7}$ eV, such that the decay of the QE dipole is determined by the self-interaction for all the distances considered in the figures: $\Gamma \simeq \alpha^0_{\rm QE}{\rm Im}\{\hat{\mathbf{z}}\,\hat{\mathbb{G}}(\mathbf{r}_{\rm QE},\mathbf{r}_{\rm QE},2\omega)\,\hat{\mathbf{z}}\}/2\omega$ (magnitude plotted in Figure 6.7b). The nonlinear dipole of the QE at the second-harmonic frequency can then be estimated from $\mathbf{P}^{\rm QE}_{2\omega} \propto \mathbf{E}^{\rm TDDFT}_{\rm ind}(\mathbf{r}_{\rm QE},2\omega)/\Gamma$ [Eq. (6.5)]. The dependence of $\mathbf{P}^{\rm QE}_{2\omega}$ on the separation distance d is thus governed by that of the self interaction $\Gamma \sim 1/|\mathbf{r}_{\rm QE}|^6$ (using $\ell = 1$ in Eq. (1.58a) as an approximation) and that of the quadrupole near field at the second harmonic $\mathbf{E}^{\rm TDDFT}_{\rm ind} \propto 1/|\mathbf{r}_{\rm QE}|^4$. As a result, $\mathbf{P}^{\rm QE}_{2\omega} \propto |\mathbf{r}_{\rm QE}|^2$, while $\mathbf{P}^{\rm MNP}_{2\omega} = \alpha_{\rm MNP}(2\omega)\hat{\mathbb{G}}_0\mathbf{P}^{\rm QE}_{2\omega} \propto 1/|\mathbf{r}_{\rm QE}|$. The largest nonlinear dipole can be finally reached at large $|\mathbf{r}_{\rm QE}|$ owing to the dipole moment of the QE. The system is in the regime where the emission from the QE dominates (Figure 6.7a) and the intensity of SHG increases as $\sim |\mathbf{P}^{\rm QE}_{2\omega}|^2 \propto |\mathbf{r}_{\rm QE}|^4$. Additionally, since ${\rm Im}\{\hat{\mathbf{z}}\hat{\mathbb{G}}(\mathbf{r}_{\rm QE},\mathbf{r}_{\rm QE},\omega)\hat{\mathbf{z}}\}$ is maximum at resonance with the DP resonance of the MNP, setting $2\omega = \omega_{\rm DP}$ leads to a larger broadening of the QE resonance (larger Γ in Eq. (6.9)) and thus to smaller SHG. Thus, the largest nonlinear signal is obtained

in this regime for the second harmonic in resonance with the quadrupolar mode of the MNP and for off-resonance conditions. Apart from the losses introduced by the MNP, the second-harmonic near field $\mathbf{E}_{\rm ind}^{\rm TDDFT}(\mathbf{r}_{\rm QE}, \omega = 2\omega)$ induced by the individual MNP is stronger for the second harmonic matching the QP resonance of the MNP [394], $2\omega = \omega_{\rm QP} = 3.4$ eV, which explains why the SHG in Figure 6.6g is largest for this frequency. Interestingly, the reduction of the second-harmonic signal at small $|\mathbf{r}_{\rm QE}|$ because of the self-interaction term has a similar physical origin as the well-known effect of QE luminescence quenching in the linear regime [40, 169].

For intermediate losses, $\gamma_{\rm QE} = 10^{-3}$ eV, the "effective" broadening Γ of the QE is given by the self-interaction at small distances d from the surface and saturates to the intrinsic value $\gamma_{\rm QE}$ at larger distances (see Figure 6.7b). As a consequence, by increasing d the induced QE dipole at the second harmonic changes its distance dependence from $\mathbf{P}_{2\omega}^{\rm QE} \propto |\mathbf{r}_{\rm QE}|^2$ to $\mathbf{P}_{2\omega}^{\rm QE} \propto 1/|\mathbf{r}_{\rm QE}|^4$ leading to a maximum of SGH for a distance range of $d = 1.5 - 2$ nm.

6.2.4 Polarization conversion of the second-harmonic field

To close this chapter, we show the possibility to control the polarization of light emitted at the second-harmonic frequency owing to the quadrupolar character of the second-harmonic near field of the MNP. We analyze in Figure 6.8b the direction of polarization of the total second-harmonic dipole $\mathbf{P}_{2\omega}$ of the system for different positions of the QE with respect to the MNP. The direction of polarization of the nonlinear dipole is defined by the angle $\beta_{\mathbf{P}_{2\omega}}$, measured between $\mathbf{P}_{2\omega}$ and the positive direction of the z-axis, as schematically shown in Figure 6.8a. The position of the QE is given by the angle $\theta_{\rm QE}$. The QE is placed at different $\theta_{\rm QE}$ while keeping a fixed distance $d = 2$ nm from the MNP surface. The calculations are performed considering intermediate intrinsic losses, $\gamma_{\rm QE} = 10^{-3}$ eV, but the same qualitative behavior is found for other situations.

When the QE is located at $\theta_{\rm QE} = 0$ or $\theta_{\rm QE} = \pi$, corresponding to the polarization direction of the external laser field, the total emitting dipole at 2ω, $\mathbf{P}_{2\omega}$, is z-polarized ($\beta_{\mathbf{P}_{2\omega}} = 0$), i.e., it is parallel to the excitation laser. In contrast, when the QE is placed at $\theta_{\rm QE} = \pi/2$, the induced second-harmonic dipole $\mathbf{P}_{2\omega}$ is x-polarized ($\beta_{\mathbf{P}_{2\omega}} = \pi/2$) due to the quadrupolar character of the induced near field at the second harmonic. This implies a full polarization conversion of the second-harmonic radiation with respect to the external illumination. This result is a robust consequence of the symmetry of the system, as discussed in previous sections. When the QE is located at the z-axis, the system has a rotation symmetry with respect to the z-axis, thus no x- or y-polarized second-harmonic dipole can be produced. In a similar way, when the QE is located at the x-axis, the system is symmetric with respect to the (x, y)-plane, and therefore the z-polarized second-harmonic dipole is forbidden.

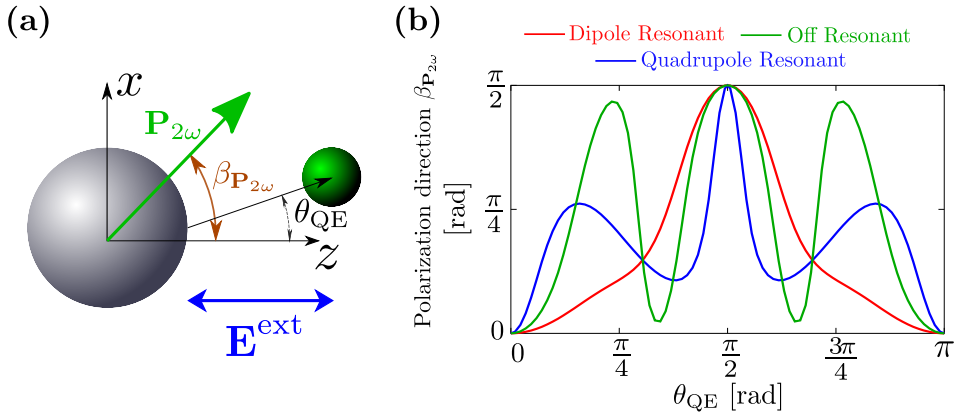

Figure 6.8: **(a)** Sketch of the QE–MNP system, where the polarization angle $\beta_{\mathbf{P}_{2\omega}}$ is defined as the angle between $\mathbf{P}_{2\omega}$ and the positive direction of the z-axis . **(b)** Polarization direction $\beta_{\mathbf{P}_{2\omega}}$ of the total emitting dipole $\mathbf{P}_{2\omega}$ as a function of the angular position θ_{QE} of the QE. The QE distance from the MNP surface is fixed to $d = 2$ nm, and $\gamma_{\mathrm{QE}} = 10^{-3}$ eV. $\theta_{\mathrm{QE}} = 0$ corresponds to the QE located at the z-axis, and $\theta_{\mathrm{QE}} = \pi/2$ corresponds to the QE located at the x-axis. We consider three different fundamental frequencies of the incident light, corresponding to $2\omega = 3.4$ eV (second harmonic at resonance with the QP resonance of the MNP, blue lines), $2\omega = 3.17$ eV (second harmonic at resonance with the DP resonance of the MNP, red lines), and $2\omega = 2.4$ eV (off-resonant conditions, green lines).

6.3 Summary

In summary, we have studied in this chapter how the electromagnetic coupling of a QE with a centrosymmetric MNP alters the nonlinear response of the coupled system and enables otherwise-forbidden SHG. Using TDDFT simulations we have shown that, when the second harmonic of the fundamental frequency is resonant with the transition frequency of the quantum emitter, the latter plays the role of an optical resonator that scatters the local second-harmonic near field created by the MNP into the far field.

For the present system, the TDDFT calculations reveal the following three-step scenario of SHG process: first, the MNP generates a second-harmonic near field in response to the incident radiation, second, the QE is resonantly excited at 2ω by this near field and, finally, the QE emits in the presence of the MNP. We would like to stress, however, that the generalization of this mechanism to other systems has to be done carefully considering the specific properties of the QE and the MNP. In particular, the polarization of the QE at the fundamental frequency could also lead to an appreciable nonlinear response of the MNP as would be, for instance, in the case of a small MNP and a strongly polarizable QE.

The insights provided by the TDDFT calculations allowed us to develop a semi-analytical model of the second-harmonic response of the QE–MNP coupled system. Using the semi-analytical model, we have demonstrated that the efficiency of the SHG, its dependence on the position of the QE, and its dependence on the

frequency match between the plasmonic modes of the MNP and the QE transition, is determined by the relative weight of the QE intrinsic losses and the broadening of the QE resonance induced by the self-interaction mediated by the MNP. We have shown that it is possible to obtain orders of magnitude stronger SHG by reducing the intrinsic losses of the QE.

Finally, we have demonstrated the possibility to control the polarization of light emitted at the second harmonic. We have shown that the polarization of the total second-harmonic dipole of the QE–MNP system depends on the position of the QE with respect to the axis defined by the polarization of the incident light. In particular, this allows us to obtain a full polarization conversion where the dipole emitting at the second harmonic is perpendicular to the external illuminating field.

Although the results shown in this chapter are obtained for a model spherical MNP and a structureless QE, the qualitative conclusions stem from the robust phenomenon of generation of even-harmonic near fields close to the MNP surface, from general symmetry constraints, and from the physics of optical resonators interacting with plasmonic nanostructures. It thus appears from our findings that the coupled QE–MNP structure can be a promising platform for creating and controlling second-harmonic generation.

CONCLUSIONS AND OUTLOOK

This thesis explores diverse quantum many-body phenomena in the optical response of metallic nanoparticles (MNPs) and in their coupling to quantum emitters (QEs) *via* plasmon–exciton interaction. In general, TDDFT has been the key tool to study a variety of quantum effects both in the linear and nonlinear regime of the optical response of the studied systems. Moreover, we have shown that overall the semiclassical surface-response formalism (SRF) based on the Feibelman parameters is a good approximation to capture quantum surface effects in the optical response of nanoscale plasmonic systems in situations where electron tunneling and nonlinear effects do not play a significant role.

The main findings and conclusions obtained in this thesis are summarized below:

- In Chapter 3, we provide a fundamental description of the electromagnetic coupling between spherical MNPs and point-dipole QEs at the nanoscale in situations where electron tunneling and any other charge-transfer process related to the electronic coupling between the QE and the MNPs can be neglected. With this purpose, we use TDDFT within the jellium model to study the impact of quantum surface effects on the self-interaction Green's function that governs the electromagnetic QE–MNPs interaction, showing that quantum many-body effects produce a redshift and broadening of plasmonic resonances not considered in classical theories that use a local dielectric response of the metals. With the help of the (standard) *nondispersive* SRF based on the long-wavelength Feibelman parameters (which neglects the nonlocality of the optical response along the metal surface), we confirm that the origin of the quantum effects can be linked to the spill out of the induced charges and surface-enabled Landau damping. Moreover, we demonstrate that, although the nondispersive SRF correctly reproduces the nonlocal surface response obtained by fully quantum TDDFT calculations for most QE–MNPs configurations, this approach fails when the QE is located in very close proximity to the MNP surface.

- In Chapter 4, we propose a *dispersive* SRF that resolves the shortcomings of the nondispersive SRF often used in the literature (and in Chapter 3) by explicitly accounting for the nonlocality of the optical response along the metal surface in the parallel direction. We first use TDDFT simulations to obtain the optical response of a metallic nanowire as described within the

jellium model, and calculate the Feibelman parameter $d_\perp(\omega, k_\parallel)$ as a function of the external excitation frequency, ω, and the wavenumber parallel to the metal surface, $k_\parallel$. Moreover, by studying the optical response of a cylindrical nanowire as well as that of spherical MNPs and their dimers using $d_\perp(\omega, k_\parallel)$, we show that by explicitly accounting for the dependence of the Feibelman parameters on $k_\parallel$ it is possible to extend the applicability range of the SRF to situations where extremely confined plasmonic fields are induced. The dispersive SRF proposed in Chapter 4 can thus be used to effectively account for quantum nonlocal effects in plasmonic systems with generality as long as charge-transfer processes and nonlinear effects are not involved.

- In Chapter 5, we analyze the effect of electronic coupling between a two-level QE and a spherical MNP dimer, in addition to the standard electromagnetic interaction. This electronic QE–MNPs coupling is often ignored in classical descriptions of the optical response as well as in other semiclassical models such as the SRF employed in Chapters 3 and 4, which treat the QEs as point-like dipoles. Using TDDFT calculations for the entire QE–MNPs hybrid system, we show that the hybridization between the electronic states of the QE and those of the MNPs strongly modifies the energy, the width and the very existence of the optical resonances of the coupled system. The QE exciton is shown to be quenched for QE–MNP surface-to-surface distances smaller than ≈ 0.5 nm. We can thus conclude that the application of a quantum many-body treatment which addresses charge-transfer processes between the QE and the MNPs is crucial to correctly address the optoelectronic response of a QE–MNPs system at (sub)-nanometer distances.

- In Chapter 6, we study nonlinear optical processes leading to second-harmonic generation (SHG) in a system comprising a QE and an individual spherical MNP, where the transition frequency of the QE is set to be resonant with the second harmonic of the incident frequency. We show that the QE enables strong SHG, otherwise forbidden due to symmetry constraints of the individual MNP. TDDFT calculations allow us to identify the main mechanism driving this nonlinear effect, where the QE plays the role of an optical resonator that experiences the nonlinear near fields generated by the metallic nanoantenna located nearby. We also develop a model that, by combining TDDFT and classical calculations, captures the main effects and contributions to this nonlinear process in a computationally simple manner. Using this model, we show that changing the position as well as the intrinsic properties of the QE and the MNP provides a high degree of control of nonlinear light emission.

We hope that the research carried out throughout this thesis has contributed to provide a deeper fundamental insight into quantum many-body phenomena that occur in (sub)-nanometric plasmonic cavities interacting with QEs. In addition, the results shown in this thesis open new questions that could also be addressed with the methodologies used and proposed here. Among others, we believe that the TDDFT methodology based on the wave-packet propagation method can

be applied e.g. to study nonlinear optoelectronic processes in plasmon–exciton systems of subnanometric dimensions, as well as charge-transfer effects in plasmonic nanocavities excited by ultrafast electromagnetic fields in situations of extremely narrow gaps where electron tunneling is important. Moreover, the quantitative accuracy of our predictions could be improved by considering atomic-scale features in the MNPs and QEs, a challenge that would require to go beyond the jellium description of the electronic structure adopted here.

On the other hand, we believe that the dispersive SRF proposed in this thesis could be straightforwardly implemented in existing numerical tools in Nanophotonics and could thus become a very valuable method for predicting optical nonlocal effects in practical nanoscale plasmonic configurations. Considering systems typically implemented in experiments would require the extraction of the dispersive Feibelman parameters as a function of $k_{\parallel}$ for materials relevant in plasmonics, such as silver or gold, where d-band electronic transitions are known to play a crucial role producing e.g. a spill in of the induced charges instead of spill out. The effect of d-electrons is neglected within the jellium model employed in this thesis, and thus more sophisticated models or improvements to the present jellium model would be needed to extract the appropriate Feibelman parameters and thus extend the dispersive SRF proposed in this thesis to experimental situations. All in all, we expect that the quantum TDDFT and the semiclassical SRF methodologies presented in this thesis can be further exploited in the future to investigate novel quantum phenomena in Nanophotonics and thus to contribute to technological advances.

Appendices

Appendix A

Atomic units

In this thesis, we use Hartree atomic units (au), where the following fundamental physical constants are all unity by definition:

- electron mass m_e,
- elementary charge e,
- Bohr radius a_0,
- Reduced Planck's constant $\hbar = h/2\pi$,
- Coulomb's constant $1/(4\pi\epsilon_0)$.

The equivalence between Hartree atomic units and the International System of Units (SI) of the main physical quantities is given in Table A.1.

Quantity	Hartree atomic units	SI units
Mass	m_e	$9.10938215 \cdot 10^{-31}$ kg
Charge	e	$1.602176487 \cdot 10^{-19}$ C
Length	a_0	$5.2917720859 \cdot 10^{-11}$ m
Angular momentum	$\hbar$	$1.054571628 \cdot 10^{-34}$ Js
Energy	$E_h = \hbar^2/(m_e a_0^2)$	$4.35974394 \cdot 10^{18}$ J
Magnetic field	$\hbar/(ea_0^2)$	$2.350517382 \cdot 10^{5}$ T
Electric dipole moment	ea_0	$8.47835281 \cdot 10^{11}$ Cm
Electric field	$E_h/(ea_0)$	$5.14220632 \cdot 10^{11}$ V/m
Time	$\hbar/E_h$	$2.418884326505 \cdot 10^{-17}$ s

Table A.1: Equivalence between Hartree atomic units and SI units of the main physical quantities.

Appendix B

Electric near field induced by a spherical nanoparticle within the classical local-response approximation (LRA)

We show in this appendix the classical LRA expression of the electric near field $\mathbf{E}^{\mathrm{ind}}(\mathbf{r},\omega)$ induced by an individual spherical nanoparticle of radius a in response to an arbitrary external illumination. Within the nonretarded approximation, $\mathbf{E}^{\mathrm{ind}}(\mathbf{r},\omega)$ is obtained from $\mathbf{E}^{\mathrm{ind}}(\mathbf{r},\omega) = -\nabla\phi^{\mathrm{ind}}(\mathbf{r},\omega)$ [Eq. (1.28)], where the induced potential $\phi^{\mathrm{ind}}(\mathbf{r},\omega)$ is given by Eq. (1.26). In spherical coordinates $\{r,\theta,\varphi\}$, the gradient ∇ is given by:

$$\nabla = \frac{\partial}{\partial r}\hat{\mathbf{r}} + \frac{1}{r}\frac{\partial}{\partial\theta}\hat{\boldsymbol{\theta}} + \frac{1}{r\sin\theta}\frac{\partial}{\partial\varphi}\hat{\boldsymbol{\varphi}}, \tag{B.1}$$

so that the components $\{\mathrm{E}_r^{\mathrm{ind}}(\mathbf{r},\omega),\ \mathrm{E}_\theta^{\mathrm{ind}}(\mathbf{r},\omega),\ \mathrm{E}_\varphi^{\mathrm{ind}}(\mathbf{r},\omega)\}$ of

$$\mathbf{E}^{\mathrm{ind}}(\mathbf{r},\omega) = \mathrm{E}_r^{\mathrm{ind}}(\mathbf{r},\omega)\hat{\mathbf{r}} + \mathrm{E}_\theta^{\mathrm{ind}}(\mathbf{r},\omega)\hat{\boldsymbol{\theta}} + \mathrm{E}_\varphi^{\mathrm{ind}}(\mathbf{r},\omega)\hat{\boldsymbol{\varphi}}$$

can be expressed as:

$$\mathrm{E}_r^{\mathrm{ind}}(\mathbf{r},\omega) = \begin{cases} -\sum\limits_{\ell,m} \ell\ Y_\ell^m(\theta,\varphi) b_{\ell m}(\omega) r^{\ell-1}/a^\ell & r < a \\ \\ \sum\limits_{\ell,m} (\ell+1)\ Y_\ell^m(\theta,\varphi) b_{\ell m}(\omega) a^{\ell+1}/r^{\ell+2} & r > a \end{cases}, \tag{B.2}$$

$$\mathrm{E}_{\varphi}^{\mathrm{ind}}(\mathbf{r},\omega)=\begin{cases}-\sum\limits_{\ell,m}\frac{im}{\sin\theta}\;Y_{\ell}^{m}(\theta,\varphi)\;b_{\ell m}(\omega)r^{\ell-1}/a^{\ell} & r\leq a\\ \\ -\sum\limits_{\ell,m}\frac{im}{\sin\theta}\;Y_{\ell}^{m}(\theta,\varphi)\;b_{\ell m}(\omega)a^{\ell+1}/r^{\ell+2} & r\geq a\end{cases}, \tag{B.3}$$

$$\mathrm{E}_{\theta}^{\mathrm{ind}}(\mathbf{r},\omega)=\begin{cases}-\sum\limits_{\ell,m}\frac{\partial}{\partial\theta}\left[Y_{\ell}^{m}(\theta,\varphi)\right]\;b_{\ell m}(\omega)r^{\ell-1}/a^{\ell} & r\leq a\\ \\ -\sum\limits_{\ell,m}\frac{\partial}{\partial\theta}\left[Y_{\ell}^{m}(\theta,\varphi)\right]\;b_{\ell m}(\omega)a^{\ell+1}/r^{\ell+2} & r\geq a\end{cases}, \tag{B.4}$$

where the coefficients $b_{\ell m}(\omega)$ are given by Eq. (1.27). In Eq. (B.4), we can calculate the derivative $\frac{\partial}{\partial\theta}\left[Y_{\ell}^{m}(\theta,\varphi)\right]$ as follows:

$$\begin{aligned}\frac{\partial}{\partial\theta}\left[Y_{\ell}^{m}(\theta,\varphi)\right]&=\sqrt{\frac{2\ell+1}{4\pi}\frac{(\ell-m)!}{(\ell+m)!}}e^{im\varphi}\frac{\partial}{\partial\theta}P_{\ell}^{m}(\cos\theta)\\&=-\sqrt{\frac{2\ell+1}{4\pi}\frac{(\ell-m)!}{(\ell+m)!}}e^{im\varphi}\frac{1}{2}\Big((\ell+m)(\ell-m+1)P_{\ell}^{m-1}(\cos\theta)\\&\qquad\qquad-P_{\ell}^{m+1}(\cos\theta)\Big),\end{aligned} \tag{B.5}$$

with $P_{\ell}^{m}(\cos\theta)$ the associated Legendre Polynomials.

Finally, we can write the components $\{\mathrm{E}_{x}^{\mathrm{ind}}(\mathbf{r},\omega),\ \mathrm{E}_{y}^{\mathrm{ind}}(\mathbf{r},\omega),\ \mathrm{E}_{z}^{\mathrm{ind}}(\mathbf{r},\omega)\}$ of $\mathbf{E}^{\mathrm{ind}}(\mathbf{r},\omega)=\mathrm{E}_{x}^{\mathrm{ind}}(\mathbf{r},\omega)\hat{\mathbf{x}}+\mathrm{E}_{y}^{\mathrm{ind}}(\mathbf{r},\omega)\hat{\mathbf{y}}+\mathrm{E}_{z}^{\mathrm{ind}}(\mathbf{r},\omega)\hat{\mathbf{z}}$ in Cartesian coordinates:

$$\begin{aligned}\begin{pmatrix}\mathrm{E}_{x}^{\mathrm{ind}}(\mathbf{r},\omega)\\ \mathrm{E}_{y}^{\mathrm{ind}}(\mathbf{r},\omega)\\ \mathrm{E}_{z}^{\mathrm{ind}}(\mathbf{r},\omega)\end{pmatrix}&=\begin{pmatrix}\sin\theta\cos\varphi & \cos\theta\cos\varphi & -\sin\varphi\\ \sin\theta\sin\varphi & \cos\theta\sin\varphi & \cos\varphi\\ \cos\theta & -\sin\theta & 0\end{pmatrix}\begin{pmatrix}\mathrm{E}_{r}^{\mathrm{ind}}(\mathbf{r},\omega)\\ \mathrm{E}_{\theta}^{\mathrm{ind}}(\mathbf{r},\omega)\\ \mathrm{E}_{\varphi}^{\mathrm{ind}}(\mathbf{r},\omega)\end{pmatrix}\\&=\begin{pmatrix}\mathrm{E}_{r}^{\mathrm{ind}}(\mathbf{r},\omega)\sin\theta\cos\varphi+\mathrm{E}_{\theta}^{\mathrm{ind}}(\mathbf{r},\omega)\cos\theta\cos\varphi-\mathrm{E}_{\varphi}^{\mathrm{ind}}(\mathbf{r},\omega)\sin\varphi\\ \mathrm{E}_{r}^{\mathrm{ind}}(\mathbf{r},\omega)\sin\theta\sin\varphi+\mathrm{E}_{\theta}^{\mathrm{ind}}(\mathbf{r},\omega)\cos\theta\sin\varphi+\mathrm{E}_{\varphi}^{\mathrm{ind}}\cos\varphi\\ \mathrm{E}_{r}^{\mathrm{ind}}(\mathbf{r},\omega)\cos\theta-\mathrm{E}_{\theta}^{\mathrm{ind}}(\mathbf{r},\omega)\sin\theta.\end{pmatrix}\end{aligned} \tag{B.6}$$

Appendix C

Dynamics of quantum emitters in the time domain

We describe in this appendix the method used in this thesis to solve Eq. (1.54) numerically in time domain, which is crucial to obtain the TDDFT results of the nonlinear optical response of a quantum emitter coupled to a metallic nanoparticle in Chapter 6. The second-order differential equation given by Eq. (1.54) can be transformed into a system of two first-order equations,

$$\begin{aligned} \dot{\mathbf{Q}}_{\mathrm{QE}}(t) + \gamma_{\mathrm{QE}}\mathbf{Q}_{\mathrm{QE}}(t) + \omega_{\mathrm{QE}}^2\mathbf{P}_{\mathrm{QE}}(t) &= \alpha_{\mathrm{QE}}^0\mathbf{E}^{\mathrm{ext}}(t), \\ \mathbf{Q}_{\mathrm{QE}}(t) &= \dot{\mathbf{P}}_{\mathrm{QE}}(t), \end{aligned} \tag{C.1}$$

which, after redefining

$$\mathbf{Q}_{\mathrm{QE}}(t) \to i\omega_{\mathrm{QE}}\tilde{\mathbf{Q}}_{\mathrm{QE}}(t)$$

and

$$\mathbf{P}_{\mathrm{QE}}(t) \to i\tilde{\mathbf{P}}_{\mathrm{QE}}(t),$$

can be written in a matrix form,

$$i\frac{\partial}{\partial t}\underbrace{\begin{bmatrix}\tilde{\mathbf{P}}_{\mathrm{QE}}(t)\\ \tilde{\mathbf{Q}}_{\mathrm{QE}}(t)\end{bmatrix}}_{\Psi_{\mathrm{QE}}(t)} = \underbrace{\begin{bmatrix}0 & i\omega_{\mathrm{QE}}\\ -i\omega_{\mathrm{QE}} & -i\gamma_{\mathrm{QE}}\end{bmatrix}}_{\hat{H}_{\mathrm{QE}}}\underbrace{\begin{bmatrix}\tilde{\mathbf{P}}_{\mathrm{QE}}(t)\\ \tilde{\mathbf{Q}}_{\mathrm{QE}}(t)\end{bmatrix}}_{\Psi_{\mathrm{QE}}(t)} + \underbrace{\begin{bmatrix}0\\ \alpha_{\mathrm{QE}}^0\mathbf{E}^{\mathrm{ext}}(t)/\omega_{\mathrm{QE}}\end{bmatrix}}_{F(t)}. \tag{C.2}$$

We have then transformed Eq. (1.54) into the following vector equation,

$$i\frac{\partial}{\partial t}\Psi_{\mathrm{QE}}(t) = \hat{H}_{\mathrm{QE}}\Psi_{\mathrm{QE}}(t) + F(t), \tag{C.3}$$

where

$$\Psi_{\mathrm{QE}}(t) \equiv \begin{bmatrix}\tilde{\mathbf{P}}_{\mathrm{QE}}(t)\\ \tilde{\mathbf{Q}}_{\mathrm{QE}}(t)\end{bmatrix}. \tag{C.4}$$

The solution to Eq. (C.3) is

$$\Psi_{\mathrm{QE}}(t) = -i \int_{-\infty}^{t} dt' e^{-i\hat{H}_{\mathrm{QE}}(t-t')} F(t'). \tag{C.5}$$

Therefore,

$$\begin{aligned}
\Psi_{\mathrm{QE}}(t+\Delta t) &= -i \int_{-\infty}^{t+\Delta t} dt' e^{-i\hat{H}_{\mathrm{QE}}(t+\Delta t-t')} F(t') \\
&= -ie^{-i\hat{H}_{\mathrm{QE}}\Delta t}\Big(\int_{-\infty}^{t} dt' e^{-i\hat{H}_{\mathrm{QE}}(t-t')} F(t') + \int_{t}^{t+\Delta t} dt' e^{-i\hat{H}_{\mathrm{QE}}(t-t')} F(t')\Big) \\
&= e^{-i\hat{H}_{\mathrm{QE}}\Delta t}\Psi_{\mathrm{QE}}(t) - i\Delta t e^{-i\hat{H}_{\mathrm{QE}}\Delta t/2} F(t+\Delta t/2) \\
&= e^{-i\hat{H}_{\mathrm{QE}}\Delta t/2}\{e^{-i\hat{H}_{\mathrm{QE}}\Delta t/2}\Psi_{\mathrm{QE}}(t) - i\Delta t F(t+\Delta t/2)\}.
\end{aligned} \tag{C.6}$$

In the last two steps of the derivation in Eq. (C.6), we have approximated the integral in the following way,

$$\int_{t}^{t+\Delta} F(t')dt' \approx \Delta t F\left(t+\Delta t/2\right). \tag{C.7}$$

To apply the operator $e^{-i\hat{H}_{\mathrm{QE}}\Delta t/2}$ in Eq. (C.6), we use the Split-Operator technique as described in Subsection 2.2.1,

$$e^{-i\frac{\Delta t}{2}\hat{H}_{\mathrm{QE}}} \approx e^{-i\frac{\Delta t}{4}\hat{\Gamma}} e^{-i\frac{\Delta t}{2}\hat{H}_0} e^{-i\frac{\Delta t}{4}\hat{\Gamma}}, \tag{C.8}$$

where

$$\hat{H}_0 = \begin{bmatrix} 0 & i\omega_{\mathrm{QE}} \\ -i\omega_{\mathrm{QE}} & 0 \end{bmatrix}, \qquad \hat{\Gamma} = \begin{bmatrix} 0 & 0 \\ 0 & -i\gamma_{\mathrm{QE}} \end{bmatrix}. \tag{C.9}$$

On the one hand, since $\hat{\Gamma}$ is a diagonal matrix, the operator

$$e^{-i\frac{\Delta t}{4}\hat{\Gamma}} = \begin{bmatrix} 1 & 0 \\ 0 & e^{-\frac{\Delta t}{4}\gamma} \end{bmatrix} \tag{C.10}$$

can be directly applied.

On the other hand, to apply the operator $e^{-i\hat{H}_0\frac{\Delta t}{2}}$, we write the matrix H_0 as

$$\hat{H}_0 = \hat{V}\hat{\Lambda}\hat{V}^{-1}, \tag{C.11}$$

where

$$\hat{V} = \frac{1}{\sqrt{2}}\begin{bmatrix} 1 & 1 \\ -i & i \end{bmatrix}, \qquad \hat{V}^{-1} = \frac{1}{\sqrt{2}}\begin{bmatrix} 1 & -i \\ 1 & i \end{bmatrix}, \tag{C.12}$$

and $\hat{\Lambda}$ is a diagonal matrix containing the eigenvalues of $\hat{H}_0$, $\lambda_1 = \omega_{\mathrm{QE}}$ and $\lambda_2 = -\omega_{\mathrm{QE}}$ as elements.

Therefore,

$$
\begin{aligned}
e^{-i\hat{H}_0\Delta t/2} =& \sum_{n=0}^{\infty}\left(\frac{-i\Delta t}{2}\right)^n \frac{1}{n!}\left(\hat{H}_0\right)^n = \sum_{n=0}^{\infty}\left(\frac{-i\Delta t}{2}\right)^n \frac{1}{n!}\left(\hat{V}\hat{\Lambda}\hat{V}^{-1}\right)^n \\
=& \hat{V}\left(\sum_{n=0}^{\infty}\left(\frac{-i\Delta t}{2}\right)^n \frac{1}{n!}\left(\hat{\Lambda}\right)^n\right)\hat{V}^{-1} = \hat{V}e^{-i\hat{\Lambda}\Delta t/2}\hat{V}^{-1} \\
=& \begin{bmatrix} V_{11} & V_{12} \\ V_{21} & V_{22} \end{bmatrix} \begin{bmatrix} e^{-i\lambda_1\Delta t/2} & 0 \\ 0 & e^{-i\lambda_2\Delta t/2} \end{bmatrix} \begin{bmatrix} V_{11} & V_{21} \\ V_{12} & V_{22} \end{bmatrix}.
\end{aligned} \tag{C.13}
$$

In summary, we solve Eq. (1.54) using Eq. (C.6) recursively, where the operator $e^{-i\hat{H}_{\mathrm{QE}}\Delta t/2}$ is approximated with the Split-Operator technique given by Eq. (C.8). Finally, $e^{-i\hat{H}_0\frac{\Delta t}{2}}$ is expressed using Eq. (C.11), Eq. (C.13) and Eq. (C.12).

Appendix D

Dispersive Feibelman parameter obtained for cylindrical nanowires of different size

We show in this appendix the dispersive Feibelman parameter $d_\perp(\omega, k_\parallel)$ obtained within TDDFT for different nanowire radius R_c such that the effective wavenumber $k_\parallel = m/R_c$ is fixed for each nanowire. Figure D.1 shows the real (panel a) and imaginary (b) parts of $d_\perp(\omega, k_\parallel)$ obtained for $R_c = 100$ a$_0$ and $R_c = 150$ a$_0$. The results for $R_c = 150$ a$_0$ are shown in Figure 4.4 (Chapter 4). The values of m for each nanowire size are chosen such that they give the same ratio $k_\parallel = m/R_c$ for the two radii R_c. $k_\parallel = 0.02$ a$_0^{-1}$, 0.1 a$_0^{-1}$ and 0.2 a$_0^{-1}$ are considered in this appendix.

As explained in Chapter 4, an effective wavenumber $k_\parallel = m/R_c$ determines the optical response of the system, and therefore Figure D.1 shows very good agreement between the results obtained for different radius as long as the ratio $k_\parallel = m/R_c$ is fixed. The invariance of the results with respect to modification of the size of the nanowire further supports that the parameter $d_\perp(\omega, m/R_c)$ obtained from TDDFT calculations for a cylindrical nanowire can be indeed interpreted as the dispersive $d_\perp(\omega, k_\parallel)$ corresponding to a planar metal surface. The small discrepancies between the results obtained for different radius and large $k_\parallel$ (i.e., for large m or small R_c) are because the coupling between the plasmon and single-particle excitations (surface-enabled Landau damping) leads to discrete features in the otherwise smooth resonance profile of $d_\perp(\omega, k_\parallel)$, which hampers the extraction of the Feibelman parameter $d_\perp(\omega, k_\parallel)$.

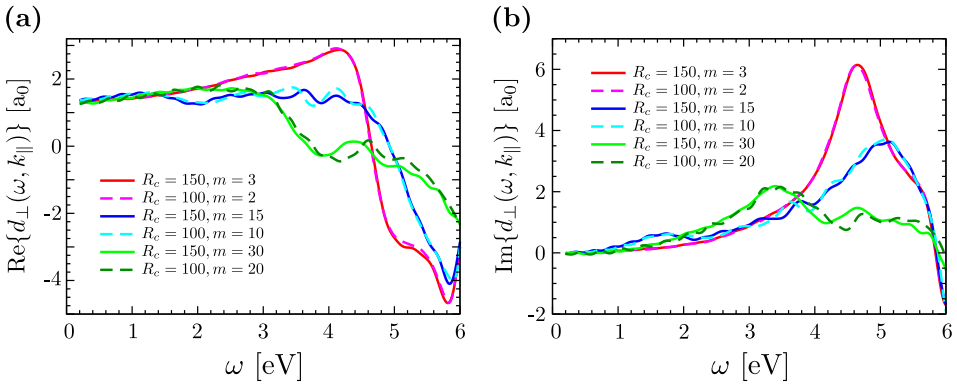

Figure D.1: **(a)** Real part of the dispersive Feibelman parameter $d_\perp(\omega, k_\parallel = m/R_c)$ for different values of m and R_c as obtained from TDDFT calculations performed for cylindrical nanowires. Results are shown as a function of the frequency, ω. The values of m and R_c are indicated in the inset. **(b)** Same as in (a) for the imaginary part. A Wigner–Seitz radius $r_s = 4$ a$_0$ corresponding to sodium is used to describe the electronic structure of the system within the jellium model.

Appendix E

Plasmon resonances sustained by a cylindrical nanowire within the surface-response formalism

We discuss in this appendix the resonance conditions of localized surface plasmons sustained by a cylindrical nanowire within the SRF, which are derived by applying the classical boundary conditions between two media. To link the SRF and the classical LRA solution of the induced potential [Eq. (4.6)],

$$\phi^{\text{ind}}(\rho,\varphi,\omega) = \sum_{m=-\infty}^{\infty} \phi_m(\rho,\omega) e^{im\varphi},$$

we assume that, outside the small region $R_c \pm \Delta$, the classical boundary condition of the continuity of the normal component of the displacement vector $\mathbf{D}(\rho,\varphi,\omega)$ holds [Eq. (1.15a) with $\sigma_s = 0$],

$$\hat{\mathbf{n}} \cdot \mathbf{D}(\rho,\varphi,\omega)\Big|_{\rho=R_c-\Delta} = \hat{\mathbf{n}} \cdot \mathbf{D}(\rho,\varphi,\omega)\Big|_{\rho=R_c+\Delta}, \tag{E.1}$$

where $\hat{\mathbf{n}}$ is the normal unit vector pointing outwards from the metal boundary. The boundary condition given by Eq. (E.1) corresponds to the one given by Eq. (2.83b) with $d_{\parallel}(\omega) = 0$.

Since $\mathbf{D}(\rho,\varphi,\omega) = \varepsilon(\omega)\mathbf{E}(\rho,\varphi,\omega)$ (with $\varepsilon(\omega)$ the dielectric function), $\hat{\mathbf{n}} = \hat{\boldsymbol{\rho}}$, and $\mathbf{E}(\rho,\varphi,\omega) = \mathbf{E}^{\text{ext}} - \nabla\phi^{\text{ind}}(\rho,\varphi,\omega)$ (with $\mathbf{E}^{\text{ext}}$ the external electric field) the boundary condition given by Eq. (E.1) yields

$$\varepsilon(\omega)\left(\hat{\boldsymbol{\rho}} \cdot \mathbf{E}^{\text{ext}} - \frac{\partial\phi^{\text{ind}}(\rho,\varphi,\omega)}{\partial\rho}\right)\Big|_{\rho=R_c-\Delta} = \left(\hat{\boldsymbol{\rho}} \cdot \mathbf{E}^{\text{ext}} - \frac{\partial\phi^{\text{ind}}(\rho,\varphi,\omega)}{\partial\rho}\right)\Big|_{\rho=R_c+\Delta}. \tag{E.2}$$

The external electric field can be expressed as $\mathbf{E}^{\text{ext}} = \sum_{m=-\infty}^{\infty} \mathbf{E}_m^{\text{ext}}(\rho) e^{im\varphi}$,

and thus Eq. (E.2) transforms into

$$\varepsilon(\omega)\left(\hat{\boldsymbol{\rho}}\cdot\mathbf{E}_m^{\rm ext}(\rho)-\frac{\partial\phi_m(\rho,\omega)}{\partial\rho}\right)\Bigg|_{\rho=R_c-\Delta}=\left(\hat{\boldsymbol{\rho}}\cdot\mathbf{E}_m^{\rm ext}(\rho)-\frac{\partial\phi_m(\rho,\omega)}{\partial\rho}\right)\Bigg|_{\rho=R_c+\Delta}. \tag{E.3}$$

Using the definitions of the potentials $\phi_m(\rho,\omega)$ given by Eq. (4.19), we obtain

$$2\pi\frac{q^{\rm cyl}(\omega,m)}{R_c}=\frac{\varepsilon(\omega)-1}{\varepsilon(\omega)\left[1-\frac{m}{R_c}d_\perp^{\rm cyl}(\omega,m)\right]+\left[1+\frac{m}{R_c}d_\perp^{\rm cyl}(\omega,m)\right]}\,\hat{\boldsymbol{\rho}}\cdot\mathbf{E}_m^{\rm ext}(\rho). \tag{E.4}$$

The surface charge $q^{\rm cyl}(\omega,m)$ per unit length in the z-coordinate (and per 2π in φ) of the nanowire within the SRF is then

$$q^{\rm cyl}(\omega,m)=\frac{\varepsilon(\omega)-1}{\varepsilon(\omega)+1-\frac{m}{R_c}d_\perp^{\rm cyl}(\omega,m)\left[\varepsilon(\omega)-1\right]}\,E_m^{\rm ext}\,\frac{R_c}{2\pi}. \tag{E.5}$$

In what follows, we assume that the metal dielectric function $\varepsilon(\omega)$ is well described with a Drude model [Eq. (1.10)], so that we obtain

$$q^{\rm cyl}(\omega,m)=-\frac{\omega_p^2}{2\omega(\omega+i\gamma_p)-\omega_p^2+\frac{m}{R_c}d_\perp^{\rm cyl}(\omega,m)\omega_p^2}\,E_m^{\rm ext}\,\frac{R_c}{2\pi}, \tag{E.6}$$

or

$$q^{\rm cyl}(\omega,m)=-\frac{\omega_p^2}{2\omega(\omega+i\gamma_p)-\omega_p^2\left[1-\frac{m}{R_c}d_\perp^{\rm cyl}(\omega,m)\right]}\,E_m^{\rm ext}\,\frac{R_c}{2\pi}. \tag{E.7}$$

The plasmon resonance frequencies ω_m are given by the poles of the denominator in Eq. (E.7)

$$2\omega_m(\omega_m+i\gamma_p)-\omega_p^2\left[1-\frac{m}{R_c}d_\perp^{\rm cyl}(\omega,m)\right]=0. \tag{E.8}$$

Thus, for $d_\perp^{\rm cyl}(\omega,m)\ll R_c$, we can express the frequency of the plasmon resonance as

$$\omega_m=\frac{\omega_p}{\sqrt{2}}\left[1-\frac{1}{2}\frac{m}{R_c}{\rm Re}\{d_\perp^{\rm cyl}(\omega=\omega_m,m)\}\right], \tag{E.9}$$

and the width as

$$\kappa_m=\frac{\omega_p}{\sqrt{2}}\,\frac{m}{R_c}{\rm Im}\left\{d_\perp^{\rm cyl}(\omega=\omega_m,m)\right\}+\gamma_p. \tag{E.10}$$

Finally, using again $k_\parallel=m/R_c$, we obtain the following expressions for the plasmon resonance frequency $\omega_s(k_\parallel)$ (see Eq. (4.20) in Chapter 4) and the width $\kappa_s(k_\parallel)$ as a function of $k_\parallel$:

$$\omega_s(k_\parallel)=\omega_{\rm SP}\Big(1-\frac{k_\parallel}{2}{\rm Re}\{d_\perp(\omega_s,k_\parallel)\}\Big), \tag{E.11}$$

$$\kappa_s(k_\parallel) = \omega_{\mathrm{SP}} k_\parallel \mathrm{Im}\{d_\perp(\omega_s, k_\parallel)\} + \gamma_p, \tag{E.12}$$

where $\omega_{\mathrm{SP}} = \frac{\omega_p}{\sqrt{2}}$ is the surface plasmon frequency for $k_\parallel = 0$.

Appendix F

Relationship between the results obtained under finite Gaussian pulses and plane-wave excitation

In Chapter 6, we first obtain the nonlinear response of the system subjected to a quasi-monochromatic Gaussian electromagnetic pulse [Eq. (6.2)], and then we obtain in Subsection 6.2.3 the corresponding results for plane-wave illumination. In this appendix, we explain how we estimate the results of the second-harmonic nonlinear response of the system under plane-wave illumination by using the results obtained for a finite Gaussian pulse: we first discuss how we connect the second-harmonic near field created by the individual MNP under finite-pulse and plane-wave illumination, and then we extend this discussion to the second-harmonic dipole moment of the coupled QE–MNP system.

Second-harmonic near field

In response to the following z-polarized plane-wave illumination,

$$\mathbf{E}^{\text{ext}}(t) = \hat{\mathbf{z}}\mathrm{E}_{\text{pw}}\cos\omega t = \hat{\mathbf{z}}\frac{\mathrm{E}_{\text{pw}}}{2}\left(e^{-i\omega t} + e^{i\omega t}\right), \tag{F.1}$$

the individual MNP (without QE) induces a nonlinear near field $\mathbf{E}^{\text{ind}}(\mathbf{r}, t)$ along the direction defined by the unit vector $\hat{\boldsymbol{\xi}}$ that can be expressed as a sum of different harmonics $\Omega = n\omega$,

$$\mathbf{E}^{\text{ind}}(\mathbf{r}, t) = \sum_n \mathrm{E}_{n\omega,\hat{\boldsymbol{\xi}}}(\mathbf{r})e^{-in\omega t}. \tag{F.2}$$

We define $\chi^{(2)}_{\text{field-field},\hat{\boldsymbol{\xi}}}(\mathbf{r})$ as the constant of proportionality relating the amplitude of the $\hat{\boldsymbol{\xi}}$-polarized second-harmonic near field $\mathrm{E}_{2\omega,\hat{\boldsymbol{\xi}}}(\mathbf{r})$ ($n = 2$) induced at position $\mathbf{r}$ near the MNP surface and the square of the amplitude of the component

$\mathrm{E}_{\omega} = \mathrm{E}_{\mathrm{pw}}/2$ of the incident plane wave $\mathbf{E}^{\mathrm{ext}}(t)$ [Eq. (F.1)] oscillating at the fundamental frequency ω, such that

$$\begin{aligned} \mathrm{E}_{2\omega,\hat{\boldsymbol{\xi}}}(\mathbf{r}) &= \chi^{(2)}_{\text{field-field},\hat{\boldsymbol{\xi}}}(\mathbf{r})\mathrm{E}_{\omega}\mathrm{E}_{\omega} \\ &= \frac{1}{4}\chi^{(2)}_{\text{field-field},\hat{\boldsymbol{\xi}}}(\mathbf{r})\mathrm{E}^2_{\mathrm{pw}}. \end{aligned} \tag{F.3}$$

Thus, for an incident plane wave the constant of proportionality $\chi^{(2)}_{\text{field-field},\hat{\boldsymbol{\xi}}}(\mathbf{r})$ is straightforwardly obtained from

$$\chi^{(2)}_{\text{field-field},\hat{\boldsymbol{\xi}}}(\mathbf{r}) = 4\mathrm{E}_{2\omega,\hat{\boldsymbol{\xi}}}(\mathbf{r})/\mathrm{E}^2_{\mathrm{pw}}. \tag{F.4}$$

However, in Chapter 6 the second-harmonic near field of the individual MNP is extracted from TDDFT simulations that consider illumination by a Gaussian pulse following [Eq. (6.2)]

$$\mathbf{E}^{\mathrm{ext}}(t) = \hat{\mathbf{z}}\mathrm{E}_0\cos(\omega(t-t_0))e^{-\left(\frac{t-t_0}{\sigma}\right)^2} = \hat{\mathbf{z}}\frac{\mathrm{E}_0}{2}\left(e^{-i\omega(t-t_0)} + e^{i\omega(t-t_0)}\right)e^{-\left(\frac{t-t_0}{\sigma}\right)^2}, \tag{F.5}$$

and, therefore, $\chi^{(2)}_{\text{field-field},\hat{\boldsymbol{\xi}}}(\mathbf{r})$ cannot be directly obtained from Eq. (F.4). In this situation, the component E_{ω} of $\mathbf{E}^{\mathrm{ext}}(t)$ oscillating at the fundamental frequency ω is given by

$$\mathrm{E}_{\omega}(t) = \frac{\mathrm{E}_0}{2}e^{-i\omega(t-t_0)}e^{-\left(\frac{t-t_0}{\sigma}\right)^2}, \tag{F.6}$$

so that, according to Eq. (F.3), the component of the near field $\mathrm{E}_{2\omega,\hat{\boldsymbol{\xi}}}(\mathbf{r},t)$ that oscillates along the $\boldsymbol{\xi}$-axis at 2ω is given in time domain by

$$\mathrm{E}_{2\omega,\hat{\boldsymbol{\xi}}}(\mathbf{r},t) = \frac{1}{4}\chi^{(2)}_{\text{field-field},\hat{\boldsymbol{\xi}}}(\mathbf{r})\mathrm{E}^2_0 e^{-i2\omega(t-t_0)}e^{-2\left(\frac{t-t_0}{\sigma}\right)^2}, \tag{F.7}$$

where we assume that $\chi^{(2)}_{\text{field-field},\hat{\boldsymbol{\xi}}}(\mathbf{r})$ is constant over the spectral width of the illumination field. Using the time-to-frequency Fourier transform $\mathcal{F}[\,]$ we get the frequency-resolved quantity

$$\begin{aligned} \mathrm{E}_{2\omega,\hat{\boldsymbol{\xi}}}(\mathbf{r},\Omega) &= \mathcal{F}\left[\mathrm{E}_{2\omega,\hat{\boldsymbol{\xi}}}(\mathbf{r},t)\right] \\ &= \frac{1}{4}\chi^{(2)}_{\text{field-field},\hat{\boldsymbol{\xi}}}(\mathbf{r})\mathrm{E}^2_0\mathcal{F}\left[e^{-i2\omega(t-t_0)}\right] * \mathcal{F}\left[e^{-2\left(\frac{t-t_0}{\sigma}\right)^2}\right], \end{aligned} \tag{F.8}$$

where the symbol * represents the convolution. Finally, the component of the near field oscillating at 2ω yields (in frequency domain)

$$\mathrm{E}_{2\omega,\hat{\boldsymbol{\xi}}}(\mathbf{r},\Omega) = \frac{1}{4}\chi^{(2)}_{\text{field-field},\hat{\boldsymbol{\xi}}}(\mathbf{r})\mathrm{E}^2_0\sqrt{\frac{\pi}{2}}\sigma e^{-(\Omega-2\omega)^2\sigma^2/8}, \tag{F.9}$$

so that, evaluating at the second-harmonic frequency $\Omega = 2\omega$,

$$\mathrm{E}_{2\omega,\hat{\boldsymbol{\xi}}}(\mathbf{r}, \Omega = 2\omega) = \frac{1}{4}\chi^{(2)}_{\text{field-field},\hat{\boldsymbol{\xi}}}(\mathbf{r})\mathrm{E}_0^2\sqrt{\frac{\pi}{2}}\sigma. \tag{F.10}$$

The electric near field $\mathrm{E}_{2\omega,\hat{\boldsymbol{\xi}}}(\mathbf{r}, \Omega = 2\omega)$ induced by the MNP at the second-harmonic is calculated within TDDFT in Section 2.4, i.e., $\mathrm{E}_{2\omega,\hat{\boldsymbol{\xi}}}(\mathbf{r}, \Omega = 2\omega) = \mathbf{E}^{\mathrm{TDDFT}}_{\mathrm{ind}}(\mathbf{r}, \Omega = 2\omega)\cdot\hat{\boldsymbol{\xi}}$. Thus, using Eq. (F.10) we can finally estimate $\chi^{(2)}_{\text{field-field},\hat{\boldsymbol{\xi}}}(\mathbf{r})$ as

$$\chi^{(2)}_{\text{field-field},\hat{\boldsymbol{\xi}}}(\mathbf{r}) = 4\sqrt{\frac{2}{\pi}}\frac{\mathbf{E}^{\mathrm{TDDFT}}_{\mathrm{ind}}(\mathbf{r}, \Omega = 2\omega)\cdot\hat{\boldsymbol{\xi}}}{\sigma\mathrm{E}_0^2}, \tag{F.11}$$

where, E_0 is the amplitude of the Gaussian electromagnetic pulse used in the TDDFT calculations. Therefore, once we have the value of $\chi^{(2)}_{\text{field-field},\hat{\boldsymbol{\xi}}}(\mathbf{r})$ and $\mathrm{E}_{2\omega,\hat{\boldsymbol{\xi}}}(\mathbf{r}, \Omega = 2\omega) = \mathbf{E}^{\mathrm{TDDFT}}_{\mathrm{ind}}(\mathbf{r}, \Omega = 2\omega)\cdot\hat{\boldsymbol{\xi}}$ obtained from TDDFT calculations, we can finally use Eq. (F.3) to estimate the second-harmonic near field that would be induced by an individual MNP in response to plane-wave illumination.

Second-harmonic dipole moment

Once the second-harmonic near field $\mathrm{E}_{2\omega,\hat{\boldsymbol{\xi}}}(\mathbf{r})$ that would be induced by a plane wave incident to an individual MNP is calculated (as explained above), we can also obtain the total second-harmonic dipole $\mathbf{P}_{2\omega}$ induced in the coupled QE–MNP system in response to plane-wave illumination, as considered in Subsection 6.2.3. $\mathbf{P}_{2\omega}$ is given by the sum of the dipole moment of the MNP, $\mathbf{P}^{\mathrm{MNP}}_{2\omega}$, and that of the QE, $\mathbf{P}^{\mathrm{QE}}_{2\omega}$. To obtain $\mathbf{P}_{2\omega}$ under plane-wave illumination, we can apply the semi-analytical model based on the self-interaction Green´s function used in Subsection 6.2.2. In particular, it is possible to apply Eq. (6.5) of Chapter 6 but substituting the dipole moments $\mathbf{p}_{\mathrm{QE}}(\Omega)$ and $\mathbf{p}_{\mathrm{MNP}}(\Omega)$, as well as the induced electric field $\mathbf{E}^{\mathrm{TDDFT}}_{\mathrm{ind}}(\mathbf{r}_{\mathrm{QE}}, \Omega)$ (obtained in response to finite-pulse excitation) by the corresponding value under plane-wave illumination. Applying this procedure results in

$$\begin{aligned}\mathbf{P}_{2\omega} &= \mathbf{P}^{\mathrm{QE}}_{2\omega} + \mathbf{P}^{\mathrm{MNP}}_{2\omega} \\ &= \underbrace{\Big(\mathbb{I} + \alpha_{\mathrm{MNP}}(2\omega)\hat{\mathbb{G}}_0\Big)\Big(\mathbb{I} - \alpha_{\mathrm{QE}}(2\omega)\hat{\mathbb{G}}(\mathbf{r}_{\mathrm{QE}}, \mathbf{r}_{\mathrm{QE}}, 2\omega)\Big)^{-1}}_{\mathbb{F}(\mathbf{r}_{\mathrm{QE}}, 2\omega)}\alpha_{\mathrm{QE}}(2\omega)\mathrm{E}_{2\omega,\hat{\boldsymbol{\xi}}}(\mathbf{r}_{\mathrm{QE}}),\end{aligned} \tag{F.12}$$

where $\mathrm{E}_{2\omega,\hat{\boldsymbol{\xi}}}(\mathbf{r}_{\mathrm{QE}})$ is obtained from Eq. (F.10) and we have defined the factor

$$\mathbb{F}(\mathbf{r}_{\mathrm{QE}}, 2\omega) = \Big(\mathbb{I} + \alpha_{\mathrm{MNP}}(2\omega)\hat{\mathbb{G}}_0\Big)\Big(\mathbb{I} - \alpha_{\mathrm{QE}}(2\omega)\hat{\mathbb{G}}(\mathbf{r}_{\mathrm{QE}}, \mathbf{r}_{\mathrm{QE}}, 2\omega)\Big)^{-1}. \tag{F.13}$$

Inserting Eq. (F.3) into Eq. (F.12), the total dipole moment $\mathbf{P}_{2\omega}$ oscillating at 2ω induced by the plane-wave illumination given by Eq. (F.1) yields

$$\begin{aligned}\mathbf{P}_{2\omega} &= \mathbb{F}(\mathbf{r}_{\mathrm{QE}}, 2\omega)\alpha_{\mathrm{QE}}(2\omega)\chi^{(2)}_{\text{field-field},\hat{\boldsymbol{\xi}}}(\mathbf{r}_{\mathrm{QE}})\mathrm{E}_{\omega}\mathrm{E}_{\omega} \\ &= \frac{1}{4}\mathbb{F}(\mathbf{r}_{\mathrm{QE}}, 2\omega)\alpha_{\mathrm{QE}}(2\omega)\chi^{(2)}_{\text{field-field},\hat{\boldsymbol{\xi}}}(\mathbf{r}_{\mathrm{QE}})\mathrm{E}^2_{\mathrm{pw}}.\end{aligned} \tag{F.14}$$

From the definition of $\chi^{(2)}_{\text{field-field},\hat{\boldsymbol{\xi}}}(\mathbf{r} = \mathbf{r}_{\mathrm{QE}})$ in Eq. (F.11), and expressing Eq. (F.14) in terms of the average intensity I_0 of the plane wave,

$$I_0 = \frac{1}{8\pi}c\mathrm{E}^2_{\mathrm{pw}}, \tag{F.15}$$

(c is the speed of light in vacuum) we finally obtain the second-harmonic dipole $\mathbf{P}_{2\omega}$ of the coupled QE–MNP system,

$$\mathbf{P}_{2\omega} = \frac{8\sqrt{2\pi}I_0}{c\sigma\mathrm{E}^2_0}\mathbb{F}(\mathbf{r}_{\mathrm{QE}}, 2\omega)\alpha_{\mathrm{QE}}(2\omega)\mathbf{E}^{\mathrm{TDDFT}}_{\mathrm{ind}}(\mathbf{r}_{\mathrm{QE}}, \Omega = 2\omega). \tag{F.16}$$

Furthermore, since

$$\mathbb{F}(\mathbf{r}_{\mathrm{QE}}, 2\omega)\alpha_{\mathrm{QE}}(2\omega)\mathbf{E}^{\mathrm{TDDFT}}_{\mathrm{ind}}(\mathbf{r}_{\mathrm{QE}}, \Omega = 2\omega)$$

is exactly the dipole moment $\mathbf{p}(\Omega = 2\omega)$ under Gaussian-pulse illumination calculated with the semi-analytical model using Eq. (6.5) in Chapter 6 (evaluated at $\Omega = 2\omega$), $\mathbf{P}_{2\omega}$ induced by a plane wave with average intensity I_0 and fundamental frequency ω can be directly obtained from

$$\mathbf{P}_{2\omega} = \frac{8\sqrt{2\pi}I_0}{c\sigma\mathrm{E}^2_0}\mathbf{p}(\Omega = 2\omega), \tag{F.17}$$

as we use in Chapter 6 [Eq. (6.7)].

List of publications

Most of the results discussed in this thesis are based on the following publications:

1. **A. Babaze**, R. Esteban, J. Aizpurua, and A. G. Borisov: "Second-Harmonic Generation from a Quantum Emitter Coupled to a Metallic Nanoantenna", ACS Photonics **7**, 701-713 (2020).
   https://doi.org/10.1021/acsphotonics.9b01569

2. **A. Babaze**, R. Esteban, A. G. Borisov, and J. Aizpurua: "Electronic Exciton–Plasmon Coupling in a Nanocavity Beyond the Electromagnetic Interaction Picture", Nano Letters **21**, 8466-8473 (2021).
   https://doi.org/10.1021/acs.nanolett.1c03202

3. **A. Babaze**, E. Ogando, P. E. Stamatopoulou, C. Tserkezis, N. A. Mortensen, J. Aizpurua, A. G. Borisov, and R. Esteban: "Quantum surface effects in the electromagnetic coupling between a quantum emitter and a plasmonic nanoantenna: time-dependent density functional theory vs. semiclassical Feibelman approach", Optics Express **30**, 21159-21183 (2022).
   https://doi.org/10.1364/OE.456338

4. **A. Babaze**, T. Neuman, R. Esteban, J. Aizpurua, and A. G. Borisov: "Dispersive surface-response formalism to address optical nonlocality in situations of extreme plasmonic field confinement", to be submitted (2022).

Bibliography

[1] M. Faraday, "Experimental relations of gold (and other metals) to light," Philosophical Transactions of the Royal Society of London , 145–181 (1857).

[2] F. Wagner, S. Haslbeck, L. Stievano, S. Calogero, Q. Pankhurst, and K. P. Martinek, "Before striking gold in gold-ruby glass," Nature **407**, 691–692 (2000).

[3] N. J. Halas, S. Lal, W. S. Chang, S. Link, and P. Nordlander, "Plasmons in strongly coupled metallic nanostructures," Chemical Reviews **111**, 3913–3961 (2011).

[4] G. Mie, "Beiträge zur optik trüber medien, speziell kolloidaler metallösungen," Annalen der Physik **330**, 377–445 (1908).

[5] J. C. Maxwell, "VIII. A dynamical theory of the electromagnetic field," Philosophical Transactions of the Royal Society of London , 459–512 (1865).

[6] J. D. Jackson, "Classical electrodynamics," (1999).

[7] C. F. Bohren and D. R. Huffman, *Absorption and scattering of light by small particles* (John Wiley & Sons, 2008).

[8] M. Kerker, *The scattering of light and other electromagnetic radiation: physical chemistry: a series of monographs*, Vol. 16 (Academic Press, 2013).

[9] K. L. Kelly, E. Coronado, L. L. Zhao, and G. C. Schatz, "The optical properties of metal nanoparticles: the influence of size, shape, and dielectric environment," The Journal of Physical Chemistry B **107**, 668–677 (2003).

[10] J. Pitarke, V. Silkin, E. Chulkov, and P. Echenique, "Theory of surface plasmons and surface-plasmon polaritons," Reports on Progress in Physics **70**, 1 (2006).

[11] S. A. Maier, *Plasmonics: fundamentals and applications*, Vol. 1 (Springer, 2007).

[12] M. I. Stockman, "Nanoplasmonics: The physics behind the applications," Phys. Today **64**, 39–44 (2011).

[13] D. Bohm and D. Pines, "A collective description of electron interactions: I. Magnetic interactions," Physical Review **82**, 625 (1951).

[14] D. Pines and D. Bohm, "A collective description of electron interactions: II. Collective vs individual particle aspects of the interactions," Physical Review **85**, 338 (1952).

[15] D. Bohm and D. Pines, "A collective description of electron interactions: III. Coulomb interactions in a degenerate electron gas," Physical Review **92**, 609 (1953).

[16] R. H. Ritchie, "Plasma losses by fast electrons in thin films," Physical Review **106**, 874 (1957).

[17] E. Ozbay, "Plasmonics: merging photonics and electronics at nanoscale dimensions," Science **311**, 189–193 (2006).

[18] H. A. Atwater, "The promise of plasmonics," Scientific American **296**, 56–63 (2007).

[19] D. K. Gramotnev and S. I. Bozhevolnyi, "Plasmonics beyond the diffraction limit," Nature Photonics **4**, 83–91 (2010).

[20] J. A. Schuller, E. S. Barnard, W. Cai, Y. C. Jun, J. S. White, and M. L. Brongersma, "Plasmonics for extreme light concentration and manipulation," Nature Materials **9**, 193–204 (2010).

[21] M. I. Stockman, "Nanoplasmonics: past, present, and glimpse into future," Optics Express **19**, 22029–22106 (2011).

[22] L. Novotny and B. Hecht, *Principles of nano-optics* (Cambridge University Press, 2012).

[23] I. Romero, J. Aizpurua, G. W. Bryant, and F. J. G. de Abajo, "Plasmons in nearly touching metallic nanoparticles: singular response in the limit of touching dimers," Optics Express **14**, 9988–9999 (2006).

[24] R. Zhang, Y. Zhang, Z. C. Dong, S. Jiang, C. Zhang, L. G. Chen, L. Zhang, Y. Liao, J. Aizpurua, Y. Luo, Y. Luo, J. L. Yang, and J. G. Hou, "Chemical mapping of a single molecule by plasmon-enhanced Raman scattering," Nature **498**, 82 (2013).

[25] J. R. Lakowicz, *Principles of fluorescence spectroscopy* (Springer science & business media, 2013).

[26] E. Fort and S. Grésillon, "Surface enhanced fluorescence," Journal of Physics D: Applied Physics **41**, 013001 (2007).

[27] S. N. Gupta, O. Bitton, T. Neuman, R. Esteban, L. Chuntonov, J. Aizpurua, and G. Haran, "Complex plasmon-exciton dynamics revealed through quantum dot light emission in a nanocavity," Nature Communications **12**, 1310 (2021).

[28] B. Doppagne, T. Neuman, R. Soria-Martinez, L. E. P. López, H. Bulou, M. Romeo, S. Berciaud, F. Scheurer, J. Aizpurua, and G. Schull, "Single-molecule tautomerization tracking through space-and time-resolved fluorescence spectroscopy," Nature Nanotechnology **15**, 207–211 (2020).

[29] B. Yang, G. Chen, A. Ghafoor, Y. Zhang, Y. Zhang, Y. Zhang, Y. Luo, J. Yang, V. Sandoghdar, J. Aizpurua, Z. Dong, and J. G. Hou, "Sub-nanometre resolution in single-molecule photoluminescence imaging," Nature Photonics , 693–699 (2020).

[30] R. Bardhan, S. Lal, A. Joshi, and N. J. Halas, "Theranostic nanoshells: from probe design to imaging and treatment of cancer," Accounts of Chemical Research **44**, 936–946 (2011).

[31] T. L. Doane and C. Burda, "The unique role of nanoparticles in nanomedicine: imaging, drug delivery and therapy," Chemical Society Reviews **41**, 2885–2911 (2012).

[32] A. R. Rastinehad, H. Anastos, E. Wajswol, J. S. Winoker, J. P. Sfakianos, S. K. Doppalapudi, M. R. Carrick, C. J. Knauer, B. Taouli, S. C. Lewis, A. K. Tewari, J. A. Schwartz, S. E. Canfield, A. K. George, J. L. West, and N. J. Halas, "Gold nanoshell-localized photothermal ablation of prostate tumors in a clinical pilot device study," Proceedings of the National Academy of Sciences **116**, 18590–18596 (2019).

[33] H. A. Atwater and A. Polman, "Plasmonics for improved photovoltaic devices," Materials for sustainable energy: a collection of peer-reviewed research and review articles from Nature Publishing Group , 1–11 (2011).

[34] S. Carretero-Palacios, A. Jiménez-Solano, and H. Míguez, "Plasmonic nanoparticles as light-harvesting enhancers in perovskite solar cells: a user's guide," ACS Energy Letters **1**, 323–331 (2016).

[35] S. K. Cushing and N. Wu, "Progress and perspectives of plasmon-enhanced solar energy conversion," The Journal of Physical Chemistry Letters **7**, 666–675 (2016).

[36] M. Kauranen and A. V. Zayats, "Nonlinear plasmonics," Nature Photonics **6**, 737 (2012).

[37] A. V. Krasavin, P. Ginzburg, and A. V. Zayats, "Nonlinear nanoplasmonics," in *Quantum Photonics: Pioneering Advances and Emerging Applications*, edited by R. W. Boyd, S. G. Lukishova, and V. N. Zadkov (Springer International Publishing, Cham, 2019) pp. 267–316.

[38] P. C. Chaumet, A. Rahmani, F. de Fornel, and J. P. Dufour, "Evanescent light scattering: The validity of the dipole approximation," Physical Review B **58**, 2310–2315 (1998).

[39] A. O. Govorov, G. W. Bryant, W. Zhang, T. Skeini, J. Lee, N. A. Kotov, J. M. Slocik, and R. R. Naik, "Exciton–plasmon interaction and hybrid excitons in semiconductor–metal nanoparticle assemblies," Nano Letters **6**, 984–994 (2006).

[40] R. Carminati, J. J. Greffet, C. Henkel, and J. M. Vigoureux, "Radiative and non-radiative decay of a single molecule close to a metallic nanoparticle," Optics Communications **261**, 368–375 (2006).

[41] A. García-Etxarri, *Modeling of plasmonic nanoantennas for optical microscopy and surface enhanced spectroscopy*, Ph.D. thesis, University of the Basque Country (2010).

[42] X. Wu, S. K. Gray, and M. Pelton, "Quantum-dot-induced transparency in a nanoscale plasmonic resonator," Optics Express **18**, 23633–23645 (2010).

[43] H. Duan, A. I. Fernández-Domínguez, M. Bosman, S. A. Maier, and J. K. Yang, "Nanoplasmonics: classical down to the nanometer scale," Nano letters **12**, 1683–1689 (2012).

[44] M. Kajetan Schmidt, *Classical and quantum approaches to the interaction of light and matter at the nanoscale*, Ph.D. thesis, University of the Basque Country (2016).

[45] Y. Zhang, Q. S. Meng, L. Zhang, Y. Luo, Y. J. Yu, B. Yang, Y. Zhang, R. Esteban, J. Aizpurua, Y. Luo, J. L. Yang, Z. C. Dong, and J. G. Hou, "Sub-nanometre control of the coherent interaction between a single molecule and a plasmonic nanocavity," Nature Communications **8**, 15225 (2017).

[46] K. J. Savage, M. M. Hawkeye, R. Esteban, A. G. Borisov, J. Aizpurua, and J. J. Baumberg, "Revealing the quantum regime in tunnelling plasmonics," Nature **491**, 574–577 (2012).

[47] J. A. Scholl, A. García-Etxarri, A. L. Koh, and J. A. Dionne, "Observation of quantum tunneling between two plasmonic nanoparticles," Nano Letters **13**, 564–569 (2013).

[48] G. Hajisalem, M. S. Nezami, and R. Gordon, "Probing the quantum tunneling limit of plasmonic enhancement by third harmonic generation," Nano Letters **14**, 6651–6654 (2014).

[49] S. F. Tan, L. Wu, J. K. Yang, P. Bai, M. Bosman, and C. A. Nijhuis, "Quantum plasmon resonances controlled by molecular tunnel junctions," Science **343**, 1496–1499 (2014).

[50] H. Cha, J. H. Yoon, and S. Yoon, "Probing quantum plasmon coupling using gold nanoparticle dimers with tunable interparticle distances down to the subnanometer range," ACS Nano **8**, 8554–8563 (2014).

[51] W. Zhu and K. B. Crozier, "Quantum mechanical limit to plasmonic enhancement as observed by surface-enhanced Raman scattering," Nature Communications **5**, 5228 (2014).

[52] F. Benz, M. K. Schmidt, A. Dreismann, R. Chikkaraddy, Y. Zhang, A. Demetriadou, C. Carnegie, H. Ohadi, B. De Nijs, R. Esteban, J. Aizpurua, and J. J. Baumberg, "Single-molecule optomechanics in "picocavities"," Science **354**, 726–729 (2016).

[53] A. Manjavacas Arévalo, *Light–matter interaction at the nanoscale*, Ph.D. thesis, Universidad Complutense de Madrid (2013).

[54] T. Christensen, *From classical to quantum plasmonics in three and two dimensions* (Springer, 2017).

[55] P. A. D. Gonçalves, *Plasmonics and Light–Matter Interactions in Two-Dimensional Materials and in Metal Nanostructures: Classical and Quantum Considerations* (Springer Nature, 2020).

[56] F. J. García de Abajo, "Nonlocal effects in the plasmons of strongly interacting nanoparticles, dimers, and waveguides," The Journal of Physical Chemistry C **112**, 17983–17987 (2008).

[57] G. Toscano, *Semiclassical theory of nonlocal plasmonic excitation in metallic nanostructures*, Ph.D. thesis, Technical University of Denmark (2013).

[58] T. V. Teperik, P. Nordlander, J. Aizpurua, and A. G. Borisov, "Robust subnanometric plasmon ruler by rescaling of the nonlocal optical response," Physical Review Letters **110**, 263901 (2013).

[59] L. Stella, P. Zhang, F. J. García-Vidal, A. Rubio, and P. García-González, "Performance of nonlocal optics when applied to plasmonic nanostructures," The Journal of Physical Chemistry C **117**, 8941–8949 (2013).

[60] S. Raza, S. I. Bozhevolnyi, M. Wubs, and N. A. Mortensen, "Nonlocal optical response in metallic nanostructures," Journal of Physics: Condensed Matter **27**, 183204 (2015).

[61] P. Apell and Å. Ljungbert, "Red shift of surface plasmons in small metal particles," Solid State Communications **44**, 1367–1369 (1982).

[62] A. Liebsch, *Electronic excitations at metal surfaces* (Springer Science & Business Media, 1997).

[63] E. J. Skjølstrup, T. Søndergaard, and T. G. Pedersen, "Quantum spill-out in few-nanometer metal gaps: Effect on gap plasmons and reflectance from ultrasharp groove arrays," Physical Review B **97**, 115429 (2018).

[64] C. Yannouleas and R. Broglia, "Landau damping and wall dissipation in large metal clusters," Annals of Physics **217**, 105 – 141 (1992).

[65] A. Vagov, I. Larkin, M. D. Croitoru, and V. M. Axt, "Role of nonlocality and Landau damping in the dynamics of a quantum dot coupled to surface plasmons," Physical Review B **93**, 195414 (2016).

[66] J. Khurgin, W. Y. Tsai, D. P. Tsai, and G. Sun, "Landau damping and limit to field confinement and enhancement in plasmonic dimers," ACS Photonics **4**, 2871–2880 (2017).

[67] J. Zuloaga, E. Prodan, and P. Nordlander, "Quantum description of the plasmon resonances of a nanoparticle dimer," Nano Letters **9**, 887–891 (2009).

[68] G. Aguirregabiria, D. C. Marinica, R. Esteban, A. K. Kazansky, J. Aizpurua, and A. G. Borisov, "Role of electron tunneling in the nonlinear response of plasmonic nanogaps," Physical Review B **97**, 115430 (2018).

[69] E. Runge and E. K. Gross, "Density-functional theory for time-dependent systems," Physical Review Letters **52**, 997 (1984).

[70] E. Gross and W. Kohn, "Time-dependent density-functional theory," in *Density Functional Theory of Many-Fermion Systems*, Advances in Quantum Chemistry, Vol. 21, edited by P. O. Löwdin (Academic Press, 1990) pp. 255 – 291.

[71] M. Marques and E. Gross, "Time-dependent density functional theory," Annual Review of Physical Chemistry **55**, 427–455 (2004).

[72] C. A. Ullrich, *Time-dependent density-functional theory: concepts and applications* (Oxford University Press, 2013).

[73] K. Yabana and G. Bertsch, "Time-dependent local-density approximation in real time," Physical Review B **54**, 4484 (1996).

[74] S. Gao, "Nonlinear response of metal nanoparticles: Double plasmon excitation and electron transfer," The Journal of Chemical Physics **142**, 234701 (2015).

[75] G. Aguirregabiria, *Theoretical study of the linear and nonlinear optical response of plasmonic tunneling gaps*, Ph.D. thesis, University of the Basque Country (2018).

[76] G. U. Kuda-Singappulige, D. B. Lingerfelt, X. Li, and C. M. Aikens, "Ultrafast nonlinear plasmon decay processes in silver nanoclusters," The Journal of Physical Chemistry C **124**, 20477–20487 (2020).

[77] M. Ludwig, G. Aguirregabiria, F. Ritzkowsky, T. Rybka, D. C. Marinica, J. Aizpurua, A. G. Borisov, A. Leitenstorfer, and D. Brida, "Sub-femtosecond electron transport in a nanoscale gap," Nature Physics **16**, 341–345 (2020).

[78] T. Takeuchi and K. Yabana, "Extremely large third-order nonlinear optical effects caused by electron transport in quantum plasmonic metasurfaces with subnanometer gaps," Scientific Reports **10**, 1–9 (2020).

[79] A. Varas, P. García-González, J. Feist, F. J. García-Vidal, and A. Rubio, "Quantum plasmonics: from jellium models to ab initio calculations," Nanophotonics **5**, 409–426 (2016).

[80] M. R. A. Barbry, *Plasmons in nanoparticles: atomistic Ab Initio theory for large systems*, Ph.D. thesis, University of the Basque Country (2018).

[81] N. A. Mortensen, "Mesoscopic electrodynamics at metal surfaces," Nanophotonics **10**, 2563–2616 (2021).

[82] P. E. Stamatopoulou and C. Tserkezis, "Finite-size and quantum effects in plasmonics: manifestations and theoretical modelling," Optical Materials Express **12**, 1869–1893 (2022).

[83] R. Esteban, A. G. Borisov, P. Nordlander, and J. Aizpurua, "Bridging quantum and classical plasmonics with a quantum-corrected model," Nature Communications **3**, 825 (2012).

[84] R. Esteban, A. Zugarramurdi, P. Zhang, P. Nordlander, F. J. García-Vidal, A. G. Borisov, and J. Aizpurua, "A classical treatment of optical tunneling in plasmonic gaps: extending the quantum corrected model to practical situations," Faraday Discussions **178**, 151–183 (2015).

[85] M. Zapata, A. S. C. Beltrán, A. G. Borisov, and J. Aizpurua, "Quantum effects in the optical response of extended plasmonic gaps: Validation of the quantum corrected model in core-shell nanomatryushkas," Optics Express **23**, 8134–8149 (2015).

[86] W. Zhu, R. Esteban, A. G. Borisov, J. J. Baumberg, P. Nordlander, H. J. Lezec, J. Aizpurua, and K. B. Crozier, "Quantum mechanical effects in plasmonic structures with subnanometre gaps," Nature Communications **7**, 11495 (2016).

[87] D. Knebl, A. Hörl, A. Trügler, J. Kern, J. R. Krenn, P. Puschnig, and U. Hohenester, "Gap plasmonics of silver nanocube dimers," Physical Review B **93**, 081405 (2016).

[88] N. A. Mortensen, S. Raza, M. Wubs, T. Søndergaard, and S. I. Bozhevolnyi, "A generalized non-local optical response theory for plasmonic nanostructures," Nature Communications **5**, 3809 (2014).

[89] G. Toscano, J. Straubel, A. Kwiatkowski, C. Rockstuhl, F. Evers, H. Xu, N. A. Mortensen, and M. Wubs, "Resonance shifts and spill-out effects in self-consistent hydrodynamic nanoplasmonics," Nature Communications **6**, 7132 (2015).

[90] S. Raza, M. Wubs, S. I. Bozhevolnyi, and N. A. Mortensen, "Nonlocal study of ultimate plasmon hybridization," Optics Letters **40**, 839–842 (2015).

[91] C. Ciracì and F. Della Sala, "Quantum hydrodynamic theory for plasmonics: Impact of the electron density tail," Physical Review B **93**, 205405 (2016).

[92] M. Kupresak, X. Zheng, G. A. Vandenbosch, and V. V. Moshchalkov, "Comparison of hydrodynamic models for the electromagnetic nonlocal response of nanoparticles," Advanced Theory and Simulations **1**, 1800076 (2018).

[93] A. Rivacoba, "Electron spill-out effects in plasmon excitations by fast electrons," Ultramicroscopy **207**, 112835 (2019).

[94] H. M. Baghramyan, F. Della Sala, and C. Ciracì, "Laplacian-level quantum hydrodynamic theory for plasmonics," Physical Review X **11**, 011049 (2021).

[95] P. Apell and Å. Ljungbert, "A general non-local theory for the electromagnetic response of a small metal particle," Physica Scripta **26**, 113 (1982).

[96] R. C. Monreal, T. J. Antosiewicz, and S. P. Apell, "Competition between surface screening and size quantization for surface plasmons in nanoparticles," New Journal of Physics **15**, 083044 (2013).

[97] Y. Yang, D. Zhu, W. Yan, A. Agarwal, M. Zheng, J. D. Joannopoulos, P. Lalanne, T. Christensen, K. K. Berggren, and M. Soljačić, "A general theoretical and experimental framework for nanoscale electromagnetism," Nature **576**, 248–252 (2019).

[98] P. J. Feibelman, "Surface electromagnetic fields," Progress in Surface Science **12**, 287–407 (1982).

[99] P. Anger, P. Bharadwaj, and L. Novotny, "Enhancement and quenching of single-molecule fluorescence," Physical Review Letters **96**, 113002 (2006).

[100] K. J. Russell, T. L. Liu, S. Cui, and E. L. Hu, "Large spontaneous emission enhancement in plasmonic nanocavities," Nature Photonics **6**, 459–462 (2012).

[101] E. M. Purcell, "Spontaneous emission probabilities at radio frequencies," in *Confined Electrons and Photons* (Springer, 1995) pp. 839–839.

[102] A. F. Koenderink, "On the use of Purcell factors for plasmon antennas," Optics Letters **35**, 4208–4210 (2010).

[103] C. Van Vlack, P. T. Kristensen, and S. Hughes, "Spontaneous emission spectra and quantum light-matter interactions from a strongly coupled quantum dot metal-nanoparticle system," Physical Review B **85**, 075303 (2012).

[104] M. V. Rybin, S. F. Mingaleev, M. F. Limonov, and Y. S. Kivshar, "Purcell effect and Lamb shift as interference phenomena," Scientific Reports **6**, 20599 (2016).

[105] J. Galego, F. J. García-Vidal, and J. Feist, "Cavity-induced modifications of molecular structure in the strong-coupling regime," Physical Review X **5**, 041022 (2015).

[106] O. Pérez-González, *Optical properties and high-frequency electron transport in plasmonic cavities*, Ph.D. thesis, University of the Basque Country (2011).

[107] P. Song, P. Nordlander, and S. Gao, "Quantum mechanical study of the coupling of plasmon excitations to atomic-scale electron transport," The Journal of Chemical Physics **134**, 074701 (2011).

[108] P. Song, S. Meng, P. Nordlander, and S. Gao, "Quantum plasmonics: Symmetry-dependent plasmon-molecule coupling and quantized photoconductances," Physical Review B **86**, 121410 (2012).

[109] V. Kulkarni and A. Manjavacas, "Quantum effects in charge transfer plasmons," ACS Photonics **2**, 987–992 (2015).

[110] J. D. Cox, M. R. Singh, C. Von Bilderling, and A. V. Bragas, "A nonlinear switching mechanism in quantum dot and metallic nanoparticle hybrid systems," Advanced Optical Materials **1**, 460–467 (2013).

[111] J. D. Cox and F. J. G. de Abajo, "Nonlinear atom-plasmon interactions enabled by nanostructured graphene," Physical Review Letters **121**, 257403 (2018).

[112] F. J. García de Abajo and A. Howie, "Retarded field calculation of electron energy loss in inhomogeneous dielectrics," Physiscal Review B **65**, 115418 (2002).

[113] A. Taflove, "Application of the finite-difference time-domain method to sinusoidal steady-state electromagnetic-penetration problems," IEEE Transactions on electromagnetic compatibility , 191–202 (1980).

[114] B. T. Draine and P. J. Flatau, "Discrete-dipole approximation for scattering calculations," Journal of the Optical Society of America A **11**, 1491–1499 (1994).

[115] M. S. Gockenbach, *Understanding and implementing the finite element method*, Vol. 97 (Siam, 2006).

[116] R. Fuchs and F. Claro, "Multipolar response of small metallic spheres: Nonlocal theory," Physical Review B **35**, 3722–3727 (1987).

[117] R. Ruppin, "Extinction properties of thin metallic nanowires," Optics Communications **190**, 205–209 (2001).

[118] C. Ciracì, R. Hill, J. Mock, Y. Urzhumov, A. Fernández-Domínguez, S. Maier, J. Pendry, A. Chilkoti, and D. Smith, "Probing the ultimate limits of plasmonic enhancement," Science **337**, 1072–1074 (2012).

[119] G. Toscano, S. Raza, A. P. Jauho, N. A. Mortensen, and M. Wubs, "Modified field enhancement and extinction by plasmonic nanowire dimers due to nonlocal response," Optics Express **20**, 4176–4188 (2012).

[120] Y. Luo, A. Fernandez-Dominguez, A. Wiener, S. A. Maier, and J. Pendry, "Surface plasmons and nonlocality: a simple model," Physical Review Letters **111**, 093901 (2013).

[121] C. David and F. J. García de Abajo, "Surface plasmon dependence on the electron density profile at metal surfaces," ACS Nano **8**, 9558–9566 (2014).

[122] C. Tserkezis, W. Yan, W. Hsieh, G. Sun, J. B. Khurgin, M. Wubs, and N. A. Mortensen, "On the origin of nonlocal damping in plasmonic monomers and dimers," International Journal of Modern Physics B **31**, 1740005 (2017).

[123] M. Khalid, F. Della Sala, and C. Ciracì, "Optical properties of plasmonic core-shell nanomatryoshkas: a quantum hydrodynamic analysis," Optics Express **26**, 17322–17334 (2018).

[124] P. Gonçalves, T. Christensen, N. Rivera, A. P. Jauho, N. A. Mortensen, and M. Soljačić, "Plasmon–emitter interactions at the nanoscale," Nature Communications **11**, 366 (2020).

[125] D. Marinica, A. Kazansky, P. Nordlander, J. Aizpurua, and A. G. Borisov, "Quantum plasmonics: Nonlinear effects in the field enhancement of a plasmonic nanoparticle dimer," Nano Letters **12**, 1333–1339 (2012).

[126] T. V. Teperik, P. Nordlander, J. Aizpurua, and A. G. Borisov, "Quantum effects and nonlocality in strongly coupled plasmonic nanowire dimers," Optics Express **21**, 27306–27325 (2013).

[127] P. Drude, "Zur elektronentheorie der metalle," Annalen der Physik **306**, 566–613 (1900).

[128] N. W. Ashcroft and N. D. Mermin, *Solid state physics* (Harcourt College Publishers, New York, 1976).

[129] N. A. Mortensen, P. Gonçalves, F. A. Shuklin, J. D. Cox, C. Tserkezis, M. Ichikawa, and C. Wolff, "Surface-response functions obtained from equilibrium electron-density profiles," Nanophotonics **10**, 3647–3657 (2021).

[130] W. H. Press, S. A. Teukolsky, W. T. Vetterling, and B. P. Flannery, *Numerical recipes 3rd edition: The art of scientific computing* (Cambridge University Press, 2007).

[131] M. Schmeits, "Surface-plasmon coupling in cylindrical pores," Physical Review B **39**, 7567 (1989).

[132] M. Schmeits and L. Dambly, "Fast-electron scattering by bispherical surface-plasmon modes," Physical Review B **44**, 12706 (1991).

[133] J. M. Fitzgerald, P. Narang, R. V. Craster, S. A. Maier, and V. Giannini, "Quantum plasmonics," Proceedings of the IEEE **104**, 2307–2322 (2016).

[134] E. Altewischer, M. Van Exter, and J. Woerdman, "Plasmon-assisted transmission of entangled photons," Nature **418**, 304–306 (2002).

[135] G. Di Martino, Y. Sonnefraud, M. S. Tame, S. Kéna-Cohen, F. Dieleman, Ş. K. Özdemir, M. S. Kim, and S. A. Maier, "Observation of quantum interference in the plasmonic Hong-Ou-Mandel effect," Physical Review Applied **1**, 034004 (2014).

[136] A. V. Zayats and I. I. Smolyaninov, "Near-field photonics: surface plasmon polaritons and localized surface plasmons," Journal of Optics A: Pure and Applied Optics **5**, S16 (2003).

[137] Y. Y. Teng and E. A. Stern, "Plasma radiation from metal grating surfaces," Physical Review Letters **19**, 511 (1967).

[138] A. Otto, "Excitation of nonradiative surface plasma waves in silver by the method of frustrated total reflection," Zeitschrift für Physik A Hadrons and nuclei **216**, 398–410 (1968).

[139] E. Kretschmann and H. Raether, "Radiative decay of non radiative surface plasmons excited by light," Zeitschrift für Naturforschung A **23**, 2135–2136 (1968).

[140] B. Hecht, H. Bielefeldt, L. Novotny, Y. Inouye, and D. Pohl, "Local excitation, scattering, and interference of surface plasmons," Physical Review Letters **77**, 1889 (1996).

[141] M. Pelton, J. Aizpurua, and G. Bryant, "Metal-nanoparticle plasmonics," Laser & Photonics Reviews **2**, 136–159 (2008).

[142] V. Myroshnychenko, J. Rodríguez-Fernández, I. Pastoriza-Santos, A. M. Funston, C. Novo, P. Mulvaney, L. M. Liz-Marzán, and F. J. G. De Abajo, "Modelling the optical response of gold nanoparticles," Chemical Society Reviews **37**, 1792–1805 (2008).

[143] A. Delga, J. Feist, J. Bravo-Abad, and F. J. García-Vidal, "Theory of strong coupling between quantum emitters and localized surface plasmons," Journal of Optics **16**, 114018 (2014).

[144] T. Neuman, R. Esteban, D. Casanova, F. J. García-Vidal, and J. Aizpurua, "Coupling of molecular emitters and plasmonic cavities beyond the point-dipole approximation," Nano Letters **18**, 2358–2364 (2018).

[145] G. W. Ford and W. H. Weber, "Electromagnetic interactions of molecules with metal surfaces," Physics Reports **113**, 195–287 (1984).

[146] L. Novotny and N. Van Hulst, "Antennas for light," Nature Photonics **5**, 83–90 (2011).

[147] R. Alvarez-Puebla, L. M. Liz-Marzán, and F. J. García de Abajo, "Light concentration at the nanometer scale," The Journal of Physical Chemistry Letters **1**, 2428–2434 (2010).

[148] N. J. Halas, S. Lal, W. S. Chang, S. Link, and P. Nordlander, "Plasmons in strongly coupled metallic nanostructures," Chemical Reviews **111**, 3913–3961 (2011).

[149] R. Ruppin, "Surface modes of two spheres," Physical Review B **26**, 3440 (1982).

[150] E. Prodan, C. Radloff, N. J. Halas, and P. Nordlander, "A hybridization model for the plasmon response of complex nanostructures," Science **302**, 419–422 (2003).

[151] P. Nordlander, C. Oubre, E. Prodan, K. Li, and M. Stockman, "Plasmon hybridization in nanoparticle dimers," Nano Letters **4**, 899–903 (2004).

[152] R. W. Boyd, *Nonlinear optics* (Elsevier, 2003).

[153] N. C. Panoiu, W. Sha, D. Lei, and G. Li, "Nonlinear optics in plasmonic nanostructures," Journal of Optics **20**, 083001 (2018).

[154] G. Aguirregabiria, D. C. Marinica, R. Esteban, A. K. Kazansky, J. Aizpurua, and A. G. Borisov, "Electric field-induced high order nonlinearity in plasmonic nanoparticles retrieved with time-dependent density functional theory," ACS Photonics **4**, 613–620 (2017).

[155] C. A. Ullrich and Z. H. Yang, "Excitons in time-dependent density-functional theory," Density-Functional Methods for Excited States , 185–217 (2014).

[156] J. Frenkel, "On the transformation of light into heat in solids. i," Physical Review **37**, 17 (1931).

[157] G. H. Wannier, "The structure of electronic excitation levels in insulating crystals," Physical Review **52**, 191 (1937).

[158] W. Liang, "Excitons," Physics Education **5**, 226 (1970).

[159] D. A. Wheeler and J. Z. Zhang, "Exciton dynamics in semiconductor nanocrystals," Advanced Materials **25**, 2878–2896 (2013).

[160] A. Kinkhabwala, Z. Yu, S. Fan, Y. Avlasevich, K. Müllen, and W. E. Moerner, "Large single-molecule fluorescence enhancements produced by a bowtie nanoantenna," Nature Photonics **3**, 654–657 (2009).

[161] T. Ming, L. Zhao, Z. Yang, H. Chen, L. Sun, J. Wang, and C. Yan, "Strong polarization dependence of plasmon-enhanced fluorescence on single gold nanorods," Nano Letters **9**, 3896–3903 (2009).

[162] G. P. Wiederrecht, G. A. Wurtz, and J. Hranisavljevic, "Coherent coupling of molecular excitons to electronic polarizations of noble metal nanoparticles," Nano Letters **4**, 2121–2125 (2004).

[163] N. T. Fofang, T.-H. Park, O. Neumann, N. A. Mirin, P. Nordlander, and N. J. Halas, "Plexcitonic nanoparticles: plasmon–exciton coupling in nanoshell–J-aggregate complexes," Nano letters **8**, 3481–3487 (2008).

[164] N. T. Fofang, N. K. Grady, Z. Fan, A. O. Govorov, and N. J. Halas, "Plexciton dynamics: exciton–plasmon coupling in a J-aggregate–Au nanoshell complex provides a mechanism for nonlinearity," Nano Letters **11**, 1556–1560 (2011).

[165] A. Manjavacas, F. J. García de Abajo, and P. Nordlander, "Quantum plexcitonics: Strongly interacting plasmons and excitons," Nano Letters **11**, 2318–2323 (2011).

[166] D. Marinica, H. Lourenço-Martins, J. Aizpurua, and A. G. Borisov, "Plexciton quenching by resonant electron transfer from quantum emitter to metallic nanoantenna," Nano Letters **13**, 5972–5978 (2013).

[167] T. Ozel, P. L. Hernandez-Martinez, E. Mutlugun, O. Akin, S. Nizamoglu, I. O. Ozel, Q. Zhang, Q. Xiong, and H. V. Demir, "Observation of selective plasmon-exciton coupling in nonradiative energy transfer: donor-selective versus acceptor-selective plexcitons," Nano Letters **13**, 3065–3072 (2013).

[168] H. Morawitz, "Self-coupling of a two-level system by a mirror," Physical Review **187**, 1792 (1969).

[169] A. Delga, J. Feist, J. Bravo-Abad, and F. J. García-Vidal, "Quantum emitters near a metal nanoparticle: strong coupling and quenching," Physical Review Letters **112**, 253601 (2014).

[170] P. Yao, C. Van Vlack, A. Reza, M. Patterson, M. Dignam, and S. Hughes, "Ultrahigh Purcell factors and Lamb shifts in slow-light metamaterial waveguides," Physical Review B **80**, 195106 (2009).

[171] S. D' Agostino, F. Alpeggiani, and L. C. Andreani, "Strong coupling between a dipole emitter and localized plasmons: enhancement by sharp silver tips," Optics Express **21**, 27602–27610 (2013).

[172] Y. Zhang, Z. C. Dong, and J. Aizpurua, "Influence of the chemical structure on molecular light emission in strongly localized plasmonic fields," The Journal of Physical Chemistry C **124**, 4674–4683 (2020).

[173] B. Luk'yanchuk, N. I. Zheludev, S. A. Maier, N. J. Halas, P. Nordlander, H. Giessen, and C. T. Chong, "The Fano resonance in plasmonic nanostructures and metamaterials," Nature Materials **9**, 707–715 (2010).

[174] M. F. Limonov, M. V. Rybin, A. N. Poddubny, and Y. S. Kivshar, "Fano resonances in photonics," Nature Photonics **11**, 543–554 (2017).

[175] C. Garrido Alzar, M. Martinez, and P. Nussenzveig, "Classical analog of electromagnetically induced transparency," American Journal of Physics **70**, 37–41 (2002).

[176] N. Liu, L. Langguth, T. Weiss, J. Kästel, M. Fleischhauer, T. Pfau, and H. Giessen, "Plasmonic analogue of electromagnetically induced transparency at the Drude damping limit," Nature Materials **8**, 758–762 (2009).

[177] L. Novotny, "Strong coupling, energy splitting, and level crossings: A classical perspective," American Journal of Physics **78**, 1199–1202 (2010).

[178] M. Barra-Burillo, U. Muniain, S. Catalano, F. Casanova, L. E. Hueso, J. Aizpurua, R. Esteban, and R. Hillenbrand, "Microcavity phonon polaritons from the weak to the ultrastrong phonon–photon coupling regime," Nature Communications **12**, 6206 (2021).

[179] M. Autore, P. Li, I. Dolado, F. J. Alfaro-Mozaz, R. Esteban, A. Atxabal, F. Casanova, L. E. Hueso, P. Alonso-González, J. Aizpurua, A. Y. Nikitin, S. Vélez, and R. Hillenbrand, "Boron nitride nanoresonators for phonon-enhanced molecular vibrational spectroscopy at the strong coupling limit," Light: Science & Applications **7**, 17172 (2018).

[180] P. Törmä and W. L. Barnes, "Strong coupling between surface plasmon polaritons and emitters: a review," Reports on Progress in Physics **78**, 013901 (2014).

[181] S. Savasta, R. Saija, A. Ridolfo, O. Di Stefano, P. Denti, and F. Borghese, "Nanopolaritons: Vacuum Rabi splitting with a single quantum dot in the center of a dimer nanoantenna," ACS Nano **4**, 6369–6376 (2010).

[182] K. Santhosh, O. Bitton, L. Chuntonov, and G. Haran, "Vacuum Rabi splitting in a plasmonic cavity at the single quantum emitter limit," Nature Communications **7**, 11823 (2016).

[183] D. Melnikau, R. Esteban, D. Savateeva, A. Sánchez-Iglesias, M. Grzelczak, M. K. Schmidt, L. M. Liz-Marzán, J. Aizpurua, and Y. P. Rakovich, "Rabi splitting in photoluminescence spectra of hybrid systems of gold nanorods and J-aggregates," The Journal of Physical Chemistry Letters **7**, 354–362 (2016).

[184] P. A. M. Dirac, "Quantum mechanics of many-electron systems," Proceedings of the Royal Society of London. Series A, Containing Papers of a Mathematical and Physical Character **123**, 714–733 (1929).

[185] R. M. Martin, L. Reining, and D. M. Ceperley, *Interacting electrons* (Cambridge University Press, 2016).

[186] P. Hohenberg and W. Kohn, "Inhomogeneous electron gas," Physical Review **136**, B864 (1964).

[187] K. Burke, "Perspective on density functional theory," The Journal of Chemical Physics **136**, 150901 (2012).

[188] T. Tsuneda, *Density functional theory in quantum chemistry* (Springer, 2014).

[189] R. O. Jones, "Density functional theory: Its origins, rise to prominence, and future," Reviews of Modern Physics **87**, 897–923 (2015).

[190] W. Kohn and L. J. Sham, "Self-consistent equations including exchange and correlation effects," Physical Review **140**, A1133 (1965).

[191] R. O. Jones and O. Gunnarsson, "The density functional formalism, its applications and prospects," Reviews of Modern Physics **61**, 689 (1989).

[192] A. Savin, C. J. Umrigar, and X. Gonze, "Relationship of Kohn–Sham eigenvalues to excitation energies," Chemical Physics Letters **288**, 391–395 (1998).

[193] G. Onida, L. Reining, and A. Rubio, "Electronic excitations: density-functional versus many-body Green's-function approaches," Reviews of Modern Physics **74**, 601 (2002).

[194] M. Brack, "The physics of simple metal clusters: self-consistent jellium model and semiclassical approaches," Reviews of Modern Physics **65**, 677 (1993).

[195] J. Perdew, E. McMullen, and A. Zunger, "Density-functional theory of the correlation energy in atoms and ions: a simple analytic model and a challenge," Physical Review A **23**, 2785 (1981).

[196] N. H. March and S. Lundqvist, *Theory of the inhomogeneous electron gas* (Plenum Press, 1983).

[197] J. P. Perdew and Y. Wang, "Accurate and simple analytic representation of the electron-gas correlation energy," Physical Review B **45**, 13244 (1992).

[198] O. Gunnarsson and B. I. Lundqvist, "Exchange and correlation in atoms, molecules, and solids by the spin-density-functional formalism," Physical Review B **13**, 4274 (1976).

[199] W. Ekardt, "Work function of small metal particles: Self-consistent spherical jellium-background model," Physical Review B **29**, 1558 (1984).

[200] W. Ekardt, "Dynamical polarizability of small metal particles: self-consistent spherical jellium background model," Physical Review Letters **52**, 1925 (1984).

[201] M. Koskinen, P. Lipas, and M. Manninen, "Electron-gas clusters: the ultimate jellium model," Zeitschrift für Physik D Atoms, Molecules and Clusters **35**, 285–297 (1995).

[202] P. Zhang, J. Feist, A. Rubio, P. García-González, and F. J. García-Vidal, "Ab initio nanoplasmonics: The impact of atomic structure," Physical Review B **90**, 161407 (2014).

[203] E. Townsend and G. W. Bryant, "Which resonances in small metallic nanoparticles are plasmonic?" Journal of Optics **16**, 114022 (2014).

[204] W. Ekardt, "Size-dependent photoabsorption and photoemission of small metal particles," Physical Review B **31**, 6360–6370 (1985).

[205] "Quantum size effects in the electronic properties of small metal particles: Self-consistent spherical jellium background model," Surface Science **152-153**, 180–188 (1985).

[206] C. Yannouleas, E. Vigezzi, and R. A. Broglia, "Evolution of the optical properties of alkali-metal microclusters towards the bulk: The matrix random-phase-approximation description," Physical Review B **47**, 9849–9861 (1993).

[207] E. Prodan, P. Nordlander, and N. Halas, "Effects of dielectric screening on the optical properties of metallic nanoshells," Chemical Physics Letters **368**, 94–101 (2003).

[208] V. Kulkarni, E. Prodan, and P. Nordlander, "Quantum plasmonics: optical properties of a nanomatryushka," Nano Letters **13**, 5873–5879 (2013).

[209] E. Selenius, S. Malola, and H. Häkkinen, "Analysis of localized surface plasmon resonances in spherical jellium clusters and their assemblies," The Journal of Physical Chemistry C **121**, 27036–27052 (2017).

[210] G. Aguirregabiria, D. C. Marinica, M. Ludwig, D. Brida, A. Leitenstorfer, J. Aizpurua, and A. G. Borisov, "Dynamics of electron-emission currents in plasmonic gaps induced by strong fields," Faraday Discussions **214**, 147–157 (2019).

[211] E. Selenius, S. Malola, M. Kuisma, and H. Häkkinen, "Charge transfer plasmons in dimeric electron clusters," The Journal of Physical Chemistry C **124**, 12645–12654 (2020).

[212] T. Perera, S. D. Gunapala, M. I. Stockman, and M. Premaratne, "Plasmonic properties of metallic nanoshells in the quantum limit: From single particle excitations to plasmons," The Journal of Physical Chemistry C (2020).

[213] R. Sinha-Roy, J. Hurst, G. Manfredi, and P. A. Hervieux, "Driving orbital magnetism in metallic nanoparticles through circularly polarized light: A real-time TDDFT study," ACS Photonics **7**, 2429–2439 (2020).

[214] M. Barbry, P. Koval, F. Marchesin, R. Esteban, A. G. Borisov, J. Aizpurua, and D. Sánchez-Portal, "Atomistic near-field nanoplasmonics: reaching atomic-scale resolution in nanooptics," Nano Letters **15**, 3410–3419 (2015).

[215] D. Snider and R. Sorbello, "Variational calculation of the work function for small metal spheres," Solid State Communications **47**, 845–849 (1983).

[216] J. P. Perdew, H. Q. Tran, and E. D. Smith, "Stabilized jellium: Structureless pseudopotential model for the cohesive and surface properties of metals," Physical Review B **42**, 11627–11636 (1990).

[217] V. Kasperovich and V. Kresin, "Ultraviolet photoabsorption spectra of silver and gold nanoclusters," Philosophical Magazine B **78**, 385–396 (1998).

[218] K. P. Charlé, L. König, S. Nepijko, I. Rabin, and W. Schulze, "The surface plasmon resonance of free and embedded Ag-clusters in the size range 1, 5 nm< d< 30 nm," Crystal Research and Technology: Journal of Experimental and Industrial Crystallography **33**, 1085–1096 (1998).

[219] A. Liebsch, "Surface-plasmon dispersion and size dependence of Mie resonance: silver versus simple metals," Physical Review B **48**, 11317 (1993).

[220] G. Vignale, C. A. Ullrich, and S. Conti, "Time-dependent density functional theory beyond the adiabatic local density approximation," Physical Review Letters **79**, 4878 (1997).

[221] Y. Kurzweil and R. Baer, "Quantum memory effects in the dynamics of electrons in gold clusters," Physical Review B **73**, 075413 (2006).

[222] R. Kosloff, "Propagation methods for quantum molecular dynamics," Annual review of Physical Chemistry **45**, 145–178 (1994).

[223] J. Z. H. Zhang, *Theory and application of quantum molecular dynamics* (World Scientific, 1998).

[224] T. N. Truong, J. J. Tanner, P. Bala, J. A. McCammon, D. J. Kouri, B. Lesyng, and D. K. Hoffman, "A comparative study of time dependent quantum mechanical wave packet evolution methods," The Journal of Chemical Physics **96**, 2077–2084 (1992).

[225] A. Borisov, A. Kazansky, and J. Gauyacq, "Resonant charge transfer in ion–metal surface collisions: Effect of a projected band gap in the H–Cu (111) system," Physical Review B **59**, 10935 (1999).

[226] A. Borisov, J. Gauyacq, and S. Shabanov, "Wave packet propagation study of the charge transfer interaction in the F—Cu (1 1 1) and –Ag (1 1 1) systems," Surface Science **487**, 243–257 (2001).

[227] F. Aguilar-Galindo, A. G. Borisov, and S. Díaz-Tendero, "Ultrafast dynamics of electronic resonances in molecules adsorbed on metal surfaces: a wave packet propagation approach," Journal of Chemical Theory and Computation **17**, 639–654 (2021).

[228] J. J. Sakurai and J. Napolitano, *Modern quantum mechanics, second edition* (Cambridge University Press, 2017).

[229] E. Chulkov, A. Borisov, J. Gauyacq, D. Sánchez-Portal, V. Silkin, V. Zhukov, and P. Echenique, "Electronic excitations in metals and at metal surfaces," Chemical Reviews **106**, 4160–4206 (2006).

[230] R. Kosloff, "Time-dependent quantum-mechanical methods for molecular dynamics," The Journal of Physical Chemistry **92**, 2087–2100 (1988).

[231] C. Leforestier, R. H. Bisseling, C. Cerjan, M. D. Feit, R. Friesner, A. Guldberg, A. Hammerich, G. Jolicard, W. Karrlein, H. D. Meyer, N. Lipkin, O. Roncero, and R. Kosloff, "A comparison of different propagation schemes for the time dependent Schrödinger equation," Journal of Computational Physics **94**, 59–80 (1991).

[232] M. Feit, J. Fleck Jr, and A. Steiger, "Solution of the Schrödinger equation by a spectral method," Journal of Computational Physics **47**, 412–433 (1982).

[233] M. Feit and J. Fleck Jr, "Solution of the Schrödinger equation by a spectral method II: Vibrational energy levels of triatomic molecules," The Journal of Chemical Physics **78**, 301–308 (1983).

[234] A. D. Bandrauk and H. Shen, "Improved exponential split operator method for solving the time-dependent Schrödinger equation," Chemical Physics Letters **176**, 428–432 (1991).

[235] F. Aguilar-Galindo, *Theoretical study of adsorption, excitation and resonant charge transfer of organic molecules on metal surfaces*, Ph.D. thesis, Universidad Autónoma de Madrid (2019).

[236] D. Kosloff and R. Kosloff, "A Fourier method solution for the time dependent Schrödinger equation as a tool in molecular dynamics," Journal of Computational Physics **52**, 35–53 (1983).

[237] C. C. Marston and G. G. Balint-Kurti, "The Fourier grid Hamiltonian method for bound state eigenvalues and eigenfunctions," The Journal of Chemical Physics **91**, 3571–3576 (1989).

[238] B. Shizgal, "Spectral methods in chemistry and physics," Scientific Computation. Springer (2015).

[239] V. Ermoshin and A. Kazansky, "Wave packet study of H- decay in front of a metal surface," Physics Letters A **218**, 99–104 (1996).

[240] D. Bohm, *Quantum theory* (Courier Corporation, 2012).

[241] G. Vignale and W. Kohn, "Current-dependent exchange-correlation potential for dynamical linear response theory," Physical Review Letters **77**, 2037–2040 (1996).

[242] H. O. Wijewardane and C. A. Ullrich, "Time-dependent Kohn–Sham theory with memory," Physical Review Letters **95**, 086401 (2005).

[243] A. Borisov, A. Kazansky, and J. Gauyacq, "Finite time effect in the charge transfer process during an ion-metal surface collision," Physical Review Letters **80**, 1996 (1998).

[244] A. Zugarramurdi, N. Zabala, and E. Chulkov, *Electronic structure, dynamics and spectroscopy of metallic nanosized systems: Pb thin overlayers and Na nanocontacts*, Ph.D. thesis, University of the Basque Country (2011).

[245] N. Koval, *Electron dynamics in the interaction of atomic particles with spherical metal clusters*, Ph.D. thesis, University of the Basque Country (2016).

[246] T. P. Rossi, M. Kuisma, M. J. Puska, R. M. Nieminen, and P. Erhart, "Kohn–Sham decomposition in real-time time-dependent density-functional theory: An efficient tool for analyzing plasmonic excitations," Journal of Chemical Theory and Computation **13**, 4779–4790 (2017).

[247] D. Beck, "Self-consistent calculation of the polarizability of small jellium spheres," Physical Review B **30**, 6935 (1984).

[248] J. Friedel, "XIV. The distribution of electrons round impurities in monovalent metals," The London, Edinburgh, and Dublin Philosophical Magazine and Journal of Science **43**, 153–189 (1952).

[249] W. Kohn and L. J. Sham, "Quantum density oscillations in an inhomogeneous electron gas," Physical Review **137**, A1697–A1705 (1965).

[250] f. W. Halperin, "Quantum size effects in metal particles," Reviews of Modern Physics **58**, 533 (1986).

[251] E. Townsend and G. W. Bryant, "Plasmonic properties of metallic nanoparticles: The effects of size quantization," Nano Letters **12**, 429–434 (2012).

[252] S. Thongrattanasiri, A. Manjavacas, and F. J. García de Abajo, "Quantum finite-size effects in graphene plasmons," ACS Nano **6**, 1766–1775 (2012).

[253] O. A. Yeshchenko, I. M. Dmitruk, A. M. Dmytruk, and A. A. Alexeenko, "Influence of annealing conditions on size and optical properties of copper nanoparticles embedded in silica matrix," Materials Science and Engineering: B **137**, 247–254 (2007).

[254] J. Tiggesbäumker, L. Köller, K. H. Meiwes-Broer, and A. Liebsch, "Blue shift of the Mie plasma frequency in Ag clusters and particles," Physical Review A **48**, R1749 (1993).

[255] L. Serra and A. Rubio, "Core polarization in the optical response of metal clusters: generalized time-dependent density-functional theory," Physical Review Letters **78**, 1428 (1997).

[256] T. Reiners, C. Ellert, M. Schmidt, and H. Haberland, "Size dependence of the optical response of spherical sodium clusters," Physical Review Letters **74**, 1558 (1995).

[257] C. Bréchignac, P. Cahuzac, N. Kebaili, J. Leygnier, and A. Sarfati, "Collective resonance in large free potassium cluster ions," Physical Review Letters **68**, 3916 (1992).

[258] J. Lerme, H. Baida, C. Bonnet, M. Broyer, E. Cottancin, A. Crut, P. Maioli, N. Del Fatti, F. Vallee, and M. Pellarin, "Size dependence of the surface plasmon resonance damping in metal nanospheres," The Journal of Physical Chemistry Letters **1**, 2922–2928 (2010).

[259] W. A. De Heer, "The physics of simple metal clusters: experimental aspects and simple models," Reviews of Modern Physics **65**, 611 (1993).

[260] T. V. Shahbazyan, "Landau damping of surface plasmons in metal nanostructures," Physical Review B **94**, 235431 (2016).

[261] N. A. Mortensen, J. B. Khurgin, and M. Wubs, *World Scientific Handbook of Metamaterials and Plasmonics*, Vol. 4 (World Scientific, 2017) Chap. 3.

[262] A. V. Uskov, I. E. Protsenko, N. A. Mortensen, and E. P. O'Reilly, "Broadening of plasmonic resonance due to electron collisions with nanoparticle boundary: a quantum mechanical consideration," Plasmonics **9**, 185–192 (2014).

[263] C. Tserkezis, *Towards quantum nanophotonics: from quantum-informed plasmonics to strong coupling*, Ph.D. thesis, Syddansk Universitet (2021).

[264] W. Kraus and G. C. Schatz, "Plasmon resonance broadening in small metal particles," The Journal of Chemical Physics **79**, 6130–6139 (1983).

[265] P. Apell and D. R. Penn, "Optical properties of small metal spheres: surface effects," Physical Review Letters **50**, 1316 (1983).

[266] M. Barma and V. Subrahmanyam, "Optical absorption in small metal particles," Journal of Physics: Condensed Matter **1**, 7681 (1989).

[267] J. Aizpurua and A. Borisov, *World Scientific Handbook of Metamaterials and Plasmonics*, Vol. 4 (World Scientific, 2017) Chap. 4.

[268] Å. Ljungbert and P. Apell, "The role of electron-hole pair excitations in the optical absorption of metals, particularly metal spheres," Solid State Communications **46**, 47–50 (1983).

[269] R. Zhang, L. Bursi, J. D. Cox, Y. Cui, C. M. Krauter, A. Alabastri, A. Manjavacas, A. Calzolari, S. Corni, E. Molinari, E. A. Carter, F. J. García de Abajo, H. Zhang, and P. Nordlander, "How to identify plasmons from the optical response of nanostructures," ACS Nano **11**, 7321–7335 (2017).

[270] J. Zuloaga, E. Prodan, and P. Nordlander, "Quantum plasmonics: optical properties and tunability of metallic nanorods," ACS Nano **4**, 5269–5276 (2010).

[271] J. Mertens, A. L. Eiden, D. O. Sigle, F. Huang, A. Lombardo, Z. Sun, R. S. Sundaram, A. Colli, C. Tserkezis, J. Aizpurua, S. Milana, A. C. Ferrari, and J. J. Baumberg, "Controlling subnanometer gaps in plasmonic dimers using graphene," Nano Letters **13**, 5033–5038 (2013).

[272] V. Kravtsov, S. Berweger, J. M. Atkin, and M. B. Raschke, "Control of plasmon emission and dynamics at the transition from classical to quantum coupling," Nano Letters **14**, 5270–5275 (2014).

[273] J. P. Kottmann and O. J. Martin, "Plasmon resonant coupling in metallic nanowires," Optics Express **8**, 655–663 (2001).

[274] J. M. McMahon, S. K. Gray, and G. C. Schatz, "Optical properties of nanowire dimers with a spatially nonlocal dielectric function," Nano Letters **10**, 3473–3481 (2010).

[275] A. I. Fernández-Domínguez, P. Zhang, Y. Luo, S. A. Maier, F. J. García-Vidal, and J. B. Pendry, "Transformation-optics insight into nonlocal effects in separated nanowires," Physical Review B **86**, 241110 (2012).

[276] W. Yan, M. Wubs, and N. Asger Mortensen, "Projected dipole model for quantum plasmonics," Physical Review Letters **115**, 137403 (2015).

[277] E. Chulkov, V. Silkin, and P. Echenique, "Image potential states on metal surfaces: binding energies and wave functions," Surface Science **437**, 330–352 (1999).

[278] M. Ludwig, A. K. Kazansky, G. Aguirregabiria, D. C. Marinica, M. Falk, A. Leitenstorfer, D. Brida, J. Aizpurua, and A. G. Borisov, "Active control of ultrafast electron dynamics in plasmonic gaps using an applied bias," Physical Review B **101**, 241412 (2020).

[279] R. R. Letfullin, C. Joenathan, T. F. George, and V. P. Zharov, "Laser-induced explosion of gold nanoparticles: potential role for nanophotothermolysis of cancer," Nanomedicine **1**, 473–480 (2006).

[280] T. Fennel, K. H. Meiwes-Broer, J. Tiggesbäumker, P. G. Reinhard, P. M. Dinh, and E. Suraud, "Laser-driven nonlinear cluster dynamics," Reviews of Modern Physics **82**, 1793–1842 (2010).

[281] M. Danckwerts and L. Novotny, "Optical frequency mixing at coupled gold nanoparticles," Physical Review Letters **98**, 026104 (2007).

[282] Y. Shen, "Surface properties probed by second-harmonic and sum-frequency generation," Nature **337**, 519 (1989).

[283] J. Rudnick and E. A. Stern, "Second-harmonic radiation from metal surfaces," Physical Review B **4**, 4274–4290 (1971).

[284] J. E. Sipe, V. C. Y. So, M. Fukui, and G. I. Stegeman, "Analysis of second-harmonic generation at metal surfaces," Physical Review B **21**, 4389–4402 (1980).

[285] M. Zavelani-Rossi, M. Celebrano, P. Biagioni, D. Polli, M. Finazzi, L. Duo, G. Cerullo, M. Labardi, M. Allegrini, J. Grand, and P. Adam, "Near-field second-harmonic generation in single gold nanoparticles," Applied Physics Letters **92**, 093119 (2008).

[286] J. Butet, G. Bachelier, I. Russier-Antoine, C. Jonin, E. Benichou, and P. F. Brevet, "Interference between selected dipoles and octupoles in the optical second-harmonic generation from spherical gold nanoparticles," Physical Review Letters **105**, 077401 (2010).

[287] J. Butet, K. Thyagarajan, and O. J. Martin, "Ultrasensitive optical shape characterization of gold nanoantennas using second harmonic generation," Nano Letters **13**, 1787–1792 (2013).

[288] X. M. Hua and J. I. Gersten, "Theory of second-harmonic generation by small metal spheres," Physical Review B **33**, 3756–3764 (1986).

[289] J. I. Dadap, J. Shan, K. B. Eisenthal, and T. F. Heinz, "Second-harmonic rayleigh scattering from a sphere of centrosymmetric material," Physical Review Letters **83**, 4045–4048 (1999).

[290] J. I. Dadap, J. Shan, and T. F. Heinz, "Theory of optical second-harmonic generation from a sphere of centrosymmetric material: small-particle limit," Journal of the Optical Society of America B **21**, 1328–1347 (2004).

[291] I. Russier-Antoine, E. Benichou, G. Bachelier, C. Jonin, and P. F. Brevet, "Multipolar contributions of the second harmonic generation from silver and gold nanoparticles," The Journal of Physical Chemistry C **111**, 9044–9048 (2007).

[292] G. Bachelier, I. Russier-Antoine, E. Benichou, C. Jonin, and P. F. Brevet, "Multipolar second-harmonic generation in noble metal nanoparticles," Journal of the Optical Society of America B **25**, 955–960 (2008).

[293] G. Bachelier, J. Butet, I. Russier-Antoine, C. Jonin, E. Benichou, and P. Brevet, "Origin of the optical second-harmonic generation in spherical gold nanoparticles: Local surface and nonlocal bulk contributions," Physical Review B **82**, 235403 (2010).

[294] P. Ginzburg, A. Krasavin, Y. Sonnefraud, A. Murphy, R. J. Pollard, S. A. Maier, and A. V. Zayats, "Nonlinearly coupled localized plasmon resonances: Resonant second-harmonic generation," Physical Review B **86**, 085422 (2012).

[295] D. Jin, Q. Hu, D. Neuhauser, F. von Cube, Y. Yang, R. Sachan, T. S. Luk, D. C. Bell, and N. X. Fang, "Quantum-spillover-enhanced surface-plasmonic absorption at the interface of silver and high-index dielectrics," Physical Review Letters **115**, 193901 (2015).

[296] T. Christensen, W. Yan, A. P. Jauho, M. Soljačić, and N. A. Mortensen, "Quantum corrections in nanoplasmonics: shape, scale, and material," Physical Review Letters **118**, 157402 (2017).

[297] H. Yang, X. Meng, S. Wu, J. I. Dadap, and R. M. Osgood, "Numerical surface-corrected nonlocal electrodynamic model for nanophotonic structures," Journal of the Optical Society of America B **35**, 1442–1449 (2018).

[298] M. K. Svendsen, C. Wolff, A. P. Jauho, N. A. Mortensen, and C. Tserkezis, "Role of diffusive surface scattering in nonlocal plasmonics," Journal of Physics: Condensed Matter **32**, 395702 (2020).

[299] A. R. Echarri, P. A. D. Gonçalves, C. Tserkezis, F. J. G. de Abajo, N. A. Mortensen, and J. D. Cox, "Optical response of noble metal nanostructures: quantum surface effects in crystallographic facets," Optica **8**, 710–721 (2021).

[300] V. Karanikolas, I. Thanopulos, J. D. Cox, T. Kuroda, J.-i. Inoue, N. A. Mortensen, E. Paspalakis, and C. Tserkezis, "Quantum surface effects in strong coupling dynamics," Physical Review B **104**, L201405 (2021).

[301] Q. Zhou, P. Zhang, and X. W. Chen, "Quasinormal mode theory for nanoscale electromagnetism informed by quantum surface response," Physical Review B **105**, 125419 (2022).

[302] F. Yang and K. Ding, "Transformation optics approach to mesoscopic plasmonics," Physical Review B **105**, L121410 (2022).

[303] U. Hohenester, *Nano and Quantum Optics* (Springer, 2020).

[304] P. Apell, "A simple derivation of the surface contribution to the reflectivity of a metal, and its use in the Van der Waals interaction," Physica Scripta **24**, 795 (1981).

[305] A. J. Bennett, "Influence of the electron charge distribution on surface-plasmon dispersion," Physical Review B **1**, 203 (1970).

[306] K. D. Tsuei, E. Plummer, A. Liebsch, K. Kempa, and P. Bakshi, "Multipole plasmon modes at a metal surface," Physical Review Letters **64**, 44 (1990).

[307] B. Persson and P. Apell, "Sum rules for surface response functions with application to the van der Waals interaction between an atom and a metal," Physical Review B **27**, 6058 (1983).

[308] T. B. Hoang, G. M. Akselrod, and M. H. Mikkelsen, "Ultrafast room-temperature single photon emission from quantum dots coupled to plasmonic nanocavities," Nano Letters **16**, 270–275 (2016).

[309] T. Wang and C. A. Nijhuis, "Molecular electronic plasmonics," Applied Materials Today **3**, 73–86 (2016).

[310] W. Du, T. Wang, H.-S. Chu, and C. A. Nijhuis, "Highly efficient on-chip direct electronic–plasmonic transducers," Nature Photonics **11**, 623–627 (2017).

[311] M. Parzefall, Á. Szabó, T. Taniguchi, K. Watanabe, M. Luisier, and L. Novotny, "Light from van der Waals quantum tunneling devices," Nature Communications **10**, 1292 (2019).

[312] R. Chikkaraddy, B. De Nijs, F. Benz, S. J. Barrow, O. A. Scherman, E. Rosta, A. Demetriadou, P. Fox, O. Hess, and J. J. Baumberg, "Single-molecule strong coupling at room temperature in plasmonic nanocavities," Nature **535**, 127–130 (2016).

[313] R. Liu, Z. K. Zhou, Y. C. Yu, T. Zhang, H. Wang, G. Liu, Y. Wei, H. Chen, and X. H. Wang, "Strong light-matter interactions in single open plasmonic nanocavities at the quantum optics limit," Physical Review Letters **118**, 237401 (2017).

[314] D. G. Baranov, M. Wersäll, J. Cuadra, T. J. Antosiewicz, and T. Shegai, "Novel nanostructures and materials for strong light–matter interactions," ACS Photonics **5**, 24–42 (2018).

[315] H. Leng, B. Szychowski, M. C. Daniel, and M. Pelton, "Strong coupling and induced transparency at room temperature with single quantum dots and gap plasmons," Nature Communications **9**, 4012 (2018).

[316] A. F. Kockum, A. Miranowicz, S. De Liberato, S. Savasta, and F. Nori, "Ultrastrong coupling between light and matter," Nature Reviews Physics **1**, 19–40 (2019).

[317] J. V. Pellegrotti, E. Cortés, M. D. Bordenave, M. Caldarola, M. P. Kreuzer, A. D. Sanchez, I. Ojea, A. V. Bragas, and F. D. Stefani, "Plasmonic photothermal fluorescence modulation for homogeneous biosensing," ACS Sensors **1**, 1351–1357 (2016).

[318] F. Madzharova, A. Nodar, V. Zivanovic, M. R. S. Huang, C. T. Koch, R. Esteban, J. Aizpurua, and J. Kneipp, "Gold- and silver-coated barium titanate nanocomposites as probes for two-photon multimodal microspectroscopy," Advanced Functional Materials **29**, 1904289 (2019).

[319] A. Trügler and U. Hohenester, "Strong coupling between a metallic nanoparticle and a single molecule," Physical Review B **77**, 115403 (2008).

[320] E. Waks and D. Sridharan, "Cavity QED treatment of interactions between a metal nanoparticle and a dipole emitter," Physical Review A **82**, 043845 (2010).

[321] R. Esteban, J. Aizpurua, and G. W. Bryant, "Strong coupling of single emitters interacting with phononic infrared antennae," New Journal of Physics **16**, 013052 (2014).

[322] Y. J. Zhao, M. Tian, X. Y. Wang, H. Yang, H. Zhao, and Y. G. Huang, "Quasi-static method and finite element method for obtaining the modifications of the spontaneous emission rate and energy level shift near a plasmonic nanostructure," Optics Express **26**, 1390–1401 (2018).

[323] T. P. Rossi, T. Shegai, P. Erhart, and T. J. Antosiewicz, "Strong plasmon-molecule coupling at the nanoscale revealed by first-principles modeling," Nature Communications **10**, 3336 (2019).

[324] T. Neuman, C. Huck, J. Vogt, F. Neubrech, R. Hillenbrand, J. Aizpurua, and A. Pucci, "Importance of plasmonic scattering for an optimal enhancement of vibrational absorption in SEIRA with linear metallic antennas," The Journal of Physical Chemistry C **119**, 26652–26662 (2015).

[325] M. Pelton, S. D. Storm, and H. Leng, "Strong coupling of emitters to single plasmonic nanoparticles: exciton-induced transparency and Rabi splitting," Nanoscale **11**, 14540–14552 (2019).

[326] S. Corni and J. Tomasi, "Lifetimes of electronic excited states of a molecule close to a metal surface," The Journal of Chemical Physics **118**, 6481–6494 (2003).

[327] O. Andreussi, S. Corni, B. Mennucci, and J. Tomasi, "Radiative and nonradiative decay rates of a molecule close to a metal particle of complex shape," The Journal of Chemical Physics **121**, 10190–10202 (2004).

[328] F. Aguilar-Galindo, S. Díaz-Tendero, and A. G. Borisov, "Electronic structure effects in the coupling of a single molecule with a plasmonic antenna," The Journal of Physical Chemistry C **123**, 4446–4456 (2019).

[329] P. García-González, A. Varas, F. J. García-Vidal, and A. Rubio, "Single-atom control of the optoelectronic response in sub-nanometric cavities," arXiv preprint arXiv:1903.08443 (2019).

[330] P. Leung, "Decay of molecules at spherical surfaces: nonlocal effects," Physical Review B **42**, 7622 (1990).

[331] M. Hider and P. Leung, "Nonlocal electrodynamic modeling of fluorescence characteristics for molecules in a spherical cavity," Physical Review B **66**, 195106 (2002).

[332] C. Tserkezis, N. Stefanou, M. Wubs, and N. A. Mortensen, "Molecular fluorescence enhancement in plasmonic environments: exploring the role of nonlocal effects," Nanoscale **8**, 17532–17541 (2016).

[333] R. Jurga, S. D' Agostino, F. Della Sala, and C. Ciracì, "Plasmonic nonlocal response effects on dipole decay dynamics in the weak-and strong-coupling regimes," The Journal of Physical Chemistry C **121**, 22361–22368 (2017).

[334] C. Tserkezis, N. A. Mortensen, and M. Wubs, "How nonlocal damping reduces plasmon-enhanced fluorescence in ultranarrow gaps," Physical Review B **96**, 085413 (2017).

[335] C. Tserkezis, M. Wubs, and N. A. Mortensen, "Robustness of the Rabi splitting under nonlocal corrections in plexcitonics," ACS Photonics **5**, 133–142 (2018).

[336] C. Ciracì, R. Jurga, M. Khalid, and F. Della Sala, "Plasmonic quantum effects on single-emitter strong coupling," Nanophotonics **8**, 1821–1833 (2019).

[337] E. B. Guidez and C. M. Aikens, "Quantum mechanical origin of the plasmon: from molecular systems to nanoparticles," Nanoscale **6**, 11512–11527 (2014).

[338] T. P. Rossi, A. Zugarramurdi, M. J. Puska, and R. M. Nieminen, "Quantized evolution of the plasmonic response in a stretched nanorod," Physical Review Letters **115**, 236804 (2015).

[339] M. Zapata Herrera, J. Aizpurua, A. K. Kazansky, and A. G. Borisov, "Plasmon response and electron dynamics in charged metallic nanoparticles," Langmuir **32**, 2829–2840 (2016).

[340] D. C. Marinica, J. Aizpurua, and A. G. Borisov, "Quantum effects in the plasmon response of bimetallic core-shell nanostructures," Optics Express **24**, 23941–23956 (2016).

[341] H. C. Weissker, *Optical Properties of Noble Metal Clusters from the Ab Initio Perspective* (Elsevier, 2018).

[342] F. Marchesin, P. Koval, M. Barbry, J. Aizpurua, and D. Sanchez-Portal, "Plasmonic response of metallic nanojunctions driven by single atom motion: quantum transport revealed in optics," ACS Photonics **3**, 269–277 (2016).

[343] X. Zambrana-Puyalto and N. Bonod, "Purcell factor of spherical Mie resonators," Physical Review B **91**, 195422 (2015).

[344] R. Kosloff, "Quantum molecular dynamics on grids," Dynamics of molecules and chemical reactions , 185–230 (1996).

[345] S. Raza, S. Kadkhodazadeh, T. Christensen, M. Di Vece, M. Wubs, N. A. Mortensen, and N. Stenger, "Multipole plasmons and their disappearance in few-nanometre silver nanoparticles," Nature Communications **6**, 8788 (2015).

[346] K. D. Tsuei, E. Plummer, A. Liebsch, E. Pehlke, K. Kempa, and P. Bakshi, "The normal modes at the surface of simple metals," Surface Science **247**, 302–326 (1991).

[347] F. P. Schmidt, H. Ditlbacher, U. Hohenester, A. Hohenau, F. Hofer, and J. R. Krenn, "Universal dispersion of surface plasmons in flat nanostructures," Nature Communications **5**, 3604 (2014).

[348] U. Hohenester and G. Unger, "Nanoscale electromagnetism with the boundary element method," Physical Review B **105**, 075428 (2022).

[349] P. Avouris and B. N. J. Persson, "Excited states at metal surfaces and their non-radiative relaxation," The Journal of Physical Chemistry **88**, 837–848 (1984).

[350] J. C. Tully, "Chemical dynamics at metal surfaces," Annual Review of Physical Chemistry **51**, 153–178 (2000).

[351] W. Gebauer, A. Langner, M. Schneider, M. Sokolowski, and E. Umbach, "Luminescence quenching of ordered π-conjugated molecules near a metal surface: Quaterthiophene and PTCDA on Ag(111)," Physical Review B **69**, 155431 (2004).

[352] M. C. Chong, G. Reecht, H. Bulou, A. Boeglin, F. Scheurer, F. Mathevet, and G. Schull, "Narrow-line single-molecule transducer between electronic circuits and surface plasmons," Physical Reiew Letters **116**, 036802 (2016).

[353] A. Fedorov, P. Krasnov, M. Visotin, F. Tomilin, S. Polyutov, and H. Ågren, "Charge-transfer plasmons with narrow conductive molecular bridges: A quantum-classical theory," The Journal of Chemical Physics **151**, 244125 (2019).

[354] A. Sundaramurthy, K. Crozier, G. Kino, D. Fromm, P. Schuck, and W. Moerner, "Field enhancement and gap-dependent resonance in a system of two opposing tip-to-tip Au nanotriangles," Physical Review B **72**, 165409 (2005).

[355] A. Szabo and N. S. Ostlund, *Modern quantum chemistry: introduction to advanced electronic structure theory* (Courier Corporation, 2012).

[356] D. C. Marinica, V. M. Silkin, A. K. Kazansky, and A. G. Borisov, "Controlling gap plasmons with quantum resonances," Physical Review B **98**, 155426 (2018).

[357] L. Wu, H. Duan, P. Bai, M. Bosman, J. K. Yang, and E. Li, "Fowler–nordheim tunneling induced charge transfer plasmons between nearly touching nanoparticles," ACS Nano **7**, 707–716 (2013).

[358] A. Zoumi, A. Yeh, and B. J. Tromberg, "Imaging cells and extracellular matrix in vivo by using second-harmonic generation and two-photon excited fluorescence," Proceedings of the National Academy of Sciences **99**, 11014–11019 (2002).

[359] P. J. Campagnola, A. C. Millard, M. Terasaki, P. E. Hoppe, C. J. Malone, and W. A. Mohler, "Three-dimensional high-resolution second-harmonic generation imaging of endogenous structural proteins in biological tissues," Biophysical Journal **82**, 493–508 (2002).

[360] V. Kravtsov, R. Ulbricht, J. M. Atkin, and M. B. Raschke, "Plasmonic nanofocused four-wave mixing for femtosecond near-field imaging," Nature Nanotechnology **11**, 459–464 (2016).

[361] F. Krausz and M. Ivanov, "Attosecond physics," Reviews of Modern Physics **81**, 163 (2009).

[362] A. Bouhelier, M. Beversluis, A. Hartschuh, and L. Novotny, "Near-field second-harmonic generation induced by local field enhancement," Physical Review Letters **90**, 013903 (2003).

[363] C. Anceau, S. Brasselet, J. Zyss, and P. Gadenne, "Local second-harmonic generation enhancement on gold nanostructures probed by two-photon microscopy," Optics Letters **28**, 713–715 (2003).

[364] K. Li, M. I. Stockman, and D. J. Bergman, "Enhanced second harmonic generation in a self-similar chain of metal nanospheres," Physical Review B **72**, 153401 (2005).

[365] S. Palomba, M. Danckwerts, and L. Novotny, "Nonlinear plasmonics with gold nanoparticle antennas," Journal of Optics A: Pure and Applied Optics **11**, 114030 (2009).

[366] C. Ciracì, E. Poutrina, M. Scalora, and D. R. Smith, "Second-harmonic generation in metallic nanoparticles: clarification of the role of the surface," Physical Review B **86**, 115451 (2012).

[367] J. Butet, P. F. Brevet, and O. J. Martin, "Optical second harmonic generation in plasmonic nanostructures: from fundamental principles to advanced applications," ACS Nano **9**, 10545–10562 (2015).

[368] M. Celebrano, X. Wu, M. Baselli, S. Großmann, P. Biagioni, A. Locatelli, C. De Angelis, G. Cerullo, R. Osellame, B. Hecht, L. Duò, F. Ciccacci, and M. Finazzi, "Mode matching in multiresonant plasmonic nanoantennas for enhanced second harmonic generation," Nature Nanotechnology **10**, 412 (2015).

[369] J. Butet, G. D. Bernasconi, M. Petit, A. Bouhelier, C. Yan, O. J. F. Martin, B. Cluzel, and O. Demichel, "Revealing a mode interplay that controls second-harmonic radiation in gold nanoantennas," ACS Photonics **4**, 2923–2929 (2017).

[370] G. D. Bernasconi, J. Butet, and O. J. Martin, "Dynamics of second-harmonic generation in a plasmonic silver nanorod," ACS Photonics **5**, 3246–3254 (2018).

[371] H. Husu, R. Siikanen, J. Makitalo, J. Lehtolahti, J. Laukkanen, M. Kuittinen, and M. Kauranen, "Metamaterials with tailored nonlinear optical response," Nano Letters **12**, 673–677 (2012).

[372] A. Slablab, L. L. Xuan, M. Zielinski, Y. de Wilde, V. Jacques, D. Chauvat, and J. F. Roch, "Second-harmonic generation from coupled plasmon modes in a single dimer of gold nanospheres," Optics Express **20**, 220–227 (2012).

[373] K. Thyagarajan, J. Butet, and O. J. F. Martin, "Augmenting second harmonic generation using Fano resonances in plasmonic systems," Nano Letters **13**, 1847–1851 (2013).

[374] P. Ginzburg, A. V. Krasavin, G. A. Wurtz, and A. V. Zayats, "Nonperturbative hydrodynamic model for multiple harmonics generation in metallic nanostructures," ACS Photonics **2**, 8–13 (2015).

[375] L. J. Black, P. R. Wiecha, Y. Wang, C. H. de Groot, V. Paillard, C. Girard, O. L. Muskens, and A. Arbouet, "Tailoring second-harmonic generation in single l-shaped plasmonic nanoantennas from the capacitive to conductive coupling regime," ACS Photonics **2**, 1592–1601 (2015).

[376] S. D. Gennaro, M. Rahmani, V. Giannini, H. Aouani, T. P. H. Sidiropoulos, M. Navarro-Cia, S. A. Maier, and R. F. Oulton, "The interplay of symmetry and scattering phase in second harmonic generation from gold nanoantennas," Nano Letters **16**, 5278–5285 (2016).

[377] A. V. Krasavin, P. Ginzburg, and A. V. Zayats, "Free-electron optical nonlinearities in plasmonic nanostructures: A review of the hydrodynamic description," Laser & Photonics Reviews **12**, 1700082 (2018).

[378] K. Thyagarajan, S. Rivier, A. Lovera, and O. J. Martin, "Enhanced second-harmonic generation from double resonant plasmonic antennae," Optics Express **20**, 12860–12865 (2012).

[379] H. Aouani, M. Navarro-Cia, M. Rahmani, T. P. H. Sidiropoulos, M. Hong, R. F. Oulton, and S. A. Maier, "Multiresonant broadband optical antennas as efficient tunable nanosources of second harmonic light," Nano Letters **12**, 4997–5002 (2012).

[380] "Nonlinear plasmonic antennas," Materials Today **17**, 478 – 485 (2014).

[381] B. Metzger, L. Gui, J. Fuchs, D. Floess, M. Hentschel, and H. Giessen, "Strong enhancement of second harmonic emission by plasmonic resonances at the second harmonic wavelength," Nano Letters **15**, 3917–3922 (2015).

[382] H. Linnenbank, Y. Grynko, J. Förstner, and S. Linden, "Second harmonic generation spectroscopy on hybrid plasmonic/dielectric nanoantennas," Light: Science and Applications **5**, e16013 (2016).

[383] K. Y. Yang, J. Butet, C. Yan, G. D. Bernasconi, and O. J. Martin, "Enhancement mechanisms of the second harmonic generation from double resonant aluminum nanostructures," ACS Photonics **4**, 1522–1530 (2017).

[384] B. Metzger, M. Hentschel, and H. Giessen, "Probing the near-field of second-harmonic light around plasmonic nanoantennas," Nano Letters **17**, 1931–1937 (2017).

[385] J. Berthelot, G. Bachelier, M. Song, P. Rai, G. C. Des Francs, A. Dereux, and A. Bouhelier, "Silencing and enhancement of second-harmonic generation in optical gap antennas," Optics Express **20**, 10498–10508 (2012).

[386] W. Cai, A. P. Vasudev, and M. L. Brongersma, "Electrically controlled nonlinear generation of light with plasmonics," Science **333**, 1720–1723 (2011).

[387] L. Kang, Y. Cui, S. Lan, S. P. Rodrigues, M. L. Brongersma, and W. Cai, "Electrifying photonic metamaterials for tunable nonlinear optics," Nature Communications **5**, 4680 (2014).

[388] R. Czaplicki, H. Husu, R. Siikanen, J. Mäkitalo, M. Kauranen, J. Laukkanen, J. Lehtolahti, and M. Kuittinen, "Enhancement of second-harmonic generation from metal nanoparticles by passive elements," Physical Review Letters **110**, 093902 (2013).

[389] M. R. Singh, "Enhancement of the second-harmonic generation in a quantum dot–metallic nanoparticle hybrid system," Nanotechnology **24**, 125701 (2013).

[390] D. Turkpence, G. B. Akguc, A. Bek, and M. E. Tasgin, "Engineering nonlinear response of nanomaterials using Fano resonances," Journal of Optics **16**, 105009 (2014).

[391] E. Shaviv and U. Banin, "Synergistic effects on second harmonic generation of hybrid CdSe–Au nanoparticles," ACS Nano **4**, 1529–1538 (2010).

[392] H. Linnenbank and S. Linden, "Second harmonic generation spectroscopy on second harmonic resonant plasmonic metamaterials," Optica **2**, 698–701 (2015).

[393] A. Babaze, R. Esteban, J. Aizpurua, and A. G. Borisov, "Second-harmonic generation from a quantum emitter coupled to a metallic nanoantenna," ACS Photonics **7**, 701–713 (2020).

[394] J. Butet, S. Dutta-Gupta, and O. J. Martin, "Surface second-harmonic generation from coupled spherical plasmonic nanoparticles: Eigenmode analysis and symmetry properties," Physical Review B **89**, 245449 (2014).

This thesis theoretically addresses the optoelectronic response of metallic nanoparticles (MNPs) as well as their coupling to quantum emitters (QEs). Nanometer-scale systems are considered where optical nonlinearity, nonlocality, or electron-transfer processes can all play an important role. To capture these quantum many-body effects, Time-Dependent Density Functional Theory (TDDFT) is used primarily, in combination with semiclassical models based on the Surface-Response Formalism (SRF) and classical calculations based on the Local-Response Approximation (LRA). We demonstrate that, at the nanometer scale, electron spill-out and surface-enabled Landau damping drastically influence the electromagnetic interaction between MNPs and QEs, which produce a redshift and broadening of plasmonic resonances not captured by classical theories. We show that these effects can be correctly described by the semiclassical SRF, in particular when one considers the nonlocal response in the direction parallel to the metal surface. In addition, we predict that the hybridization between the electronic states of the QE and those of the MNPs drastically modifies the optical response of the coupled system in situation involving subnanometric distances, since the exciton in the QE is found to be quenched due to electronic coupling. This quenching dramatically influences the frequency and the width of the optical resonances sustained by the coupled structure. Finally, we demonstrate that the electromagnetic coupling of a QE to a spherical MNP can also affect the nonlinear optical response of the system, enabling otherwise-forbidden second-harmonic generation (SHG). The content of this thesis thus presents a quantum mechanical many-body approach to the optical response of plasmonic cavities, which provides new insights into coupling with emitters, electron transfer processes and nonlinear effects. All these effects are of paramount importance in nowadays state-of-the-art Nanophotonics.

CSIC
Consejo Superior de Investigaciones Científicas
Centro de Física de Materiales
Materials Physics Center
Ismo